Dimitri Volchenkov *Editor*

The Many Facets of Complexity Science

In Memory of Professor Valentin Afraimovich

Higher Education Press

Springer

Nonlinear Physical Science

Laurent Raymond, Centre de Physique Théorique, Aix-Marseille University, Marseille, France

Victor I. Shrira, School of Computing and Maths, Keele University, Keele, Staffordshire, UK

C. Steve Suh, Department of Mechanical Engineering, Texas A&M University, College Station, TX, USA

Jian-Qiao Sun, School of Engineering, University of California, Merced, Merced, CA, USA

J. A. Tenreiro Machado, ISEP-Institute of Engineering, Polytechnic of Porto, Porto, Portugal

Simon Villain-Guillot, Laboratoire Ondes et Matière d'Aquitaine, Université de Bordeaux, Talence, France

Michael Zaks, Institute of Physics, Humboldt University of Berlin, Berlin, Germany

Nonlinear Physical Science focuses on recent advances of fundamental theories and principles, analytical and symbolic approaches, as well as computational techniques in nonlinear physical science and nonlinear mathematics with engineering applications.

Topics of interest in *Nonlinear Physical Science* include but are not limited to:

- New findings and discoveries in nonlinear physics and mathematics
- Nonlinearity, complexity and mathematical structures in nonlinear physics
- Nonlinear phenomena and observations in nature and engineering
- Computational methods and theories in complex systems
- Lie group analysis, new theories and principles in mathematical modeling
- Stability, bifurcation, chaos and fractals in physical science and engineering
- Discontinuity, synchronization and natural complexity in physical sciences
- Nonlinear chemical and biological physics

This book series is indexed by the SCOPUS database.

To submit a proposal or request further information, please contact Dr. Mengchu Huang(Email: mengchu.huang@springer.com).

More information about this series at http://www.springer.com/series/8389

Dimitri Volchenkov
Editor

The Many Facets
of Complexity Science

In Memory of Professor Valentin Afraimovich

Higher
Education
Press

Springer

Editor
Dimitri Volchenkov
Mathematics and Statistics
Texas Tech University
Lubbock, TX, USA

In memoriam of Prof. Valentin Afraimovich (1945–2018), a visionary scientist, respected colleague, generous mentor, and loyal friend.

Preface

The present volume on *The Many Facets of Complexity Science* explores recent developments in theoretical research and data analysis of real-world complex systems. The volume is dedicated to the memory of our colleague Valentin Afraimovich (1945–2018), a visionary scientist, respected colleague, generous mentor, and loyal friend. Professor Afraimovich was a Soviet, Russian, and Mexican mathematician known for his works in dynamical systems theory, qualitative theory of ordinary differential equations, bifurcation theory, concept of attractor, strange attractors, space-time chaos, mathematical models of nonequilibrium media and biological systems, traveling waves in lattices, complexity of orbits, and dimension-like characteristics in dynamical systems.

The collection of works in this edited volume opens with the contribution of Maurice Courbage on the directional entropy for spatially extended systems. Other works discuss entropy, information, and complexity functions in complexity science, including selective chaos of traveling waves in feedforward chains of bistable maps, hidden periodic motions for brushless motor with unsteady torque excitation, chunking rhythmic synchronization in globally coupled phase oscillators. We discuss multistability, oscillations, and rhythmic synchronization in complex systems, mixed diffusion, nonlinear dynamics of deep open-ocean convection, solvability for some Non-Fredholm operators with drift, complex dynamics of solutions in rotating fluids, dynamics of water-constrained economies, and the use of anisotropic random walks for the study of isolation and integration patterns in urban environments. The volume facilitates a better understanding of the mechanisms and phenomena in nonlinear dynamics and develops the corresponding mathematical theory to apply nonlinear design to practical engineering.

Valentin Afraimovich was a generous, gregarious, energetic presence at the very heart of nonlinear dynamics and complexity science communities, all of which were transformed by his presence. We hope that the scientific community will benefit from this edited volume.

Lubbock, TX, USA   Dr. Dimitri Volchenkov

Contents

The Directional Entropy for Spatially Extended Dynamical Systems

Maurice Courbage

Abstract In investigating the complexity of dynamical systems, entropy and quantities connected with it play an important role. The nonlinear dynamics of a spatially extended physical, chemical or biological system is complex, as for example in the case of turbulent flows, unlike the simple motion of laminar fluids. The complexity of spatially extended dynamical systems has been described in many ways using several models. We will address issues related to the role of directional entropy in Lattice Dynamical Systems (LDS) and lifts of circle maps on the plane.

1   Introduction

Valentin Afraimovich had a great culture and an intellectual curiosity concerning the relation of the theory of Dynamical Systems with physical phenomena. He had many collaborations with physicists, especially Misha Rabinovich and George Zaslavsky. With Valentin Afraïmovich, I had many discussions about Chaos and especially the spatio-temporal chaos, during his visits to Paris. Chaotic phenomena in spatially extended systems were well known to physicists (e.g. [21, 30]). Quite quickly, in order to avoid the mathematical difficulties of PDEs, Coupled Map Lattices (CML) have been proposed as models of spatially extended dynamical systems where both space and time take discrete values (e.g. [23]). The construction of SRB measures for CML [14] was a first attempt at a mathematical model of spatio-temporal chaos. It was followed by [13, 22] and others (e.g. [15]).

The topological properties of CML were not as well known (see the review [2]). There was particular results about chaos of traveling wave solutions ([8]) and about the abundance of such solutions in CML [3] generalizing results found about density

M. Courbage (✉)
Laboratoire Matière et Systèmes Complexes (MSC), UMR 7057 CNRS et Université
Paris 7- Denis Diderot, Case 7056, Bâtiment Condorcet, 10, rue Alice Domon et Léonie Duquet,
75205 Paris Cedex 13, France
e-mail: maurice.courbage@univ-paris-diderot.fr

of periodic traveling waves in Cellular Automata (CA) with chaotic behavior [17]. Such property is reminiscent to the abundance of periodic orbits in hyperbolic sets describing chaotic behavior.

The role of directional topological entropy in terms of the velocity of moving of the Lab frame (or Observer) was introduced by Milnor in CA [24, 25], and studied later (e.g. [18, 26, 27]). Collet and Eckmann [16] have defined and studied the topological entropy density in parabolic PDEs. The directional topological entropy in Lattice Dynamical Systems (LDS) was introduced and studied in [5]. We shall come back to this subject in Sect. 2.

Entropy, a notion derived from thermodynamics, has been adapted to other disciplines by Boltzmann, Shannon and Kolmogorov. This story of metamorphosis of scientific concepts has, as a common thread, the quantification of disorder. Shannon, an engineer and mathematician working at Bell Labs, carried it into the theory of telecommunications and message coding. This was the starting point of information theory. Shannon's idea was to quantify the degree of stochasticity of random or periodic messages by a formula borrowed from Boltzmann. Kolmogorov has partitioned the phase space of a dynamical system into cells, coding a trajectory by the sequence of its passages between the cells thus providing a message. Considering an invariant measure of the dynamical system, Kolmogorov then introduced a probabilistic notion of entropy of the paths (the above sequences) in order to classify systems according to their degree of "stochasticity". If the paths are periodic, no stochasticity can be expected. Conversely, when the trajectories of the system are very irregular, the paths are similar to a sequence of a random walk. Seeking for a solution to the isomorphism problem of dynamical systems, he brought a great novelty in ergodic theory, introducing a notion of entropy associated with measure-theoretical deterministic dynamical systems. Subsequently, another notion of entropy of dynamical systems was introduced to characterize the topological aspects of complexity related to the sensitive separation of neighboring trajectories and to better illustrate the Kolmogorov-Sinai entropy (KS). Inspired by the Kolmogorov-Thikomorov abstract works associated with ϵ-capacity of a set, Dinaburg and Bowen formulated the notion of topological entropy of dynamical system [12, 20] based on fast time increase of the number of distinct trajectories up to a given precision ε (see below), highlighting an exponential or non-exponential abundance. A non-probabilistic topological complexity is thus introduced. The rate of abundance of distinct trajectories in chaotic systems, becomes a measure of complexity. For weakly chaotic systems this is more difficult to quantify, so only a limiting trend with scale laws can be illustrated in some examples ([9]). But in spatially extended systems, to this temporal complexity is added a spatiotemporal complexity which manifests the action of time in space.

The Dinaburg-Bowen entropy is based on the count of trajectories of a dynamical system, as a function of the length of the temporal segment. A trajectory of the map F on the space X: $(x^0, x^1, x^2, ..., x^n, ...)$, $x^n \in X$ where

$$x^n = F^n(x^0) = F(F...F(x^0))$$

The finite sequence $(x^0, x^1, x^2, ..., x^T)$ is called a **T-segment**.

Let $(y^0, y^1, y^2, ..., y^n, ...)$ be another trajectory. These two trajectories are $(\epsilon - T)$ separated if there is $n \leq T$, such that $d(x^n, y^n) > \epsilon$. Let K be a compact subset of X and let S be a packet of T-segments starting from K and pairwise $(\epsilon - T)$ separated. The maximal number of elements of such S is finite as a consequence of the compacity of K. Let $C_\epsilon(K, T)$ be this number, i.e.

$$C_\epsilon(K, T) = \max\{card \ (S), \ S \ \text{is} \ (\epsilon, T) - \text{separated}\},$$

One may visualize each such packet reminding the definition of the compacity in $\mathbb{R}^2$. A compact set K is in this case a subset that can contain only finite number of discs of diameter 2ϵ, whatever small is ϵ. Substitute $\mathbb{R}^2$ by the space of the T-segments, putting each segment in the center of a tube of diameter 2ϵ.

Imagine a dynamic system that amplifies the initial differences (for example the application $F(x) = 2x \ (\text{mod } 1)$, $x \in [0, 1]$) then, if we consider a sufficiently large T, we can fit more and more close initial conditions that will separate in this time interval of length T. It is a multiplication of trajectories under the T-increase. Of course, these trajectories are also erratic, but what matters is their mutual separation. If $C_\epsilon(K, T)$ exponentially increases with T, then we obtain a topological entropy for the set K as the rate of the exponential:

$$\lim_{\epsilon \to 0} \lim_{T \to \infty} \frac{1}{T} \ln C_\epsilon(K, T) = h_{top}(K)$$

In other words, $C_\epsilon(K, T) \curvearrowleft A e^{h_{top}(K)T}$, when ϵ goes to zero. Its supremum on all K defines *the topological entropy* of F (a concept otherwise introduced by Adler et al. in 1965 [1] by counting recoveries of X). It is called topological entropy because it is invariant when two applications F and G are topologically equivalent (i.e. when all the trajectories of G are trajectories of F transported by a *continuous* transformation and vice versa). Of course, the analytical calculation of entropy is generally very difficult because of the complexity of the previous explicit formulas. In some classes of dynamic systems, formulas could be derived. Numerical algorithms make it possible to estimate the entropy of a dynamic system, in particular the algorithm of Grassberger and Procaccia [32].

The entropy introduced above is associated with a single map F. For an extended system, there is a natural symmetry defined by the space translation. In [9] a notion of directional complexity was introduced by Afraïmovich and Zaslasky for lifts of circle maps acting on $\mathbb{R}^2$. The directional entropy of lifts of a Markov circle map has been studied in [6].

2 LDS and Directional Entropy

An observer in a frame moving with some constant velocity, looking to a fluid flow in a pipe, could indicate that the system exhibits a variety of localized structures moving down the pipe along the stream (see for example [11]). A great number of patterns

Fig. 1 The parallelogram
$W(m, T, \theta)$
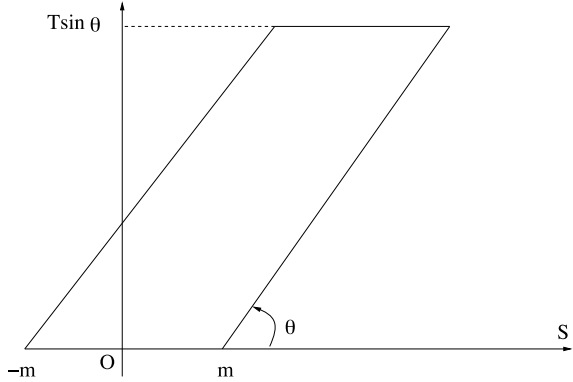
appear for some time interval and change in such a way that the behavior of the system for different velocities may be different. The dependence of the complexity on the frame velocity is caught using space-time parallelograms, with two sides parallel to the space-time direction corresponding to this velocity (Fig. 1).

A characteristic of such complexity has been introduced in [24, 25] for the cellular automata (CA) and it was called the directional entropy. It was shown in a family of (CA) that, the number of different pictures in the parallelogram with two sides of length T parallel to a prescribed angle θ in the space–time coordinate system, and the two others "horizontal" sides of length L parallel to the space-axis, behaves asymptotically as Ce^{TH_θ}, $T >> 1$, where the constant C depends on L. The quantity H_θ is said to be the topological entropy in the direction θ.

The continuity of this entropy as a function of θ has been studied. It was shown in [29] that, as a function of the direction θ, the directional entropy may be discontinuous. The continuity of the measure-theoretic directional entropy as a function of θ has been proved [26, 27]. In this case, the directional entropy is always finite and bounded, an optimal bound depending only on the range of the local interaction has been given in [18]. In [10], the topological directional entropy of permutative CA was estimated.

2.1 LDS

Here we consider the case of one dimensional lattice. Let I be a compact subset of a metric space and let $d(\cdot, \cdot)$ be the corresponding distance. Consider the direct product $I^{\mathbb{Z}}$ endowed with the product topology and assume the existence of a compact subset $\mathscr{M} \subset I^{\mathbb{Z}}$ and the existence of a map F from $\mathscr{M}$ into itself. The pair $(\mathscr{M}, F)$ is called a lattice dynamical system (LDS). More information about this system (continuity, expansivity, etc.) are specified elsewhere (e.g. [15]).

Some examples are of the following type:

(i) Linearly coupled Lattice Dynamical System [4], for which $\mathcal{M} \subset I^{\mathbb{Z}}$ where I is a compact interval and the map is given by

$$(Fu)_s = \sum_{n \in \mathbb{Z}} l_n f(u_{s-n}), \ s \in \mathbb{Z},$$

(ii) Coupled map lattice (CML): discrete versions of PDEs of the evolutional type. The following one is the discrete version of a reaction-diffusion equation:

$$(Fu)_s = u_s + f(u_s) + \epsilon(u_{s-1} - 2u_s + u_{s+1}), \ s \in \mathbb{Z},$$

where $\epsilon \geq 0$ is the coupling parameter and f, the local map, has a compact absorbing region.

Other interesting examples can be found in the literature, see for instance [13, 15, 22, 23] and references therein.

2.2 Definitions and Properties of Directional Entropy

The definitions are inspired from the Milnor's definition of directional entropy for cellular automata [24, 25]. An orbit of F in $\mathcal{M}$ is a sequence $\{u^t\}_{t \in \mathbb{Z}^+} = \{u^t_s\}_{s \in \mathbb{Z}, \ t \in \mathbb{Z}^+}$ where $u^t = \{u^t_s\}_{s \in \mathbb{Z}}$, $u^t \in \mathcal{M}$ and $u^{t+1} = Fu^t$ for all $t \in \mathbb{Z}^+$ ($\mathbb{Z}^+$ is the set of non-negative integers). Define the following window as:

$$W(m, T, \theta) = \{(x + t \cos\theta, t \sin\theta) : \ -m < x < m, \ t \in [0, T]\} \cap (\mathbb{Z} \times \mathbb{Z}^+). \tag{1}$$

Given $W(m, T, \theta)$ and a number $\epsilon > 0$, a set $K \subset \mathcal{M}$ is called $(\epsilon, W(m, T, \theta))$-separated if for every pair of distinct elements $u, \bar{u} \in K$, there exists $(s, t) \in W(m, T, \theta)$ such that

$$d((F^t u)_s, (F^t \bar{u})_s) \geq \epsilon.$$

The number of distinct orbits with accuracy ϵ in the window $W(m, T, \theta)$ (1) is defined by

$$N(\epsilon, W(m, T, \theta)) = \max\{\#(K) \ : \ K \text{ is an } (\epsilon, W(m, T, \theta)) - separated \text{ set}\}.$$

One can compute its exponential growth with T, with the size m and when ϵ decreases.

Definition 1 The topological entropy of $(\mathcal{M}, F)$ in the direction θ is defined by

$$H_\theta(\mathcal{M}, F) = \lim_{\epsilon \to 0} \left(\overline{\lim_{m \to \infty}} \left(\overline{\lim_{T \to \infty}} \frac{1}{T} \log N(\epsilon, W(m, T, \theta)) \right) \right),$$

$N(\epsilon, S_T)$ is a non-decreasing function of m and a non-increasing function of ϵ. Moreover, $H_\theta(\mathcal{M}, F) \in [0, +\infty]$.

Remark 1 More general definition of the directional entropy can be given by using a more general kind of windows, as in [5]. However, it is proved that it is equal to the one given here.

Remark 2 In many important cases like the above (CML), $H_\theta(\mathcal{M}, F) = +\infty$. One may normalize by the spatial length as in the thermodynamic limit in classical statistical mechanics [28]:

Definition 2 The density of topological entropy of $(\mathcal{M}, F)$ in the direction θ is defined by

$$h_\theta(\mathcal{M}, F) = \lim_{\epsilon \to 0} \left(\overline{\lim_{m \to \infty}} \frac{1}{2m+1} \left(\left(\overline{\lim_{T \to \infty}} \frac{1}{T \sin\theta} \log N(\epsilon, W(m, T, \theta)) \right) \right) \right).$$

As for the topological entropy in the direction θ, the quantity $h_\theta(\mathcal{M}, F)$ exists and belongs to $[0, +\infty]$.

Note that $(2m + 1)T\sin\theta$ represents the surface of the parallelogram $W(m, T, \theta)$.

It is shown that:

(i) the directional entropy and the density of directional entropy have a property invariance under topological conjugacy [5].

(ii) In many examples of lattice dynamical systems as those given above, the map F commutes with spatial translations [23], i.e. $F \circ \sigma = \sigma \circ F$, where $(\sigma u)_s = u_{s+1}$, $s \in \mathbb{Z}$. For a lattice dynamical transformation F commuting with the shift transformation the density of the directional entropy coincides with the Conze-Katznelson-Weiss entropy of the $\mathbb{Z}^2$-action defined by (F, σ) i.e. it is a constant function with respect to the direction [5, 7]. It is also proved in counterexamples that this result fails to be true when the space invariance is broken [7].

(iii) By using symbolic dynamics a formulae for the directional entropy density for weakly coupled hyperbolic maps.

(iv) A measure-theoretical density of directional entropy for LDS has been constructed in [19] with similar properties.

3   Directional Entropy in Lifts Dynamical Systems

The relationship between deterministic dynamics and irreversible stochastic processes is so complex to understand that several simple models have been used to address them. One of them is the Sinaï billiard where a billiard particle has a chaotic motion which is approximated by a random walk. A toy model to this motion is the random walk on the line due to lifts of circle map. The complexity of such motion is described by topological entropy, as proposed Afraïmovich and Zaslavsky [9],

by extending the concept of directional entropy to trajectories of lift maps. Let us introduce some definitions.

Definition 3 A continuous function f of the unit circle S^1 into itself is a continuous map f onto $[0, 1]$ such that $f(0) = f(1) \,(\mathrm{mod}\,1)$. A Lift of f is a continuous function $F : \mathbb{R} \to \mathbb{R}$ such that $f(x) = F(x) \bmod 1$. It follows that

$$F(x + 1) = p + F(x)$$

where p is an integer, called the degree of f.

If the degree of f is 1, then:

$$F(x + p) = p + f(x)$$

$x \in [0, 1]$ and $p \in \mathbb{Z}$. We shall briefly account here of the study in [6, 9] based on an example of the so-called Markov map (Fig. 2) also denoted $f(x)$.

The step of the trajectory of $F(x)$ at time n, $F^{(n+1)}(x) - F^{(n)}(x) = f^{(n+1)}(x) - f^{(n)}(x)$, represents the step of a deterministic walk on the line $\mathbb{R}$, at time n. The step $F^{(n+1)}(x) - F^n(x)$ is non-negative since $f(x) - x$ is so. Given an invariant measure under f, one obtains a probabilistic random walk. In this sense, we have a *deterministic diffusion*. In the example shown in Figure 2, on account of the expansiveness for x such that $|f'(x)| > 1$, the trajectory is irregular and unstable. The question of whether such a process converges to a normal law or not will be studied separately. The following limit:

$$\lim_{n\to\infty} \frac{(F^{(n)}(x) - F^{(n-1)}(x)) + \ldots + (F^1(x) - x)}{n} = \rho$$

Fig. 2 Example of Markov map of the circle
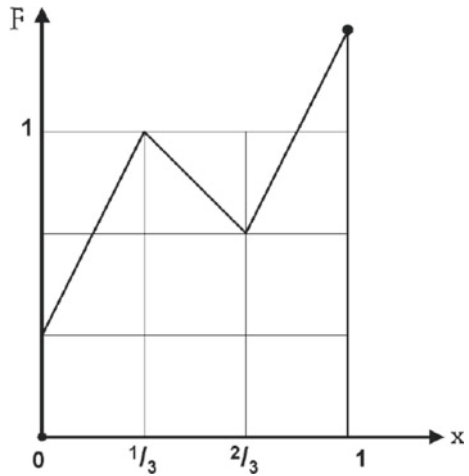
which represents the average speed of the trajectory is the so-called *rotation number* of f introduced by Poincaré in 1855. He showed that if f is monotonous, this limit exists and does not depend on x. In general, the previous limit may not exist for any initial condition. But, for a non-monotonic application F, a largest definition is introduced by using the upper limit instead of the limit in the equality. The upper limit can then depend on the initial condition:

The set:

$$\bigcup_{x\in[0,1]} \overline{\lim_{n\to\infty}} \frac{F^{(n)}(x) - x}{n} = J,$$

is a closed interval called the rotation interval of f. For any $\mu \in J$, there is a point $x \in [0, 1]$ such that $\lim\limits_{n\to\infty} \dfrac{F^{(n)}(x) - x}{n} = \mu$.

The notion of directional entropy is defined for this class of systems. The trajectories from x, $y \in \mathbb{R}$ are said $(\epsilon, W(m, T, \theta))$-separated if $((n, F^{(n)}(x)), (n, F^{(n)}(y))) \subset W(m, T, \theta))$ for all $n \leq T$, and if there is $0 \leq n \leq T$ such that $|F^{(n)}(x) - F^{(n)}(y)| \geq \epsilon$.

The subset $S \subset \mathbb{R}$ is $(\epsilon, W(m, T, \theta))$-separated if any couple x, y of S, $x \neq y$, is $(\epsilon, W(m, T, \theta))$-separated.

The number

$$C_\epsilon(W, T) = \max\{card(S), S \text{ is } (\epsilon, W, T) - \text{separated}\},$$

is called ϵ-directional complexity in direction θ.

We define the directional entropy in the space interval $[-m, m]$ by the function:

$$H_\theta(m) = \lim_{\epsilon\to 0} \overline{\lim_{T\to\infty}} \frac{\ln C_\epsilon(W, T)}{T}$$

The limit:

$$H_\theta = \lim_{m\to\infty} H_\theta(m)$$

is called the directional entropy in the direction θ. We can interpret C_ϵ and H_θ as quantities that reflect the number of trajectories traveled with a speed that converges to $\cot \theta$, because, to be in the window $W(m, T, \theta)$ the point $(F^{(n)}(x), n)$ must satisfy

$$-m + n \cot \theta \leq F^n x \leq m + n \cot \theta, \tag{2}$$

It is produced in [6] a combinatorial algorithm that calculates the directional entropy in the above class of maps. The graph of this entropy in the above example shows that the entropy is zero beyond the interval $[0, 1/2]$, which happens to be the interval of rotation. This is a general property that states that support for the entropy function is included in the rotation interval (that is, entropy counts paths that have a defined
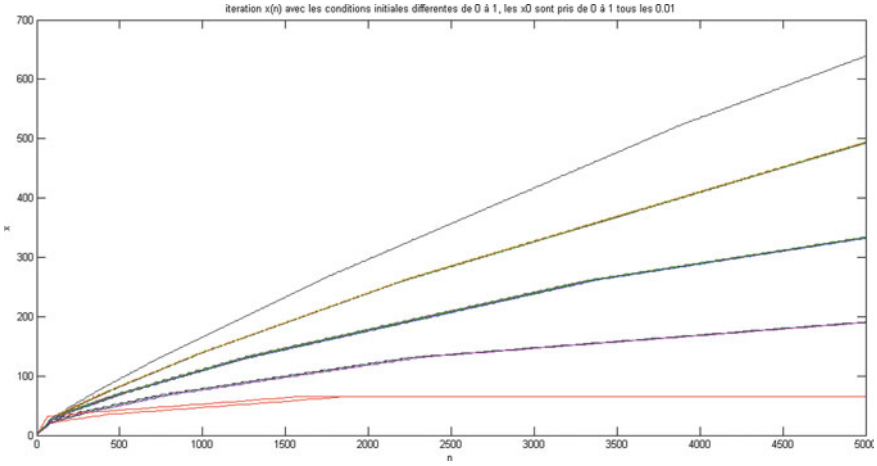
Fig. 3 Trajectories corresponding to a set of initial conditions taken from 0 to 1 every 0.01

rotation numbers). It describes the density of the trajectories in terms of rotation number and there is a value of the rotation number where the entropy is maximum.

We have drawn (Fig. 3) the distribution of 100 trajectories by considering 100 initial conditions taken from 0 to 1 every 0.01. The figure shows five lines in different colors. In fact, an enlargement of each line shows that it corresponds to several trajectories. There are five beams of trajectories that are distinguished by their rotation numbers (averaged speed), the directional entropy describes the density in trajectories of each beam, the greater the entropy in a direction θ and the more dense trajectories is the corresponding beam. Although each beam seems to evolve asymptotically regularly at a given speed, in fact it is not the case for the trajectories. The trajectories in each beam remain chaotic as shown by an enlargement of a beam piece in Fig. 4.

4 Conclusion

In formulating the ergodic hypothesis that a gas explores all regions of the state space, Boltzmann initiated the ergodic theory of the complexity of moving systems. The link between complexity and entropy has been highlighted by Boltzmann in his statistical theory of gas thermodynamics and his famous formula of entropy. Thanks to Shannon and Kolmogorov the link between complexity and entropy has appeared in other science disciplines such as probability and information theory and the theory of chaotic dynamical systems. While the Kolmogorov-Sinai (KS) is defined by a probabilistic formula like that of Shannon, the topological entropy is global because
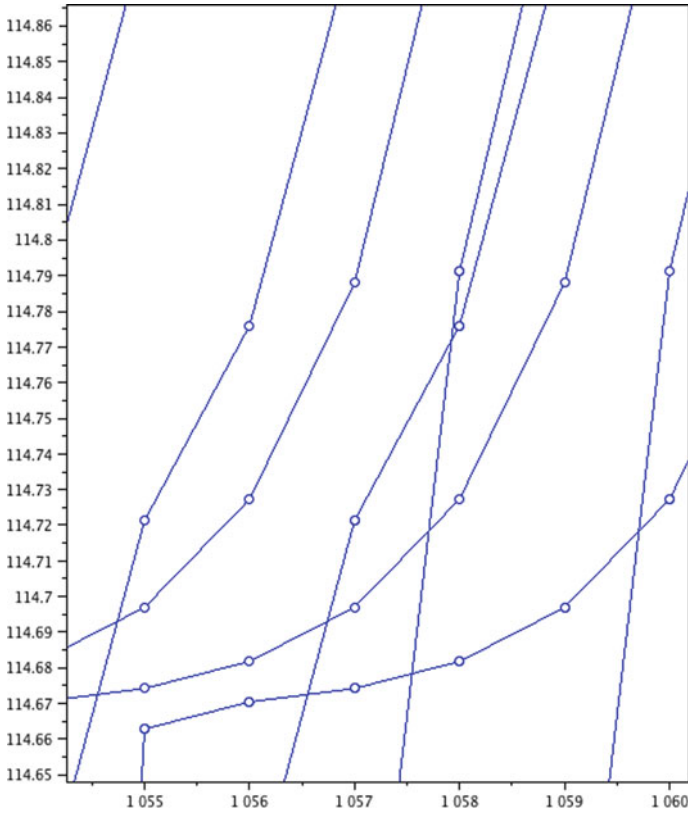
Fig. 4 Some neighboring trajectories extracted from a single beam of Fig. 3

it encompasses all the trajectories and not the more or less probable. This is why, under certain specifications, it is equal to the maximum of all the KS entropies associated with the multiple invariant probability distributions of a dynamical system.

The complexity of a deterministic dynamical system in a spatially extended environment must incorporate other parameters such as the translational frame velocity in this medium and not just the temporal sensitivity to the initial conditions (SIC). This dependence of complexity on the speed of a translational frame motion offers new insights of the dynamic complexity. A more general dependence on other spatial actions than translation must be considered in order to understand the spatio-temporal nature of extended systems.

References

1. Adler RL, Konheim AG, McAndrew MH (1965) Topological entropy. Trans Amer Math Soc 114:309–319
2. Afraimovich V, Some topological properties of lattice dynamical systems. In: Dynamics of coupled map lattices and of related spatially extended systems. Lecture notes in physics, vol 671. Springer, Berlin, Heidelberg
3. Afraimovich V, Courbage M (2000) On the abundance of traveling waves in coupled expanding circle maps. Amer Math Soc Transl 2(200):15–21
4. Afraimovich V, Fernandez B (2000) Topological properties of linearly coupled expanding map lattices. Nonlinearity 13:973–993
5. Afraïmovich V, Courbage M, Fernandez B, Morante A (2002) Directional entropy in lattice dynamical systems. In: Lerman, Shilnikov (ed) Progress in nonlinear science, vol 1 (Nizhny Novgorod, 2001), Mathematical problemes of nonlinear dynamics. Nizhny, RAS, Inst Appl Phys, Nizhny Novgorod, 9–30
6. Afraïmovich V, Courbage M, Glebsky L (2015) Directional complexity and entropy for lift mappings, discrete and continuous dynamical system, series B, 3385-340. arXiv:1212.0174
7. Afraïmovich V, Morante A, Ugalde E (2004) On the density of directional entropy in lattice dynamical systems. Nonlinearity 17:105–116
8. Afraïmovich V, Nekorkin VI (1994) Chaos of travelling waves in a discrete chain of diffusively coupled maps. Internat J Bifur Chaos 4:631–637
9. Afraïmovich V, Zaslavsky GM (2003) Space-time complexity in Hamiltonian dynamics. Chaos 13(2):519–532
10. Bernardo M, Courbage M (2000) Topological directional entropy of permutative cellular automata, preprint
11. Bohr T, Rand DA (1991) A mechanism of localized turbulence. Phys D 52:532–543
12. Bowen Rufus (1971) Entropy for group endomorphisms and homogenous spaces. Trans Amer Math Soc 154:404–414
13. Bricmont J, Kupiainien A (1995) Coupled analytic maps. Nonlinearity 8:379–396
14. Bunimovich LA, Sinaï YG (1988) Space-time chaos in coupled map lattices. Nonlinearity 1:491–516
15. Chaté H, Courbage M (eds) (1997) Lattice dynamics. Phys D 103:1–612
16. Collet P, Eckmann J-P (1999) The definition and measurement of the topological entropy per unit volume in parabolic PDEs. Nonlinearity 12:451–473
17. Courbage M (2001) On the abundance of traveling waves in infinite 1-D cellular automata. Phys D 103:133–144. Courbage M, Mercier D, Yasmineh S (1997) Travelling waves and chaotic properties in cellular automata. Chaos 9:893–901. A 35 Courbage M, Yasmineh S (1999) Wavelengths distributions of chaotic travelling waves in some cellular automata. Phys D 150:63–83
18. Courbage M, Kamiński B (2002) On the directional entropy of generated by cellular automata. Studia Math 153:285–295
19. Courbage M, Kaminski B (2008) Density of measure-theoretical directional entropy for lattice dynamical systems. Int J Bifurc Chaos 18:161–168
20. Dinaburg EI (1969) A correlation between topological entropy and metric entropy. Soviet Math Dokl 11:13–16
21. Fenstermacher PR, Swinney HL, Gollub JP (1979) Dynamical instabilities and the transition to chaotic Taylor vortex flow. J Fluid Mech 94(1):103–128
22. Jiang M, Pesin Ya (1998) Equilibrium measures for coupled map lattices: existence, uniqueness and finite-dimensional approximations. Commun Math Phys 193:675–711
23. Kaneko K (ed) (1993) Theory and applications of coupled map lattices. Wiley, Chichester
24. Milnor J (1986) Directional entropies of cellular automaton-maps. In: Disordered systems and biological organization. Springer, Berlin, pp 113–115
25. Milnor J (1988) On the entropy geometry of cellular automata. Complex Syst 2:357–385

26. Park KK (1994) Continuity of directional entropy. Osaka J Math 31:613–628
27. Park KK (1999) On directional entropy functions. Israel J Math 113:243–267
28. Robinson DW, Ruelle D (1967) Mean entropy of states in classical statistical mechanics. Commun Math Phys 5:288–300
29. Smillie J (1988) Properties of the directional entropy function for cellular automata. In: Dynamical systems. Lectures notes in math, vol 1342. Springer, Berlin, pp 689–705
30. Swinney HL, Gollub JP (ed) (1981) Hydrodynamic instabilities and the transition to turbulence. Springer
31. Katok A, Hasselblatt B (1995) Introduction to the modern theory of dynamical systems. Cambridge University Press, Cambridge
32. Grassberger P, Procaccia I (1983) Estimation of the Kolmogorov entropy from a chaotic signal. Phys. Rev. A 28:2591–2593

Detecting Regularity with Complexity Functions

Olivier Bui and Xavier Leoncini

Abstract In this chapter we consider using complexity function as proposed by V. Afraimovich to detect the presence of regularity in a priori chaotic systems. When dealing with systems in high dimensional phase space, a form of master-slave system is proposed. The complexity is measured, tested in the standard map and is able to detect sticky regions with long lived portions of coarse-grained regular trajectories. It is then applied to the Hamiltonian Mean Field (HMF) model. Surprisingly in this last setting, complexity shows that strong regular behavior is observed with a characteristic exponent of power law decays between 2 and 3 and does not seem to depend on the considered dimensions of the phase space, giving rise to future investigations in what may happen in this system.

1 Introduction

Understanding of complex dynamical systems in high dimensions has always been a difficult task [1]. If the dimensions of the system are quite large, one is undoubtedly looking for some randomness in order to use some statistical approach deriving some equilibrium statistical physics, or out of equilibrium ones, or various forms of kinetic equations. Conversely one may be looking for some regularity, or synchronization phenomena that would lead to an effectively simple low dimensional dynamical system. However most of these considerations are usually falling apart when looking already at low dimensional Hamiltonian chaos [2–12]. The presence of so-called mixed phase space with a mixture of regions with regular motion (islands) and chaotic regions (chaotic sea) implies de facto that simple chaotic system can have non trivial dynamics, with a non unique ergodic measure. These systems can display as well the phenomenon of stickiness that generates a slow decay of correlation functions and induces non trivial anomalous transport properties [3, 6, 13–25]. In order to

O. Bui (✉) · X. Leoncini
Aix Marseille Univ, Université de Toulon CNRS CPT, Marseille, France
e-mail: olivi.bui@gmail.com

X. Leoncini
e-mail: Xavier.Leoncini@cpt.univ-mrs.fr

track these phenomena, different tools have been used like finite time Lyapunov exponents [26], Poincaré recurrences [21, 27–30], Birkhoff sums [31, 32], among these possibilities the use of tools inspired by complexity functions such as so-called chaotic jets has been quite successful when considering low dimensional systems [19, 22, 33, 34]. When considering higher dimensions besides synchronization, regular behavior can as well be observed in high dimensional Hamiltonian system, and self-organized regularization has been observed in systems with long range interactions [35–38]. However as will be seen from the brief introduction to complexity function, measuring complexity becomes very quickly intractable in high-dimensional phase space. In order to circumvent we propose to consider a master slave system, where the slave dynamics will be taking place in a low dimensional phase space and driven by the high-dimensional one in consideration.

What follows is probably not conventional in a regular book chapter, but since it is the main driving force of the presented results we believe it is worth mentioning as these were inspired by Valentin Afraimovich to whom this book is dedicated. In fact, these ideas came up during the visit of Valentin Afraimovich in the Centre de Physique Théorique in Marseille during the summer of 2013. He was invited by Xavier Leoncini for a short month as an invited Professor of the University of Toulon. After that period a rough draft of definitions and set up of looking at practical work was written, mostly by Valentin Afraimovich himself. We reproduce in the first parts some of this draft paper that never came to realization. Indeed, due to various reasons, it took some time to get to the practical work, in fine this lead to a Ph.D. proposal and is one of the main motivations of the Ph.D. work of Olivier Bui. But his first visit to Mexico was unfortunately planned in 2017 and scheduled for the summer of 2018.

In this chapter we show some preliminary results obtained from this approach, considering only Hamiltonian systems, the goal being to identify and characterize regularity phenomena within chaotic areas of certain systems.

The chapter is organized as follows, first in Sect. 2, we briefly recall the definition of complexity functions and set up the general context of master-slave systems we had in mind with Valentin Afraimovich. Then, in Sect. 4, we check the diagnostic in low dimensions using the standard map as a test bed, finally in Sect. 5 we apply it to a system with many degrees of freedom before concluding.

2   Complexity Functions

2.1   Complexity Function

A metric complexity function is a characteristic of instability of trajectories of a dynamical system that shows how fast they diverge in the phase space. The definition was first introduced by Bowen [39] who used the classical notion of $\varepsilon-$separability [40]. Let

$$T^t \, : \, M \longrightarrow M, \ t \geq 0 \, ,$$
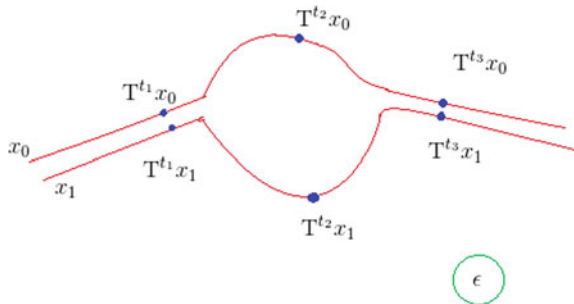
Fig. 1 Trajectories of x_0 and x_1. We note $T^t x_i$ the position of x_i at time t. ϵ is the diameter of the green circle. In this illustration x_0 and x_1 are (ϵ, t_2) but also (ϵ, t_3)−separated, meaning that even if the trajectories come close to each other again they are still considered as separated. There is thus a minimal time τ such that two points are (ϵ, τ)−separated; τ is the first time when they get separated

be an evolution operator of a dynamical system with a phase space M that is endowed with a distance $d(x, y)$. Given an initial point $x_0 \in M$, let $T^t x_0 = x(t)$ be the representative point on the trajectory $\{T^t x_0\}_{t \geq 0}$. One can introduce a collection of distances on M:

$$d_t(x_0, y_0) = \sup_{0 \leq \tau \leq t} d(T^\tau x_0, T^\tau y_0) .$$

We say that x_0 and y_0 are (ε, t)−separated if $d_t(x_0, y_0) \geq \varepsilon$. It means that on the segments

$$\bigcup_{\tau \in [0,t]} T^\tau x_0, \quad \bigcup_{\tau \in [0,t]} T^\tau y_0$$

of trajectories going through x_0, y_0 correspondingly, there are representative points $T^{\tau_0} x_0, T^{\tau_0} y_0$ such that $d(T^{\tau_0} x_0, T^{\tau_0} y_0) \geq \varepsilon$.

Given a set A of initial points, we say that a set $B \subset A$ is (ε, t)−separated if each pair x_0, y_0 of points in B is (ε, t)−separated.

A description of the notion is depicted in Fig. 1.

Definition 1 The quantity

$$C_{\varepsilon,t}(A) = \max\{\text{card}(B), B \subset A, \text{ is } (\varepsilon, t) - \text{separated}\} , \tag{1}$$

where card(B) is the number of elements (cardinality) in B and max is taken over all (ε, t)−separated subsets of A, is called the (ε, t)−Complexity of the set A. As a function of t it is called the ε−complexity function. The number $\ln C_{\varepsilon,t}(A)$ is called the (ε, t)−capacity of A. A discussion on the introduced definition can be found in [22, 41–43].

The asymptotic behavior of $C_{\varepsilon,t}(A)$ as $t \to \infty$ or $\varepsilon \to 0$, is determined by two quantities:

- The topological entropy

$$h = h_{top}(A) := \lim_{\varepsilon \to 0} \overline{\lim_{t \to \infty}} \frac{\ln C_{\varepsilon,t}(A)}{t} \; . \tag{2}$$

- The fractal (upper box) dimension of A

$$b := \lim_{t \to \infty} \overline{\lim_{\varepsilon \to 0}} \frac{\ln C_{\varepsilon,t}(A)}{-\ln \varepsilon} \; . \tag{3}$$

Thus, if $0 < b < \infty$, $0 < h < \infty$, and $t \gg 1$, $\varepsilon \ll 1$, one can believe that

$$C_{\varepsilon,t}(A) = \varepsilon^{-b} \, e^{ht} \, \Theta(\varepsilon, t) \; , \tag{4}$$

where Θ is a subexponential function of t and $\ln \varepsilon$.

But if ever t and $\ln(1/\varepsilon)$ are not large, the value $C_{\varepsilon,t}(A)$ reflects an "amount of instability" that becomes feasible during the interval $[0, t]$ of time in the scale determined by the value of ε.

2.2 Local Complexity Function

Thinking about applications one has to take into account the fact that if the set A is large (in any reasonable sense), then it would be very difficult or impossible to perform numerical simulations that would be needed to find $C_{\varepsilon,t}(A)$. Moreover, sometimes it is useful to know the evolution of instability around one fixed trajectory. According to the aforementioned reasons we impose the following definition of local complexity function [43].

Fix a trajectory $\left\{ T^t x_0 \right\}_{t \geq 0}$ going through the initial point x_0 (we call it the basic trajectory) and a set A of initial points in the δ−neighborhood of x_0, such that $\delta \ll \varepsilon$. A set $B \subset A$, is said to be locally ε−separated if :

1. for every $x \in B$ there exists $\tau \in [0, t]$ such that

$$d(T^\tau x, T^\tau x_0) \geq \varepsilon$$

   and

$$d(T^s x, T^s x_0) < \varepsilon \, , \, 0 \leq s \leq \tau \; .$$

2. For every pair $x, \, x' \in B$

$$d(T^\tau x, T^{\tau'} x') \geq \varepsilon$$

   (where $d(T^{\tau'} x', T^{\tau'} x_0) \geq \varepsilon$).

Definition 2 The number

$$C_{\varepsilon,t}(x_0, A) = \max\{\text{card}(B), B \subset A, \text{ is locally } (\varepsilon, t) - \text{separated}\} \qquad (5)$$

where the maximum is taken over all locally $(\varepsilon, t)-$separated subsets of A, is called the local complexity function.

This definition works well, at least for simple systems (see for instance [33]). One may consider an ensemble of basic trajectories and study average complexity functions. But now let us consider situations in high-dimensional phase space.

3 A Master-Slave Case

We consider the following system of ODE

$$\dot{x}_i = F_i(\mathbf{x}), \ i = 1, \ldots, N \qquad (6)$$
$$\dot{y} = G(\mathbf{x}, y), \qquad (7)$$

where $\mathbf{x} = (x_1, \ldots, x_N), x_i \in \mathbb{R}^m, i = 1, \ldots, N, y \in \mathbb{R}^m, \mathbf{F} = (F_1, \ldots, F_N), i.e.$ we deal with a master-slave situation. Our goal is to study local complexity functions for each coordinates x_i using the system (7). We will proceed as follows. Fix a basic trajectory $\{T^t \mathbf{x}_0 = \mathbf{x}(t, \mathbf{x}_0), \ t \geq 0\}$ where $\mathbf{x}_0 = (x_{10}, \ldots, x_{N0})$. Given $i \in \{1, \ldots, N\}$ let us consider the $\delta-$neighborhood U_i of x_{i0}, in $\mathbb{R}^m, \delta \ll \varepsilon$, and a set $A_i \subset U_i$. Denote by $y(t, y_0)$ the solution of the equation

$$\dot{y} = G(\mathbf{x}(t, \mathbf{x}_0), y), \qquad (8)$$

satisfying $y(0, y_0) = y_0$, where $y_0 \in A_i$.

We say that two of such solutions are locally $(\varepsilon, t)-$separated if there are instants τ and $\tau', 0 \leq \tau \leq t, 0 \leq \tau' \leq t$ such that:

1. $d_i(y(\tau, y_0), x_i(\tau, \mathbf{x}_0)) \geq \varepsilon, d_i(y(\tau', y_0'), x_i(\tau', \mathbf{x}_0)) \geq \varepsilon$ and
2. $d_i(y(\tau, y_0), y(\tau', y_0') \geq \varepsilon)$, i.e. the points $y(\tau, y_0)$ and $y(\tau', y_0')$ are $\varepsilon-$distinguishable.

A set $B \subset A_i$ is locally $(\varepsilon, t)-$separated if for every pair y_0, y_0' in B the corresponding solutions $y(\tau, y_0)$ and $y(\tau', y_0')$ are locally $(\varepsilon, t)-$separated

Definition 3 The number

$$C^i_{\varepsilon,t}(x_0, A) = \max\{\text{card}(B), B \subset A_i, \text{ is locally } (\varepsilon, t) - \text{separated}\}, \qquad (9)$$

where the maximum is taken over all locally $(\varepsilon, t)-$separated subsets of A_i, is called the $i-$th local complexity function of the set A_i. As a function of t, it is called the $i-$Complexity function.

The defined quantity has a different meaning for dissipative and conservative systems.

Dissipative systems

When the coupling between the master and slave system is large enough one may observe the regime of synchronization. Then systems (8) with different initial conditions can be seen as an ensemble of auxiliary systems in the approach of [44]. According to [44] all the solutions of (8) become $\varepsilon-$indistinguishable as $t \gg 1$, so the $i-$th local Complexity function stops growing, beginning with some instant of time independently on the number of initial points in A_i.

If the rate of coupling is not sufficient to generate the synchronization regime, then this function can serve to indicate how far the system is from the synchronization regime.

Hamiltonian Case

We assume that the $i-$th subsystem in (6) corresponds to the $i-$th degree of freedom of a Hamiltonian system so $m = 2$, $x_i = (p_i, q_i)$. The system (7) can be treated as an "average" system related to the mean field approach (see below). The solution $\mathbf{x}(t, \mathbf{x}_0)$ is an external force (field) that fully (or partially) determines the dynamics of (7). Changing initial conditions in (7) we obtain a bunch of solutions that can serve as a device to measure the dynamics of the $i-$th degree of freedom of the original system (6). And the local $i-$th complexity function is a suitable quantity to reflect the amount of instability stored in the $i-$th degree of freedom. Moreover, the shape of the function can indicate subintervals of time with different rates of instability.

3.1 A Physical Interpretation of $(\varepsilon, t)-$Separability

If we give ourselves a measuring instrument with a certain precision and this precision represents a distance of δ in phase space, two points will be indistinguishable by the instrument if the distance between them is less than δ. In this case if these two indistinguishable points end up after a certain time separating by a distance of ε that is larger than δ by several orders of magnitude then this separation will appear to the observer as two points of the same initial conditions moving towards "two completely different futures" with the idea that the threshold ε defines what "two completely different futures" means, at the same time he will be only able to know there were actually two different trajectories after the separation occurs. Thus this concept encompasses the idea of unpredictability that is often associated with chaos. Thus basing a diagnostic aiming at quantifying chaos on the notion of $(\varepsilon, t)-$separability or the Complexity function is reasonable.

Definition 4 The Local Complexity function we defined in Sect. 2.2 and Sect. 3 only describes one single point x_0 of phase space. But if we take a set Q of points distributed over the whole space or a part of it, we could make the sum or the average of the complexity functions evaluated in each of these points and therefore define

$C_{\varepsilon,t}(Q, \{A\})$ with $\{A\}$ a set of neighborhoods (a neighborhood for each point of Q). We will note $A = \{A\}$ and they all will be disks of radius δ centered around a point of Q. Note: the sample of points Q we want to use should not be uniformly distributed over the space, instead the points are sampled along a trajectory. For example: if the chosen trajectory tends to remain for a long time in certain areas, the set of Q points will have to be more concentrated at these locations. Since a trajectory, in chaotic systems, may travel through the whole phase space or large part of it, the sample Q will be representative of the dynamic of the system and the associated underlying ergodic measure.

There is a similarity between complexity functions and Lyapunov's exponent since both are interested in how two adjacent initial conditions move away. The major difference between Complexity and Lyapunov's exponent is that the Complexity function ignores what happens beyond a threshold it is set by neighborhoods A that sets a size for errors δ on our initial conditions as well as a threshold ϵ through which we look at the trajectories. Thus the complexity function could detect "coarse-grained" regularities (regularities of size ε which we can vary) even if the system is chaotic at smaller scales. This can be an advantage over the Lyapunov exponent, for instance when considering particle dispersion and associated diffusion like phenomena.

3.2 Numerical Measurement of the Complexity Function

First of all, given the number of parameters that $C_{\varepsilon,t}(Q, A)$ has, we must agree on how to choose them. ε will be decided at the start of each simulation and the influence of this parameter will be analyzed. For the set Q, as we explained in Sect. 3.1, we want to sample along a trajectory: at the start of the simulation we choose an initial condition x_0, simulate its evolution in phase space and Q are positions this "particle" took at different time , we call this particle traveling the phase space the "tracer". In this case we understand that as long as the chaotic area is of a finite volume our tracer will travel across all the corners of this area and Q will be well distributed over this space. Neighborhoods A will be disks of radii $\delta \ll \varepsilon$: thus we can write our Local Complexity function as $C_{\varepsilon,t}(Q, \delta)$. The parameter t does not have to be set, because our simulation will not actually calculate $C_{\varepsilon,t}(Q, \delta)$ directly but will give the graph of a function related to $\dfrac{\mathrm{d}}{\mathrm{d}t}\left(C_{\varepsilon,t}(Q, \delta)\right)$ as a function of time. But before we can explain this last point, we need to describe our numerical program.

We will call trapping time, which we note τ, the minimum duration taken for two "particles" in phase space to be $(\varepsilon, \tau)-$separable, i.e. the first moment they are $\varepsilon-$distinguishable.

At the beginning of the simulation we choose an initial condition for our tracer whose trajectory we will follow, but we will also follow the trajectory of a second point/particle which we call "ghost" taken at a distance δ of the tracer. The simulation
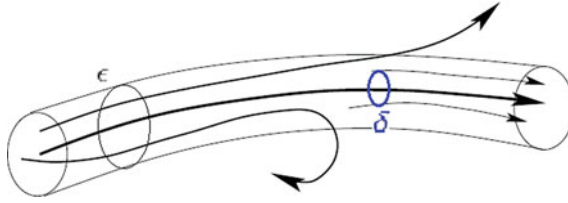
Fig. 2 Illustration of how the simulation operates. At each instant, we follow the trajectory of our tracer (here illustrated by the trajectory at the center of the tube of radius ε) and also note the trajectories of some ghosts which were generated at a distance δ of the tracer. Once a ghost escapes from the tube we generate a new one. We note the duration τ each ghost spent inside the tube before escaping it

will then measure the trapping time τ between the ghost and the tracer, and once we got the τ for this ghost we stop following the movement of the ghost and generate a new ghost at a distance δ of the tracer and measure its τ etc.

An illustration of this process is given in Fig. 2. On this figure, we associated two ghosts to the tracer instead of only one. In this case, the individual trapping time of each of them should be measured. Increasing the number of ghosts increases the number of data and therefore refines the graph we will create. This graph being a histogram of the recorded τ. Normalizing this histogram will then give us a curve that we can interpret as a probability density on the τ, noted $\rho(\tau)$ (probability that a point initially generated at δ of the tracer to have a trapping time of a certain value τ). We should insist as well that, for reasons of simplicity unlike what our definition of Complexity function would have suggested, we do not really generate the ghosts in the disk of radius δ around the tracer but on the circle of radius δ.

Now let's come back to the link between this probability density that we will measure and the Complexity function. On the following segment we will change the notation of $C_{\varepsilon,t}(Q, \delta)$ into $C(\varepsilon, t, Q, \delta)$. $C(\varepsilon, \tau + \Delta t, Q, \delta) - C(\varepsilon, \tau, Q, \delta)$ corresponds to a number of trajectories escaping from a tube of size ε around the tracer in a time Δt and it is possible to prove under certain conditions, for example if the chaotic space we consider has a finite volume, that by posing $\rho(\varepsilon, \tau, Q, \delta)$, the probability that a ghost has a trapping time of τ, we have[42]:

$$\frac{1}{C(\epsilon, \tau, Q, \delta)}[C(\epsilon, \tau + \Delta t, Q, \delta) - C(\epsilon, \tau, Q, \delta)] \approx \rho(\epsilon, \tau, Q, \delta)\Delta t \qquad (10)$$

Thus our histogram which corresponds to this probability density ρ will be linked to how the proliferation of trajectories varies over time as it is related to the (logarithmic) derivative of the Complexity function.

4   Application to the Standard Map

4.1   Brief Introduction to the Standard Map

The Standard Map is a discrete dynamical system governed by the following equations:

$$p_{n+1} = p_n + K \sin(q_n) \, [2\pi] \tag{11}$$
$$q_{n+1} = q_n + p_{n+1} \, [2\pi]$$

Given the presence of the modulo 2π, the phase space is a torus. K is a positive parameter. The phase portrait of the system is very dependent on the K parameter (see Fig. 3), which is why we will perform our simulations for different values of K. The Standard Map is a standard system if we want to study Hamiltonian chaos as it illustrates quite well the situation where chaotic zones and regular zones coexist in the phase space. At $K = 0$, the trajectories are all regular but chaotic areas appear very quickly and grow as K is increased (see Fig. 3). From $K \simeq 1$, chaotic areas fill more than half of the torus. However, instead of focusing solely on the fact that the proportion of chaotic zones increases with K, we want to address the question of the behavior of trajectories within the chaotic zones themselves. Chaotic trajectories near the boundaries between regular and chaotic areas are expected to have regularities that would not be seen in the absence of these "frontiers".

If we want to study the influence of the existence of regular zones on chaotic trajectories then the Standard Map is an excellent object of study since we have this parameter, K, which allows to make these zones appear or disappear at will. In addition, the Standard Map being a discrete dynamic system allows us to avoid errors caused by numerical integration algorithms. In a discrete system, the only limitation is the accuracy of the machine itself.

4.2   Study Framework

Let's look at the different plots depicted in Fig. 3. We can see then that when K is large enough, we have a large "chaotic sea" in which are some islands of regular trajectories. The islands disappear as K grows until the system is completely chaotic. These pictures, although useful, do not inform us about the phenomena within each chaotic sea for the different values of K. We need to diagnose the potential regularities that the trajectories in these chaotic seas may have. We need to check whether the diagnostics described in Sect. 3.2 can identify these patterns and if so how are they characterized? Although we suspect that regularities will only appear when there are islands it is important to test our diagnosis for $K = 10$ since in their absence the

(a) K=0.1

(b) K=1.1

(c) K=1.5

(d) K=10
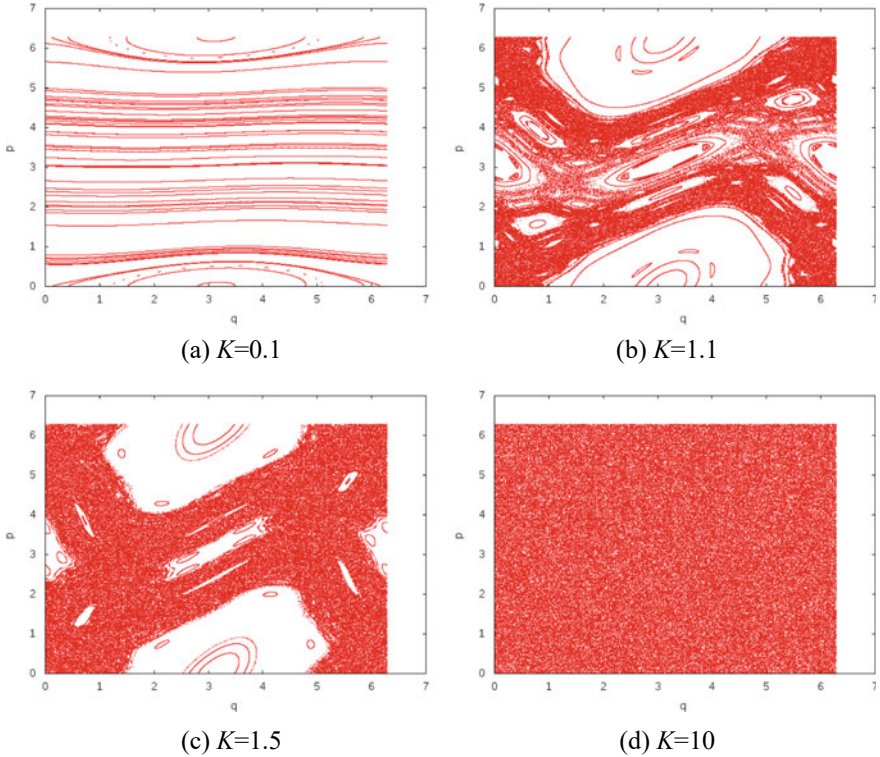
Fig. 3 Phase portrait of the Standard Map for different value of parameter K. For $K = 1.1$ and $K = 1.5$, we see coexisting chaotic seas and regular island

system is supposed to be completely chaotic; making our measurements for $K = 10$ then gives us a reference concerning the results we should expect for a system that is completely chaotic and should lead to Gaussian statistics (see for instance) and thus we can make a comparison with the case presenting islands.

Reminder: the simulation measures the time it takes for two neighboring points to separate, noted τ, in order to determine its probability density noted $\rho(\tau)$. The tracer we choose will always be in the chaotic sea since we are studying the chaos of the Standard Map. How $\rho(\tau)$ decays when τ approach ∞ is what we are looking at to describe the presence or absence of regularities. We imagine that a system with more regularities than another should have a slower decay of $\rho(\tau)$. On the other hand, we do not expect that the decay of ρ will be slower than $1/\tau^2$ since otherwise the average trapping time $\langle \tau \rangle = \int \rho(\tau) \cdot \tau \, d\tau$ would be infinite, and that would need to be further investigated.

(a) $K = 10$. Semi-log plot.

(b) Log-log plot for different values of K.
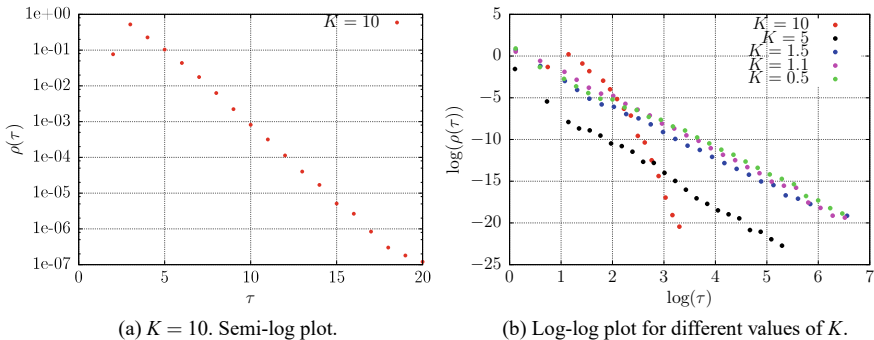
Fig. 4 Fig. 4a shows that when we have global chaos we get and exponential decay of $\rho(\tau)$. The presence of regular islands, on the other hand, leads to a power law behavior and $\rho(\tau) \sim 1/\tau^{\alpha}$ Fig. 4b: in red we have $K = 10$ and its exponential decay. The color code is (black : $K = 5$), (blue : $K = 1.5$), (magenta : $K = 1.1$), (green : $K = 0.5$). The curves for $K = 1.5$, 1.1 and 0.5, which corresponds to cases where we see very large islands, are very similar and have a slope $\alpha \approx 3$. Even the case $K = 5$, where the islands almost disappear, $\rho(\tau)$ is still very similar to the other "island-cases": the slope α for $\tau \to \infty$ is similar and the only differences appear for low τ

4.3 Results on the Trapping Times τ

The histograms obtained for the different values of K are normalized. The result is that $\rho(\tau)$ quickly reaches a maximum and then decays either exponentially or in power law. The figures obtained are those of Fig. 4. We see that global chaos is characterized by an exponential decrease while the presence of islands shows longer trapping times that decrease algebraically, in $1/\tau^{\alpha}$. Thus, making a diagnostic based on the measurement of trapping time effectively allows us to detect regularities in a chaotic space by looking at how $\rho(\tau)$ decays: regularities related to the islands of stability are characterized by an algebraic decrease in $\rho(\tau)$ instead of an exponential one.

That said, we can try to ensure that this algebraic decay characterizes the phenomena around the islands we mentioned: we can try to locate where the tracer-ghost couples were located when they contributed to these "high" τ. We are locating these areas of high τ in Fig. 5 for $K = 1.5$. What we did was choose a high time $\tau_{threshold}$ which corresponds to a time located in the $1/\tau^{\alpha}$ tail in Fig. 4b.

In conclusion, diagnostics based on trapping times may allow us to study phenomena at the boundary between islands of stability and the chaotic sea. Among the known phenomena happening at these boundaries is the phenomenon of "stickiness" [45]. It is the phenomenon by which trajectories remain around the border of an island for very large times giving the impression, if we limited ourselves to small time scales, that they would be regular and would never visit the chaotic zone. Stickiness manifests itself the most strongly around the smallest islands, these islands typically also feature fractal structures [45]. The stickiness phenomena can be detected, for example, by using Poincaré recurrences. But we may also ask ourselves if our diag-
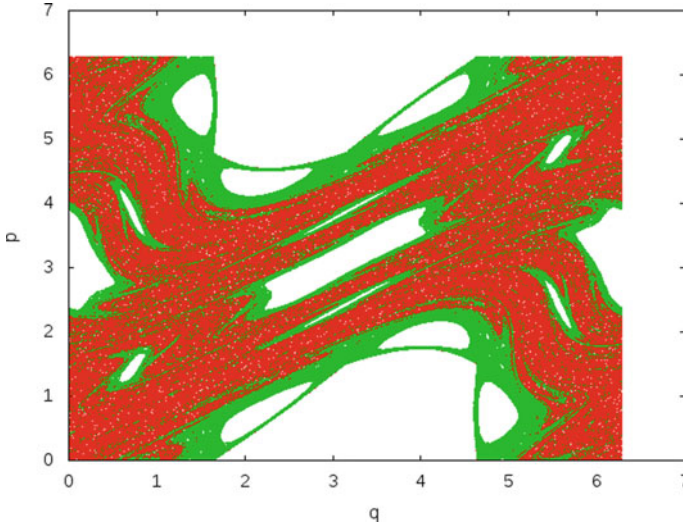
Fig. 5 Regions with large trapping time is colored in green. We considered here the case with $K = 1.5$, The chaotic see is plotted in red. We notice that large τ are located at the vicinity of islands, and confirm the stickiness phenomenon with the presence of regular coarse-grained trajectories in the vicinity of islands

nostic based on trapping times within these jets (regular coarse-grained tubes) can capture this kind of phenomena. Indeed, we can suspect that the sticking trajectories are also trajectories with certain regularities in terms of $(\epsilon, t)-$separability and they may even be the trajectories that generated the very long τ we found in our plots.

To test this hypothesis we use the same method used for plotting Fig. 5 but using a $\tau_{threshold}$ much larger: we obtain Fig. 6 and we can see that the contributors to very long trapping times τ are sticking regions (Fig. 7).

4.4 Summary of the Efficiency of Detecting Regularity with Complexity for the la Standard Map

Let's come back to the algebraic or exponential decrease of the probability density function of τ. Remember that the formula (10) indicates that $\rho(\tau)$ is related to the logarithmic derivative of the complexity function with respect to time. In the case of $K = 10$, that is globally chaotic, this exponential decrease indicates that Complexity "reaches" its asymptotic value after a very short time: "all" the $\epsilon-$separations are done after a few iterations of the map. This behavior seems intuitive and logical for a globally hyperbolic system. On the contrary, in the presence of islands, the much slower decrease (algebraic) shows that even after a long time all the trajectories have
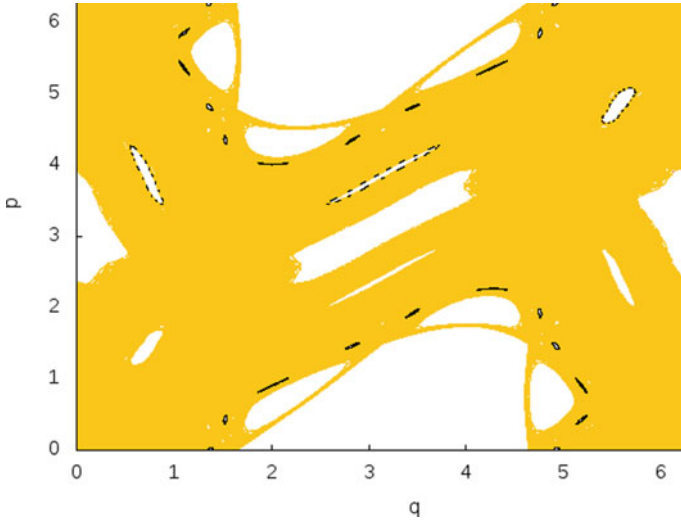
Fig. 6 Here we plot the parts of the trajectory which have the longest lived jets in black. The chaotic see is plotted in yellow. We can notice that these long lived jest are sticking to the small islands (when comparing to Fig. 5)
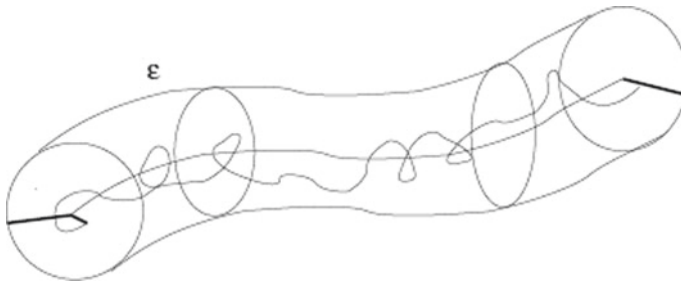
Fig. 7 Representation of a <<jet>> of coarse-grained regular trajectories (on the picture a ghost and a tracer remain together for large times). Within a jet, we may have, as depicted, some chaotic dynamics

not finished separating: we have even seen (see Fig. 6) "jets" of coherent trajectories that last a long time and that moreover "stick" to the islands.

Conclusion on the Use of Complexity in the Standard Map

In the end, we may say that the diagnostic fulfills its objectives on the Standard Map by correctly detecting regularity phenomena in a chaotic space. And it can easily be extrapolated that it would also work on system similar to the Standard Map namely those showcasing coexistence between chaotic seas and islands of stability. At least

in this particular system, this time-trapping approach could detect the transition, that appears when K is reduced, from the globally chaotic case to the coexistence case. But this approach also made it possible to locate areas with little dispersion but also to probe the "jets". We may emphasize that it is actually the first time that jets are used to characterize stickiness around islands, in previous papers they were used to probe some possible stickiness phenomenon when due to its large dimension or the non periodic nature of the driving, we could not visualize phase space.

4.5 Influence of the Parameters

We give here some details of the numerical simulations, and how we obtained the data.

Simulations Times, Reliability of the Results and Initial Conditions

In our simulations we followed the tracer's trajectory over a period of about 10^8 iterations. The number of ghosts that accompanied it at any given time was 3, so we have a program that runs fairly quickly but with fairly reliable results, i. e. by running the program for the same K (and the same ϵ and δ) several times we have the same curves (see Fig. 8). The initial conditions for the tracer does not seem to affect the results either suggesting that 10^8 iterations are more than enough to properly sample the totality of the chaotic space of this system.

Influence of ε and δ

On the Standard Map ε and δ do not change the overall density rate: the exponent α in $1/\tau^\alpha$ is a constant. Changing ε and/or δ will actually only shift the curve, but only if the ratio ε/δ changes. That said, all this obviously implies that we have already taken sufficiently small ε, in our case 10^{-3} or smaller, if the parameter has the size of an island (i.e. a characteristic size of the Map) then unexpected phenomena are possible. But the conclusion of this is that despite all these parameters that we have to manage, at least one characteristic variable of the system (which is this exponent α) emerges.
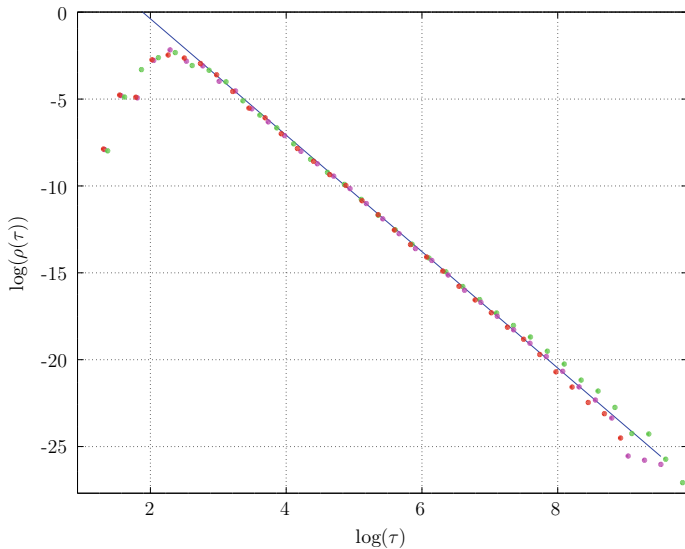
Fig. 8 Three different simulations for the same K ($K = 1.5$) with different initial conditions of both the tracer and the ghosts. We see that all curve fall on the same line. Errors may grow a bit for large trapping times τ and this would indicate when our density functions are not really reliable anymore

5 Application to the HMF

5.1 Introduction

After having measured complexity functions on a simple system like the Standard Map which has only two dimensions, we will now consider a Hamiltonian system with N particles, each described by a position q and an momentum p. Such a system has a $2N$ dimensional phase space which is significantly larger than 2 simple dimensions; indeed we will consider systems with the numbers of degree of freedom N varying from a hundred to a million, it will be in fact our parameter, analogous to how we were varying the K parameter to detect a transition using the trapping time diagnostic. The idea being that here the degree of chaos in the system can be linked to the number of particles N [35, 36, 38]. However, although our diagnostic worked well in a phase space with a small number of dimensions, it can be difficult to imagine and implement it with a much "larger" phase space considering the number of calculations needed to generate randomly ghosts at a distance δ or keeping track of their distance with the tracer. The workaround is then to reduce the dimension of the phase space to be studied. Since in the considered system with N identical particles interacting with each other through the same interaction, we may expect that the study of a single particle should already contain a lot of information about the entire

system, because no particle is more special than another. We will thus implement the master-slave idea proposed earlier and see how it fares.

5.2 Introduction of the HMF Model, and the Master-Slave Implementation

The Hamiltonian Mean Field (HMF) system is a Hamiltonian system with N bodies interacting with each other [46]. We note q_i and p_i respectively the position and momentum coordinates of particle i. The HMF is the system described by the following Hamiltonian:

$$H = \sum_{i=1}^{N} \left(\frac{p_i^2}{2} + \frac{1}{2N} \sum_{j=1}^{N} \left[1 - \cos(q_i - q_j)\right] \right) . \tag{12}$$

It should be noted that the position coordinates q_i can be interpreted as angles, as such this Hamiltonian can be seen as mean field system of ferromagnetic $XY-$spins to which a classical kinetic energy part has been added, so it is possible to deduce that the HMF system physically describes a system of rotators (e.g. spins), each of which creates a field (e.g. magnetic) that "tends" to align its neighbours with itself. Due to the mean field nature, this model has been since its inception a paradigmatic one to study systems with long range interactions. From a purely statistical equilibrium point of view an order parameter $\overrightarrow{M}$, the magnetization, which is the average vector of all spins

$$\overrightarrow{M} = \frac{1}{N} \left(\begin{array}{c} \sum \cos(q_i) \\ \sum \sin(q_i) \end{array} \right) = M \left(\begin{array}{c} \cos(\phi) \\ \sin(\phi) \end{array} \right) ,$$

can be defined and a second order phase transition is observed at a critical temperature $T_c = 1/2$ or critical energy density $e = 3/4$ [46, 47]. There is a long history of studying systems with long range interactions, as these may lead to inequivalence to statistical ensemble and negative specific heats in the micro-canonical one. Moreover its out of equilibrium features and slow relaxation towards equilibrium has been thoroughly investigated. Indeed the relaxation dynamics in the large N limit can be well describe using a Vlasov equation, and in many situations the system can be trapped in long lived quasi-stationary states, whose lifetime diverges with the number of constituents [47–57]. The mean field results obtained with this model have also been shown to capture or be equivalent to more complex long range system of XY-spins, even when considering the interactions on regular networks with finite range or complex networks with small-world properties [58–61]. Regarding the dynamics of the relaxation, specific behaviors related to long-range systems have been observed. But the one that will particularly interest us in the present case, is the fact that even at statistical equilibrium the system display self-organized regularity [35, 36, 38]. Let

us now turn to some specificities of the model The equations of the motions derived from the Hamiltonian

$$\dot{p}_i = -\frac{\partial H}{\partial q_i} = -\frac{1}{N} \sum_{j=1}^{N} \sin\left(q_i - q_j\right) \tag{13}$$

$$\dot{q}_i = \frac{\partial H}{\partial p_i} = p_i \ . \tag{14}$$

which if we develop the sinus can then be rewritten as :

$$\begin{aligned} \dot{p}_i &= -M\sin(q_i - \phi) \\ \dot{q}_i &= p_i \ . \end{aligned} \tag{15}$$

During our simulations the initial conditions of the rotators will be generated with an equilibrium distribution which will be parametrized by its temperature, so we will only treat the case at equilibrium in the same spirit as was performed in [38],

$$\rho(p,q) = \sqrt{\frac{2\pi}{\beta}} \frac{1}{I_0(\beta M)} \exp\left(-\beta\left(\frac{p^2}{2} - M\cos q\right)\right) , \tag{16}$$

with the norm of the magnetization M solution of the implicit equation

$$M = \frac{I_1(\beta M)}{I_0(\beta M)} , \tag{17}$$

Once data is collected we "center" the initial conditions so that the initial phase of the magnetization ϕ is zero.

We now define the slave system: we have seen that the N spins of the HMF are subjected to a uniform average field created by all the spins, the slave dynamics is then naturally chosen to be driven by the following Hamiltonian

$$H = \frac{p^2}{2} - M(q_1, \ldots, q_n) \cos(q - \phi(q_1, \ldots, q_n)) ,$$

resulting in the dynamics given by a driven pendulum

$$\begin{aligned} \dot{q} &= p \\ \dot{p} &= -M\sin(q - \phi) , \end{aligned}$$

where M and ϕ are computed from the master system and are the global mean fields driven by the trajectory of the N couple (p_i, q_i) of the particles. We are then indeed in a master slave situation and the slave system does not affect the master system nor its magnetization. It is on this slave system that we will launch our tracer and ghosts and compute complexity functions.

5.3   *Chaos as a Function of the Number of Particles N*

Before taking care of the trapping times of the slave system. Let us start by getting an overview of how the HMF behaves and more precisely how each particle moves in their restricted 2*D* phase space. Indeed as already seen in [35, 36, 38] , and guessed from the equation of motion themselves, if we are near a statistical equilibrium the magnetization should be almost constant, hence the particle's motion (15) should as well mimic those of a pendulum. Of course the magnetization is expected to fluctuate less and less the more particles are driving the master system, so we can expect their dynamics to be more and more regular. This lead to the notion of what was dubbed self-organized regularity in [38]. So let us consider various systems size and vary the number of particles N and see how individual particle moves. The results are displayed in Fig. 9. Since it is more common to chose $\phi = 0$ for a real pendulum, for example in the case of the pendulum under gravity, in order to take into account the fluctuations of the phase which may blur the trajectory we draw the individual trajectories of the particles in the frame (p_i, $q_i - \phi$).

It appears that by increasing the number of particles, they are increasingly confined around a pendulum orbit, whereas if we have few particles each make very large jumps from one orbit to another. These displacements indicate the fluctuation of particle energy since it is recalled that the orbits of the pendulum are isoenergies. Thus the more particles there are, the less each particle will have a fluctuating energy. Now, we can wonder if what looks like a decrease in chaos and a rise of regular motion is in fact something similar to what was observed in the Standard Map caused by the appearance of islands and stickiness phenomenon, and if this regularization can be detected by measuring complexity in the low dimensional slave system: this is where the slave particle and the time of trapping of ghosts come into play.

5.4   *Simulations of the HMF*

We ran simulations for N from 10 to approximatively $N = 10^5$ and for an equilibrium temperature $T = 0.1$ and $T = 0.4$. The simulation time was $T_f = 10^5$. The results are given in Fig. 10. We recognize the algebraic decay of $\rho(\tau)$ we saw in the Standard Map. But even for low N, there is nothing similar to the exponential decay in the Standard Map in the globally chaotic case. We notice that the figures overlap strongly: our results do not depend on the N we choose. This seems strange since we have seen in Fig. 9 that chaos appeared we decrease N. Nevertheless surprising, these results as mentioned all display a power law behavior, which are puzzling, as we could have expected chaos in low dimensional phase space to give rise to exponential decay, so in fact this system appears to be much more regular than we initially anticipated. We probably will need to refine our diagnostic, maybe taking to account as well the vicinity of a real trajectory as proposed in the definition (the point 1 in the definition of separability in Sect. 3 that we neglected) could solve the problem. Another possibility

(a) $N=10^3$

(b) $N=10^4$

(c) $N=5\cdot10^5$
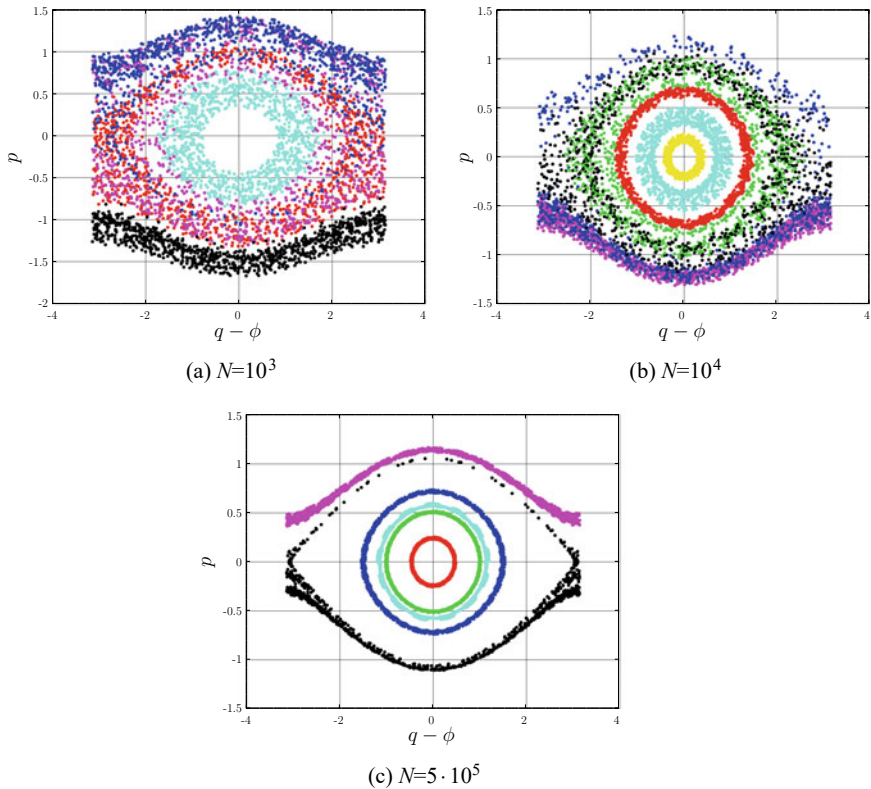
Fig. 9 Trajectories of some particles of the HMF in their own reduced phase space, plots are superimposed. Each color corresponds to a given particle. Different values of N are considered. Initial conditions for the different values of N were chosen so that the energy per particle is preserved (constant temperature T at equilibrium, here $T = 0.48$). We notice clearly that the trajectories become more and more regular as the size of the system is increases

is that given the dynamics of the ghost, we are facing a configuration giving rise to adiabatic invariants which could be not so sensitive to the fluctuations of the magnetization, unless we are considering trajectories close to the separatrix of the pendulum [62–64], but then we may just endup tracing chaos in the stochastic layer, as was already somewhat performed in our study of the standard map (Fig. 11).

Trajectory of the Tracers and Influence of ε

By looking at Fig. 10 in conjunction to Fig. 10, we can see that distribution of trapping of trapping times τ does not detect the vast difference in trajectory taken by the different tracers. For $\varepsilon = 0.05$, it seems having its trajectory confined on a narrow

(a) Temperature $T = 0.4$ (b) Temperature $T = 0.1$
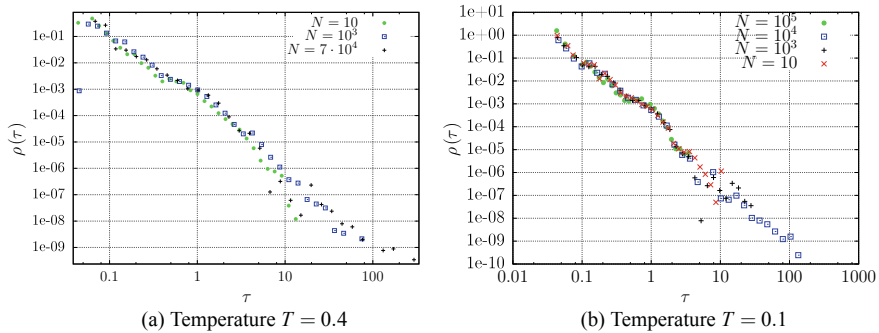
Fig. 10 Plots in log-log of $\rho(\tau)$ for different N and T. $\epsilon = 0.05$ and $\delta = 0.002$. Initial condition of the tracer ($p = 0$, $q - \phi = \pi/2$). For the different values of N and T chosen, we do not notice any major differences in $\rho(\tau)$. We can see $\rho(\tau)$ decays as $1/\tau^{\alpha}$ with α being slightly lower than 3 for both figures

Fig. 11 For $T = 0.4$, we plot the trajectory of the tracers we used for the Fig. 10 in the cases $N = 10$ (in yellow) and $N = 7 \cdot 10^4$ (in black)
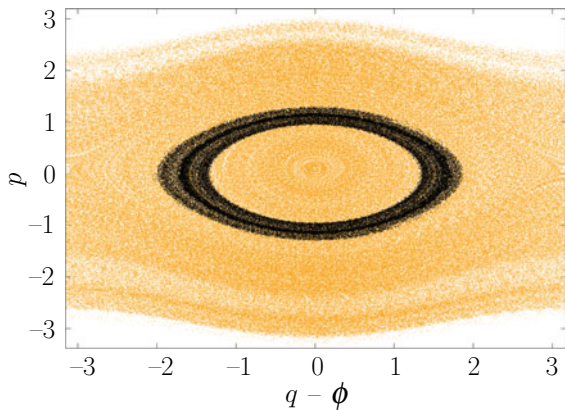
rings does not have a particular effect on its ϵ−separability compared to being able to explore the whole region enclosed by the separatrices and even more. But we may want to know whether having ε closer to the width of the ring in which the tracer is confined may change the distribution. This is was we verified in Fig. 12. Changing ε mainly shifts the distribution. This result was also replicated for other values of N such as $N = 2 \cdot 10^4$ and $N = 10$.

Conclusion on the HMF

The (ε, t)−separability properties of the slave system of the HMF does not seem to change for different N. So far, our diagnostic failed to perceive the differences

Fig. 12 For $T = 0.4$ and $N = 7 \cdot 10^4$: plots of $\rho(\tau)$ for different values of ε. We notice that increasing ε does not affect the overall form of the distribution but only shift to the right
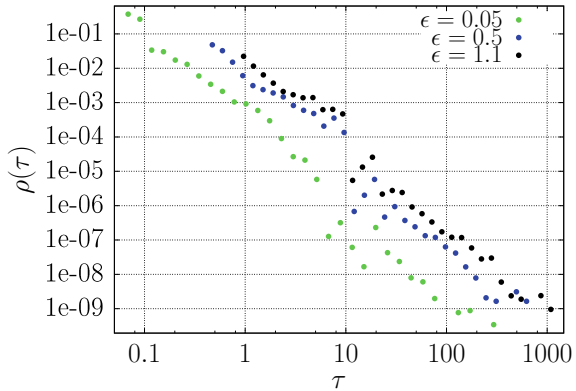
between the different values of N. However, it is not impossible there would exist values for ε, δ or N that would yield interesting observations and further investigations are needed.

6 Conclusion

In conclusion, we obtain a very relevant approach for two-dimensional systems with islands of stability stranded in a chaotic sea like the Standard Map. Moreover, the idea of trapping time opens up possibilities such as probing these long jets or trying to locate them in the phase space. For the large mean-field Hamiltonian we considered, thus far we could surprisingly only detect characteristics of regular power law behavior with a typical slope of trapping time between 2 and 3, indicating most likely anomalous transport properties and memory effects generated by some form of stickiness, however we were not able to see any effect of regularization of the dynamics induced by increasing the size of the system. This leads to some open questions and more work to be done to apprehend clearly the obtained results. Either we are falsely induced by the regular trajectories depicted Fig. 9 and there is some not obvious renormalizable regularity in this system, or we have to delve deeper in implementing the master-salve scenario in order to clearly understand what is happening.

References

1. Fermi E, Pasta J, Ulam S (1955) Los Alamos Reports, (LA-1940)
2. Zaslavsky GM (1985) Chaos in dynamic systems. Harwood Academic Publishers
3. Zaslavsky GM, Sagdeev RZ, Usikov DA, Chernikov AA (1991) Weak chaos and quasiregular patterns. Cambridge University Press, Cambridge
4. Zaslavsky George M (1999) Chaotic dynamics and the origin of statistical laws. Physics Today 52(8):39–45
5. Neishtadt AI (1997) Scattering by resonances. Celestial Mech Dyn Astron 65:1–20
6. Xavier Leoncini (2011) Hamiltonian chaos and anomalous transport in two dimensional flows. In: Luo ACJ, Afraimovich V (eds) Hamiltonian chaos beyond the KAM theory, Nonlinear physical science, pp 143–192. Springer, Berlin Heidelberg
7. Klages R (1996) Deterministic diffusion in one dimensional chaotic dynamical systems. Wissenschaft and Technik Verlag
8. Kolmogorov AN (1954) Dokl Akad Nauk SSSR 98:527
9. Laskar J (1989) Nature 338:237
10. Chirikov BV (1979) Universal instability of many-dimensional oscillator systems. Phys. Rep. 52:263
11. Chandre C, Jauslin HR (2002) Renormalization-group analysis for the transition to chaos in Hamiltonian systems. Phys Rep 365:1–64
12. Escande DF (1985) Stochasticity in classical Hamiltonian systems: universal aspects. Phys Rep 121
13. Artuso R, Cristadoro G (2004) Periodic orbit theory of strongly anomalous transport. J Phys A Math Gener 37:85–103
14. Artuso R, Cavallasca L, Cristadoro G (2008) Dynamical and transport properties in a family of intermittent area-preserving maps. Phys Rev E 77:046206
15. Artuso R, Manchein C (2009) Instability statistics and mixing rates. Phys Rev E (80):036210
16. Castiglione P, Mazzino A, Mutatore-Ginanneschi P, Vulpiani A (1999) On strong anomalous diffusion. Phys D 134:75–93
17. Chernikov AA, Petrovichev BA, Rogal'sky AV, Sagdeev RZ, Zaslavsky GM (1990) Anomalous transport of streamlines due to their chaos and their spatial topology. Phys Lett A 144:127
18. Dickman R (2004) Fractal rain distributions and chaotic advection. Brazil J Phys 34:337–346
19. Leoncini X, Agullo O, Benkadda S, Zaslavsky GM (2005) Anomalous transport in Charney-Hasegawa-Mima flows. Phys Rev E 72(2):026218
20. Leoncini X, Kuznetsov L, Zaslavsky GM (2001) Chaotic advection near a 3-vortex collapse. Phys Rev E 63(3):036224
21. Leoncini Xavier, Kuznetsov Leonid, Zaslavsky George M (2004) Evidence of fractional transport in point vortex flow. Chaos Solitons Fractals 19:259–273
22. Leoncini X, Zaslavsky GM (2002) Jets, stickiness and anomalous transport. Phys Rev E 65(4):046216
23. Rom-Kedar V, Leonard A, Wiggins S (1990) An analytical study of transport mixing and chaos in an unsteady vortical flow. J Fluid Mech 214:347
24. Solomon TH, Gollub JP (1988) Chaotic particle transport in Rayleigh-Bénard convection. Phys Rev A 38:6280–6286
25. Chirikov BV, Shepelyansky DL (1984) Correlation properties of dynamical chaos in Hamiltonian systems. Phys D (13):395
26. da Silva RM, Manchein C, Beims MW, Altmann EG (2015) Characterizing weak chaos using time series of Lyapunov exponents. Phys Rev E (91):062907
27. Kuznetsov L, Zaslavsky GM (2000) Passive particle transport in three-vortex flow. Phys Rev E 61:3777–3792
28. Bachelard R, Benzekri T, Chandre C, Leoncini X, Vittot M (2007) Targeted mixing in an array of alternating vortices. Phys Rev E 76(4):046217
29. Altmann EG, Tél T (2008) Poincaré recurrences from the perspective of transient chaos. Phys Rev Lett (100):174101

30. Faranda D, Leoncini X, Vaienti S (2014) Mixing properties in the advection of passive tracers via recurrences and extreme value theory. Phys Rev E 89(5):052901
31. Leoncini Xavier, Chandre Cristel, Ourrad Ouerdia (2008) Ergodicité, collage et transport anomal. C R Mecanique 336:530–535
32. Bouchara L, Ourrad O, Vaienti S, Leoncini X (2015) Anomalous transport and observable average in the standard map. Chaos Solitons Fractals 78:277–284
33. Afraimovich VA, Rechtman R (2009) Local complexity function of interval exchange transformation. Commun Nonlinear Sci Numer Simul 14(4):1454–1460
34. Leoncini Xavier, Zaslavsky George M (2003) Chaotic jets. Commun Nonlinear Sci Numer Simul 8:265–271
35. Bachelard R, Chandre C, Fanelli D, Leoncini X, Ruffo S (2008) Abundance of regular orbits and out-of-equilibrium phase transitions in the thermodynamic limit for long-range systems. Phys Rev Lett 101(26):260603
36. Leoncini X, Van den Berg TL, Fanelli D (2009) Out of equilibrium solutions in the XY-Hamiltonian mean field model. EPL 86:20002
37. Van den Berg TL, Fanelli D, Leoncini X (2010) Stationary states and fractional dynamics in systems with long range interactions. EPL 89:50010
38. Leoncini X (2015) Self-organized regularity in long-range systems. In: Nonlinear dynamics new directions: models and applications, volume 12 of nonlinear systems and complexity, pp 79–109. Springer
39. Bowen R (1973) Topological entropy for non-compact sets. Trans Amer Math Soc 184:125–136
40. Kolmogorov AN, Tikhomirov VM (1959) ε-entropy and ε-capacity of sets in functional spaces. Usp Mat Nauk 14:3–86
41. Afraimovich V, Glebsky L (2005) Complexity, fractal dimensions and topological entropy in dynamical systems, pp 35–72. Springer, Netherlands, Dordrecht
42. Afraimovich V, Zaslavsky GM (2003) Space-time complexity in Hamiltonian dynamics. Chaos 13(2):519–532
43. Zaslavsky GM, Afraimovich V (2005) Working with complexity functions. Springer Netherlands, Dordrecht, pp 73–85
44. Abarbanel HDI, Rulkov NF, Sushchik MM (1996) Generalized synchronization of chaos: the auxiliary system approach. Phys Rev E 53:4528
45. Zaslavsky GM (2002) Chaos, fractional kinetics, and anomalous transport. Phys Rep 371:641
46. Antoni M, Ruffo S (1995) Phys Rev E 52:3261
47. Campa Alessandro, Dauxois Thierry, Ruffo Stefano (2009) Statistical mechanics and dynamics of solvable models with long-range interactions. Phys Rep 480:57–159
48. Lynden-Bell D (1967) Statistical mechanics of violent relaxation in stellar systems. Mon Not R Astron Soc 136:101–121
49. Chavanis PH (2006) Lynden-bell and Tsallis distributions for the HMF model. Eur Phys J B 53(4):487–501
50. Chavanis PH, De Ninno G, Fanelli D, Ruffo S (2008) Out of equilibrium phase Transitions in mean-field Hamiltonian dynamics. In: Chandre C, Leoncini X, Zaslavsky G (eds) Chaos. Complexity and transport. World Scientific, Singapore, pp 3–26
51. Barre J, Bouchet F, Dauxois T, Ruffo S (2005) Large deviation techniques applied to systems with long-range interactions. J Stat Phys 119(3–4):677–713
52. Barré J, Mukamel D, Ruffo S (2001) Phys Rev Lett 87:030601
53. Antoniazzi A, Fanelli D, Barre J, Chavanis P-H, Dauxois T, Stefano R (2007) Maximum entropy principle explains quasistationary states in systems with long-range interactions: the example of the Hamiltonian mean-field model. Phys Rev E 75:011112
54. Califano F, Fanelli D, Ruffo S, Antoniazzi A (2007) Exploring the thermodynamical limit of Hamiltonian models: convergence to the Vlasov equation. Phys Rev Lett 98:150602
55. Bachelard R, Dauxois T, De Ninno G, Ruffo S, Staniscia F (2011) Vlasov equation for long-range interactions on a lattice. Phys Rev E 83:061132
56. Bouchet F, Dauxois T, Barre J, Ruffo S (2002) Out-of-equilibrium states as statistical equilibria of an effective dynamics in a system with long-range interactions. Phys Rev Lett 89:110601

57. Pakter Renato, Levin Yan (2011) Core-Halo distribution in the Hamiltonian mean-field model. Phys Rev Lett 106:200603
58. De Nigris S, Leoncini X (2013) Emergence of a non trivial fluctuating phase in the XY model on regular networks. EPL (Europhys Lett) 101:10002
59. De Nigris Sarah, Leoncini Xavier (2013) Critical behaviour of the XY-rotors model on regular and small world networks. Phys Rev E 88(1–2):012131
60. De Nigris S, Leoncini X (2015) Crafting networks to achieve, or not achieve, chaotic states. Phys Rev E 91:042809
61. Belger Martin, De Nigris Sarah, Leoncini Xavier (2016) Slowing down of chaotic states: freezing the initial state. Discontinuity Nonlinear Complex 5(4):427–435
62. Tennyson J, Cary JR, Escande DF (1986) Change of the adiabatic invariant due to separatrix crossing. Phys Rev Lett 56:2117–2120
63. Neishtadt AI (1986) On the change of adiabatic invariant due to separatrix crossing. Sov Phys Plasma Phys 12:568–573
64. Leoncini Xavier, Neishtadt Anatoly, Vasiliev Alexei (2009) Directed transport in a spatially periodic harmonic potential under periodic nonbiased forcing. Phys Rev E 79(2):026213

Local Complexity Functions of the Ehrenfest's Wind-Tree Model

Raúl Rechtman

Abstract We present numerical results of two local complexity functions of the Ehrenfest's wind-tree model [1]. This is a simple model originally used to present Boltzmann's transport equation. It is a Lorentz gas in which particles collide with fixed obstacles. We show that both local complexity functions scale linearly with the number of obstacles, the initial separation between pairs of particles, and the time.

In 1912 Tatiana and Paul Ehrenfest presented what they called the wind-tree model in order to discuss Boltzmann's transport equation (BTE) and the hypothesis of molecular chaos [1]. Paul Ehrenfest had been invited by Felix Klein to contribute to the Mathematics Encyclopedia with a paper explaining Boltzmann's ideas. For this model, BTE is a set of four linear differential equations with analytical solutions. Then Boltzmann's H-function can be evaluated. On a two dimensional space there are wind (point) particles that move with one of four unit velocities $c_0 = (1, 0)$, $c_1 = (0, 1)$, $c_2 = (-1, 0)$ and $c_3 = (0, -1)$ and may eventually collide with fixed trees that are squares of a fixed size and diagonals along the axes as shown in Fig. 1. In a collision, the velocity of the wind particle changes by $\pm \pi/2$. The model has been discussed extensively; by adding an internal degree of freedom to the wind particles [3, 5] and by rounding the edges of the trees [6]. The thermodynamics of the model has a closed expression [4]. The wind-tree model is the basis of the flipping mirror model (FMM) [7] and the flipping rotator model (FRM) [8] that in a sense are a restriction to a two dimensional lattice. In both models the particles move in $\mathbb{Z}^2$ with a fraction of sites occupied by obstacles, which in the FMM model are mirrors placed at 45° or 135° and after a specular reflection, the mirror flips. In the FRR the obstacles are right and left rotators so that in a collision, the particle turns to its right (or left) and the rotator changes its direction. The two models are related in the sense that given a walk on one of the two, there is an equivalent walk on the other one [9].

Another line of research has to do with diffusion and recurrence in the wind-tree model [10] and particularly on the periodic wind-tree model where the trees are

R. Rechtman (✉)

Instituto de Energías Renovables, Universidad Nacional Autónoma de México, Mexico city, Mexico
e-mail: rrs@ier.unam.mx

centered on $\mathbb{Z}^2$, may be rectangles and the wind particles can travel initially in some given direction and are reflected specularly by the trees [11–13] and the references cited in these papers. There are periodic and divergent trajectories on these billiards. The dynamics can be studied in a fundamental cell with the appropriate boundary conditions.

The wind-tree model is an example of a Lorentz gas in which particles collide with fixed obstacles. If these objects are disks, the trajectories are chaotic and the largest Lyapunov exponent depends on the curvature of the obstacles. For the wind-tree model, the curvature is zero and the trajectory of any wind particle is not chaotic. However, two initially close wind particles can separate at some time t_s, the separation time, and the two local complexities C_1 and C_2 found from an ensemble of trajectories with different t_s are an approximation of the local ϵ-complexity [14]. In what follows we present the definitions of the two local complexities C_1 and C_2 and show that they scale linearly with time t, the number of trees N_t, and the initial separation ϵ between trajectories.

The wind particles can move in one of four directions $c_0 = (1, 0)$, $c_1 = (0, 1)$, $c_2 = (-1, 0)$ and $c_3 = (0, -1)$, as mentioned before. When a wind particle with velocity c_k collides with a tree, the velocity changes to c_j with $j = (4 + k \pm 1)$ mod 4 turning $\pm \pi/2$ as shown in Fig. 1.

Two wind particles initially close and with the same velocity will eventually separate as we show in Fig. 2a where the initial position of the particles is marked by a small circle in the bottom. The trees are put at random with the condition that they do not overlap. After several reflections with the trees, the two wind particles separate as shown in the area inside the black circle in the bottom left of the figure shown in detail in Fig. 2 (b). The green particle is reflected by the tree while the red one continues to travel in a straight direction.

For this model, one would like to find the local complexity function, [14–16] and instead we can define two complexity functions, C_1 and C_2 defined below which are closely related in the case of interval exchange maps [14].

To evaluate C_1 we put N_t trees at random inside a square of side L and then put one wind particle at a random position in the square (and not inside a tree) with velocity c_0 and another a distance smaller than ϵ in the vertical direction of the first one and with the same velocity. Then we find the separation time t_s and repeat this for N couples of wind particles initially placed at random and separated less than ϵ. We find the histogram of separation times and C_1 is the integral of this histogram.

The other quantity, C_2, is the integral of the histogram of the separation times of an interval of initial conditions of length 2ϵ of wind particles. This is evaluated numerically by taking N_t trees placed at random inside a box of sides L, and N wind particles with random initial positions and moving with velocity c_0. For each wind particle with random initial position (x_0, y_0) with velocity c_0, called the central particle, we put two more a distance ϵ, one at $(x_0, y_0 - \epsilon)$ and the other one at $(x_0, y_0 + \epsilon)$ with the same initial velocity. One must take care that the three initial positions are not inside any tree. The separation time t_s is the time when the orbit of the central wind particle and one of the other two separate.
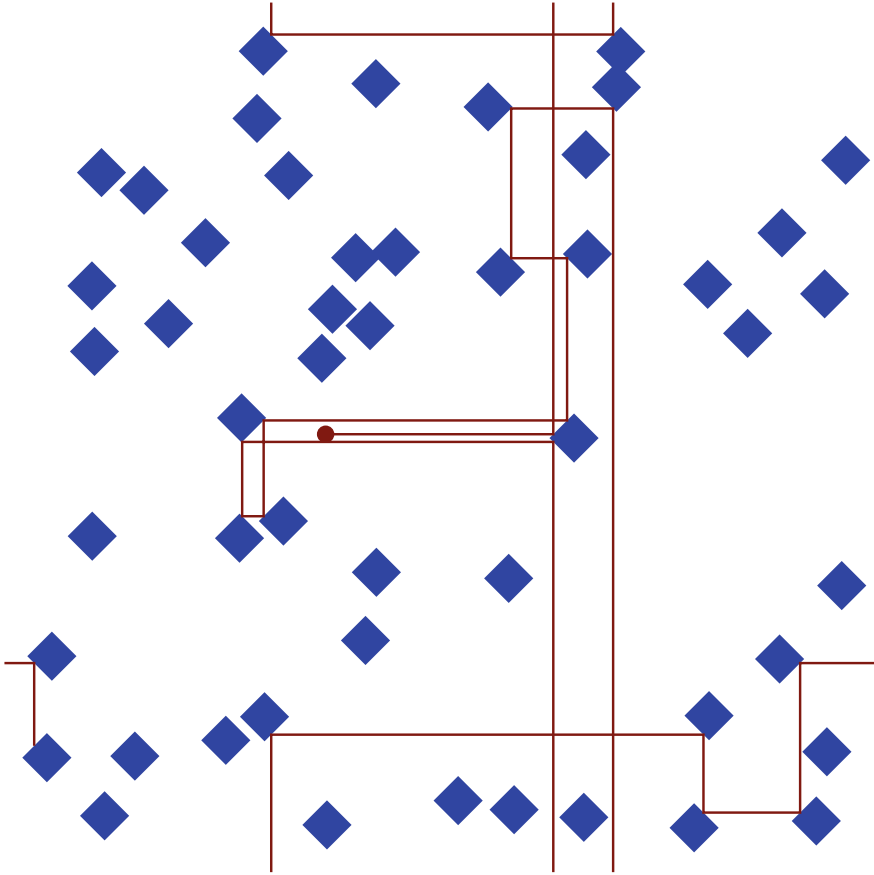
Fig. 1 Trajectory of a wind particle. There are $N_t = 50$ trees of side $d = 4$ put at random in a square of side $L = 100$ with the condition that they do not overlap. The wind particle is initially at the point marked by a small circle and moves with periodic boundary conditions

The trees have random positions and it may happen that a wind particle never collides with a tree. Then, to measure the local complexities, we only take into account wind particles that collide with trees. If there is no collision, the particle will be at its initial position after a time L, and this particle is not taken into account in the numerical evaluation of C_1 or C_2. Thus the flight time between collisions has to be smaller than L to be considered. In Fig. 3a, b we show C_1 as a function of the separation time t_s for three values of ϵ. The straight lines in black are $C_1 = A\epsilon t_s$ with A that should depend on N_t, d and L.

In Fig. 4 we show C_1 as a function of the separation time t_s for different number of trees N_t in the same area, that is, as N_t grows, the density of trees grows. For the interval exchange map C_1 scales linearly with number of discontinuities of the map, here the number of vertices of the trees plays the same role.

(a)

(b)
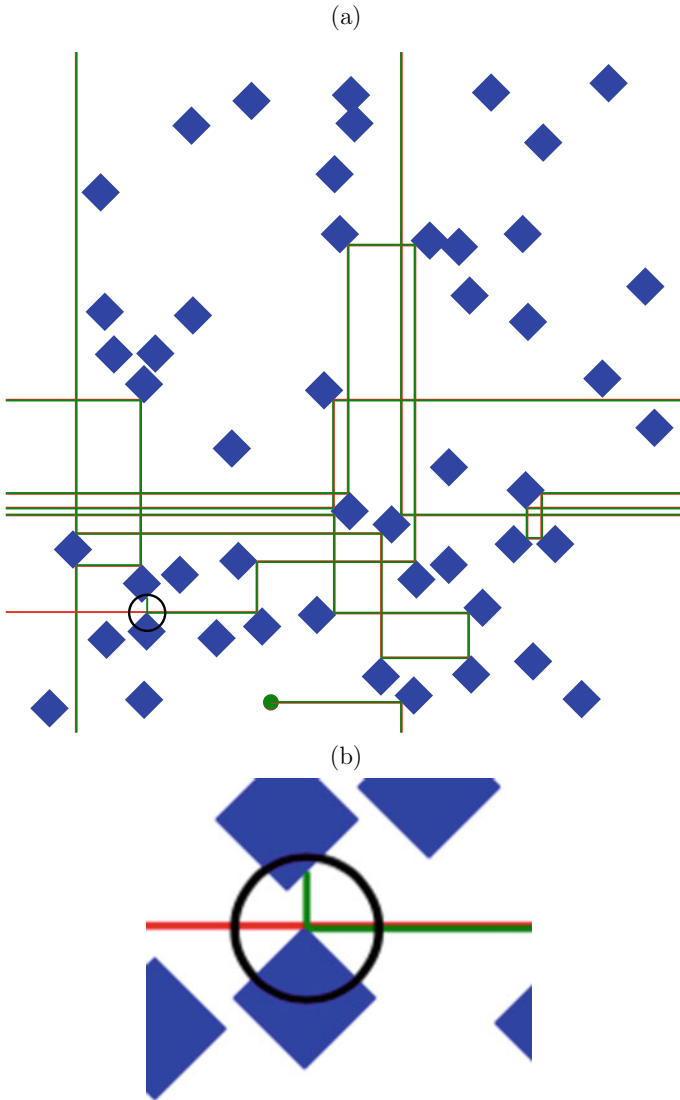
Fig. 2 **a** Trajectories of two wind particles initially a distance $\epsilon = 1$. The initial position of the particles is marked by circles, the first in red, the other in green, in the bottom part of the figure and both with velocity c_0. After several collisions with the trees, the two particles separate, close to the lower left corner of the figure and marked by a circle. **b** An amplification at the time of separation t_s. There are fifty trees of side $d = 4$ put at random in a square of side $L = 100$ with the condition that they do not overlap and the wind particles move with periodic boundary conditions
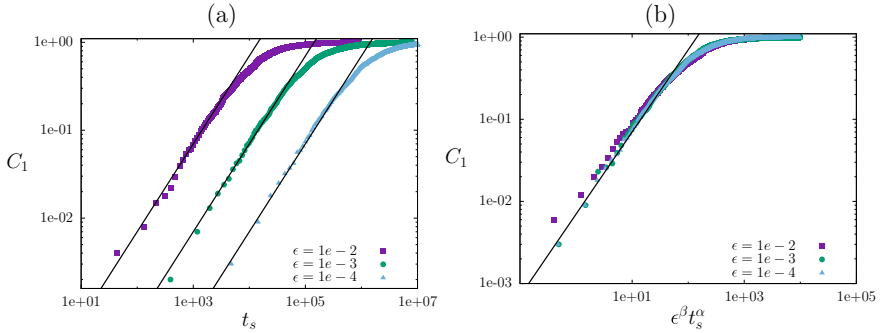
Fig. 3 **a** The local complexity C_1 as a function of the separation time t_s for three values of ϵ. The curves in black are $C_1 = A\epsilon t_s$ with $A = 7e - 3$. These are a fit to the eye. **b** The data of the previous figure scale with ϵ. The curve in black is $C_a = At_s$. There are $N_t = 200$ trees of side $d = 4$ located at random in a square box of sides $L = 200$ and $N = 1,000$ wind particles are located initially at random with velocity c_0 and move with periodic boundary conditions
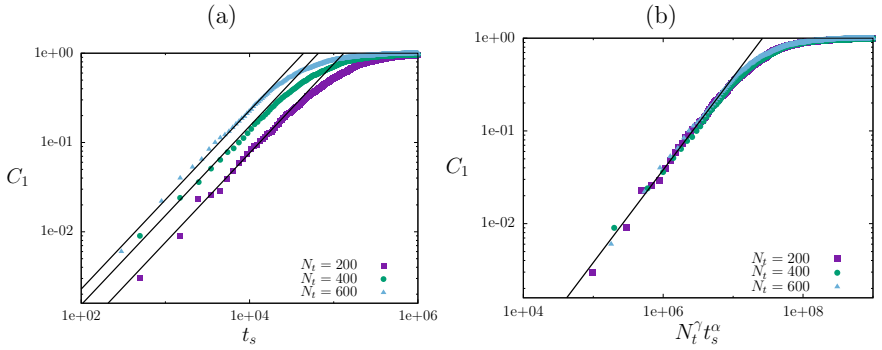
Fig. 4 **a** The quantity C_1 as a function of the separation time t_s for different numbers N_t of trees. The curves in black are $C_1 = AN_t t_s$ with $A = 3.8e - 8$. **b** The data of **a** as a function of $N_t t_s$. The curve in black is $C_1 = At_s$. In each numerical simulation, there are N_t trees of side $d = 4$ with position at random inside a square of side $L = 200$ and $N = 1,000$ wind particles with random initial position and velocity c_0, move with periodic boundary conditions and $\epsilon = 1e - 3$. For each value of N_t, the position of the trees is fixed

In Figs. 5 and 6 we show the corresponding results for the local complexity C_2. Both quantities scale as

$$C_x \sim N_t^\gamma \epsilon^\beta t^\alpha$$

with $x = 1, 2$ and $\alpha \sim 1$, $\beta \sim 1$ and $\gamma \sim 1$. The Ehrenfest's wind-tree model behaves, in terms of the local complexities C_1 and C_2, as the interval exchange map [14].
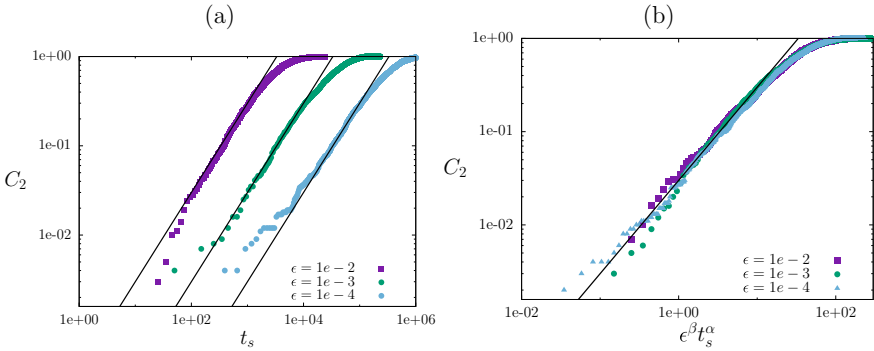
Fig. 5 **a** The quantity C_2 as a function of the separation time t_s for different values of ϵ. The curves in black are $C_2 = A\epsilon t_s$ with $A = 3e - 2$. **b** The data of **a** as a function of ϵt_s. The curve in black is $C_2 = At_s$. In each numerical simulation, there are $N_t = 200$ trees of side $d = 4$ with position at random inside a square of side $L = 200$ and $N = 1,000$ wind particles with random initial position and velocity $\boldsymbol{c}_0$. For each value of N_t, the position of the trees is fixed
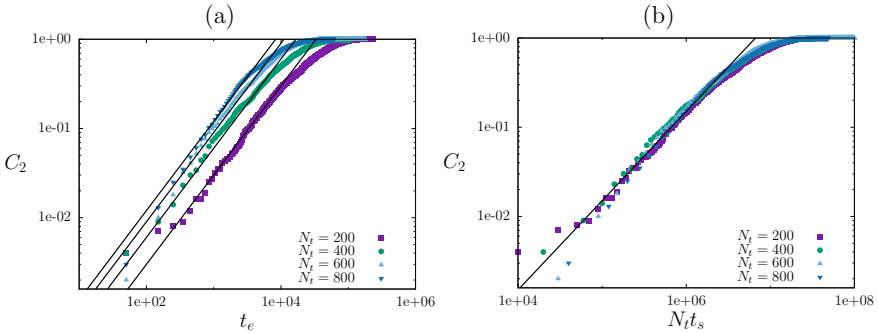
Fig. 6 **a** The local complexity C_2 as a function of the separation time t_s for different numbers N_t of trees. The curves in black are $C_2 = AN_t t_s$ with $A = 1.5e - 07$. **b** The data of **a** as a function of $N_t t_s$. The curve in black is $C_2 = At_s$. In each numerical simulation, there are N_t trees of side $d = 4$ with position at random inside a square of side $L = 200$ and $N = 1,000$ wind particles with random initial position and velocity $\boldsymbol{c}_0$ and $\epsilon = 1e - 3$. For each value of N_t, the position of the trees is fixed

References

1. Afraimovich V, Rechtman R (2008) Local complexity functions of interval exchange transformations. Commun Nonlinear Sci Numer Simul 14:1454–1460
2. Afraimovich V, Zaslavsky GM (2003) Space-time complexity in Hamiltonian dynamics. Chaos 13:519
3. Bagnoli F, Rechtman R, Zanette D (1993) Termodinámica de equilibrio de sistemas con velocidades discretas. Revista Mexicana de F'isica 39(5):763
4. Delecroix V (2013) Divergent trajectories in the periodic wind-tree model. J Modern Dyn 7:1
5. Ehrenfest P, Ehrenfest T (1959) Begriffliche Grundlagen der statistischen Auffasung in der Mechanik. In: Klein TF y Müller C (eds) Encylopädie der Mathematischen Wissenschaften

mit Einschluss ihrer Anwendunge, Band IV, 2. Teubner, Leipzig, pp 3–90. English transltion: Moravczik MJ The conceptual foundations of the statistical approach in mechanics. Cornell University Press

6. Güemez J, Cervero JM, Velasco S (1994) The Wind-round-tree model and the 2-dimensional Lorentz gas. Phys Lett A 190:434

7. Gunn JMF, Ortuño M (1985) Percolation and motion in a simple random environment. J Phys A 18:L1095

8. Hardy J, Weber J (1980) Diffusion in a periodic wind-tree model. J Math Phys 21:1802

9. Hauge EH, Cohen EGD (1969) Normal and abnormal diffusion in Ehrenfest's wind-tree model. J Math Phys 10:397

10. Hubert P, Lelièvre S, Troubetzkoy S (2011) The Ehrenfest wind-tree model: periodic directions, directions, diffusion. J Reine Angew Math 656:223

11. Rechtman A, Rechtman R (2017) Equivalence of deterministic walks on the plane. Phys A 466:69

12. Rechtman R, Salcido A, Calles A (1991) The Ehenfest's wind-tree model and the hypothesis of molecular chaos. Eur J Phys 12:27

13. Ruijgrok ThW, Cohen EGD (1988) Anomalous diffusion in a lattice-gas wind-tree model. Phys Lett A 133:415

14. Schultze U, Penson KA, Perera A, Moreau M (1993) Wind-tree model in two dimensions with internal degrees of freedom: exact solution. Phys Rev E 47:4589

15. Schultze U, Penson KA, Perera A, Moreau M (1994) Dynamics of discrete models of binary mixtures in 2 dimensions: exact solution Phys Rev E 50:3641

16. Zaslavsky GM, Afraimovich V (2005) Working with complexity functions. In: Collet P et al. (eds) Chaotic dynamics and transport in classical and quantum systems. Kluwer Academic Publishers, p 78

Selective Chaos of Travelling Waves in Feedforward Chains of Bistable Maps

Bastien Fernandez

Abstract We study the chaos of travelling waves (TW) in unidirectional chains of bistable maps. Previous numerical results suggested that this property is selective, *viz.* given the parameters, there is at most a single (non-trivial) velocity for which the corresponding set of wave profiles has positive topological entropy. However, mathematical proofs have remained elusive, in particular because the related symbolic dynamics involves entire past sequences. Here, we consider instead finite (short) rank approximations for which the symbolic dynamics has finite memory. For every possible velocity, we compute the existence domains of all possible finite type subshifts of TW with positive entropy. In all examples, chaos of TW turns out to be selective, indeed.

1 Introduction

Valentin Afraimovich had a strong interest for lattices of coupled dynamical systems, the so-called Lattice Dynamical Systems (LDS). He made a number of diverse and important theoretical contributions to this field; a summary of them can be found in the notes of his lecture at the CML2004 school in Paris [1]. In short terms, a LDS is a (continuous or discrete time) dynamical system whose phase space is $\mathcal{M}^{\mathbb{Z}^d}$ (lattice configurations), where $\mathcal{M}$ is a subset of $\mathbb{R}$ or of a (compact) manifold, and $d \in \mathbb{N}$ is the lattice dimension.

In this setting, Valentin introduced me to the problem of the detection of a *preferred direction in space-time* (from his own words, often accompanied with expressive hand motions!), presumably a measure of the velocity of information flow in the system. During several years, we frequently spent time together in various places, San Luis Potosi, Marseille, etc. While he continuously showed receptive patience, Valentin was

---

Dedicated to the memory of Valentin Afraimovich.

B. Fernandez (✉)

Laboratoire de Probabilités, Statistique et Modélisation, CNRS - Univ. Paris - Sorbonne Univ., 75205 Paris CEDEX 13, France

e-mail: fernandez@lpsm.paris

moved by a strong will, which manifested itself as a vigorous stimulation. A young
fellow at that time, I had no previous experience of interaction with a senior colleague
who was both scientifically demanding and open to feedback and discussion. This
collaborative experience has been truly beneficial to me, and also a particularly good
time of a close relationship.

Valentin's incentive brought us (also with Antonio Morante) to extend Milnor's
notion of directional entropy in cellular automata [2, 3] to lattice dynamical systems
[4]. Two context-dependent definitions emerged. The first one involved space-time
normalisation and was intended for systems with chaotic (temporal) dynamics. The
second one used temporal normalisation only and was aimed at the case of regular
dynamics.

We proceeded to an extended investigation of basic characteristics, by analogy
with the analysis of the topological entropy in dynamical systems [5]. Furthermore,
we obtained explicit estimates in simple examples, which unexpectedly showed that
the space-time normalised quantity did not depend on the direction. This invariance
was later confirmed to hold in every translation invariant LDS,[1] thanks to a decisive
contribution by Afraimovich et al. [6].[2] Therefore, the directional entropy unfortu-
nately appears to be insufficient to detect preferred space-time directions, at least for
chaotic systems whose dynamics commutes with spatial translations.

What about systems with regular dynamics? The space-time normalised direc-
tional entropy would have to vanish but not necessarily the time normalised one.
Moreover, the examples below [4] show non trivial dependence and call for further
investigation.

2 Unidirectional Systems, Chaos of Travelling Waves and Symbolic Dynamics

The probably simplest (non trivial) example of LDS with regular dynamics is the
direct product (over $\mathbb{Z}$) of bistable one-dimensional maps (*i.e.* maps of the interval
having two stable fixed points). Explicitly, the dynamics of configurations $x \in [0, 1]^{\mathbb{Z}}$
is generated by the map F defined by

$$(F(x))_s = f(x_s), \ \forall s \in \mathbb{Z}.$$

Assuming that $f(0) = 0$ and $f(1) = 1$ are the two stable fixed points of f, any
configuration in $\{0, 1\}^{\mathbb{Z}}$ must be a (stable) fixed point of F. This property is an

---

[1] Translation invariant means that the dynamics commutes with the operator σ of spatial translations,
which is defined below.

[2] More precisely, the entropy as defined in [4] depended on the direction. However, [6] showed that
this dependence was trivial, because it could be removed by suitable renormalisation.

instance of *spatial chaos* in LDS,[3] and it implies that the (time normalised) directional entropy vanishes in the direction of time and is maximal in the direction of space.

The next example is when this uncoupled system is combined with the spatial transition operator σ, *viz.*

$$(\sigma \circ F(x))_s = f(x_{s-1}), \ \forall s \in \mathbb{Z}.$$

Under the same circumstances, the system $\sigma \circ F$ has a spatial chaos, now of (convectively stable) travelling waves of velocity 1. Its directional entropy vanishes in the direction of wave propagation (corresponding to the angle $\frac{\pi}{4}$ in the space-time) and, as before, is maximal in the orthogonal direction.

These examples are somewhat naive and rather irrelevant. As modelling of transport phenomena is concerned, it would be more interesting to have similar information for the following unidirectional chain of coupled (bistable) maps

$$(F_\epsilon(x))_s = (1 - \epsilon) f(x_s) + \epsilon f(x_{s-1}), \ \forall s \in \mathbb{Z}, \tag{1}$$

for $\epsilon \in [0, 1]$ (NB: this system reduces to the previous examples for the limit values $\epsilon = 0$ and $\epsilon = 1$ respectively). So far, estimates of the directional entropy for this chain have remained elusive (expected in the neighbourhood of the limit cases, using perturbative arguments). To address this issue, the considerations in the limit cases above suggest to investigate the chaos of travelling waves (TW) for an arbitrary velocity.

Travelling waves in (continuous or discrete time) LDS can be defined following the basic notion in physics, namely that they are trajectories given by $x_s^t = u(s - vt)$ for some profile $u : \mathbb{R} \to \mathbb{R}$ and some velocity $v \in \mathbb{R}$ [9]. However, TW in discrete-time LDS can also be characterised using spatial translations [10], including for irrational velocities [11]. In particular, any solution of the equation

$$G^q(x) = \sigma^p(x), \tag{2}$$

where $p \in \mathbb{Z}$ and $q \in \mathbb{N}$, defines a TW of velocity $v = \frac{p}{q}$ for the LDS generated by the map G. Of note, the velocity is constrained by the coupling range, in particular we must have $v \in [0, 1]$ for the LDS (1).

Extending the notion above, the LDS generated by G is said to have (spatial) *chaos of TW* of velocity $\frac{p}{q}$ if the action of σ on the set of solutions of (2) has positive topological entropy. Together with Vladimir Nekorkin, Valentin has asserted the existence of chaos of TW in some examples of LDS by constructing horseshoes of the profile generating dynamics associated with Eq. (2) [12]. This approach can be viewed as a nonlinear extension of the transfer matrix technique in theoretical solid-

---

[3] Another area of Valentin's expertise, a LDS is said to have spatial chaos when the action of the spatial translations $(\sigma(x))_s = x_{s-1}$ on the set of LDS fixed points (viewed as a dynamical system whose time is given by the spatial variable s [7, 8]), is chaotic, typically with positive topological entropy [1].

state physics. However, the construction is velocity specific and makes it difficult to evaluate the velocity dependence on parameters, not to mention to portray a global description of the chaos of TW in parameter space.

To address this issue, we considered a special case of the unidirectional chain (1) above, when the individual map f is piecewise affine with two branches of unique slope, separated by a discontinuity. Formally speaking, the map writes

$$f(u) = au + (1-a)H(u-T), \ \forall u \in [0, 1], \tag{3}$$

where H is the (right continuous) Heaviside function, the slope $a \in [0, 1)$ and the discontinuity $T \in (0, 1)$. That this map is a piecewise contraction implies that any TW away from the discontinuity must be convectively stable [9], and in particular that any chaos of TW must be a chaos of stable TW.

By using symbolic dynamics (see below), we numerically discovered [13, 14] that, given any values of the parameters, there is at most one (non-trivial) velocity $v \in (0, 1)$ for which the corresponding TW set may have positive entropy,[4] see Fig. 1
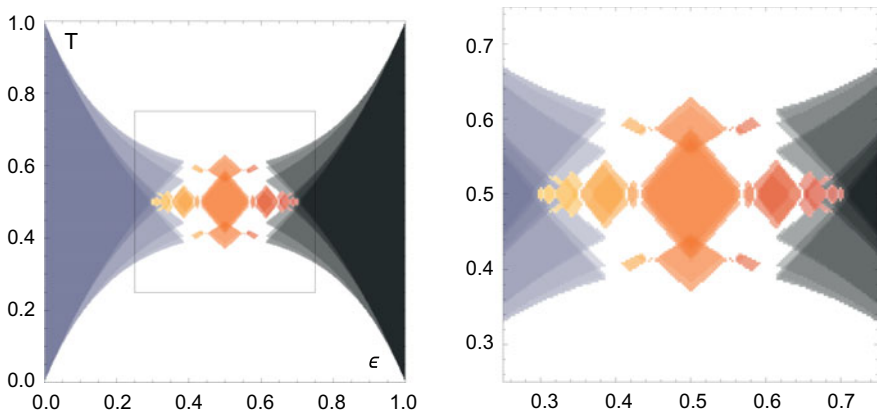
Fig. 1 Entropy-velocity diagrams of TW of the LDS (1) with individual map (3) for $a = 0.6$ (*Left*: Original diagram in the full square of the parameters (ϵ, T). *Right*: Zoom into the central region delimited by the square). Painted points represent the velocity dependent quantity $\frac{\log P_{13,v}}{13}$ (approximation of the TW entropy), based on color and intensity. The color indicates the velocity $v \in V \cup 1 - V$ where $V = \{0, \frac{1}{6}, \frac{1}{5}, \frac{1}{4}, \frac{1}{3}, \frac{2}{5}, \frac{3}{7}, \frac{1}{2}\}$, 0 (resp. 1) is painted in gray (resp. black) and the other velocity colors monotonically range from yellow to red. The intensity is proportional to the entropy, from 0 to $\log 2$. Positive entropy domain of intermediate velocities $v \in (0, 1)$ appear to be pair-wise disjoints. However, the domains with small velocities overlap with the one at $v = 0$ (and similarly in the right part of the pictures) indicating that a chaos of fixed points (resp. of TW with $v = 1$) may coexist with a chaos of patterns with intermediate velocity

---

[4] In symbolic systems, the topological entropy can be defined as the exponential growth rate of the number of admissible blocks [15]. For numerical purposes, following [16], we used instead the number of periodic points and assumed that the entropy of the set of TW profiles with velocity v is given by $\limsup_{L \to +\infty} \frac{\log P_{L,v}}{L}$ where $P_{L,v}$ is the number of L-periodic blocks of velocity v.

for an illustration for $a = 0.6$. Depending on the parameters, either there is no chaos of TW, or we have a chaos of TW with trivial velocity 0 or 1, or such chaos is combined with a chaos of TW with $v \in (0, 1)$, but we have never observed two chaos of TW with distinct non-trivial velocities. This observation might not be what Valentin had expected but it can be considered as a selection of a unique, if not preferred, direction in space-time (when one discards the background velocities 0 and 1).

Besides its obvious symmetric features,[5] the numerical results called for rigorous explanation. That a chaos of TW with $v \in (0, 1)$ could coexist with one at $v \in \{0, 1\}$, combined with proofs of parameter dependent coexistence of TW with different velocities [13], suggested that the proof could not be elementary. In fact, excepted for the extreme velocities $v = 0$ and $v = 1$ for which the exact parameter domain for existence of full chaos could be determined [17], for arbitrary velocities, only estimates of pairwise disjoint domains of existence of chaotic sets of TW were available, based on shadowing arguments. In order to provide further insights into analytic arguments, we need to introduce considerations about symbolic dynamics.

A convenient aspect of the piecewise affine system (1) with individual map (3) is that its symbolic description is easily accessible. Indeed, any trajectory $\{x^t\}$ (where $x^{t+1} = F_\epsilon(x^t)$) can be coded by a space-time symbolic sequence $\{\theta_s^t\}$ via the relation $\theta_s^t = H(x_s^t - T) \in \{0, 1\}$. Conversely, and more importantly, symbolic sequences uniquely determine trajectories in the attractor of the LDS. Indeed, solving the iterations associated with trajectories whose components exist and are bounded for all $t \in \mathbb{Z}$ yields the following expression [9, 13]

$$x_s^t = (1 - a) \sum_{k=1}^{\infty} a^{k-1} \sum_{n=0}^{k} \ell_{n,k} \theta_{s-n}^{t-k} \qquad (4)$$

where the coefficients $\ell_{n,k} = \binom{k}{n}(1 - \epsilon)^{k-n}\epsilon^n \geq 0$ satisfy the evident normalisation

$$\sum_{n=0}^{k} \ell_{n,k} = 1, \ \forall k \in \mathbb{N}$$

Not only the LDS attractor can be fully specified using symbolic dynamics, but so do the topological properties of the dynamics in this set, when symbolic sequences are endowed with a suitable topology. In particular chaos of TW can be analyzed and quantified in the symbolic context.

This topological equivalence between the dynamics in the original space and its symbolic representation is standard in the theory of dynamical systems. However, what is specific to the current setting is the following iterative process for symbolic codes

---

[5] The symmetric features of Fig. 1 are consequence of the following symmetries of the LDS:

- If $\{x_s^t\}$ is a trajectory for T (with all $x_s^t \neq T$), then $\{1 - x_s^t\}$ is a trajectory for $1 - T$.
- If $F_\epsilon^q(x) = \sigma^p(x)$ then $F_{1-\epsilon}^q \circ R(x) = \sigma^{q-p} \circ R(x)$ where $(R(x))_s = x_{-s}$ for all s.

.

$$\theta_s^{t+1} = H\left((1-a)\sum_{k=0}^{\infty} a^k \sum_{n=0}^{k+1} \ell_{n,k+1}\theta_{s-n}^{t-k} - T\right), \quad \forall s, t \in \mathbb{Z} \qquad (5)$$

obtained by stipulating that the code of any trajectory given by (4) must coincide with the input symbolic sequence. In other words, the LDS attractor and its topological properties can be captured by an explicit iteration scheme for symbolic codes. This formulation has proved useful in several cases [9, 13, 17], for instance to obtain the estimates mentioned above about chaos of TW.

3 Selective Chaos of Travelling Waves for Finite Rank Approximations

A full mathematical proof of the numerical results of [13] remains elusive, especially because the iterations (5) involve the entire past sequence (*i.e.* the series in k is infinite when $a > 0$) and this makes it virtually impossible to determine all solutions for arbitrary values of the parameters. Here, we suggest to investigate instead the following finite rank iteration schemes, obtained by truncating the series in the expression (4) (and using a suitable normalisation)

$$\theta^{t+1} = \mathcal{F}_R(\theta^{t-R+1}, \dots, \theta^t) \quad \text{where} \quad \left(\mathcal{F}_R(\theta^{-R+1}, \dots, \theta^0)\right)_s \qquad (6)$$
$$= H\left(\frac{1-a}{1-a^R}\sum_{k=0}^{R-1} a^k \sum_{n=0}^{k+1} \ell_{n,k+1}\theta_{s-n}^{-k} - T\right).$$

The iteration scheme $\mathcal{F}_R$ can be viewed as a kind of cellular automaton (CA), which, thanks to the updated normalisation, actually shows the same symmetries as the original LDS. Our goal is to systematically determine the existence domains of TW for increasing values of R. Exponential decay of the coefficients a^k suggests that the $\mathcal{F}_R$ should be good approximations of the LDS; the larger R, the better the approximation. The dependence on a indicates that the approximation should be better for smaller values of this parameter.

Since $\mathcal{F}_R$ only involves input symbols in a time window of length R, the velocity of the TW $\mathcal{F}_R^q(\theta) = \sigma^p(\theta)$ must be of the form $\frac{p}{q}$ for $q \in \{1, \dots, R\}$ and $p \in \{0, \dots, q\}$ (and assuming wlog that p and q are co-prime). Similarly, the inputs are limited to the $R+1$ neighbour sites, so the TW profile $\{\theta_s\}$, when read from left to right, can be regarded as being generated by a topological Markov chains (subshift of finite type); given an arbitrary site s and an admissible $(R+1)$-block $\theta_{s-R+1}\cdots\theta_s$, the subshift specifies those subsequent admissible blocks $\theta_{s-R+2}\cdots\theta_{s+1}$ at the next site. This viewpoint is convenient for the computation of the TW entropy, as the logarithm of the largest eigenvalue of the corresponding transition matrix (see [15] for more details on finite-type subshift and the computation of their entropy).

3.1 Rank 1 Approximation

The simplest approximation is when the summation on k only has one term ($R = 1$) so that the iterative process on symbolic sequences reduces to one for elements of $\{0, 1\}^{\mathbb{Z}}$, *viz.* we have the following (genuine) CA

$$(\mathcal{F}_1(\theta))_s = H\left((1 - \epsilon)\theta_s + \epsilon\theta_{s-1} - T\right)$$

The TW velocities of $\mathcal{F}_1$ are $v \in \{0, 1\}$ are trivial. By the symmetry $v \leftrightarrow 1 - v$, it suffices to study the fixed points ($v = 0$). To that goal, let

$$X_1(\theta_1\theta_0) = (1 - \epsilon)\theta_0 + \epsilon\theta_1.$$

It is simple to check that

- In the interval $0 < T \leq \min\{X_1(10), X_1(01)\} = \min\{\epsilon, 1 - \epsilon\}$, the only possible fixed points are the homogeneous ones $0^{\mathbb{Z}}$ and $1^{\mathbb{Z}}$, and $\{H(s)\}$ mod σ.[6] Indeed, we then have $H(X_1(01) - T) = H(X_1(10) - T) = 1$. Furthermore, using that $X_1(01) = 1 - X_1(10)$, a symmetric conclusion holds for $T \in (X_1(01), 1]$.
- In the interval $\epsilon = X_1(10) < T \leq X_1(01) = 1 - \epsilon$, (which is non-empty obviously iff $\epsilon < \frac{1}{2}$) every element of $\{0, 1\}^{\mathbb{Z}}$ is a fixed point of $\mathcal{F}_1$ (full chaos of fixed points, with entropy equal to $\log 2$).

The entropy-velocity diagram of TW for $\mathcal{F}_1$ is given in Fig. 2. The situation is pretty obvious in this case as the two domains of existence of chaos of TW do not overlap.

3.2 Rank 2 Approximation

We now turn to the analysis of waves for $\mathcal{F}_2$. The only possible TW velocities in this case are $v \in \{0, \frac{1}{2}, 1\}$. Let

$$X_2\begin{pmatrix} \theta_2^1\theta_1^1\theta_0^1 \\ \theta_1^0\theta_0^0 \end{pmatrix} = \frac{1}{1+a}\sum_{k=0}^{1}a^k\sum_{n=0}^{k+1}\ell_{n,k+1}\theta_n^k,$$

(where sub- and super-scripts are denoted with non-negative integers for simplicity) which obviously depends on a and ϵ.

---

[6] All the LDS here are translation invariant; hence all their trajectories come as equivalence classes $\{x^t\}$ mod σ or $\{\theta^t\}$ mod σ.
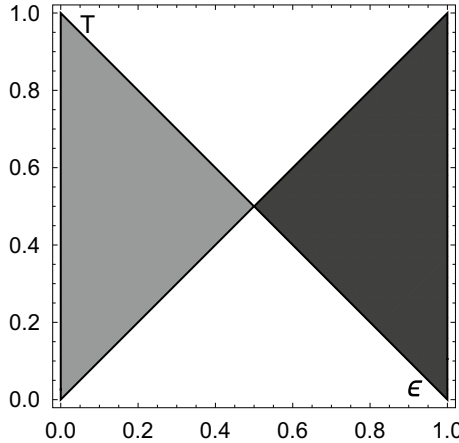
Fig. 2 Entropy-velocity diagrams of TW of the cellular automaton $\mathcal{F}_1$. The square of parameters (ϵ, T) decomposes into 4 regions. In the left grey triangle, every element $\theta \in \{0, 1\}^{\mathbb{Z}}$ is invariant under the dynamics (full chaos of fixed points). In the lower white triangle, the only non-homogeneous TW profiles are $\{H(s)\} \bmod \sigma$ ($v = 0$) and $\{H(-s)\} \bmod \sigma$ ($v = 1$). The TW in the other domains follow from symmetries

3.2.1 Analysis of Fixed Points

In order to determine the existence of fixed points ($v = 0$), one needs to order the values of X_2 for $\theta^1 = \theta^0$. Using the symmetry $X_2(1 - \cdot) = 1 - X_2(\cdot)$, it suffices to consider those $\theta^1 = \theta^0$ with $\theta_0^1 = \theta_0^0 = 0$. Using for simplicity, only the top row to identify the 3-blocks in this case, one can show that the corresponding values comply with the lexicographic order, *i.e.* we have

$$0 = X_2(000) < X_2(100) < X_2(010) < X_2(110).$$

Now, $\theta \in \{0, 1\}^{\mathbb{Z}}$ is a fixed point of $\mathcal{F}_2$ iff the following constraint holds on its 3-blocks $\{\theta_{s-2}\theta_{s-1}\theta_s\}_{s\in\mathbb{Z}}$

$$H\left(X_2\left(\theta_{s-2}\theta_{s-1}\theta_s\right) - T\right) = \theta_s, \ \forall s \in \mathbb{Z}.$$

As mentioned above, this constraint is regarded as defining a subshift over 3-blocks, which depends on parameters, see Fig. 4 for the graphs obtained from the analysis to follow.

By considering the relative position of T with respect to the ordered values of X_2 above, the following claims result about the existence of fixed point subshifts. Needless to say that similar conclusions immediately follow for the TW with $v = 1$, from the symmetry $\epsilon \leftrightarrow 1 - \epsilon$.
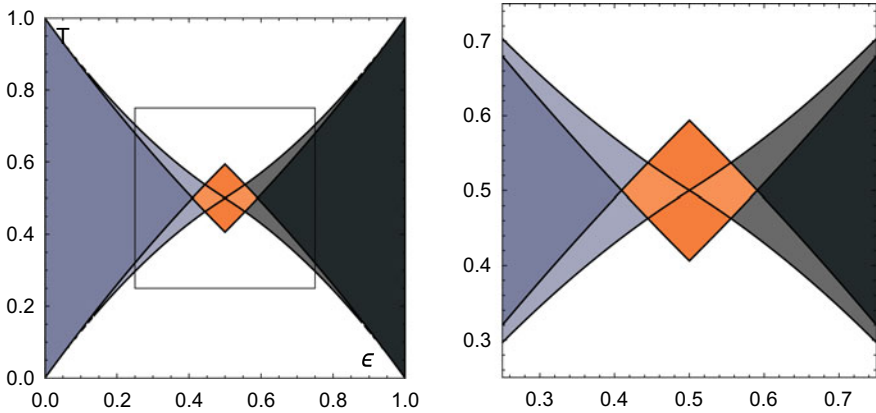
Fig. 3 Entropy-velocity diagram of TW of the cellular automaton $\mathcal{F}_2$ (and zoom into the central region). Chaos of fixed points is full in the central blue region (all 3-blocks are admissible and entropy $= \log 2$) and partial in the two other blue domains (either 110 or 001 is forbidden, depending on the domain/entropy $= \log \frac{1+\sqrt{5}}{2}$ in both cases). In the black domains, the same comments apply to $v = 1$ TW. Orange domains correspond to chaos of TW with $v = \frac{1}{2}$. In particular, in low intensity domains (left and right), both 010 and 101 are forbidden (entropy $= \log \frac{1+\sqrt{5}}{2}$). In each of the high intensity domains (bottom and top), only one of these words is forbidden (entropy $= \log 1.755$). Finally, the only admissible non-homogeneous profiles in the white domains are the same as in Fig. 2

- The full shift is admissible[7] iff $X_2(110) < T \leq 1 - X_2(110)$.
- The subshift for which all 3-blocks but 110 are allowed is admissible iff[8]

$$X_2(010) < T \leq \min\{X_2(110), X_2(001)\}.$$

  By symmetry $T \leftrightarrow 1 - T$, the subshift for which all 3-blocks but 011 are allowed is admissible iff $1 - T$ satisfies the same condition.
- There are no other possibly admissible subshifts of positive entropy. In particular, the only non-homogeneous fixed points which exist for $0 < T \leq \min\{X_2(010), X_2(001)\}$, write $\{H(s)\} \bmod \sigma$.[9] By symmetry $T \leftrightarrow 1 - T$, the only non-trivial fixed points for $\max\{X_2(001), X_2(110)\} < T \leq 1$ are $\{1 - H(s)\} \bmod \sigma$.

As before, the intervals in either of the first two items are non-empty iff ϵ is not too large (and smaller than some threshold smaller than $\frac{1}{2}$ that depends on a). Moreover,

---

[7] This means that every element in this set if a fixed point.

[8] To see this, note that we have $H(X_2(\theta_2 \theta_1 0, \theta_1 0) - T) = 0$ except when $\theta_2 = \theta_1 = 1$ and $H(X_2(\theta_2 \theta_1 1, \theta_1 1) - T) = 1$ for every $\theta_2, \theta_1 \in \{0, 1\}$.

[9] Indeed, we then have $H\left(\binom{\theta 1 0}{1 0} - T\right) = 1$ for $\theta \in \{0, 1\}$. Alternatively, one first observes that the new constraint $T \leq X_2(010)$ immediately implies that 010 is forbidden. The transition graph on Fig. 4 then implies that the block 101, and then also 100, cannot be accessed either. The only non-trivial admissible path is the one that joins 000 to 111. Notice also that these fixed points exist in the larger interval $0 < T \leq \min\{X_2(110), X_2(001)\}$.
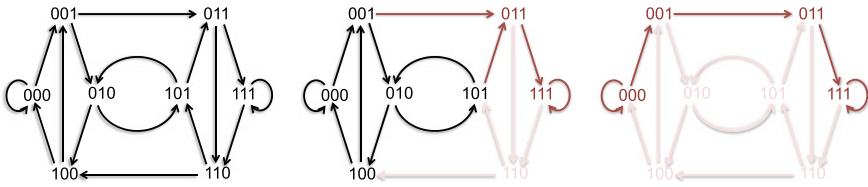
Fig. 4 Graphs associated with the (nested) 3-blocks subshifts that generate the (parameter dependent) fixed point sets of the cellular automaton $\mathcal{F}_2$. *Left*. DeBruijn graph $B(2, 3)$ (see Wikipedia or [18]) associated with the full shift. *Center*. All 3-blocks but 110 are allowed. *Right*. The four blocks 110, 010, 101 and 100 are forbidden. Light red color corresponds to blocks/transitions that are forbidden. Dark red color corresponds to transient blocks/transitions that do not contribute to the subshift entropy

they are adjacent when all non-empty. The intervals in the third claim are never empty, see Fig. 3.

As entropy is concerned, it is obviously equal to $\log 2$ in the first case. To compute it in the second case (and also for any other subshift in the sequel), we consider that this quantity is not affected by passing to non-wandering sets, so that the transitions painted in red in the central picture of Fig. 4 can be ignored. The remaining subshift turns out to be identical to the *golden shift*, Fig. 6a, whose entropy can be easily computed as the logarithm of the largest eigenvalue $\frac{1+\sqrt{5}}{2} \simeq 1.618$ of the matrix $\begin{pmatrix} 1 & 1 \\ 1 & 0 \end{pmatrix}$.

3.2.2 Analysis of TW with Velocity $v = \frac{1}{2}$

A configuration $\theta \in \{0, 1\}^{\mathbb{Z}}$ of a TW with velocity $v = \frac{1}{2}$ is defined by $\theta = \mathcal{F}_2(\sigma^{-1}(\theta), \theta)$ (or equivalently by $\sigma(\theta) = \mathcal{F}_2(\theta, \sigma(\theta))$). In this case, the analysis of admissible 3-blocks then amounts to consider both quantities $X_2 \begin{pmatrix} \theta_2\theta_1\theta_0 \\ \theta_1\theta_0 \end{pmatrix}$ and $X_2 \begin{pmatrix} \theta_2\theta_1\theta_0 \\ \theta_2\theta_1 \end{pmatrix}$ and to obtain conditions so that its output is equal to θ_1 in both cases. The results are given below and the corresponding transition graphs are presented in Fig. 5.

- The subshift for which all 3-blocks but 101 are allowed (Fig. 5 left) is admissible iff[10]

$$\max \left\{ X_2 (001), X_2 \begin{pmatrix} 100 \\ 10 \end{pmatrix} \right\} < T \le \min \left\{ X_2 (010), X_2 \begin{pmatrix} 010 \\ 01 \end{pmatrix} \right\}.$$

---

[10] Indeed, we then have $H \left(X_2 \begin{pmatrix} \theta_2\theta_1\theta_0 \\ \theta_1\theta_0 \end{pmatrix} - T \right) = H \left(X_2 \begin{pmatrix} \theta_2\theta_1\theta_0 \\ \theta_2\theta_1 \end{pmatrix} - T \right) = \theta_1$ for all $\theta_2\theta_1\theta_0 \neq$ 101. Conversely, that the block 101 is not admissible is obvious from the condition on T. (NB: When the space-time symbol block corresponds to a fixed point, we use the simplified notation).
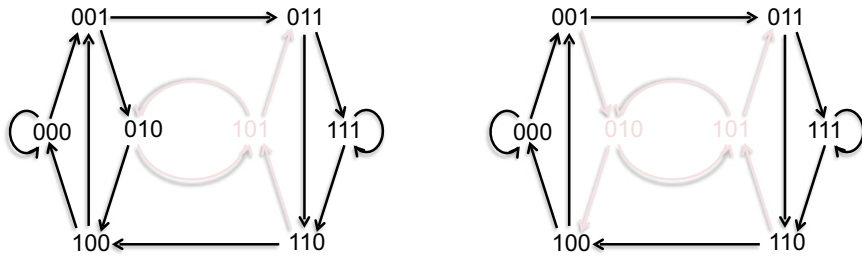
Fig. 5 Graphs associated with subshifts that generate TW of velocity $\frac{1}{2}$ of the CA $\mathcal{F}_2$. *Left.* The block 101 is the only forbidden one. *Right.* Both 101 and 010 are forbidden. Same color codes as in Fig. 4

By the symmetry $T \leftrightarrow 1 - T$, the subshift in which no 3-block is equal to 010 is admissible iff $1 - T$ satisfies the same condition (which amounts to reflect the interval wrt to $\frac{1}{2}$).

- The subshift for which all 3-blocks but 101 and 010 are allowed (Fig. 5 right) is admissible iff

$$\max \left\{ X_2 \left(001 \right), X_2 \begin{pmatrix} 100 \\ 10 \end{pmatrix} \right\} < T \leq \min \left\{ X_2 \left(110 \right), X_2 \begin{pmatrix} 011 \\ 01 \end{pmatrix} \right\}.$$

- There are no other possibly admissible subshifts of positive entropy. In particular, no non-homogeneous TW with $v = \frac{1}{2}$ exists when the previous condition fails.

As before, the intervals for T depend on ϵ, but this time they are non-empty only when ϵ is close enough to $\frac{1}{2}$ (again depending on a), and complement existence domains of chaos of fixed points and TW with $v = 1$, see Fig. 3. Moreover, the interval in the second item contains the two ones in the first item.[11] These two intervals never intersect,[12] which means that it is impossible to have full chaos of TW with $v = \frac{1}{2}$.

As entropy is concerned, using a similar non-wandering argument as above, we obtain that the entropy of the subshift(s) in the first item is obtained from the largest eigenvalue $\lambda \sim 1.755$ of the transition matrix $\begin{pmatrix} 1 & 1 & 0 \\ 0 & 1 & 1 \\ 1 & 0 & 0 \end{pmatrix}$ associated with the graph

---

[11] Indeed, we have $\min \left\{ X_2 \begin{pmatrix} 010 \\ 10 \end{pmatrix}, X_2 \begin{pmatrix} 010 \\ 01 \end{pmatrix} \right\} < \min \left\{ X_2 \begin{pmatrix} 011 \\ 01 \end{pmatrix}, X_2 \begin{pmatrix} 110 \\ 10 \end{pmatrix} \right\} = 1 - \max \left\{ X_2 \begin{pmatrix} 100 \\ 10 \end{pmatrix}, X_2 \begin{pmatrix} 001 \\ 01 \end{pmatrix} \right\}$.

[12] Because $\min \left\{ X_2 \begin{pmatrix} 010 \\ 10 \end{pmatrix}, X_2 \begin{pmatrix} 010 \\ 01 \end{pmatrix} \right\} \leq \frac{1}{2}$.
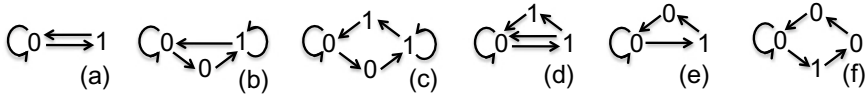
Fig. 6 Transitions graphs of some simple subshifts, which capture the entropy of TW profile subshifts in the CA $\mathcal{F}_R$, see text more details
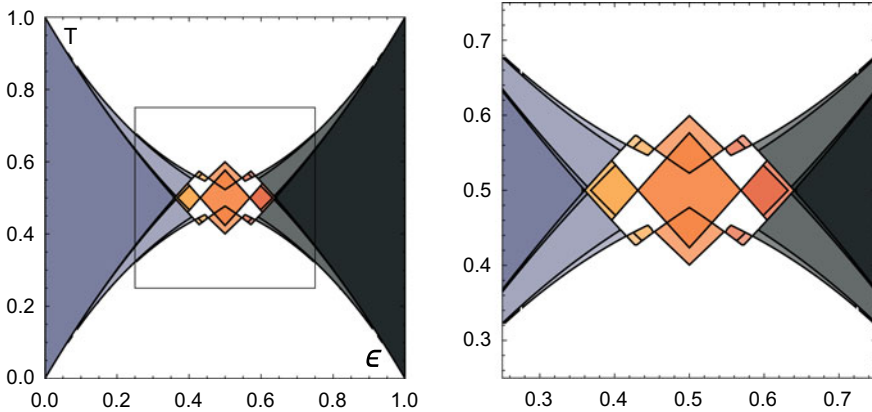
Fig. 7 Entropy-velocity diagram of TW of the cellular automaton $\mathcal{F}_3$ (and zoom into the central region). As before, chaos of fixed points is full in the central blue region and the successive lower blue domains correspond to successive subshifts in Table 1/Fig. 8. The central orange domains is where we have chaos of TW with $v = \frac{1}{2}$ (Table 2 and Fig. 9). The intermediate yellow and red domains respectively correspond to $v = \frac{1}{3}$ and $v = \frac{2}{3}$, see Table 3 and Fig. 9 for a description of these domains, together with the corresponding subshifts

in Fig. 6b. The entropy of the subshift in the second item is equal to that of the one depicted in Fig. 6c, which turns out to be equal to that of the golden shift $\log \frac{1+\sqrt{5}}{2}$ ($< \log 1.755$).

3.3 Rank 3 Approximation

In order to obtain further refinement of the entropy-velocity diagram, the next logical step is to consider the rank 3 approximation $\mathcal{F}_3$. The analysis is similar to as before and we only provide the results here, which are illustrated by the entropy-velocity diagram in Fig. 7. To that goal, we shall need to investigate the values of the function

$$X_3 \begin{pmatrix} \theta_3^2 \theta_2^2 \theta_1^2 \theta_0^2 \\ \theta_2^1 \theta_1^1 \theta_0^1 \\ \theta_1^0 \theta_0^0 \end{pmatrix} = \frac{1-a}{1-a^3} \sum_{k=0}^{2} a^k \sum_{n=0}^{k+1} \ell_{n,k+1} \theta_n^k,$$

Table 1 Summary of possibly admissible (nested) subshifts of fixed points in the CA $\mathcal{F}_3$, together with references to the graphs in Fig. 8, to their simplification in Fig. 6 (where it applies), to entropy estimates and to the intervals of the parameter T where they are admissible. (NB: The constraint in the first column means that words that are *not* forbidden are all admissible. The symbol $+$ means *in addition to forbidden blocks in the previous row*.)

Forbidden 4-blocks	Graphs	Entropy	Existence condition
None	Figure 8a	$\log 2$	$X_3(1110) < T \leq X_3(0001) =$ $1 - X_3(1110)$
1110	Figures 8b/6d	$\log 1.839$	$X_3(0110) < T \leq \min\{X_3(1110), X_3(0001)\}$
$+$ 0110, 1100, 1101	Figures 8c/6a	$\log \frac{1+\sqrt{5}}{2}$	$X_3(1010) < T \leq \min\{X_3(0110), X_3(0001)\}$
$+$ 1010	Figures 8d/6e	$\log 1.466$	$X_3(0010) < T \leq \min\{X_3(1010), X_3(0001)\}$
all non-homogenous	Figure 8e	0	$0 < T \leq \min\{X_3(0010), X_3(0001)\}$

Fixed points. As before, one can check that the values of this function, for configurations $\theta^2 = \theta^1 = \theta^0$ that are associated with fixed points, are ordered according the lexicographic order. We have for $\epsilon \in (0, \frac{1}{2})$, and using similar notation as for rank-2 fixed points,

$$X_3(1000) < X_3(0100) < X_3(1100) < X_3(0010) < X_3(1010) < X_3(0110) < X_3(1110).$$

The admissible 4-blocks subshifts depend on the relative location of the threshold T with respect to this ordering. The possibly admissible subshifts are those listed in Table 1—there are no other possibly admissible subshifts of positive entropy, excepted, evidently those obtained by the exchanging 0 and 1—and illustrated in Fig. 8.

As for the rank-2 fixed points, the intervals in T are only non-empty when ϵ is not too large. When non-empty, these intervals are adjacent to each other. The subshift are nested, with decreasing entropy, when T moves away from $\frac{1}{2}$.

TW with velocity $v = \frac{1}{2}$. For $v = \frac{1}{2}$ TW, one needs to check that we simultaneously have

$$X_3 \begin{pmatrix} \theta_3\theta_2\theta_1\theta_0 \\ \theta_2\theta_1\theta_0 \\ \theta_2\theta_1 \end{pmatrix} = \theta_1 \quad \text{and} \quad X_3 \begin{pmatrix} \theta_3\theta_2\theta_1\theta_0 \\ \theta_3\theta_2\theta_1 \\ \theta_2\theta_1 \end{pmatrix} = \theta_2,$$

for every 4-block in the presumed subshifts. Candidate subshifts can be obtained from the 4-block graph associated with the full shift on 2 symbols, de Bruijn graph $B(2, 4)$, Fig. 8a. The possibly admissible subshifts are listed in Table 2—there are no other possibly admissible subshifts of positive entropy, excepted,[13] evidently, those obtained by the exchanging 0 and 1—and illustrated in Fig. 9.

---

[13] In particular, the analysis shows that no subshift can be admissible without 1001 and 0110 being admissible. Similarly, the numerical computations of the existence conditions show that no admissible subshift can allow for 0101 or 1010.
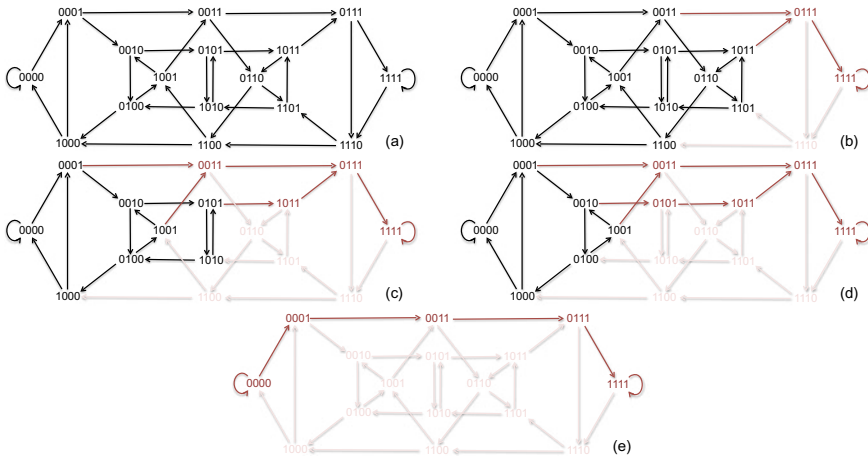
Fig. 8 Graphs associated with the (nested) 4-blocks subshifts in Table 1. Details as in Fig. 4

Table 2 Summary of possibly admissible subshifts of TW $v = \frac{1}{2}$ in the CA $\mathcal{F}_3$, together with references to the graphs in Fig. 9, to their simplification in Fig. 6 (where it applies), to entropy estimates and to existence domains, expressed in terms of intervals for the parameter T. In particular, the intervals in the middle row are symmetric wrt $\frac{1}{2}$

Graphs	Entropy	Existence condition
Figures 9b/6e	log 1.446	$\max \left\{ X_3 \begin{pmatrix} 0100 \\ 100 \\ 10 \end{pmatrix}, X_3 \begin{pmatrix} 0010 \\ 001 \\ 10 \end{pmatrix} \right\} < T \leq$
		$\min \left\{ X_3 \begin{pmatrix} 0010 \\ 010 \\ 01 \end{pmatrix}, X_3 \begin{pmatrix} 0100 \\ 010 \\ 10 \end{pmatrix} \right\}$
Figures 9d/6c	$\log \frac{1+\sqrt{5}}{2}$	$\max \left\{ X_3 \begin{pmatrix} 0011 \\ 001 \\ 01 \end{pmatrix}, X_3 \begin{pmatrix} 1100 \\ 100 \\ 10 \end{pmatrix} \right\} < T \leq$
		$\min \left\{ X_3 \begin{pmatrix} 1100 \\ 110 \\ 10 \end{pmatrix}, X_3 \begin{pmatrix} 0011 \\ 011 \\ 01 \end{pmatrix} \right\}$
Figure 9e	log 1.674	Intersection of previous conditions

As for the rank-2 TW $v = \frac{1}{2}$, the intervals in T are non-empty when ϵ is close to $\frac{1}{2}$. However, when both non-empty, the intervals in the first and second rows overlap and enhancement of the entropy results when either T or $1 - T$ lies in their intersection (Notice also, that the interval in the first row never intersects its reflected image wrt $\frac{1}{2}$).
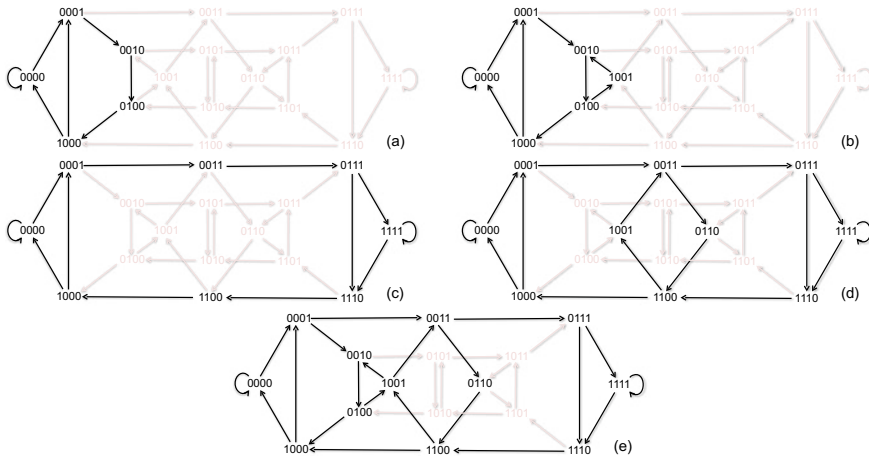
Fig. 9 Graphs associated with the subshifts in Tables 2 and 3

TW with velocity $v = \frac{1}{3}$. In addition to fixed points and $v = \frac{1}{2}$ TW, the rank 3 approximation may also have $v = \frac{1}{3}$ (and $v = \frac{2}{3}$) TW. We focus on $v = \frac{1}{3}$ since the other one can be deduced from the symmetry $\epsilon \leftrightarrow 1 - \epsilon$. In this case, a 4-block $\theta_3 \theta_2 \theta_1 \theta_0$ is admissible iff the following three conditions simultaneously hold

$$X_3 \begin{pmatrix} \theta_3 \theta_2 \theta_1 \theta_0 \\ \theta_2 \theta_1 \theta_0 \\ \theta_1 \theta_0 \end{pmatrix} = X_3 \begin{pmatrix} \theta_3 \theta_2 \theta_1 \theta_0 \\ \theta_2 \theta_1 \theta_0 \\ \theta_2 \theta_1 \end{pmatrix} = X_3 \begin{pmatrix} \theta_3 \theta_2 \theta_1 \theta_0 \\ \theta_3 \theta_2 \theta_1 \\ \theta_2 \theta_1 \end{pmatrix} = \theta_1,$$

As before, candidate subshifts can be obtained by pruning the de Bruijn graph $B(2, 4)$. Up to the symmetry $0 \leftrightarrow 1$, the resulting possibly admissible subshifts are listed in Table 3 (again, no other subshift of positive entropy can be admissible), where the existence conditions have been simplified by assuming $\epsilon \leq \frac{1}{2}$. The corresponding existence domains do not intersect those of previous velocities, except for some boundaries (complementary domains). The corresponding intervals in T are only non-empty when ϵ lies in a intermediate range, between existence domains of velocities 0 and $\frac{1}{2}$. The subshifts are similar to those associated with $v = \frac{1}{2}$ TW (NB: in particular, no admissible subshift can allow for 0101 or 1010); however, there are two significant differences

- The admissibility of the blocks 1001 and 0110 is not a consequence of that of other blocks; hence there are additional (nested) existence domains (see 2nd and 4th rows in Table 3).
- The existence domains do not overlap as they did; so that there no enhancement effect on the entropy exists in this case.

Table 3 Summary of possibly admissible subshifts of TW $v = \frac{1}{3}$ in the CA $\mathcal{F}_3$, together with references to the graphs in Fig. 9, their simplification in Fig. 6 (where it applies), entropy estimates and existence domains. The intervals in the last two rows are symmetric wrt to $\frac{1}{2}$. The interval in the 2nd (resp. 4th) row is contained in the one of the 1st (resp. 3rd) row. The entropy of the subshift in rows 2 and 3 are unexpectedly equal

Graphs	Entropy	Existence condition	
Figures 9a/6f	log 1.380	$\max \left\{ X_3\,(0001)\,, X_3 \begin{pmatrix} 0100 \\ 010 \\ 10 \end{pmatrix} \right\}$	$< T \le$
		$\min \left\{ X_3\,(0010)\,, X_3 \begin{pmatrix} 0010 \\ 001 \\ 01 \end{pmatrix} \right\}$	
Figures 9b/6e	log 1.446	$\max \left\{ X_3\,(1001)\,, X_3 \begin{pmatrix} 0100 \\ 010 \\ 10 \end{pmatrix} \right\}$	$< T \le$
		$\min \left\{ X_3\,(0010)\,, X_3 \begin{pmatrix} 0010 \\ 001 \\ 01 \end{pmatrix} \right\}$	
Figure 9c	log 1.466	$\max \left\{ X_3\,(0001)\,, X_3 \begin{pmatrix} 1100 \\ 110 \\ 10 \end{pmatrix} \right\}$	$< T \le$
		$\min \left\{ X_3\,(1110)\,, X_3 \begin{pmatrix} 0011 \\ 001 \\ 01 \end{pmatrix} \right\}$	
Figures 9d/6c	$\log \frac{1+\sqrt{5}}{2}$	$\max \left\{ X_3\,(1001)\,, X_3 \begin{pmatrix} 1100 \\ 110 \\ 10 \end{pmatrix} \right\}$	$< T \le$
		$\min \left\{ X_3\,(0110)\,, X_3 \begin{pmatrix} 0011 \\ 001 \\ 01 \end{pmatrix} \right\}$	

4   Concluding Remarks

The analysis above has revealed that chaos of TW is selective in basic finite rank approximations $\mathcal{F}_R$ of the LDS F_ϵ, with unique velocity depending on parameters. More than in F_ϵ, in the $\mathcal{F}_R$, this uniqueness applies to all velocities and not only to $v \in (0, 1)$. For $\mathcal{F}_3$, some boundaries curves in the (ϵ, T) square, of the domains associated with $v = \frac{1}{3}$, coincide with some boundaries associated with $v = 0$ (Fig. 7) (and a similar coincidence holds for $v = \frac{1}{2}$ and $v = 0$ in Fig. 3). This suggests that some overlap between the domains for $v = 0$ and $v = \frac{1}{R}$ might exist for R large enough.

   Moreover, even though this analysis is too preliminary to anticipate full results for larger values of R, some systematic features have emerged. In particular, the fact that for any R, the following *extreme* subshifts can certainly admissible, depending on the parameters:

- B_R: every block of consecutive 0's (or consecutive 1's) must be of length R or longer; a generalisation of the graphs in Fig. 5 right and Fig. 9c.
- A_R: every block of consecutive 0's must be of length R or larger, and every 1 must be isolated (or the subshift resulting from exchanging 0's and 1's); a generalisation of the graphs in Fig. 9a.

Sufficient existence conditions for these subshifts have been provided in [13], in term of existence regions of fronts and solitary waves respectively. Namely, domains in the (ϵ, T) square have been given, so that the subshift B_R (resp. A_R) of TW with $v = \frac{p}{q}$ given and R sufficiently large, is admissible. However, to compute existence conditions of A_R and B_R for any R, is not totally obvious, even though there are some similarities between the case $R = 2$ and $R = 3$. Those computations could be part of a continuation to this paper.

References

1. Afraimovich VS (2005) Some topological properties of lattice dynamical systems. In: Chazottes J-R, Fernandez B (eds) Dynamics of coupled map lattices and of related spatially extended systems, vol 671. Springer, pp 153–179
2. Milnor J (1986) Directional entropies of cellular automaton maps. In: Disordered systems and biological organization, pp 113–115. Springer
3. Milnor J (1988) On the entropy geometry of cellular automata. Complex Syst 2:357–385
4. Afraimovich VS, Courbage M, Fernandez B, Morante A (2002) Directional entropy in lattice dynamical systems. In: Progress in nonlinear science, vol 1, pp 9–30. RAS, Institute of Applied Physics, Nizhny Novgorod
5. Robinson C (1999) Dynamical systems, 2nd edn. CRC Press
6. Afraimovich VS, Morante A, Ugalde E (2003) On the density of directional entropy in lattice dynamical systems. Nonlinearity 17:105–116
7. Coullet P, Elphick C, Repaux D (1987) Nature of spatial chaos. Phys Rev Lett 58:431
8. Eckmann J-P, Proccacia I (1991) Onset of defect-mediated turbulence. Phys Rev Lett 66:891
9. Coutinho R, Fernandez B (1997) Extended symbolic dynamics in bistable CML: Existence and stability of fronts. Physica D 108:60–80
10. Afraimovich VS, Pesin Y (1993) Travelling waves in lattice models of multi-dimensional and multi-component media. I. General hyperbolic properties. Nonlinearity 6:429–455
11. Afraimovich VS, Fernandez B (2000) Topological properties of linearly coupled expanding map lattices. Nonlinearity 13:973–993
12. Afraimovich VS, Nekorkin VI (1994) Chaos of traveling waves in a discrete chain of diffusively coupled maps. Int J Bif Chaos 4:631–637
13. Fernandez B, Luna B, Ugalde E (2009) Spatial chaos of travelling waves has a unique velocity. Phys Rev E 80:025203(R)

14. Fernandez B, Luna B, Ugalde E (2011) Erratum: Spatial chaos of traveling waves has a given velocity. Phys Rev E 83:039906
15. Lind D, Marcus B (1995) An introduction to symbolic dynamics and coding. Cambridge University Press
16. Badii R, Politi A (1997) Complexity: hierarchical structures and patterns in Physics. Cambridge University Press
17. Fernandez B, Coutinho R (1997) On the global orbits in a bistable CML. Chaos 7:301–310
18. de Bruijn NG (1946) A combinatorial problem. Koninklijke Nederlandse Akademie v. Wetenschappen 49:758–764

On Periodic Motions in a van der Pol Oscillator

Check for updates

Yeyin Xu and Albert C. J. Luo

Abstract In this chapter, symmetric periodic motions in a periodically forced van der Pol oscillator is presented. To obtain the periodic motions, the discrete maps of the van der Pol oscillator are developed through the discretization of the corresponding differential equations. Through mapping structures of periodic motions, stable and unstable periodic motions are obtained. A sequence of symmetric periodic motions to chaos with $1(S) \triangleleft 3(S) \triangleleft \cdots \triangleleft (2l-1)(S) \triangleleft \cdots$ is presented. The numerical simulations of the periodic motions are completed for illustration of motion complexity. This chapter is for a memory of Valentin Afraimovich for 20-year friendship.

1 Introduction

In 1788, Langrage [1] used the method of averaging for the periodic motions of a three-body problem from the perturbation of a two-body problem. The method of averaging was based on the solutions of the corresponding linear systems with coefficients slowly varying. At the end of the 19th century, Poincaré [2] extended the idea of averaging and developed the perturbation method for the approximate analytical solutions of periodic motions of the celestial bodies. In 1920, van der Pol [3] used the method of averaging to determine periodic oscillation in the circuits. In 1928, Fatou [4] gave a proof of the asymptotic validity of the method of averaging through the solution existence theorem of differential equations. In 1935, Krylov and Bogoliubov [5] further extended the method of averaging for nonlinear oscillations in nonlinear vibration systems. Since then, the perturbation method has become a popular approach for periodic solutions in nonlinear dynamical systems. In 1964, Hayashi [6] used the perturbation and traditional harmonic balance methods for periodic motions in nonlinear systems. The multiscale perturbation method was extensively used for nonlinear vibration (e.g., Nayfeh [7]; Nayfeh and Mook [8]). Recently, one also used the perturbation method for periodic motions and chaos in nonlinear

Y. Xu · A. C. J. Luo (✉)

Department of Mechanical and Industrial Engineering, Southern Illinois University Edwardsville, Edwardsville, IL 62026-1805, USA

e-mail: aluo@siue.edu

systems. In 2016, Maaita [9] discussed the bifurcation of the slow invariant manifolds of completed oscillators. In 2017, Yamgoue et al. [10] studied the approximate analytical solutions of a constrained nonlinear mechanical system. Shayak and Vyas [11] used the Kyylov-Bogoliubov method to the Mathieu equation. Rajamani and Rajasekar [12] discussed the response amplitude of the parametrical Duffing oscillator. Though chaotic motions in nonlinear systems were studied by the perturbation method, such a way for chaotic motions in nonlinear dynamical systems may not be adequate. The perturbation methods require the corresponding linear solutions to determine the approximate periodic solutions of original nonlinear systems, and the perturbation expansion with small parameters was adopted.

To avoid the aforementioned puzzling issues for the traditional analytical methods, in 2012, Luo [13] developed the generalized harmonic balance method for analytical periodic motions in nonlinear dynamical systems. Luo and Huang [14] employed such a method for approximate analytical solutions of periodic motions in the Duffing oscillator, and Luo and Huang [15] gave the analytical bifurcation trees of period-m motions to chaos in the Duffing oscillator. For the twin-well Duffing oscillator, bifurcation trees of periodic motions to chaos are presented in Luo and Huang [16, 17]). In 2013, Luo and Lakeh [18] obtained the analytical solutions of period-m motions of the van der Pol-Duffing oscillator. From the generalized harmonic balance method, Xu et al. [19] studied periodic motions in a first-order nonlinear dynamic system. Luo and Wang [20] used the generalized harmonic balance method for approximate analytical solutions of periodic motions in the rotor dynamical systems. The generalized harmonic balance methods and applications can be found in Luo [21, 22]

The generalized harmonic balance method is very good for polynomial nonlinear systems. However, it is difficult to apply such a method to non-polynomial nonlinear systems. Thus, in 2015, Luo [23] developed a semi-analytical method for the prediction of periodic motions in nonlinear dynamic systems. This approach discretizes nonlinear differential equations into discrete mappings. Using mapping structures to construct periodic motions, the corresponding algebraic equations are used to determine the discrete nodes of periodic motions. Further, the periodic motions in the corresponding nonlinear systems are obtained. Such a method can control computational errors of periodic motions. Luo and Guo [24] used such a semi-analytical method for the bifurcation trees of periodic motions to chaos in the hardening Duffing oscillator. Periodic motions to chaos in such a twin-well Duffing oscillator were also studied in Guo and Luo [25]. In addition, Luo and Guo [26] used such a semi-analytical method to investigate bifurcation trees of periodic motions to chaos in periodically excited pendulum (also see, Guo and Luo [27]). Guo and Luo [28] presented the bifurcation trees of periodic motions in parametrically driven pendulum. Such a method was systematically presented in Luo [29]. The semi-analytical method was also developed for time-delay nonlinear systems.

In 2015, Luo and Xing [30, 31] applied such semi-analytical method to investigate a time-delay hardening Duffing oscillator. Luo and Xing [32] also discussed time-delay effects on periodic motions in the time-delay Duffing oscillator. In Xing and Luo [33], discovered was possible infinite bifurcation trees of period-1 motions

to chaos in the time-delay, twin-well Duffing oscillator. Luo [34] systematically presented the semi-analytical method for time-delayed nonlinear systems. In 2018, Xu and Luo [35] used the semi-analytical method studying periodic motions in a two-degrees-of-freedom van der Pol Duffing oscillator, and a periodic motion series was determined. Xu and Luo [36] found a sequential order of period-(2 m-1) motions in a periodically forced van der Pol oscillator.

In this chapter, periodic motions in the periodically forced van der Pol oscillator will be discussed for a better understanding of dynamics of the van der Pol oscillators. The corresponding stability and bifurcations of periodic motions will be analyzed. Numerical simulations will be carried out for illustrations of motion complexity in the van der Pol oscillator.

2 A Semi-analytical Method

Consider a periodically forced, van der Pol oscillator as

$$\ddot{x} - (\alpha_1 - \alpha_2 x^2)\dot{x} + \beta x = Q_0 \cos \Omega t \qquad (1)$$

where α_1 and α_2 are linear and nonlinear damping coefficients. β is the linear stiffness coefficient; Q_0 and Ω are excitation amplitude and frequency, respectively. The state space form of Eq. (1) is

$$\dot{x} = y,$$
$$\dot{y} = (\alpha_1 - \alpha_2 x^2)\dot{x} - \beta x + Q_0 \cos \Omega t. \qquad (2)$$

From Luo [25], for $t \in [t_{k-1}, t_k]$, Eq. (2) is discretized by a midpoint scheme and a mapping P_k ($k = 1, 2, 3, \cdots$) as

$$P_k : \mathbf{x}_{k-1} \to \mathbf{x}_k \Rightarrow \quad \mathbf{x}_k = P_k \mathbf{x}_{k-1} \qquad (3)$$

where $\mathbf{x}_k = (x_k, y_k)^T$ is the node of motion in the van der Pol oscillator. The algebraic equations of discrete implicit mapping for P_k ($k = 1, 2, \cdots, N$) are

$$x_k = x_{k-1} + \tfrac{1}{2}h(y_k + y_{k-1}),$$
$$y_k = y_{k-1} + h\{\tfrac{1}{8}[4\alpha_1 - \alpha_2(x_k + x_{k-1})^2](y_k + y_{k-1})$$
$$\quad - \tfrac{1}{2}\beta(x_k + x_{k-1}) + Q_0 \cos \Omega (t_{k-1} + \tfrac{1}{2}h)\} \qquad (4)$$

where $h = t_k - t_{k-1}$ is the time step, and t_0 is the initial time.

For the semi-analytical solutions of period-m motions in the van der Pol oscillator, the mapping in Eq. (3) becomes for $k = 1, 2, \cdots mN$

$$P_k^{(m)} : \mathbf{x}_{k-1}^{(m)} \to \mathbf{x}_k^{(m)} \implies \mathbf{x}_{k-1}^{(m)} = P_k^{(m)} \mathbf{x}_k^{(m)}, \tag{5}$$

where $\mathbf{x}_k^{(m)} = (x_k^{(m)}, y_k^{(m)})^{\mathrm{T}} (k = 1, 2, \cdots, mN)$. The mapping structure of period-m motions of the van der Pol oscillator is

$$P^{(m)} : \mathbf{x}_0^{(m)} \to \mathbf{x}_{mN}^{(m)} \implies \mathbf{x}_{mN}^{(m)} = P^{(m)} \mathbf{x}_0^{(m)} \tag{6}$$

where $P^{(m)} = P_{mN}^{(m)} \circ P_{mN-1}^{(m)} \circ \cdots \circ P_2^{(m)} \circ P_1^{(m)} (m = 1, 2, \cdots)$. The corresponding algebraic equations for $P_k^{(m)} (k = 1, 2, \cdots, mN)$ are

$$
\begin{aligned}
x_k^{(m)} &= x_{k-1}^{(m)} + \tfrac{1}{2}h(y_k^{(m)} + y_{k-1}^{(m)}), \\
y_k^{(m)} &= y_{k-1}^{(m)} + h\{\tfrac{1}{2}(y_{1,k}^{(m)} + y_{1,k-1}^{(m)})[\alpha_{11} - \tfrac{1}{4}\alpha_{12}(x_{1,k}^{(m)} + x_{1,k-1}^{(m)})^2] \\
&\quad - \tfrac{1}{2}\beta_{11}(x_{1,k}^{(m)} + x_{1,k-1}^{(m)}) + Q_0 \cos \Omega (t_{k-1} + \tfrac{1}{2}h)\} .
\end{aligned}
\tag{7}
$$

The periodicity conditions are

$$x_{mN}^{(m)} = x_0^{(m)}, \, y_{mN}^{(m)} = y_0^{(m)}. \tag{8}$$

Based on Eqs. (7) and (8), the periodic solutions of a period-m motion in the van der Pol oscillator can be obtained by solving $2(mN + 1)$ equations. Thus, the nodes $\mathbf{x}_k^{(m)*} (k = 0, 1, 2, \cdots, mN)$ give the semi-analytical solution of the period-m motion.

For the mapping structure in Eq. (5), consider a small disturbance $\Delta\mathbf{x}_{k-1}$ in the vicinity of $\mathbf{x}_{k-1}^{(m)*}$ (i.e., $\mathbf{x}_{k-1}^{(m)} = \mathbf{x}_{k-1}^{(m)*} + \Delta\mathbf{x}_{k-1}^{(m)}, k = 1, 2, \cdots, mN)$. With the variation of $\Delta\mathbf{x}_k^{(m)}$, Eq. (7) can be linearized by

$$\frac{\partial \mathbf{f}_k}{\partial \mathbf{x}_{k-1}^{(m)}}|_{(\mathbf{x}_{k-1}^{(m)*}, \mathbf{x}_k^{(m)*})} \Delta\mathbf{x}_{k-1}^{(m)} + \frac{\partial \mathbf{f}_k}{\partial \mathbf{x}_k^{(m)}}|_{(\mathbf{x}_{k-1}^{(m)*}, \mathbf{x}_k^{(m)*})} \Delta\mathbf{x}_k^{(m)} = \mathbf{0} \tag{9}$$

where $\mathbf{f}_k = (f_{1,k}, f_{2,k})^{\mathrm{T}}$ with

$$
\begin{aligned}
f_{1,k} &= x_k^{(m)} - x_{k-1}^{(m)} - \tfrac{1}{2}h(y_k^{(m)} + y_{k-1}^{(m)}), \\
f_{2,k} &= y_k^{(m)} - y_{k-1}^{(m)} - h\{\tfrac{1}{8}[4\alpha_1 - \alpha_2(x_k^{(m)} + x_{k-1}^{(m)})^2](y_k^{(m)} + y_{k-1}^{(m)}) \\
&\quad - \tfrac{1}{2}\beta(x_k^{(m)} + x_{k-1}^{(m)}) + Q_0 \cos \Omega (t_{k-1} + \tfrac{1}{2}h)\}.
\end{aligned}
\tag{10}
$$

Equation (8) gives

$$\Delta\mathbf{x}_k^{(m)} = -\left[\frac{\partial \mathbf{f}_k}{\partial \mathbf{x}^{(m)}}\right]^{-1}\left[\frac{\partial \mathbf{f}_k}{\partial \mathbf{x}_{k-1}^{(m)}}\right]_{(\mathbf{x}_{k-1}^{(m)*}, \mathbf{x}_k^{(m)*})} \Delta\mathbf{x}_{k-1}^{(m)} = DP_k^{(m)}\Delta\mathbf{x}_{k-1}^{(m)} \tag{11}$$

where

$$DP_k^{(m)} = \left[\frac{\partial \mathbf{x}_k^{(m)}}{\partial \mathbf{x}_{k-1}^{(m)}} \right]_{(\mathbf{x}_k^{(m)*}, \mathbf{x}_{k-1}^{(m)*})} = \left[\begin{matrix} \frac{\partial x_k^{(m)}}{\partial x_{k-1}^{(m)}} & \frac{\partial x_k^{(m)}}{\partial y_{k-1}^{(m)}} \\ \frac{\partial y_k^{(m)}}{\partial x_{k-1}^{(m)}} & \frac{\partial y_k^{(m)}}{\partial y_{k-1}^{(m)}} \end{matrix} \right]_{(\mathbf{x}_{k-1}^{(m)*}, \mathbf{x}_k^{(m)*})} \tag{12}$$

for $k = 1, 2, \cdots, mN$ and

$$\frac{\partial x_k^{(m)}}{\partial x_{k-1}^{(m)}} = \frac{8 - h^2(\alpha_2 \Delta_1 - 2\beta + 4h\beta) + \Delta_2}{8 + h^2 \alpha_2 \Delta_1 + 2h^2 \beta + \Delta_2},$$

$$\frac{\partial x_k^{(m)}}{\partial y_{k-1}^{(m)}} = \frac{[(16 + \Delta_2) - (2\beta - \Delta_2)h^2]h}{2(8 + h^2 \alpha_2 \Delta_1 + 2h^2 \beta + \Delta_2)},$$

$$\frac{\partial y_k^{(m)}}{\partial x_{k-1}^{(m)}} = -\frac{4h(\alpha_2 \Delta_1 + 2h\beta)}{8 + h^2 \alpha_2 \Delta_1 + 2h^2 \beta + \Delta_2},$$

$$\frac{\partial y_k^{(m)}}{\partial y_{k-1}^{(m)}} = \frac{8 - h^2(\alpha_2 \Delta_1 + 4\beta - \Delta_2)}{8 + h^2 \alpha_2 \Delta_1 + 2h^2 \beta + \Delta_2},$$

$$\Delta_1 = (x_k^{(m)} + x_{k-1}^{(m)})(y_k^{(m)} + y_{k-1}^{(m)}),$$

$$\Delta_2 = -4\alpha_1 + \alpha_2(x_k^{(m)} + x_{k-1}^{(m)})^2. \tag{13}$$

The resultant variation $\Delta \mathbf{x}_{mN}^{(m)}$ with variation $\Delta \mathbf{x}_0^{(m)}$ is given by

$$\Delta \mathbf{x}_{mN}^{(m)} = DP^{(m)} \Delta \mathbf{x}_0^{(m)} = \underbrace{DP_{mN}^{(m)} \cdot DP_{mN-1}^{(m)} \cdot \ldots \cdot DP_2^{(m)} \cdot DP_1^{(m)}}_{mN-\text{multiplication}} \Delta \mathbf{x}_0^{(m)}. \tag{14}$$

where

$$\begin{aligned} DP^{(m)} &= \left[\frac{\partial \mathbf{x}_{mN}^{(m)}}{\partial \mathbf{x}_0^{(m)}} \right]_{(\mathbf{x}_0^{(m)*}, \mathbf{x}_1^{(m)*}, \cdots, \mathbf{x}_{mN}^{(m)*})} \\ &= DP_{mN}^{(m)} \cdot DP_{mN-1}^{(m)} \cdot \ldots \cdot DP_2^{(m)} \cdot DP_1^{(m)} \\ &= \prod_{k=mN}^{1} \left[\frac{\partial \mathbf{x}_k^{(m)}}{\partial \mathbf{x}_{k-1}^{(m)}} \right]_{(\mathbf{x}_0^{(m)*}, \mathbf{x}_1^{(m)*}, \cdots, \mathbf{x}_{mN}^{(m)*})} \end{aligned} \tag{15}$$

The stability and bifurcation of period-m motion are determined by the eigenvalues, i.e.,

$$\left| DP^{(m)} - \lambda \mathbf{I}_{2 \times 2} \right| = 0 \tag{16}$$

From Luo [25], the stability of period-m motion can be determined as follows.

i.   If the magnitudes of all eigenvalues of DP are within the unit cycle (i.e.,$|\lambda_i| < 1$, $i = 1, 2$), the periodic solution is stable.
ii. If at least one magnitude of the eigenvalues is out of the unit cycle (i.e.,$|\lambda_i| > 1$, $i \in \{1, 2\}$), the periodic solution is unstable.
iii. The boundaries between stable and unstable periodic motions with higher order singularity generate bifurcation conditions.

The bifurcation conditions are determined as follows.

iv. If $\lambda_i = 1$ with $|\lambda_j| < 1$ ($i, j \in \{1, 2\}, i \neq j$), the saddle-node bifurcation (SN) occurs.
v.   If $\lambda_i = -1$ with $|\lambda_j| < 1$ ($i, j \in \{1, 2\}, i \neq j$), the period-doubling bifurcation (PD) occurs.
vi. If $|\lambda_{i,j}| = 1$ ($i, j \in \{1, 2\}$, $\lambda_i = \bar{\lambda}_j$), the Neimark bifurcation (NB) occurs.

3   Finite Fourier Series

Since the discrete node vectors $\mathbf{x}^{(m)} = (x_k^{(m)}, y_k^{(m)})$ ($k = 1, 2, \cdots, mN$) of period-m motions are obtained, the period-m motions can be approximately expressed by the finite Fourier series. i.e.,

$$\mathbf{x}^{(m)}(t) \approx \mathbf{a}_0^{(m)} + \sum_{j=1}^{M} [\mathbf{b}_{j/m} \cos(\frac{j}{m}\Omega t) + \mathbf{c}_{j/m} \sin(\frac{j}{m}\Omega t)]. \tag{17}$$

Setting $M = mN/2$, the node vectors $\mathbf{x}^{(m)}$ for the period-m motion are expressed with $t \in [0, mT]$ as

$$\mathbf{x}^{(m)}(t_k) = \mathbf{x}_k^{(m)} \approx \mathbf{a}_0^{(m)} + \sum_{j=1}^{mN/2} \mathbf{b}_{j/m} \cos(\frac{j}{m}\Omega t_k) + \mathbf{c}_{j/m} \sin(\frac{j}{m}\Omega t_k)$$

$$\approx \mathbf{a}_0^{(m)} + \sum_{j=1}^{mN/2} \mathbf{b}_{j/m} \cos(\frac{j}{m}\frac{2\pi k}{N}) + \mathbf{c}_{j/m} \sin(\frac{j}{m}\frac{2\pi k}{N}) \tag{18}$$

where $\Delta t = T/N = 2\pi/(\Omega N)$, $t_k = t_0 + k\Delta t = 2\pi k/(\Omega N)$ for ($t_0 = 0$, $j = 0, 1, \cdots, mN$). The coefficients of $\mathbf{a}_0^{(m)}$, $\mathbf{b}_{j/m}$ and $\mathbf{c}_{j/m}(j = 1, 2, \cdots, mN/2)$ are computed by

$$\mathbf{a}_0^{(m)} = \frac{1}{mN} \sum_{k=0}^{mN-1} \mathbf{x}_k^{(m)}$$

$$\mathbf{b}_{j/m} = \frac{2}{mN} \sum_{k=0}^{mN-1} \mathbf{x}_k^{(m)} \cos(\frac{j}{m} \frac{2\pi k}{N}),$$

$$\mathbf{c}_{j/m} = \frac{2}{mN} \sum_{k=0}^{mN-1} \mathbf{x}_k^{(m)} \sin(\frac{j}{m} \frac{2\pi k}{N}) \tag{19}$$

where

$$\mathbf{a}_0^{(m)} = (a_{1,0}^{(m)}, a_{2,0}^{(m)})^{\mathrm{T}},$$
$$\mathbf{b}_{j/m} = (b_{1,j/m}, b_{2,j/m})^{\mathrm{T}},$$
$$\mathbf{c}_{j/m} = (c_{1,j/m}, c_{2,j/m})^{\mathrm{T}}. \tag{20}$$

The harmonic amplitudes and phases for the period-m motion are

$$A_{1,j/m} = \sqrt{(b_{1,j/m})^2 + (c_{1,j/m})^2}, \varphi_{1,j/m} = \arctan \frac{c_{1,j/m}}{b_{1,j/m}},$$

$$A_{2,j/m} = \sqrt{(b_{2,j/m})^2 + (c_{2,j/m})^2}, \varphi_{2,j/m} = \arctan \frac{c_{2,j/m}}{b_{2,j/m}}. \tag{21}$$

The periodic solutions of the period-m motion in Eq. (17) is

$$\begin{Bmatrix} x^{(m)} \\ y^{(m)} \end{Bmatrix} \approx \begin{Bmatrix} a_{1,0}^{(m)} \\ a_{2,0}^{(m)} \end{Bmatrix} + \sum_{j=1}^{mN/2} \begin{Bmatrix} A_{1,j/m} \cos(\frac{j}{m}\Omega t - \varphi_{1,j/m}) \\ A_{2,j/m} \cos(\frac{j}{m}\Omega t - \varphi_{2,j/m}) \end{Bmatrix}. \tag{22}$$

The displacement for the period-m motion is

$$x^{(m)}(t) \approx a_0^{(m)} + \sum_{j=1}^{mN/2} b_{j/m} \cos(\frac{j}{m}\Omega t) + c_{j/m} \sin(\frac{j}{m}\Omega t) \tag{23}$$

Thus,

$$x^{(m)}(t) \approx a_0^{(m)} + \sum_{j=1}^{mN/2} A_{j/m} \cos(\frac{j}{m}\Omega t - \varphi_{j/m}) \tag{24}$$

where

$$A_{j/m} = \sqrt{(b_{j/m})^2 + (c_{j/m})^2}, \varphi_{j/m} = \arctan \frac{c_{j/m}}{b_{j/m}}. \tag{25}$$

4 Semi-analytical Solutions

To keep periodic solutions of the accuracy of 10^{-9}, $h = \Delta t < 10^{-3}$ for such a discrete scheme. $N = T/\Delta t = 2\pi/\Omega h$. For period-$m$ motions, the Poincaré mapping section is defined as

$$\sum_m = \left\{ (x_k^{(m)}, y_k^{(m)}) \left| \begin{array}{l} t_k = t_0 + kT/N, t_0 = 0, T = 2\pi/\Omega \\ k = 0, 1, 2, \cdots, mN, \mathrm{mod}(k, N) = 0 \\ m = 1, 2, \cdots \end{array} \right. \right\}. \qquad (26)$$

Period-m motions in the van der Pol oscillator are presented through $(x_k^{(m)}, y_k^{(m)})$ with $\mathrm{mod}(k, N) = 0$. In all the plots, the solid and dashed curves represent the stable and unstable solutions of periodic motions, respectively. The acronym "SN" is used for the saddle-node bifurcation.

For sequent periodic motions to chaos in the van der Pol oscillator, consider the parameters as

$$\alpha_1 = 16, \alpha_2 = 1, \beta = 5, Q_0 = 100. \qquad (27)$$

In Fig. 1, a sequence of symmetric period-m motions is presented within $\Omega \in (0, 21)$. Eight independent periodic motions of symmetric period-1 to period-19 motion is presented in this frequency range. In Figs. 1i, ii, a global view of displacement $x_k^{(m)}$ and velocity $y_k^{(m)}$ ($\mathrm{mod}(k, N) = 0$) of periodic solutions is presented. In Fig. 2iii, iv, the zoomed windows for the displacement $x_k^{(m)}$ and velocity $y_k^{(m)}$ is presented for a better view of periodic motions in such a sequence. The period-17 to

Table 1 Saddle-node bifurcation points of period-m motions ($\alpha_1 = 16$, $\alpha_2 = 1$, $\beta = 5$, $Q_0 = 100$, $\Omega \in (0, 18.6)$, $m = 1, 3, \cdots, 19$)

	Frequency range	SN(L)	SN(R)	Branches
P-1	(0, 2.645)	–	2.64	1 (S)
	(2.645, +∞)	2.64	–	1 (U)
P-3	(2.449, 4.462)	2.449	4.462	3 (S,U)
P-5	(4.441, 6.205)	4.441	6.205	5 (S,U)
P-7	(6.333, 7.902)	6.333	7.902	7 (S,U)
P-9	(8.248, 9.574)	8.248	9.574	9 (S,U)
P-11	(10.229, 11.239)	10.229	11.239	11 (S,U)
P-13	(12.219, 12.920)	12.219	12.920	13 (S,U) (S,U)branches
P-15	(14.190, 14.637)	14.190	14.637	15 (S,U) (S,U)branches
P-17	(16.136, 16.405)	16.136	16.405	17 (S,U) branches
P-19	(18.063, 18.220)	18.063	18.220	19 (S,U) (S,U)branches

U-unstable periodic motion, S- stable periodic motion
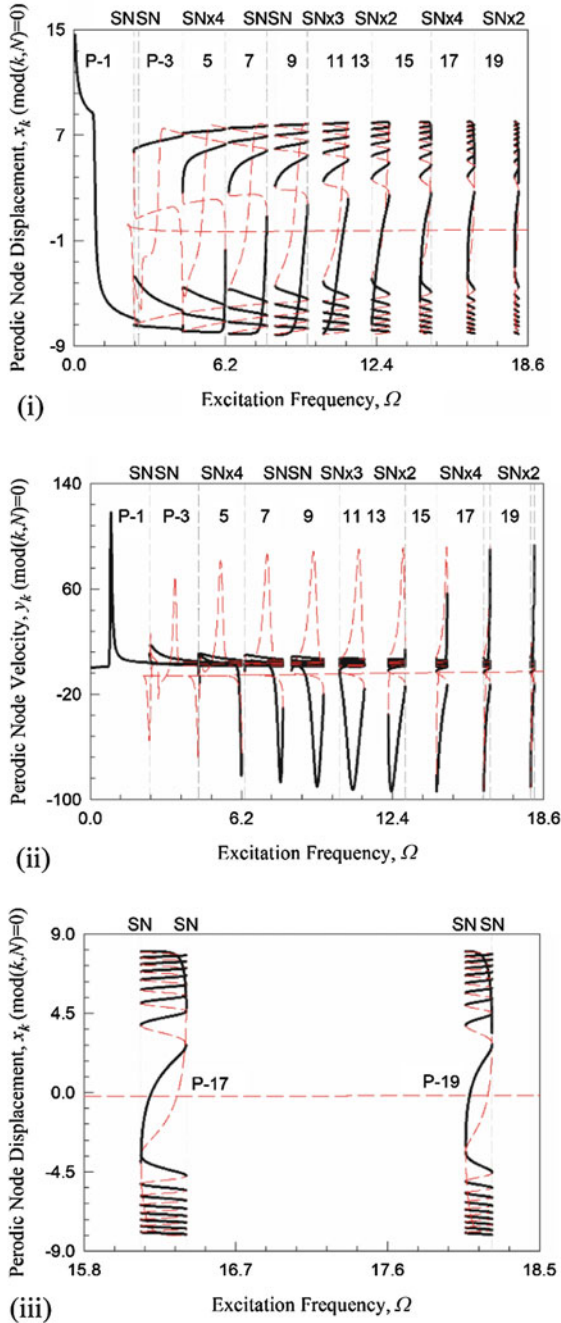
Fig. 1 Period-m motions varying with excitation frequency. Global view ($\Omega \in (0, 21)$): (i) displacement $x_k^{(m)}$, (ii) velocity $y_k^{(m)}$. The zoomed view ($\Omega \in (15.8, 18.5)$): (iii) displacement $x_k^{(m)}$, (iv) velocity $y_k^{(m)}$. $\alpha_1 = 16$, $\alpha_2 = 1$. $\beta = 5$, $Q_0 = 100$. ($\mathrm{mod}(k, N) = 0$, $k = 0, 1, \cdots, mN - 1$, $m = 1, 3, \cdots, 19$)
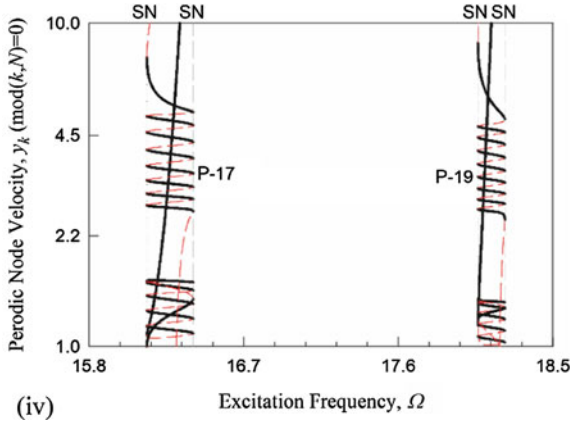
Fig. 1 (continued)

period-19 motions are presented, and the branches of displacement and velocity are clearly presented for the slow varying portions in the periodic motion in the van der Pol oscillator. The frequency ranges and bifurcations are listed in Table 1.

From the global view, a sequential order of periodic motions is

$$1(S) \triangleleft 3(S) \triangleleft 5(S) \triangleleft \cdots \triangleleft (2j-1)(S) \triangleleft \cdots (j = 1, 2, \cdots) \tag{28}$$

From the periodic motion sequence in Eq. (28), the symmetric period-1 motion appears first, which is represented by $1(S)$. When the stable period-1 motion vanishes, the symmetric period-3 motion appears (i.e., $3(S)$) numerically from the period-1 motion through jumping or chaotic transient motions. The symmetric period-3 motion occurs in a frequency interval. With another two stable branches adding, the period-3 motion turns to a symmetric period-5 motion (i.e., $5(S)$). After symmetric period-5 motion, with two new branches of stable solutions adding, the symmetric period-5 motion becomes symmetric period-7 motion. Such periodic motion evolution continues to period-$(2l-1)$ motion toward chaos when $l \rightarrow +\infty$. The bifurcation points and frequency range of period-$(2l-1)$ (i.e., P - $(2l-1)$) motions are tabulated in Table 1. When the periodic motion switches to another periodic motion, only saddle-node bifurcations exist. The jumping or chaotic transient motion exists between the two adjacent symmetric periodic motions.

For the period-1 motion, the saddle-node bifurcation occurs at $\Omega_{cr} \approx 2.645$. The period-1 motion is stable in $\Omega \in (0, 2.645)$ and unstable in $\Omega \in (2.645, +\infty)$. The symmetric period-3 motion exists in $\Omega \in (2.449, 4.462)$. Thus, from the period-1 to period-3 motion, the jumping phenomenon is observed. The symmetric period-5 motion exists in $\Omega \in (4.441, 6.205)$. The frequency intervals for the period-3 and period-5 motions overlap partially each other. Thus, the jumping phenomenon will be observed numerically. The symmetric period-7 motion is

Fig. 2 Period-1 motion in the van der Pol oscillator ($\Omega = .77$): (i) displacement, (ii) velocity, (iii) trajectory, (iv) harmonic amplitudes, (v) harmonic phases. (IC: $x_0 \approx 8.6315$, $\dot{x}_0 \approx 4.5216$) ($\alpha_1 = 16$, $\alpha_2 = 1$, $\beta = 5$, $Q_0 = 100$). SV-slow varying, FV-fast varying
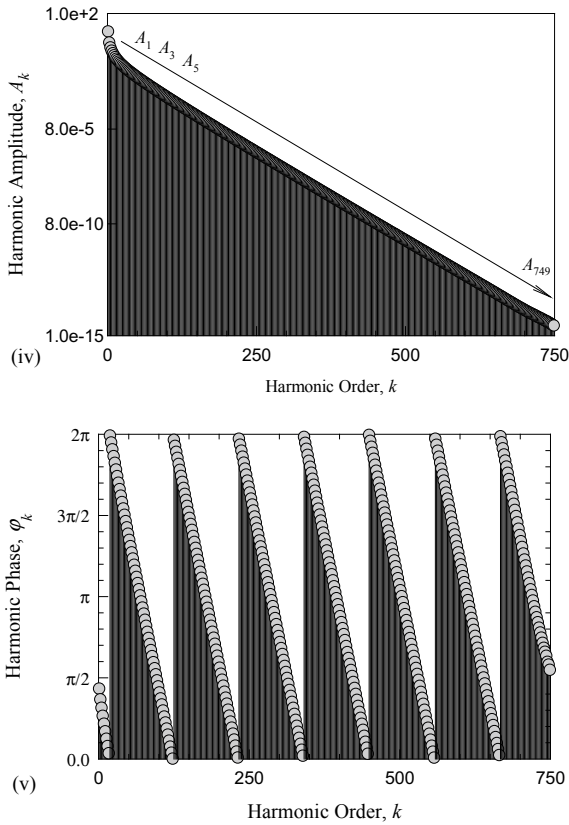
Fig. 2 (continued)

in $\Omega \in (6.333, 7.902)$. The frequency intervals between period-5 and period-7 motions do not overlap each other. Thus, the switching between the period-5 and period-7 motions are chaotic in frequency range of $\Omega \in (6.205, 6.333)$. The symmetric period-9, period-11 to period-19 motions exist in the frequency intervals of $\Omega \in (8.248, 9.574)$, $(10.229, 11.239)$, $(12.219, 12.920)$, $(14.190, 14.637)$, $(16.136, 16.405)$ and $(18.063, 18.220)$, respectively. The frequency intervals of the adjacent periodic motions do not overlap each other. Thus the frequency interval gap exists for the two adjacent periodic motions in the motion sequence. The switching between the two adjacent periodic motions are chaotic. The saddle-nodes occur on the boundaries of the frequency intervals of a symmetric periodic motion.

5 Numerical Illustrations

For illustration of periodic motions complexity in the van der Pol oscillator, numerical simulations of periodic motions are completed herein with the midpoint integration method. The initial conditions for numerical solutions are obtained from the semi-analytical solutions. In all the following plots, circular symbols and solid curves represented analytical and numerical solutions, respectively. The acronym "I.C." means the initial condition.

In Fig. 2, displacement and velocity, trajectory and harmonic amplitude spectrum of a period-1 motion are presented with $\Omega = 0.77$. As in Eq. (27), the system parameters ($\alpha_1 = 16$, $\alpha_2 = 1$, $\beta = 5$, $Q_0 = 100$) are used. The initial condition for such a numerical simulation is $x_0 \approx 8.6315$ and $\dot{x}_0 \approx 4.5216$ from the semi-analytical prediction. In Fig. 2i, the displacement response has a one-quarter wave for each slowly-varying zone and two fast-varying spikes. In Fig. 2ii, the velocity response has a slowly-varying zone and two fast-varying spikes. For each slowly-varying segment zone, there is a one-quarter wave. The circular symbols are very dense for slowly-varying segments but very sparse for fast-varying spikes. In Fig. 2iii, the corresponding phase trajectory of the stable period-1 motion in the van der Pol oscillator is presented. To measure the slow-fast varying van der pol oscillator, the harmonic amplitudes distributions are presented in Fig. 2iv. For harmonic amplitudes, $a_0^{(1)} = 0$, $A_{2l} = 0$ and $A_{(2l-1)} \neq 0$ ($l = 1, 2, \cdots$). The main harmonic amplitudes are $A_1 \approx 11.3397$, $A_3 \approx 2.9291$, $A_5 \approx 1.6138$, $A_7 \approx 1.0805$, $A_9 \approx 0.7932$, $A_{11} \approx 0.6144$, $A_{13} \approx 0.4927$, $A_{15} \approx 0.4049$, $A_{17} \approx 0.3387$, $A_{19} \approx 0.2872$, $A_{21} \approx 0.2461$, $A_{23} \approx 0.2128$, $A_{25} \approx 0.1852$, $A_{27} \approx 0.1621$, $A_{29} \approx 0.1426$, $A_{31} \approx 0.1259$, and $A_{33} \approx 0.1115$. The rest harmonic terms are $A_{(2l-1)} < 10^{-2}$ ($l = 18, 19, \cdots$) with $A_{749} \approx 3.4e^{-15}$. To keep the accuracy of $\varepsilon = 10^{-13}$, 375 odd harmonic terms are used to approximately describe the period-1 motion. Such fast-varying spikes are strongly dependent on $A_1 \approx 11.3397$. To fully determine the complex motions, the harmonic phase should be presented, as shown in Fig. 2v. The corresponding solution of period-1 motion is expressed by

$$x(t) \approx \sum_{k=1}^{375} A_{(2l-1)} \cos[(2l-1)\Omega t - \varphi_{2l-1}]. \qquad (29)$$

To show motion complexity, period-9 motion with $\Omega = 8.5$ is simulated with an initial condition of $x_0 \approx -4.7470$ and $\dot{x}_0 \approx 8.5784$. In Fig. 3i, the displacement response has four small slowly-varying waves for each slowly-varying zone and two fast-varying spikes. In Fig. 3ii, the velocity response has a slowly-varying zone and two fast varying spikes. The two fast-varying spike almost forms a wave to complete 9-periods. In Fig. 3iii, the corresponding phase trajectory (x, y) of the stable period-9 motion is presented. There are eight slowly-varying waves plus two-half, fast-varying spikes. To know such wavy in the slowly-varying zones, the harmonic amplitude distributions should be presented for such period-9 motions. $a_0^{(9)} = 0$, $A_{2l/9} = 0$ and $A_{(2l-1)/9} \neq 0$ ($l = 1, 2, \cdots$). The main harmonic amplitudes are $A_{1/9} \approx 8.4456$,
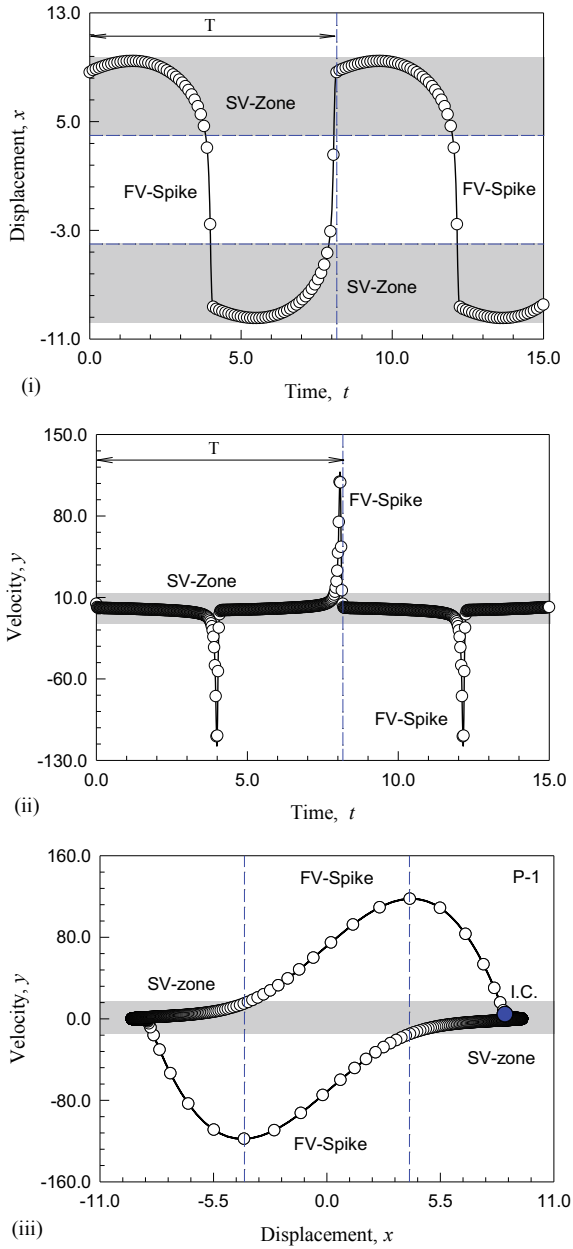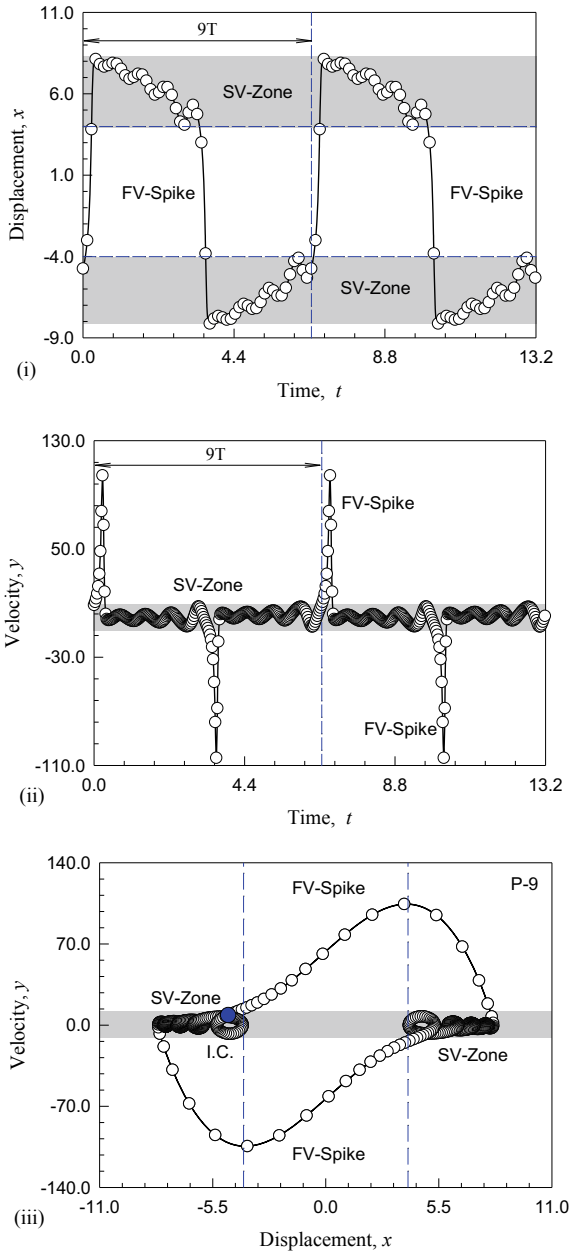
Fig. 3 Period-9 motion in the van der Pol oscillator ($\Omega = 8.5$): (i) displacement, (ii) velocity, (iii) trajectory, (iv) harmonic amplitudes. (IC: $x_0 \approx -4.7470$, $\dot{x}_0 \approx 8.5784$) ($\alpha_1 = 16$, $\alpha_2 = 1$, $\beta = 5$, $Q_0 = 100$). SV-slowly varying, FV-fast varying

(iv)

(v)
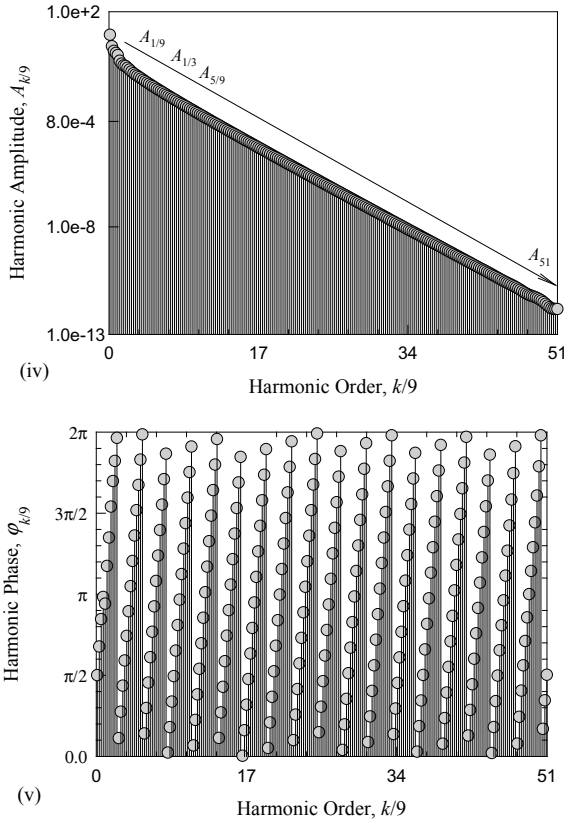
Fig. 3 (continued)

$A_{1/3} \approx 2.4779$, $A_{5/9} \approx 1.4995$, $A_{7/9} \approx 1.2066$, $A_1 \approx 0.9641$, $A_{11/9} \approx 0.5259$, $A_{13/9} \approx 0.3846$, $A_{5/3} \approx 0.3147$, $A_{17/9} \approx 0.2982$, $A_{19/9} \approx 0.2459$, $A_{7/3} \approx 0.2038$, $A_{23/9} \approx 0.1662$, $A_{25/9} \approx 0.1379$, $A_3 \approx 0.1199$ and $A_{29/9} \approx 0.1043$. The other harmonic terms are $A_{(2l-1)/9} < 10^{-2} (l = 15, 16, \cdots)$ with $A_{51} \approx 1.4988e^{-12}$. To keep the accuracy of $\varepsilon = 10^{-12}$, 230 odd harmonic terms are used to approximately describe the period-9 motion. The slowly-varying waves are strongly dependent on and other way on the small waves are dependent on $A_{1/9} \approx 8.4456$, $A_{1/3} \approx 2.4779$, $A_{5/9} \approx 1.4995$, $A_{7/9} \approx 1.2066$ and $A_1 \approx 0.9641$. The harmonic phases are presented in Fig. 3v. The analytical expression of period-9 motion is

$$x^{(9)}(t) \approx \sum_{l=1}^{202} A_{(2l-1)/9} \cos[\tfrac{(2l-1)}{9}\Omega t - \varphi_{(2l-1)/9}] \tag{30}$$

Period-19 motions is simulated in Fig. 4 for $\Omega = 18.15$ with an initial condition $(x_0 \approx -4.1403031, \dot{x}_0 \approx 5.630878)$. In Fig. 4 i, the displacement response has
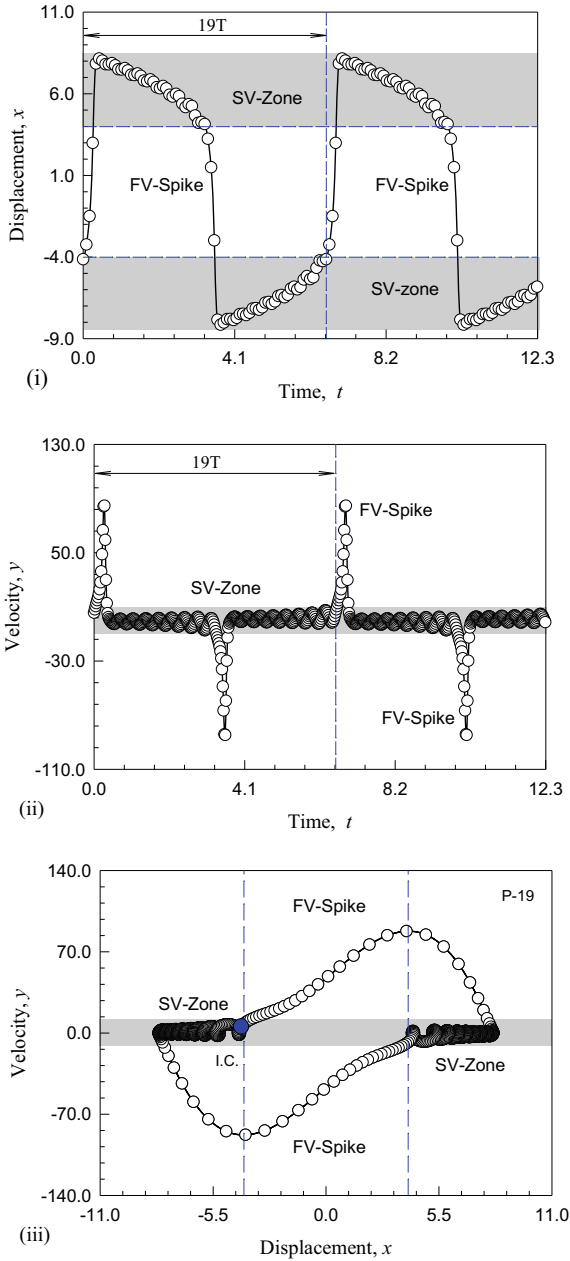
Fig. 4 Period-19 motion in the van der Pol oscillator ($\Omega = 18.15$): (i) displacement, (ii) velocity, (iii) trajectory, (iv) harmonic amplitudes. (IC: $x_0 \approx -4.1403031$, $\dot{x}_0 \approx 5.630878$) ($\alpha_1 = 16$, $\alpha_2 = 1$, $\beta = 5$, $Q_0 = 100$). SV-slow varying, FV-fast varying

(iv)

(v)
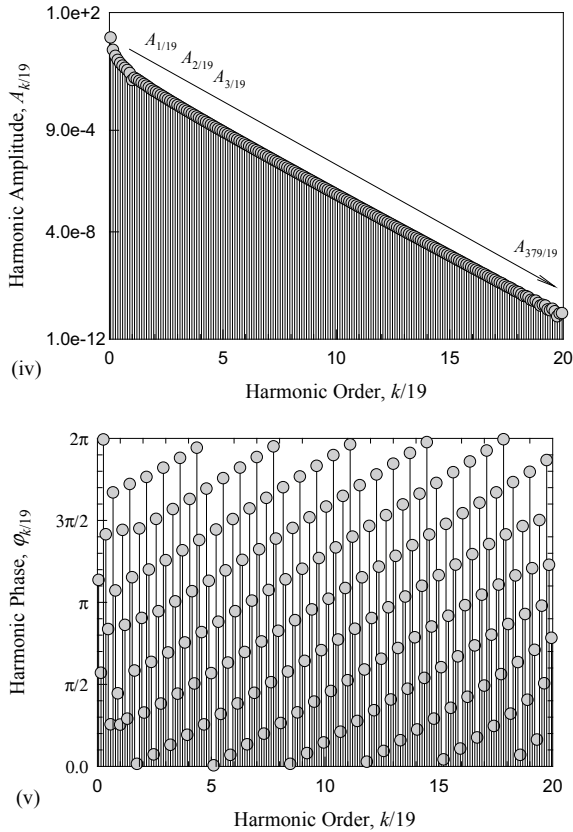
Fig. 4 (continued)

two-segments for slowly varying zones and two fast varying spikes. Its velocity response has a slowly varying zone and two fast varying spikes. In Fig. 4iii, the phase trajectory (x, y) of a stable period-19 motion is presented. There are 18 slowly varying waves plus two-half, fast varying spikes. For harmonic amplitudes, $a_0^{(19)} = 0, A_{2l/19} = 0$ and $A_{(2l-1)/19} \neq 0$ ($l = 1, 2, \cdots$). The main harmonic amplitudes are $A_{1/19} \approx 8.4876$, $A_{3/19} \approx 2.4879$, $A_{5/19} \approx 1.3857$, $A_{7/19} \approx 0.9289$, $A_{9/19} \approx 0.6816$, $A_{11/19} \approx 0.5277$, $A_{13/19} \approx 0.4220$, $A_{15/19} \approx 0.3401$, $A_{17/19} \approx 0.2546$, $A_1 \approx 0.1263$, $A_{21/19} \approx 0.1590$, $A_{23/19} \approx 0.1370$ and $A_{25/19} \approx 0.1170$. The other harmonic terms are $A_{(2l-1)/9} < 10^{-2}$($l = 14, 15, \cdots$) with $A_{20} \approx 1.2893\mathrm{e}^{-11}$. To keep the accuracy of $\varepsilon = 10^{-11}$, 180 odd harmonic terms are used to approximately describe period-19 motion in the van der Pol oscillator possessing the slow-fast movements. In Fig. 4v, the corresponding harmonic phase are presented.

6   Conclusions

In this chapter, periodic motions in the periodically forced van der Pol oscillator were studied for a better understanding of motion complexity. From the semi-analytical method, the discrete maps of the van der Pol oscillator were obtained and developed via the discretization of the corresponding differential equations. Through mapping structures of periodic motions, stable and unstable periodic motions are achieved. Presented is a sequence of symmetric periodic motions to chaos with $1(S) \triangleleft 3(S) \triangleleft \cdots \triangleleft (2l-1)(S) \triangleleft \cdots$ in the van der Pol oscillator. For such a slow-fast oscillator, many super-harmonic and sub-harmonic terms should be included to describe the complexity of periodic motions.

References

1. Lagrange JL (1788) Mecanique analytique, vol 2. (edition Albert Balnchard: Paris,). 1965
2. Poincaré H (1899) Methodes Nouvelles de la Mecanique Celeste, vol 3. Gauthier-Villars, Paris
3. van der Pol B (1920) A theory of the amplitude of free and forced triode vibrations. Radio Rev 1, 701–710, 754–762
4. Fatou P (1928) Sur le mouvement d'un systeme soumis 'a des forces a courte periode. Bull Soc Math 56:98–139
5. Krylov NM, Bogolyubov NN (1935) Methodes approchees de la mecanique non-lineaire dans leurs application a l'Aeetude de la perturbation des mouvements periodiques de divers phenomenes de resonance s'y rapportant. Academie des Sciences d'Ukraine, Kiev (in French)
6. Hayashi C (1964) Nonlinear oscillations in physical systems. McGraw-Hill Book Company, New York
7. Nayfeh AH (1973) Perturbation methods. John Wiley, New York
8. Nayfeh AH, Mook DT (1979) Nonlinear oscillation. John Wiley, New York
9. Maaita JO (2016) A theorem on the bifurcations of the slow invariant manifold of a system of two linear oscillators coupled to a k-order nonlinear oscillator. J Appl Nonlinear Dyn 5(2):193–197
10. Yamgoué SB, Nana B, Pelap FB (2017) Approximate analytical solutions of a nonlinear oscillator equation modeling a constrained mechanical system. J Appl Nonlinear Dyn 6(1):17–26
11. Shayak B, Vyas P (2017) Krylov Bogoliubov type analysis of variants of the Mathieu equation. J Appl Nonlinear Dyn 6(1):57–77
12. Rajamani S, Rajasekar S (2017) Variation of response amplitude in parametrically driven single Duffing oscillator and unidirectionally coupled Duffing oscillators. J Appl Nonlinear Dyn 6(1):121–129
13. Luo ACJ (2012) Continuous dynamical systems. HEP/L&H Scientific, Beijing/Glen Carbon
14. Luo ACJ, Huang JZ (2012) Approximate solutions of periodic motions in nonlinear systems via a generalized harmonic balance. J Vib Control 18:1661–1871
15. Luo ACJ, Huang JZ (2012) Analytical dynamics of period-m flows and chaos in nonlinear systems. Int J Bifurc Chaos 22, Article No. 1250093 (29 pages)
16. Luo ACJ, Huang JZ (2012) Analytical routines of period-1 motions to chaos in a periodically forced Duffing oscillator with twin-well potential. J Appl Nonlinear Dyn 1:73–108
17. Luo ACJ, Huang JZ (2012) Unstable and stable period-m motions in a twin-well potential Duffing oscillator. Discontin Nonlinearity Complex 1:113–145
18. Luo ACJ, Lakeh AB (2013) Analytical solutions for period-m motions in a periodically forced van der Pol oscillator. Int J Dyn Control 1:99–115

19. Xu Y, Luo ACJ, Chen Z (2017) Analytical solutions of periodic motions in 1-dimensional nonlinear systems, Chaos. Solitons Fractals 97:1–10
20. Luo H, Wang Y (2016) Nonlinear dynamics analysis of a continuum rotor through generalized harmonic balance method. J Appl Nonlinear Dyn 5(1):1–31
21. Luo ACJ (2014) Toward analytical chaos in nonlinear systems. Wiley, New York
22. Luo ACJ (2014) Analytical routes to chaos in nonlinear engineering. Wiley, New York
23. Luo ACJ (2015) Periodic flows in nonlinear dynamical systems based on discrete implicit maps. Int J Bifurc Chaos 25(3), Article No.:1550044
24. Luo ACJ, Guo Y (2015) A semi-analytical prediction of periodic motions in Duffing oscillator through mappings structures. Discontin Nonlinearity Complex 4:121–150
25. Guo Y, Luo ACJ (2017) Periodic motions in a double-well Duffing oscillator under periodic excitation through discrete implicit mappings. Int J Dyn Control 5(2):223–238
26. Guo Y, Luo ACJ (2016) Periodic motions to chaos in pendulum. Int J Bifurc Chaos 26, 1650159 [64 pages]
27. Guo Y, Luo ACJ (2017) Routes of periodic motions to chaos in a periodically forced pendulum. Int J Dyn Control 5(3):551–569
28. Guo Y, Luo ACJ (2017) Complete Bifurcation Trees of a Parametrically Driven Pendulum. J Vib Test Syst Dyn 1:93–134
29. Luo ACJ (2016) Discretization and implicit mapping dynamics. Springer/Higher Education Press, Heidelberg\Beijing
30. Luo ACJ, Xing SY (2016) Symmetric and asymmetric period-1 motions in a periodically forced, time-delayed, hardening Duffing oscillator. Nonlinear Dyn 85:1141–1166
31. Luo ACJ, Xing SY (2016) Multiple bifurcation trees of period-1 motions to chaos in a periodically forced, time-delayed, hardening Duffing oscillator. Chaos, Solitons Fractals 89:405–434
32. Luo ACJ, Xing SY (2017) Time-delay effects on periodic motions in a periodically forced, time-delayed, hardening Duffing oscillator. J Vib Test Syst Dyn 1:73–91
33. Xing SY, Luo ACJ (2017) Towards infinite bifurcation trees of period-1 motions to chaos in a time-delayed, twin-well Duffing oscillator. J Vib Test Syst Dyn 1:353–392
34. Luo ACJ (2017) Memorized discrete systems and time-delay. Springer, New York
35. Xu Y, Luo ACJ (2018) a series of symmetric period 1 motion to chaos in a two degree of freedom van der Pol duffing oscillator. J Vib Test Syst Dyn 2(2):119–153. https://doi.org/10.5890/JVTSD.2018.06.003
36. Xu Y, Luo ACJ (2018) "Sequent period-(2 m- 1) motions to chaos in the van der Pol oscillator. Int J Dyn Control, 1–13

Hidden Periodic Motions for Brushless Motor with Unsteady Torque Excitation

Jianzhe Huang and Fuhong Min

Abstract Due to the coupling between the direct-axis current, quadrature-axis current and rotor speed, the dynamic response could be strongly nonlinear. Besides, if the working condition is severe, the loading is no longer constant and multiple harmonics could be introduced. In this chapter, a 3-D model for brushless motor is discussed, and an excitation with single harmonic will be considered. With discrete implicit maps algorithm, complex dynamical behaviors can be obtained for such a brushless motor. With bifurcation analysis, the parameter sensitivity can be obtained which can be a suggestion for design and operation. This chapter is dedicated to Valentin Afraimovich for his fabulous achievement in the scientific world.

1 Introduction

A brushless motor is an important power source which can be used in various fields such as robotics and aerospace. The vibration of such a motor could affect the performance of the loading, the comfort of the environment, the fatigue life of the entire system etc. Therefore, vibration issues should be considered in the design stage of a brushless motor. Due to the variation of the rotor speed, it could cause the torsional vibration of the rotor system and then affect the vibration of the whole structure. Hemati [1, 2] formulated a mathematical model for a brushless motor in a rotating coordinate frame through Park's transformation to investigate the global and local dynamics of such a direct-drive brushless motor. Such a model of brushless motor is a set of three dimensional first order autonomous differential equations system. Kang et al. [3] applied nonideal trapezoidal back EMF to attenuate the undesired torque fluctuation for the brushless dc motor, and a high precision encoder was used to measure the instantaneous torque ripple. Rubaai et al. [4] constructed a three-layer feedforward network to identify and control brushless dc motor drives. The

J. Huang (✉) · F. Min
School of Aeronautics and Astronautics, Shanghai Jiao Tong University, Shanghai 200240, China

differential equations for the stator current were transformed to a single second-order nonlinear differential equation, and the solution was worked out by second-order central difference approximation. In 2003, Ge and Chang [5] transformed the brushless motor system into a compact form to study the chaos synchronization of identical systems through four methods such as the adaptive control, the backstepping design method, the Gerschgorin theorem and the addition of a monitor. Lee and Ehsani [6] effectively analyzed the speed, torque, voltages and currents of PWM inverter components using a developed model based on MATLAB environment. The trapezoidal back EMF waveforms were modeled as a function of rotor position. Jabbar et al. [7] introduced a methodology of modeling and numerical simulation of BLDCM with time-stepping approach. Finite element method (FEM) was considered to be practical to compute the performance of electrical machines. The simulation results correlated well with the experimental results which indicated that the model was significant. Luo [8, 10] studied the application of the combination of dynamic surface control (DSC) technology, radial basis function (RBF) neural network, and adaptive method, in the control of chaos for the BLDCM system. The same model with Hemati was applied, and the tangent barrier Lyapunov function (TBLF) was used for a time-delay nonlinear system. Zhang et al. [9] investigated the boundedness solutions of BLDCM. The generalized Lyapunov function stability theory and the extremum principle of function were used to analyze global attractive and positively invariant sets. The efficiency has been verified through the numerical simulations. Jagiea and Gwozdz [11] introduced a time-periodic finite element model of a brushless dc motor to evaluate the machine characteristic and the power losses. Cho et al. [12] analyzed the vibration characteristics of a brushless direct current motor through an entire finite element model, and electromagnetic-structural weak coupled analysis was carried out to give the transient response.

In this chapter, a brushless motor will be expressed with a set of three-dimensional nonlinear different equations. The electrical states (quadrature-axis current and direct-axis current) and mechanical state (rotor speed) are coupled. In the history of development of techniques for solving the steady-state response analytically of a nonlinear system, perturbation method [13] and harmonic balance method [14] are two of the most famous methods, but small parameter assumption for nonlinear terms was made. In order to remove such a limitation and deal with systems with strong nonlinearity, a generalized harmonic balanced method was developed and the effectiveness of such a method was verified with the Duffy oscillator [15], nonlinear Jeffcott oscillator [16] etc. Further, a semi-analytic methodology called discrete implicit maps was introduced [17] to give the analytic solution of periodic motions for any type of nonlinear system which possesses ordinary differential equations. With such a method, the bifurcation of analytic steady state solution for nonlinear systems such as piston in a high pressure gas cylinder [18], hardening Duffing oscillator with time-delay [19] and Parametrically Excited Pendulum [20] etc. have been obtained.

Since such a discrete implicit map method can be easily applied to solve nonlinear systems, and the stability and bifurcation condition can also be accurately calculated with which a large dimension of sparse Jacobian matrix is avoided, the analytic solution of periodic motions for nonlinear equations for brushless motor system will

be calculated using such a technique herein. Additionally, the number of harmonic terms does not need to be determined before the calculation, thus the accuracy of the analytic solution can be guaranteed. For a brushless motor with loading, the loading can cause the torque fluctuation when the loading increases which may dramatically change the dynamic characteristics for brushless motor dramatically, for instance the steady state motion may become other type of periodic motion or chaos when the periodical torque is introduced.

2 Motion Discretization and Mapping Reconstruction for Periodic Motions

In Fig. 1, a three-phase brushless motor with drive circuit is illustrated. The relationship between the input voltage and the back EMF in the motor will be expressed as

$$u_a = Ri_a + L\frac{di_a}{dt} + e_a,$$
$$u_b = Ri_b + L\frac{di_b}{dt} + e_b,$$
$$u_c = Ri_c + L\frac{di_c}{dt} + e_c. \tag{1}$$

Through Park transformation and a periodical torque excitation is considered, the dynamical equations for such a brushless motor in the d-q coordinates can be expressed as

$$\frac{di_q}{dt} = L^{-1}(v_q - Ri_q - n_p L\omega i_d - n_p k_t \omega),$$
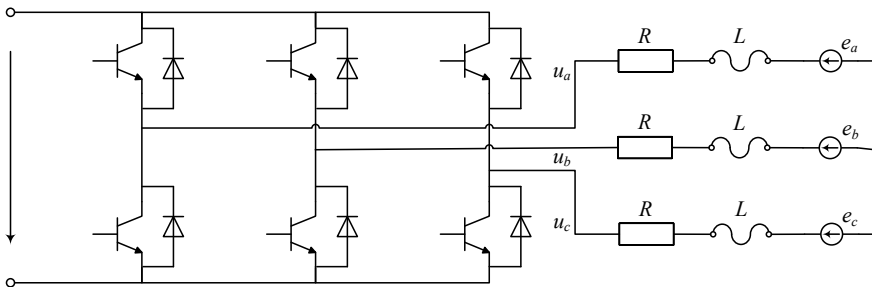
Fig. 1 Illustration of three-phase brushless motor with drive circuit

$$\frac{di_d}{dt} = L^{-1}(-Ri_d + n_p L_q \omega i_q + v_d),$$

$$\frac{d\omega}{dt} = J^{-1}(n_p k_t i_q - b\omega + T_{L0} + T_L \cos \Omega t) \qquad (2)$$

where i_q and i_d are the quadrature-axis and direct-axis current; v_q and v_d are the quadrature-axis and direct-axis voltage; L is the fictitious inductance; R is winding resistance; n is number of pole pairs; ω is the rotor speed; J is the inertia of rotor; b is the viscous damping coefficient; T_L is the torque due to external load; T_L and Ω are the magnitude and frequency of the torque fluctuation due to the external load; $k_t = \sqrt{\frac{3}{2}k_e}$ and k_e is the permanent-magnet flux constant.

One define the state variables for such a motor as

$$\mathbf{x} \triangleq (x, y, z) \equiv (i_q, i_d, \omega) \qquad (3)$$

For a period-1 motion of such a brushless motor system, it can be discretized into multiple mappings with constant time step. For a certain map P_k ($k = 0, 1, 2, \ldots$), it maps from one state $(x_{k-1}, y_{k-1}, z_{k-1})$ at $t = t_{k-1}$ to another (x_k, y_k, z_k) at $t = t_k$ with a mapping criteria based on the midpoint algorithm given as follows.

$$P_k : (x_{k-1}, y_{k-1}, z_{k-1}) \rightarrow (x_k, y_k, z_k) \Rightarrow (x_k, y_k, z_k) = P_k(x_{k-1}, y_{k-1}, z_{k-1}). \quad (4)$$

$$\begin{aligned}
x_k &= x_{k-1} + hL^{-1}\big[v_q - R(x_{k-1} + x_k)/2 - n_p L(y_{k-1} + y_k) \\
&\quad (z_{k-1} + z_k)/4 - n_p k_t(z_{k-1} + z_k)/2\big], \\
y_k &= y_{k-1} + hL^{-1}\big[-R(y_{k-1} + y_k)/2 \\
&\quad + n_p L_q(x_{k-1} + x_k)(z_{k-1} + z_k)/4 + v_d\big], \\
z_k &= z_{k-1} + hJ^{-1}\big[n_p k_t(x_{k-1} + x_k)/2 - b(z_{k-1} + z_k)/2 \\
&\quad + T_{L0} + T_L \cos \Omega(t + dt/2)\big].
\end{aligned} \qquad (5)$$

where $h = t_k - t_{k-1}$.

Then the mapping structure for such a period-m motion which is divided into mN partitions becomes

$$P = P_{mN} \circ P_{mN-1} \circ \cdots \circ P_2 \circ P_1 : (x_0, y_0, z_0) \rightarrow (x_{mN}, y_{mN}, z_{mN}). \qquad (6)$$

Due to periodicity, the initial position for the first map and the final position of the final map should be overlapped, and the time span equals the time period of the external torque.

$$x_0 = x_N, \ y_0 = y_N \text{ and } t_N = t_0 + \frac{2\pi m}{\Omega} \tag{7}$$

For a period-m motion with mN maps, it has $3mN$ equations and the state variables for those nodes are unknown, the number of which is $3mN + 3$. But with the constraint given in Eq. (7), three more equations are added such that the node points for such a period-1 motion can be solved analytically through Newton-Raphson method.

To determine the stability of a period-1 motion, the small neighborhood of the node point $\mathbf{x}_k^*$ can be written as $\mathbf{x}_k = \mathbf{x}_k^* + \Delta\mathbf{x}_k$, $(k = 0, 1, 2, \cdots, N)$. Then linearize Eq. (6) at the equilibrium and the first order of the Taylor's expansion is kept, it gives

$$\Delta\mathbf{x}_N = DP \Delta\mathbf{x}_0 = \underbrace{DP_{mN} \cdot DP_{mN-1} \cdot \ldots \cdot DP_2 \cdot DP_1}_{mN-\text{multiplication}} \Delta\mathbf{x}_0 \tag{8}$$

where

$$DP_k = \left[\frac{\partial\mathbf{x}_k}{\partial\mathbf{x}_{k-1}} \right]_{(\mathbf{x}_k^*, \mathbf{x}_{k-1}^*)}, \ \text{for } k = 1, 2, \cdots, N \tag{9}$$

Solve the Jacobian matrix $\mathbf{DP}$, and it gives three eigenvalues such as λ_i ($i = 1, 2, 3$). According to theory of the continuous system, the periodic motion is stable only if all of magnitudes of the eigenvalues are less than 1, e.g. $|\lambda_i| < 1$ ($i = 1$ and 2 and 3). Otherwise, the motion is unstable. At the boundary between the stable and unstable motions, it is the bifurcation point, of which the magnitude of one of the eigenvalues is 1:

I.   If one of the eigenvalues is 1, the saddle-node bifurcation of period-1 motion occurs;

II.   If one of the eigenvalues is -1, the period-doubling bifurcation of period-1 motion occurs;

III. If a pair of eigenvalues are complex with magnitude equating to 1, the Neimark bifurcation of period-1 motion occurs.

For a given resolution mN, a period-m motion can be divided into mN segments with constant time interval of mT/N where T is one period of excitation ($T = 2\pi/\omega$). Then a set of node points of periodic motions with ($mN + 1$) points per one period of excitation can be expressed as. Furthermore, the set of node points of period-m motion with ($mN + 1$) node points for one period can be expressed as

$$\Xi = \{ (x_k, y_k, z_k) | t_k = t_0 + \frac{2k\pi}{N\Omega}; t_0 = 0; k = 0, 1, 2, \ldots, mN \} \tag{10}$$

Instead of presenting all node points of periodic motions, the node points per each period of excitation frequency are collected in the Poincaré mapping section for period-1 motions. Such Poincaré mapping is defined as

$$\Xi_{PM} = \{ (x_k, y_k, z_k) \mid \mathrm{mod}\,(k, N) = 0, \tau_k = \tau_0 + \frac{kT}{N};$$

$$\tau_0 = 0; k = 0, 1, 2, \ldots, mN \} \tag{11}$$

By analyzing the aforementioned set Ξ via Discrete Fourier Transform, the analytic solution for such a period-m motion can be recovered as

$$\mathbf{x}(t) \approx \mathbf{a}_0^{(m)} + \sum_{j=1}^{mN/2} \mathbf{b}_{j/m} \cos(\tfrac{j}{m}\Omega t) + \mathbf{c}_{j/m} \sin(\tfrac{j}{m}\Omega t) \tag{12}$$

and

$$\mathbf{a}_0^{(m)} = \frac{1}{mN} \sum_{k=0}^{mN-1} \mathbf{x}_k,$$

$$\mathbf{b}_{j/m} = \frac{2}{mN} \sum_{k=0}^{mN-1} \mathbf{x}_k \cos(\tfrac{j}{m}\Omega t_k),$$

$$\mathbf{c}_{j/m} = \frac{2}{mN} \sum_{k=0}^{mN-1} \mathbf{x}_k \sin(\tfrac{j}{m}\Omega t_k),$$

$$t_k = \frac{2k\pi}{\Omega mN}, \tag{13}$$

where $\mathbf{a}_0^{(m)} = (a_{01}^{(m)}, a_{02}^{(m)}, a_{03}^{(m)})$, $\mathbf{b}_{j/m} = (b_{j/m(1)}, b_{j/m(2)}, b_{j/m(3)})$ and $\mathbf{c}_{j/m} = (c_{j/m(1)}, c_{j/m(2)}, c_{j/m(3)})$.

The highest order of the harmonic depends on the number of the partition which the motion is divided into. The amplitude and phase for each order of harmonic for the period-1 motion are expressed by

$$\mathbf{A}_{k/m} = \sqrt{\mathbf{b}_{k/m}^2 + \mathbf{c}_{k/m}^2}, \quad \varphi_{k/m} = \arctan \frac{c_{k/m}}{b_{k/m}} \tag{14}$$

3   Analytical Bifurcation

For an eight-pole brushless motor, the system parameters are given as

$$R = 0.9, n_p = 4, L = 0.01425, k_t = 0.031, \xi = 0.0162, J = 0.000047 \tag{15}$$

For the loading condition, it is assumed as $T_{L0} = 0$, $T_L = 0.2$ and $\Omega = 10$. The quadrature-axis voltage v_q is set to be zero and direct-axis voltage v_d is varied from -9.0 V to -6.0 V. The analytical bifurcation diagram of node point sets of period-1 motion, which is expressed as in Eq. (10), for such a brushless motor is illustrated in Fig. 2. The solid curve is stable motion and the dashed curved is unstable motion. For the upper branch of the stable period-1 solution, the periodic nodes of the states for such a brushless motor system (such as quadratic-axis current, direct-axis current, and rotation speed) are almost invariant when the direct-axis voltage increases. The period-doubling bifurcation ("PD") of the period-1 motion occurs at $v_d = -7.769$ V, and the saddle-node bifurcation ("SN") of the period-1 motion is at $v_d = -7.752$ V.

Since the rotor speed is the mechanical state, by which the vibration of such a brushless motor can be affected it can reflect the vibration characteristics of such a brushless motor, the harmonic amplitudes of rotor speed for such a motor when the direct-axis varies in the range of $v_d \in [-9, -6]$ are presented In Fig. 3. The constant terms a_{03} gives the average value of the rotor speed versus direct-axis voltage, which is shown in Fig. 3a. For constant term a_{03} which is nonzero, the periodic motion is asymmetric to the rotor speed. Otherwise, the periodic motion is symmetric to the rotor speed. In Figs. 3b–d, the first three orders of the harmonic amplitudes are illustrated. For the analytical solution of the periodic motion which is symmetric to the rotor speed, the even orders of the harmonic amplitude for $A_{k(3)}$ ($k = 2, 4, 6, \ldots$) are all zero. It can be seen that the third order of the harmonics for the period-1 motions still has a quantity level of 10^1, which indicates that higher orders of harmonic are required. The harmonic amplitude of $A_{2(3)}$ goes to zero at $v_d = -7.557$ V which is the unstable saddle-node bifurcation, and the unstable periodic solution has jump phenomenon when the direct-axis voltage continues to increases. In Figs. 3e, f, the harmonic amplitudes of $A_{59(3)}$ and $A_{60(3)}$ are shown, respectively. The quantity level of harmonic amplitude for stable period-1 motion which is asymmetric to rotor speed has dropped to 10^{-4} when the order increases to 60, and the quantity level of harmonic amplitude for stable period-1 motion which is symmetric to rotor speed has dropped to 10^{-2} when the order increases to 59.

For period-2 motion, it only exists in a very narrow range. The periodic nodes for period-2 motion in the range of $v_d = [-7.764, -7.745]$ are shown in Fig. 4. The period-doubling bifurcation occurs at $v_d = -7.752408$ V and -7.754412 V. In Fig. 5a, for the constant term a_{03} of stable period-2 motion, it increases and then decreases when the direct-axis voltage increases. But the average rotation speed only varies from 9.452250 to 10.632700 rad/s. For the period-2 motion, the subharmonic terms of $A_{k/2(3)}$ ($k = 1, 3, 5, \ldots$) is non-zero, as shown in Fig. 5b–g. For $k = 6$, the harmonic amplitude still has a quantity level of 10^1. For $k = 94$ and 95 which is shown in Fig. 5h, i, the quantity level decreases to 10^{-2}, and it becomes 10^{-3} when $k = 96$ as is given in Fig. 5j.
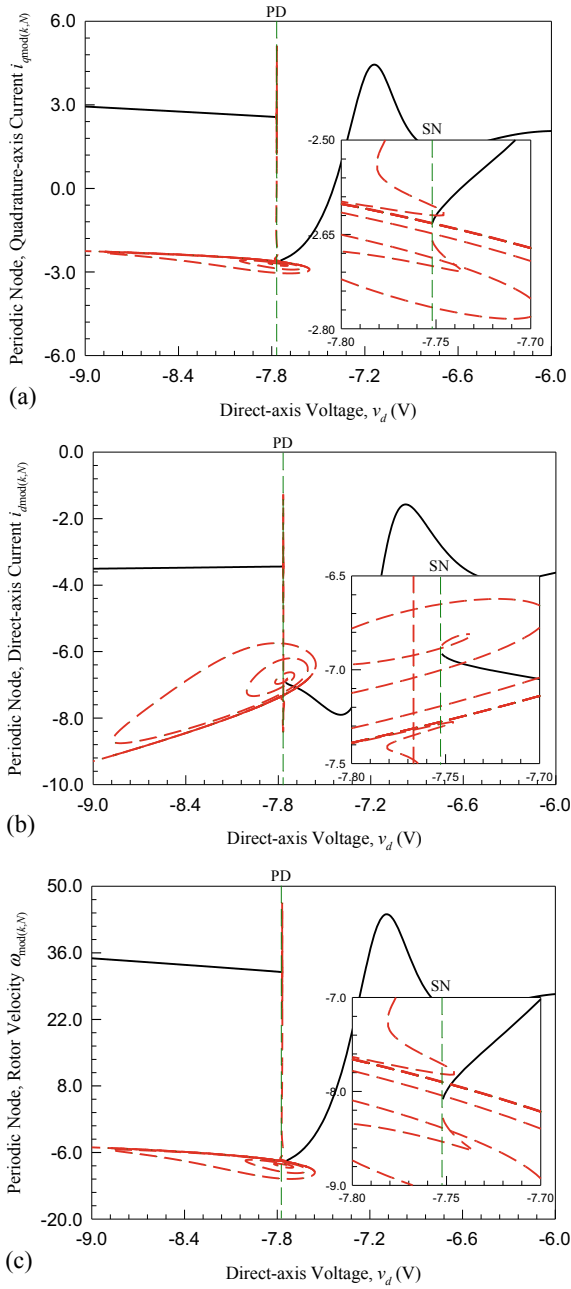
Fig. 2 Analytical bifurcation of periodic nodes of period-1 motion for brushless motor ($R = 0.9$, $n_p = 4$, $L = 0.01425$, $k_t = 0.031$, $\xi = 0.0162$, $J = 0.000047$) with working condition $T_{L0} = 0$, $T_L = 0.2$, $\Omega = 10$ and $v_q = 0$: **a** quadrature-axis current, **b** direct-axis current and **c** rotor velocity
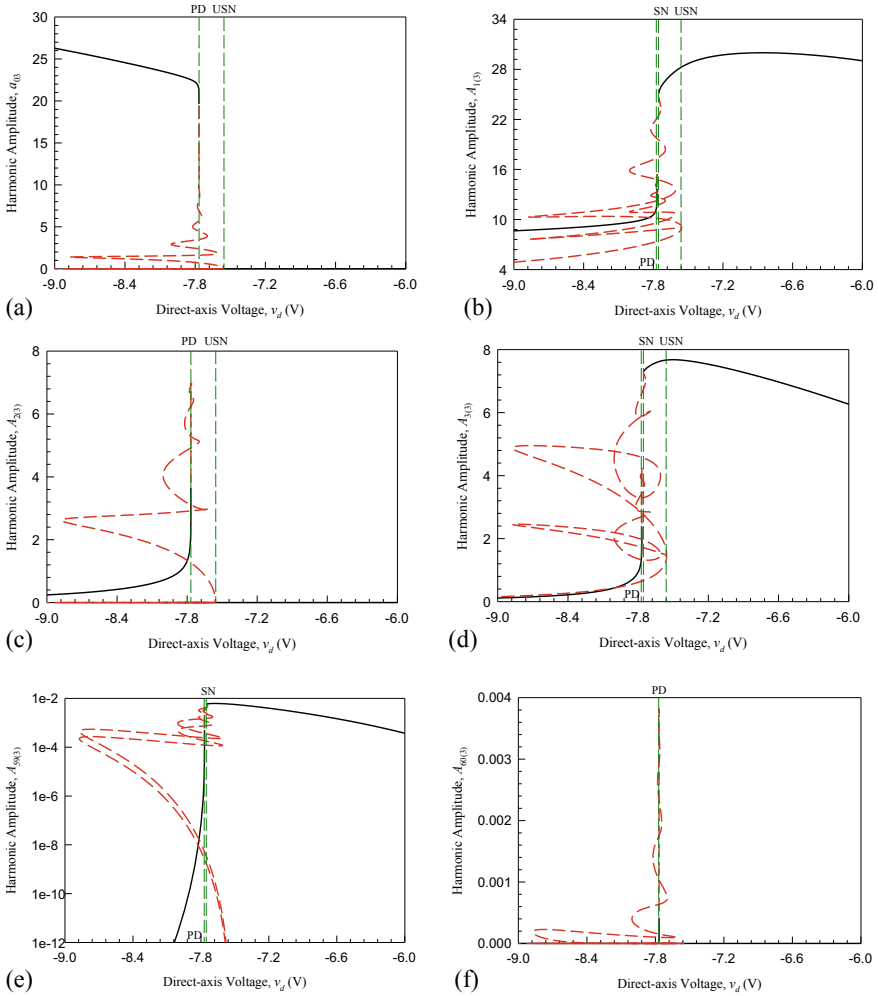
Fig. 3 Harmonic amplitude of rotor speed for brushless motor ($R = 0.9$, $n_p = 4$, $L = 0.01425$, $k_t = 0.031$, $\xi = 0.0162$, $J = 0.000047$) with working condition $T_{L0} = 0$, $T_L = 0.2$, $\Omega = 10$ and $v_q = 0$: **a** constant term, **b–d** first three orders of harmonics, **e** harmonic amplitude of $A_{59(3)}$ and **f** harmonic amplitude of $A_{60(3)}$

4   Periodic Motions

In this section, periodic motions in the brushless motor with loading fluctuation will be discussed. The initial conditions are calculated by the analytical solution which is obtained through implicit discrete map method at the phase $t = 0$ which is given by the green solid circle ("I.C."). The solid curve is the numerical prediction, and the red fork symbols are the analytical solution.
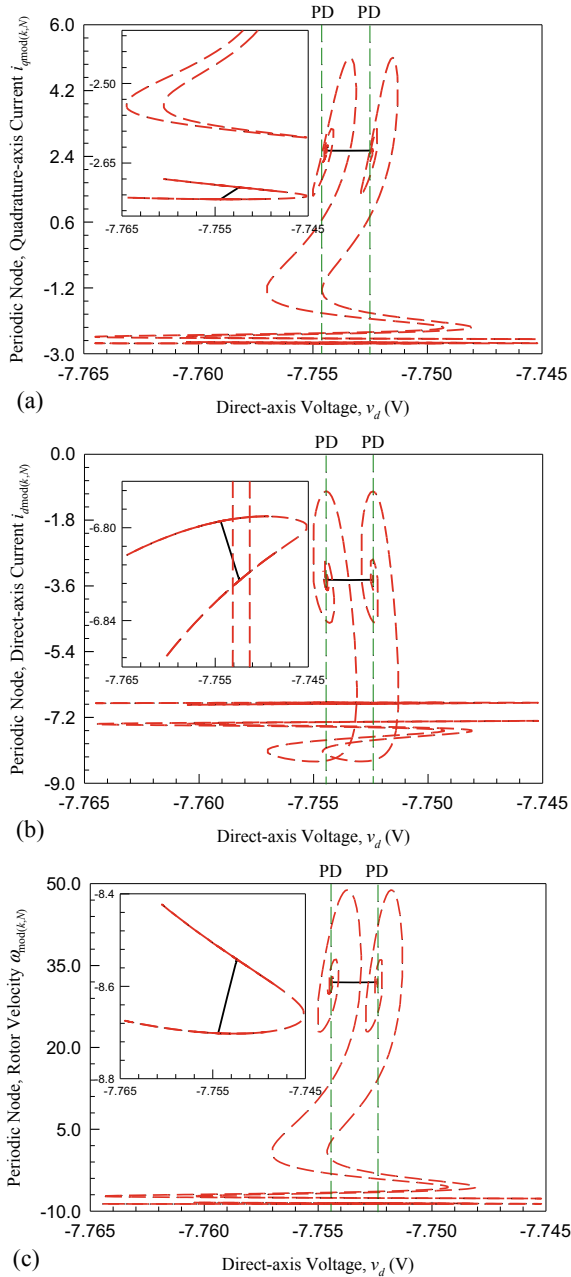
Fig. 4 Analytical bifurcation of periodic nodes of period-2 motion for brushless motor ($R = 0.9$, $n_p = 4$, $L = 0.01425$, $k_t = 0.031$, $\xi = 0.0162$, $J = 0.000047$) with working condition $T_{L0} = 0$, $T_L = 0.2$, $\Omega = 10$ and $v_q = 0$: **a** quadrature-axis current, **b** direct-axis current and **c** rotor velocity
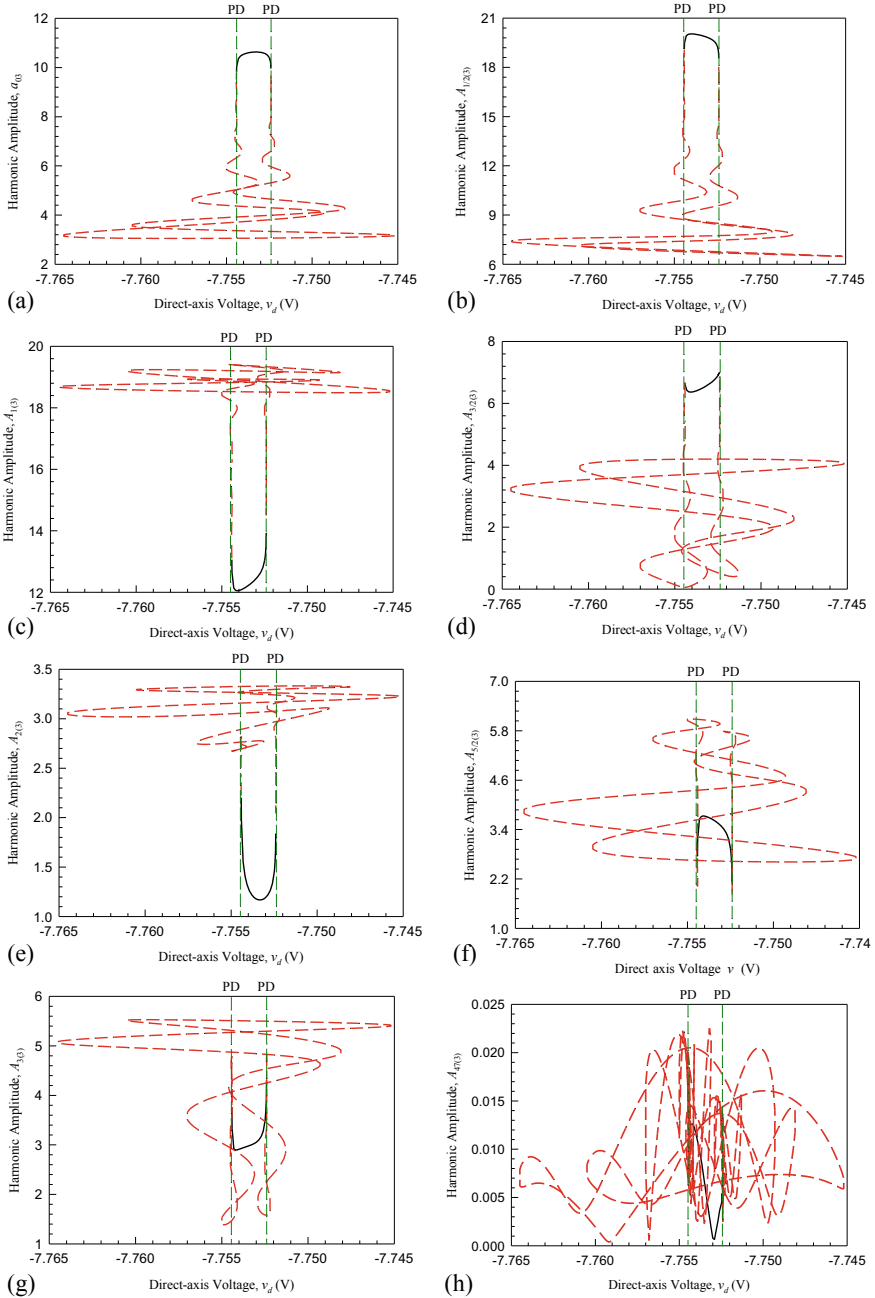
Fig. 5 Harmonic amplitude of rotor speed of period-2 motions for brushless motor ($R = 0.9$, $n_p = 4$, $L = 0.01425$, $k_t = 0.031$, $\xi = 0.0162$, $J = 0.000047$) with working condition $T_{L0} = 0$, $T_L = 0.2$, $\Omega = 10$ and $v_q = 0$: **a** constant term, harmonic amplitudes of **b** $A_{1/2(3)}$, **c** $A_{1(3)}$, **d** $A_{3/2(3)}$, **e** $A_{2(3)}$, **f** $A_{5/2(3)}$, **g** $A_{3(3)}$, **h** $A_{47(3)}$, **i** $A_{95/2(3)}$, **j** $A_{48(3)}$
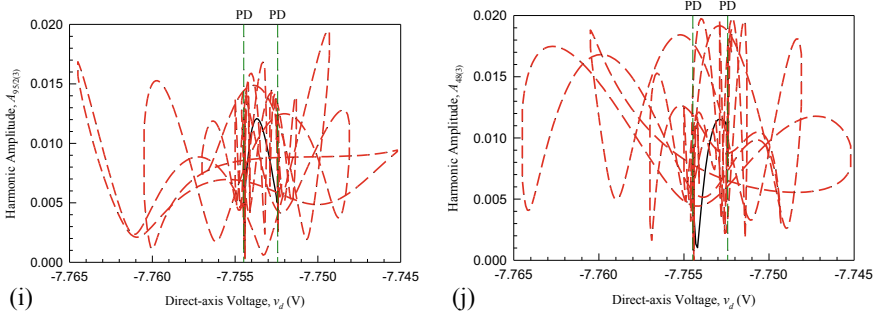
Fig. 5 (continued)

A stable period-1 motion at $v_d = -7.73$ V is presented in Fig. 6a–c, and the initial conditions are $(i_{q0}, i_{d0}, \omega_0) \approx (-2.558350, -6.994479, -7.567532)$. It can be found that the numerical simulation correlates with the analytical solution very well. In Fig. 6b, the rotor speed versus time is illustrated and one period is labeled. For the harmonic amplitudes of the rotor speed, which are presented in Fig. 6c, the constant term is zero and the first harmonic is 25.9979 rad/s. The amplitudes of even orders ($A_{k(3)}$ for $k = 2, 4, 6, \ldots$) for such a stable period-1 motion are all zero, and the amplitudes of the order orders drop asymptotically with the increase of the order. The harmonic amplitude stay above 1 for $k < 21$, and the quantity level drops to 10^{-2} until $k = 39$. The quantity level goes to 10-4 when k increases to 73. With the same system parameters, there is another unstable motion coexisted which is presented in Figs. 6d–f. The initial conditions for such a unstable period-1 motion are given as $(i_{q0}, i_{d0}, \omega_0) \approx (-2.779143, -6.624351, -9.195011)$, for which the initial current for quadratic-axis and direct-axis is very close to those for the aforementioned stable period-1 motion. As shown in Fig. 6e, the numerical prediction stay on the unstable period-1 orbit for the first half cycle and then leaves due to the error accumulation of the numerical simulation and the strong attraction of the stable orbit. In order to illustrate all the coexisting periodic motions at $v_d = -7.73$, the analytical solutions of the stable and unstable motions are plotted in Fig. 7. The black solid curve is the stable period-1 motion, and there are other six unstable period-1 motions which are represented by the color dashed curves.

In Fig. 8, a stable and unstable period-2 motion at $v_d = -7.754$ V are demonstrated. As shown in Fig. 8c, f, the frequency spectrum for period-2 motions becomes more dense than that for period-1 motion since the subharmonics such as $A_{k/2(3)}$ ($k = 1, 3, 5, \ldots$) are introduced. There are one stable period-2 motion and eight unstable period-2 motions coexisting at $v_d = -7.754$ V which is plotted in Fig. 9. It can be found that the lower part of all the periodic motions is almost overlapped.

(a)

(b)

(c)
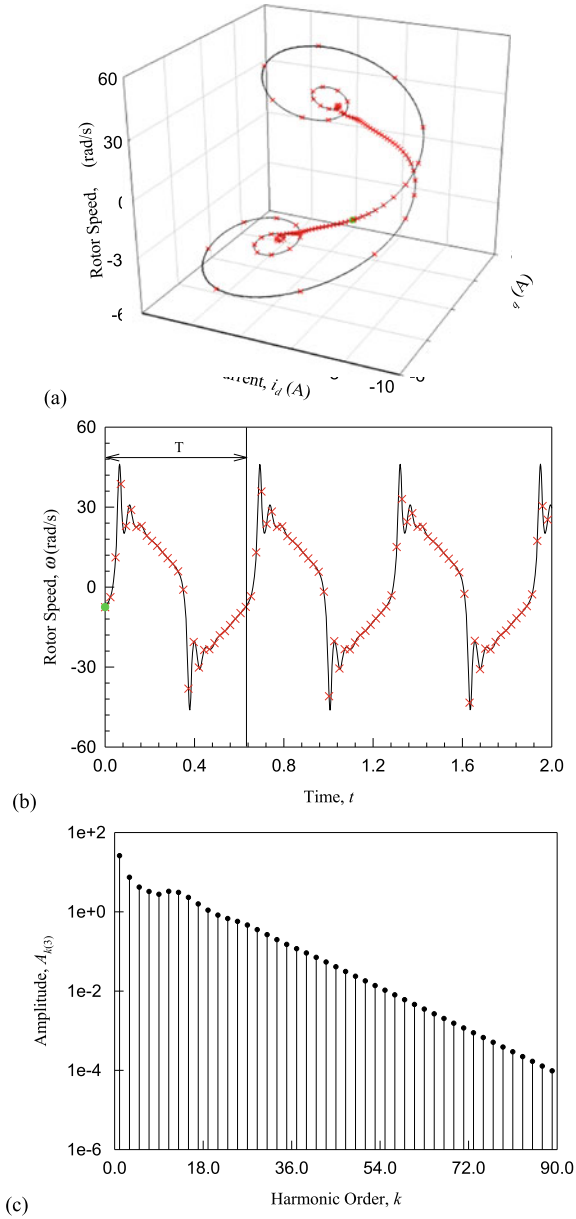
Fig. 6 Period-1 motion for $v_d = -7.73$: stable motion **a** 3-D trajectory **b** time history of rotation speed ω, **c** harmonic amplitude of $A_{k(3)}$ (initial conditions: $(i_{q0}, i_{d0}, \omega_0) \approx (-2.558350, -6.994479, -7.567532)$; unstable motion **d** 3-D trajectory **e** time history of rotation speed ω, **c** harmonic amplitude of $A_{k(3)}$ (initial conditions: $(i_{q0}, i_{d0}, \omega_0) \approx (-2.779143, -6.624351, -9.195011)$, $(R = 0.9, n_p = 4, L = 0.01425, k_t = 0.031, \xi = 0.0162, J = 0.000047)$

(d)

(e)

(f)
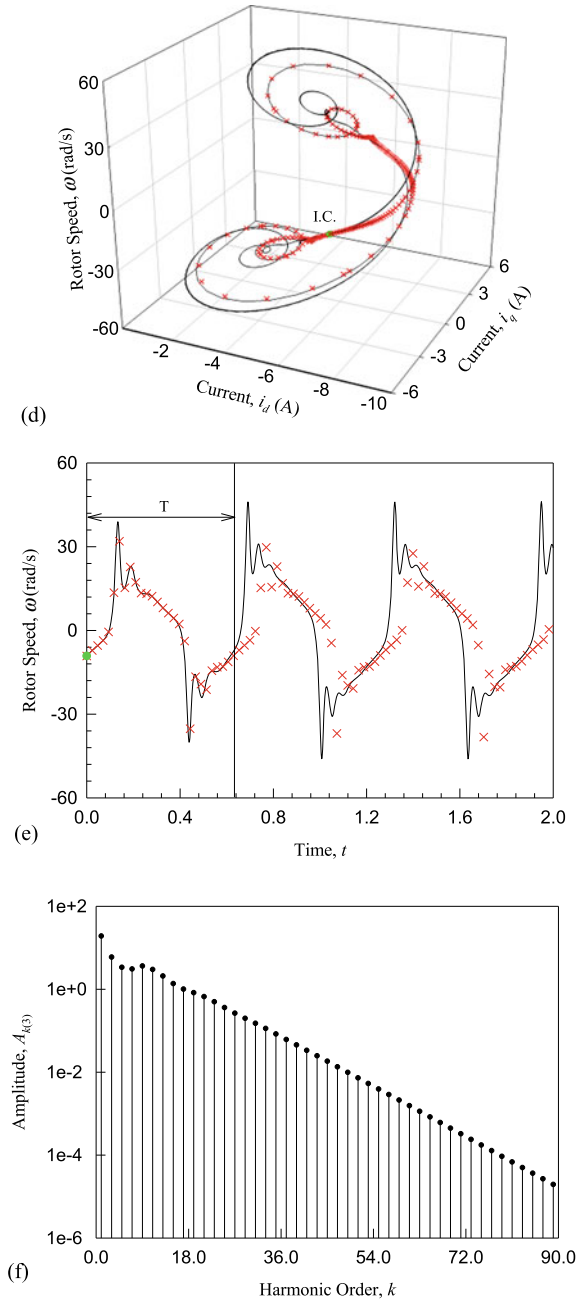
Fig. 6 (continued)
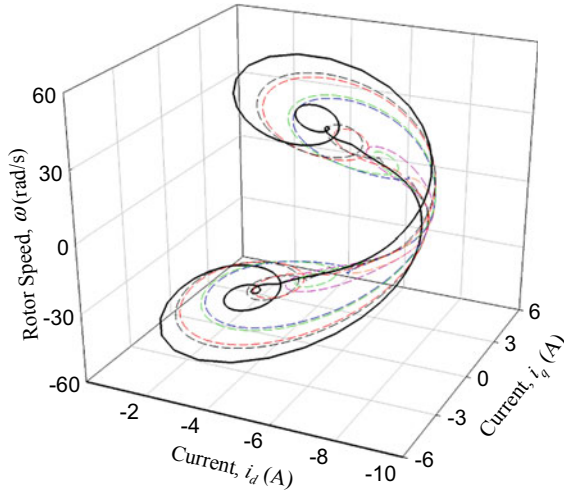
Fig. 7 Coexisting analytical orbits for period-1 motions for $v_d = -7.73$ ($R = 0.9$, $n_p = 4$, $L = 0.01425$, $k_t = 0.031$, $\xi = 0.0162$, $J = 0.000047$)

5 Conclusions

In this chapter, the discrete implicit maps method is adopted to investigate the nonlinear dynamic behavior of a brushless motor. A periodic torque is introduced to model the loading fluctuation. Period-m motion is discretized and mappings are described using a set of algebraic equations. Through Newton-Raphson method, the node points of mappings of period-1 motion for such a brushless motor can be easily solved and the eigenvalue analysis has been carried out through the reduced system. By selecting specific parameters, analytic bifurcation for Poincaré section and solution of period-1 motion varying direct-axis voltage have been presented. A strong nonlinear characteristic for such a brushless motor with periodically excited loading can be observed, and higher orders of harmonics should be kept in the solution which may be difficult to solve for traditional analytical method of solving nonlinear problems such as harmonic balance method. With such a technique, many coexisting unstable periodic motions can be obtained, and with proper control such unstable periodic motions can be altered to be stable if the motions are desired for operation.

(a)

(b)

(c)
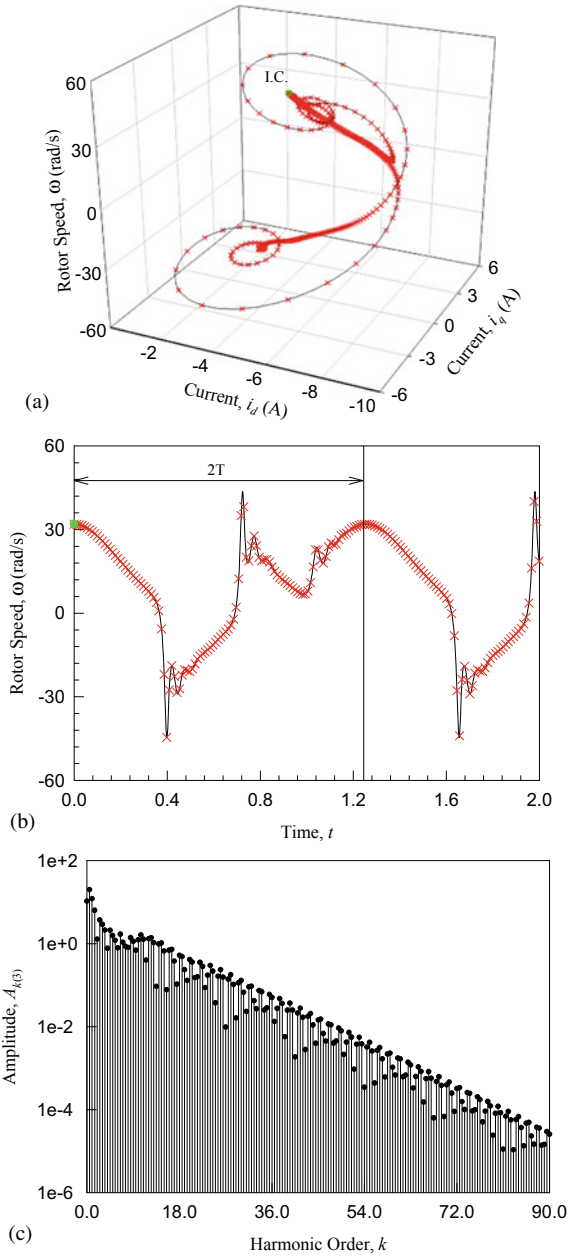
Fig. 8 Period-2 motion for $v_d = -7.754$: stable motion **a** 3-D trajectory **b** time history of rotation speed ω, **c** harmonic amplitude of $A_{k(3)}$ (initial conditions: $(i_{q0}, i_{d0}, \omega_0) \approx (2.557057, -3.437199, 31.922249)$; unstable motion **d** 3-D trajectory **e** time history of rotation speed ω, **c** harmonic amplitude of $A_{k(3)}$ (initial conditions: $(i_{q0}, i_{d0}, \omega_0) \approx (-.582655, -8.315973, 5.041553), R = 0.9, n_p = 4, L = 0.01425, k_t = 0.031, \xi = 0.0162, J = 0.000047$)

(d)

(e)

(f)
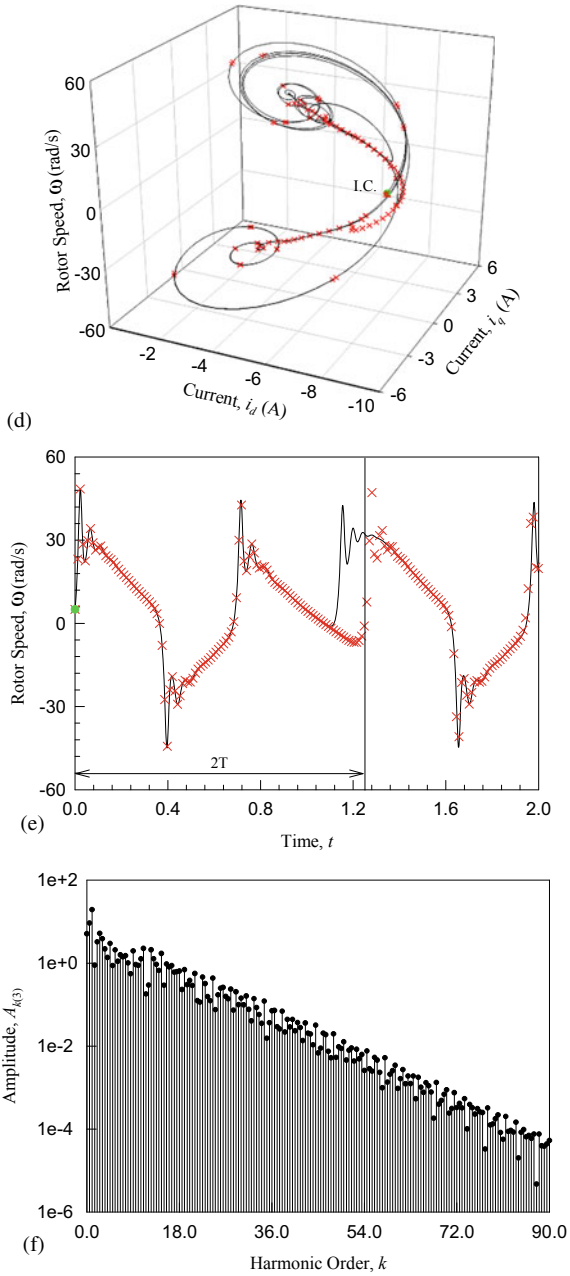
Fig. 8 (continued)
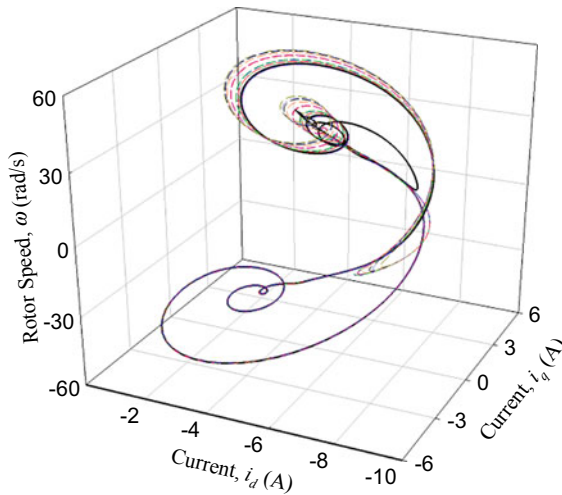
Fig. 9 Coexisting analytical orbits for period-1 motions for $v_d = -7.754$ ($R = 0.9$, $n_p = 4$, $L = 0.01425$, $k_t = 0.031$, $\xi = 0.0162$, $J = 0.000047$)

References

1. Hemati N (1992) The global and local dynamics of direct-drive brushless dc motors. In: the 1992 IEEE International conference on robotics and automation. Nice, France, May 12–14
2. Hemati N (1993) Dynamic analysis of brushless motors based on compact representations of equations of motion. In: the 1993 IEEE industry applications conference 28th IAS annual meeting. Toronto, Canada, October 2–8
3. Kang SJ, Sul SK (1995) Direct torque control of brushless dc motor with nonideal trapezoidal back EMF. IEEE Trans Power Electron 10(6):796–802
4. Rubaai A, Kotaru R, Kankam MD (2000) A continually online-trained neural network controller for brushless dc motor drives. IEEE Trans Ind Appl 36(2):475–483
5. Ge ZM, Chang CM (2004) Chaos synchronization and parameters identification of single time scale brushless dc motors. Chaos Solitons Fractals 20(4):883–903
6. Lee BK, Ehsani M (2003) Advanced simulation model for brushless dc motor drives. Electr Power Compon Syst 31(9):841–868
7. Jabbar MA, Phyu HN, Liu ZJ, Bi C (2004) Modeling and numerical simulation of a brushless permanent-magnet dc motor in dynamic conditions by time-stepping technique. IEEE Trans Ind Appl 40(3):763–770
8. Luo Shaohua, Wang Jiaxu, Songli Wu (2014) Chaos RBF dynamics surface control of brushless dc motor with time delay based on tangent barrier Lyapunov function. Nonlinear Dyn 78(2):1193–1204
9. Zhang F, Lin D, Xiao M, Li H (2014) Dynamical behaviors of the chaotic brushless dc motors model. Complexity 21(4):79–85
10. Luo S, Wu S, Gao R (2015) Chaos control of the brushless direct current motor using adaptive dynamic surface control based on neural with the minimum weights. Chaos 25(7) 073102:8
11. Jagiela M, Gwozdz J (2015) Steady-state time-periodic finite element analysis of a brushless dc motor drive considering motion. Arch of Electr Eng 64(3):471–486
12. Cho S, Hwang J, Kim CW (2018) A study on vibration characteristics of brushless dc motor by electromagnetic-structural coupled analysis using entire finite element model. IEEE Trans Energy Convers. https://doi.org/10.1109/TEC.2018.2833493

13. Hayashi G (1964) Nonlinear oscillations in physical systems. McGraw-Hill Book Company
14. Nayfeh AH, Singh V (1978) Perturbation methods. IEEE Trans Syst Man Cybern 8(4):417–418
15. Luo ACJ, Huang JZ (2013) Analytical solutions for asymmetric periodic motion to chaos in a hardening Duffing oscillator. Nonlinear Dyn 72(1–2):417–438
16. Huang JZ, Luo ACJ (2015) Periodic motions and bifurcation trees in a buckled, nonlinear Jeffcott rotor system. Int J Bifurc Chaos 25(1):1550002
17. Luo ACJ (2015) Periodic flows in nonlinear dynamical systems based on discrete implicit maps. Int J Bifurc Chao 25, 1550044: 62
18. Wang D, Huang JZ (2016) Periodic motions and chaos for a damped mobile piston system in a high pressure gas cylinder with P control. Chaos Solitons Fractals 95:168–178
19. Luo ACJ, Xing SY (2016) Multiple bifurcation tress of period-1 motions to chaos in a periodically forced, time-delayed, hardening Duffing oscillator. Chaos Solitons Fractals 89:405–434
20. Guo Y, Luo ACJ (2017) Period-1 motions to chaos in a parametrically excited pendulum. In: ASME 2017 International mechanical engineering congress and exposition. Tampa, USA, November 3–9

Chunking Rhythmic Synchronization: Bellerophon States and Quantized Clusters of Globally Coupled Phase Oscillators

S. Boccaletti, H. Bi, T. Qiu, I. Bonamassa, and S. Guan

Abstract The emergence of phase coherence in interacting oscillators is one of the main phenomena for the coordination of events that make a system to behave cooperatively. Examples range from rhythmic physiological processes to the collective behaviors of technological and natural networks. We concentrate here on Bellerophon states, which are coherent states of rhythmic synchrony occurring in globally coupled oscillators close to the point where the transition from disorder to phase order converts from abrupt to continuous. Within Bellerophon states, oscillators form quantized clusters, where their instantaneous phases and frequencies are unlocked. Within each cluster, the oscillators' instantaneous frequencies form a characteristic cusped pattern and, more importantly, they behave periodically in time, so that their long-time average values are the same. Along the manuscript, we give analytical and numerical description of these states, and we discuss their general appearance behind the collective rhythms reported in other systems of interacting oscillators.

1 Introduction

The authors are honored of having written the present manuscript in memory of Valentin S. Afraimovich, a fantastic person and a great scientist whose contributions to dynamical systems and complexity theory inspired literally hundreds of nonlinear physicists and applied mathematicians in the world. Together with being protagonist behind some of the most important accomplishments of the last 40 years in complex systems theory, Valentin was a man always open to share new ideas with his col-

---

S. Boccaletti (✉)
CNR-Institute of Complex Systems, Via Madonna del Piano, 10, 50019 Sesto Fiorentino, Florence, Italy
e-mail: stefano.boccaletti@gmail.com; stefano@ino.it

H. Bi · T. Qiu · S. Guan
Department of Physics, East China Normal University, Shanghai 200241, China

I. Bonamassa
Department of Physics, Bar-Ilan University, 52900 Ramat Gan, Israel

leagues, always curious and excited to learn about the mechanisms underlying the phenomena which emerge from interacting objects in nature, and as so he represented a real mentor for at least three generations of complexity scientists.

One of those phenomena which intrigued Valentin along his career is certainly the emergence of coherent phases in interacting oscillators, which very often is observed in nature and represents the basis for the cooperative functioning of a wealth of different systems. On the same line of Valentin's pioneering work on stochastic synchronization in dissipative systems [1], physicists always tried to gather insights and understanding on the mechanisms and reasons underlying synchronization by means of simplified models, as the Kuramoto [2] and Kuramoto-like [3–5] models, where a variety of collective states were described, as e.g. full synchronization [6, 7], or cluster [8] and explosive synchronization (ES) [5, 9].

In recent years, interest has been devoted to the coexistence of coherent and incoherent domains in locally coupled identical oscillators, a state which has been termed as Chimera state (CS) [10–12]. Various types of CSs have been described theoretically, such as the breathing CS [13], the clustered CS [14] and the multi-CS [15], and also experimental evidence of CSs has been given [16]. Furthermore, CSs had attracted the attention of Valentin Afraimovich, during his last years of activity [17].

We here report on a novel coherent phase of global synchrony which is proper of nonidentical oscillators having widely different frequencies. We find that such states generally emerge in the presence of first-order synchronization phase transitions, as soon as the forward threshold characterizing the explosive branch precedes the backward one. At this point, which for the model system discussed below coincides with a tricritical point, a novel non-stationary rhythmic states spontaneously emerge. In this phase, oscillators form quantized clusters, and in each cluster the oscillators are neither phase- nor frequency-locked. On the contrary, each of the oscillators' instantaneous frequency is different within the clusters, but the instantaneous frequencies form a time dependent cusped pattern, similar to the stationary one characterizing the average frequencies within the incoherent domain of CSs. This means that the instantaneous frequencies of the oscillators behave periodically in time, so that their long time average values are the same. These new phases and their attributes are hence intrinsically specular to those characterizing CSs and, as such, they were termed as *Bellerophon* states [18], since Bellerophon was the name of the great hero who, in the Greek mythology, confronted with (and eventually killed) the monster Chimera.

In what follows we will discuss our main results characterizing the microscopic and macroscopic attributes of these states in a particular model system of interacting phase oscillators. In this path, we will follow four main steps: (1) after presenting the model, we will describe the numerical results and unveil the phase diagram of the model and its phase transitions; (2) we will seek for an analytic solution of the forward critical threshold for the explosive phase transition and characterize it in terms of the control parameters of the system; (3) after gaining control on the choice of parameters where Bellerophon states emerge, we characterize their small-to-large scale organization, unveiling the self-organization of these rhythmic states into quantized clusters of mode-locked oscillators; (4) finally we complete
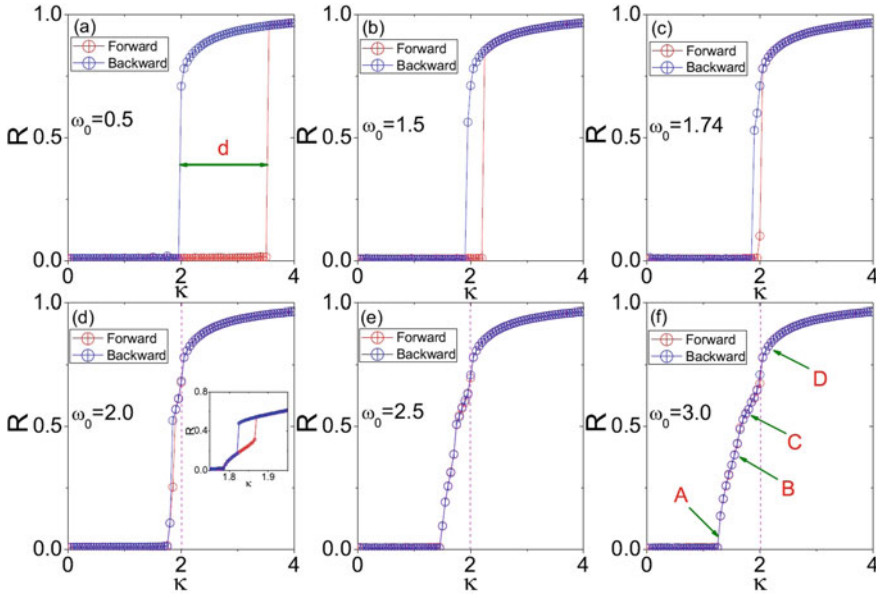
Fig. 1 Explosive and continuous transitions to synchronization. (Color online). *R versus* κ for model (1). $\Delta = 1$ and $\omega_0 = 0.5$ (**a**), 1.5 (**b**), 1.74 (**c**), 2.0 (**d**), 2.5 (**e**), and 3.0 (**f**). Simulations have been performed by adopting a fourth order Runge-Kutta integration method with step size 0.005, and system's size $N = 10,000$. Notice that all other parameters used in the numerical simulations are specified in the text. Reprinted from Ref. [18]

our discussion by comparing these states with other phases reported in interacting oscillators, together with their potential relevance in the theoretical study of rhythmic synchronization.

2 Results

We start by considering a system of N globally coupled phase oscillators, whose dynamics is ruled by a generalized Kuramoto model of the form:

$$\dot{\theta}_i = \omega_i + \frac{\kappa|\omega_i|}{N} \sum_{j=1}^{N} \sin(\theta_j - \theta_i), \quad i = 1, ..., N, \tag{1}$$

where θ_i and ω_i are, respectively, the instantaneous phase and the natural frequency of the ith oscillator. Furthermore, in Eq. (1) the dot symbol denotes a temporal derivative, and κ is the coupling strength, hereafter assumed to be positive.

The level of synchrony can be monitored by measuring the Kuramoto order parameter

$$R = \frac{1}{N} \left\langle \left| \sum_{j=1}^{N} e^{i\theta_j} \right| \right\rangle_T,$$

where $| \cdot |$ and $\langle \cdot \rangle_T$ stand for module and time average, respectively.

In general, the set of natural frequencies $\{\omega_i\}$ is taken from a given frequency distribution (FD) $g(\omega)$, which is here assumed to be an even function $[g(\omega) = g(-\omega)]$, smooth, and centered at 0. A common representative of such class of frequency distributions which we will consider in this study is the bimodal Lorentzian

$$g(\omega) = \frac{\Delta}{2\pi} \left[\frac{1}{(\omega - \omega_0)^2 + \Delta^2} + \frac{1}{(\omega + \omega_0)^2 + \Delta^2} \right],$$

where Δ is the width parameter (half width at half maximum) of each peak, and $\pm\omega_0$ are the center frequencies. Depending on the ratio ω_0/Δ, the frequency distribution can be either uni-modal (for $\omega_0/\Delta \leq \sqrt{3}/3$) or bimodal (for $\omega_0/\Delta > \sqrt{3}/3$), and such crossover between the two regimes has dramatic effects on the synchronization transitions of the system. It is important to stress here that both the particular model and the specific frequency distribution that are discussed here have been adopted for the sake of illustration. *Bellerophon* states, in fact, are not limited to these arrangements and are instead observed in a variety of models and arrangements of interacting oscillators featuring phases of periodic synchronization [19].

As a first step of our analysis, we study numerically the transition to synchronization in Eq. (1). For the sake of simplicity, we start by considering a fixed value of the half-width parameter $\Delta \equiv 1$ and let ω_0 to increase, which corresponds to a progressive growth of the distance between the two peaks of the frequency distribution. Physically speaking, this could be interpreted as the progressive formation of two, say, energetically equivalent ground states, around which the system's oscillators tend to settle. As summarized in Fig. 1, when ω_0 is small one observes a first-order synchronization phase transition [Fig. 1a] featuring an hysteresis area of width $d = \kappa_b - \kappa_f$, where κ_b and κ_f being the critical points for the backward (hybrid) and forward (explosive) transitions, respectively. As shown in Figs. 1b–c, increasing values of ω_0 result into a progressive shrinking of the hysteresis area, which occurs throughout an adiabatic decrease of the forward threshold κ_f. When instead ω_0 is large enough [as it is the case of Figs. 1d–f], a two-stage continuous phase transition – first from a stationary incoherent state to a non-stationary one, and then from the latter one towards a coherent stationary phase – is observed. Therefore, the model system Eq. (1) sustains both a first- and second-order-like synchronization phase transitions. Inspecting more in depth the features of the first-order transitions reported for low values of ω_0, it turns out that the backward threshold is always given by $\kappa_b = 2$ [4] for symmetric FDs, as confirmed by our simulations [see panels (a)-(c) of Fig. 1]. The forward critical threshold (κ_f) varies instead with ω_0 (at $\Delta = 1$). This

fact induces the hysteresis area to shrink, and leads eventually to a conversion from an explosive to a continuous transition to synchronization at $\omega_0 \approx 1.7$.

The second step of our study is to seek an analytic solution for the forward critical threshold κ_f. Following the approach of Refs. [4, 6], a linear stability analysis of the model Eq. (1) can be performed, leading to the secular equation

$$1 = \frac{\kappa}{2} \int\limits_{-\infty}^{+\infty} \frac{\lambda|\omega|}{\lambda^2 + \omega^2} g(\omega) d\omega, \qquad (2)$$

relating the coupling strength κ to the eigenvalue λ [4]. From Eq. (2), one obtains

$$1 = \frac{k}{2\pi} \int\limits_{0}^{+\infty} \frac{\lambda\omega}{\lambda^2 + \omega^2} \left[\frac{\Delta}{(\omega - \omega_0)^2 + \Delta^2} + \frac{\Delta}{(\omega + \omega_0)^2 + \Delta^2} \right] d\omega. \qquad (3)$$

By further setting $\omega/\Delta \to \omega,\ \omega_0/\Delta \to \delta,$ and $\lambda/\Delta \to \lambda$, Eq. (3) becomes

$$1 = \frac{k\lambda}{2\pi} \left[\int\limits_{0}^{+\infty} \frac{\omega}{\lambda^2 + \omega^2} \cdot \frac{1}{(\omega - \delta)^2 + 1} d\omega + \int\limits_{0}^{+\infty} \frac{\omega}{\lambda^2 + \omega^2} \cdot \frac{1}{(\omega + \delta)^2 + 1} d\omega \right] = \frac{k\lambda}{2\pi}(I_1 + I_2), \qquad (4)$$

where I_1 and I_2 denote the two integrals, respectively. Performing the integration, one gets:

$$
\begin{aligned}
I_1 &= \frac{k\lambda}{2\pi} \int\limits_{0}^{+\infty} \frac{1}{4i} \left(\frac{1}{\omega - i\lambda} + \frac{1}{\omega + i\lambda} \right) \left(\frac{1}{\omega - \delta - i} - \frac{1}{\omega - \delta + i} \right) d\omega \\
&= \frac{1}{4} \left[\frac{1}{1 - \lambda - i\delta} \ln\frac{\delta + i}{i\lambda} + \frac{1}{1 + \lambda - i\delta} \ln\frac{-\delta - i}{i\lambda} + \frac{1}{1 - \lambda + i\delta} \ln\frac{-\delta + i}{i\lambda} + \frac{1}{1 + \lambda + i\delta} \ln\frac{\delta - i}{i\lambda} \right], \\
&= \frac{1}{4} \left\{ \left(\ln\frac{\sqrt{1 + \delta^2}}{\lambda} - i\theta \right) \frac{(1 - \lambda) + i\delta}{(1 - \lambda)^2 + \delta^2} + \left[\ln\frac{\sqrt{1 + \delta^2}}{\lambda} + i(\pi - \theta) \right] \frac{(1 + \lambda) + i\delta}{(1 + \lambda)^2 + \delta^2} \right. \\
&\quad \left. + \left(\ln\frac{\sqrt{1 + \delta^2}}{\lambda} + i\theta \right) \frac{(1 - \lambda) - i\delta}{(1 - \lambda)^2 + \delta^2} + \left[\ln\frac{\sqrt{1 + \delta^2}}{\lambda} - i(\pi - \theta) \right] \frac{(1 + \lambda) - i\delta}{(1 + \lambda)^2 + \delta^2} \right\} \\
&= \frac{1}{4} \left\{ \frac{2}{(1 - \lambda)^2 + \delta^2} \left[(1 - \lambda)\ln\frac{\sqrt{1 + \delta^2}}{\lambda} + \theta\delta \right] + \frac{2}{(1 + \lambda)^2 + \delta^2} \left[(1 + \lambda)\ln\frac{\sqrt{1 + \delta^2}}{\lambda} - (\pi - \theta)\delta \right] \right\} \\
&\equiv F(\delta), \qquad (5)
\end{aligned}
$$

where $\theta = \arctan(\delta)$, with $\delta > 0$.

One should notice that $I_2 = I_1(\delta \to -\delta)$, and therefore Eq. (4) becomes

$$1 = \frac{k\lambda}{2\pi}[F(\delta) + F(-\delta)] = \frac{k\lambda}{2\pi}\left\{\ln\frac{\sqrt{1+\delta^2}}{\lambda}[\frac{1-\lambda}{(1-\lambda)^2+\delta^2} + \frac{1+\lambda}{(1+\lambda)^2+\delta^2}]\right\}.$$
(6)

Substituting what above in Eq. (3), one arrives at the secular equation

$$\frac{2\pi}{\kappa} = f(\lambda, \delta) = \lambda\left[\frac{1-\lambda}{(1-\lambda)^2+\delta^2} + \frac{1+\lambda}{(1+\lambda)^2+\delta^2}\right]\ln\frac{\sqrt{1+\delta^2}}{\lambda}.$$
(7)

Generally, the eigenvalue λ is a complex number, and the transition occurs when the eigenvalues cross the imaginary axis. Thus, we set $\lambda = iy$ and substitute it into $f(\lambda, \delta)$. From Eq. (7), the following two equations are obtained:

$$Im[f(\lambda, \delta)] = \frac{2[y(1+\delta^2-y^2)+2y^3]}{(1+\delta^2-y^2)^2+4y^2} \cdot (\ln\sqrt{1+\delta^2} - \ln y) = 0,$$
(8)

and

$$Re[f(\lambda, \delta)] = \pi \cdot \frac{y(1+\delta^2-y^2)+2y^3}{(1+\delta^2-y^2)^2+4y^2} = \frac{2\pi}{k}.$$
(9)

From Eq. (8), one can solve y as $y = \sqrt{1+\delta^2}$. Then, from Eq. (9), the critical point of the forward transition comes out to be:

$$\kappa_f = \frac{4}{\sqrt{1+(\omega_0/\Delta)^2}}.$$
(10)

Looking at Eq. (10), one immediately sees that the forward critical threshold is uniquely determined by the dimensionless ratio ω_0/Δ. In particular, when $\omega_0 = 0$, the frequency distribution becomes the typical unimodal Lorentzian distribution, and one has $\kappa_f = 4$ in agreement with what reported in Ref. [4]. In Fig. 2, the reader can see that Eq. (10) is remarkably well verified by numerical simulations (at all values of Δ and within the entire range of ω_0/Δ).

Equation (10) also explains the conversion from the first- to the second-order-like transition observed in Fig. (1). Indeed, as it can be seen in Fig. (2), κ_f decreases monotonically as ω_0/Δ increases, thus causing (as $\kappa_b = 2$ always) a monotonic shrinking of the hysteresis area. For $\omega_0/\Delta = \sqrt{3}$ one has $\kappa_f = \kappa_b = 2$, and the forward and backward transition points coincide [visible in Fig. 1c]. When ω_0/Δ exceeds $\sqrt{3}$, the hysteresis area does not immediately disappear [see the inset of Fig. 1d], and a Hopf bifurcation occurs at $\omega_0/\Delta = \sqrt{3}$ for both the forward and backward processes (and both bifurcations are continuous). For the forward direction, the system first undergoes a continuous transition, and then it undergoes an explosive transition as κ further increases. A similar scenario of transitions characterizes also the backward direction. A regime ($\omega_0/\Delta > \sqrt{3}$) then exists, where the system undergoes a two-stage transition, first continuous and then explosive, during both (forward and backward) processes. Eventually, a further increase of ω_0/Δ causes the hysteresis

area observed in the upper branches to disappear [see Figs. 1e, f], leading to a situation where only continuous transitions occur in the system. It is in this regime, i.e. close to a tricritical point in parameter space, that *Bellerophon* states emerge.

The third step of our analysis is devoted to fully characterizing such a novel state, and to discuss the relevant differences that exist between them and other typical coherent states emerging in Kuramoto-type models. For the sake of exemplification, let us focus on the case of $\omega_0/\Delta = 3$ [see Fig. 1f]. In these conditions, the system features two continuous transitions at $\kappa_1 = 4/\sqrt{10} \approx 1.26$ and $\kappa_2 = 2$, respectively. As a consequence, three parameter regions can be defined: $\kappa < \kappa_1$ (regime I), $\kappa_1 < \kappa < \kappa_2$ (regime II), and $\kappa > \kappa_2$ (regime III). In regime I, the system exhibits the trivial incoherent state, as the coupling strength is small. In regime III, instead, the coupling is so strong that the system reaches the fully synchronized state, in which all oscillators split into two fully synchronized clusters. *Bellerophon* phases are steady states emerging in the middle regime II, i.e. along the path leading the system from decoherence to its synchronized behaviour. In Fig. 3 four typical conditions are illustrated, that correspond to the κ values denoted by letters A, B, C, and D in Fig. 1f. The emerging states are characterized by three quantities: the instantaneous phases θ_i, the instantaneous frequencies (or speed) $\dot{\theta}_i$, and the long time average frequency $\langle \dot{\theta}_i \rangle$. The panel (a) of Fig. 3 reports the results for $\kappa = 1.28$. One can see that, as κ just exceeds $\kappa_1 = 1.26$, two small symmetric clusters emerge, with average frequencies that are equal to each other in absolute value, but opposite in sign. Oscillators belonging to the two clusters rotate with the same average speed, but with different instantaneous phases and frequencies. At $\kappa = 1.60$ [see panel (b) of Fig. 3] a state emerges made of multiple clusters. The number of clusters increases
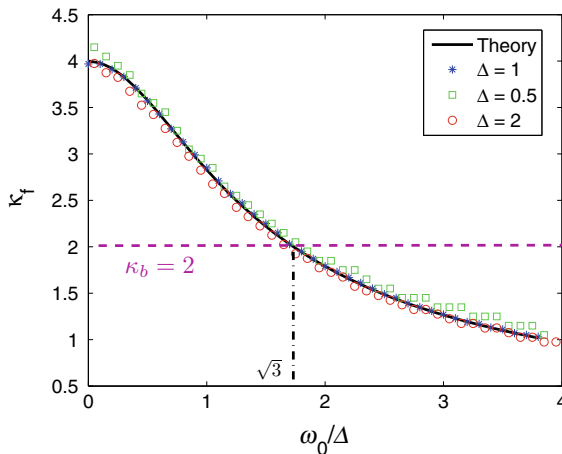
Fig. 2 The critical point for the forward transition. (Color online) κ_f versus ω_0/Δ. The black curve corresponds to the analytic solution Eq. (10). The purple dashed line marks the backward transition point. Notice that the theoretical prediction for the forward critical threshold and the numerical results coincide perfectly. Reprinted from Ref. [18]
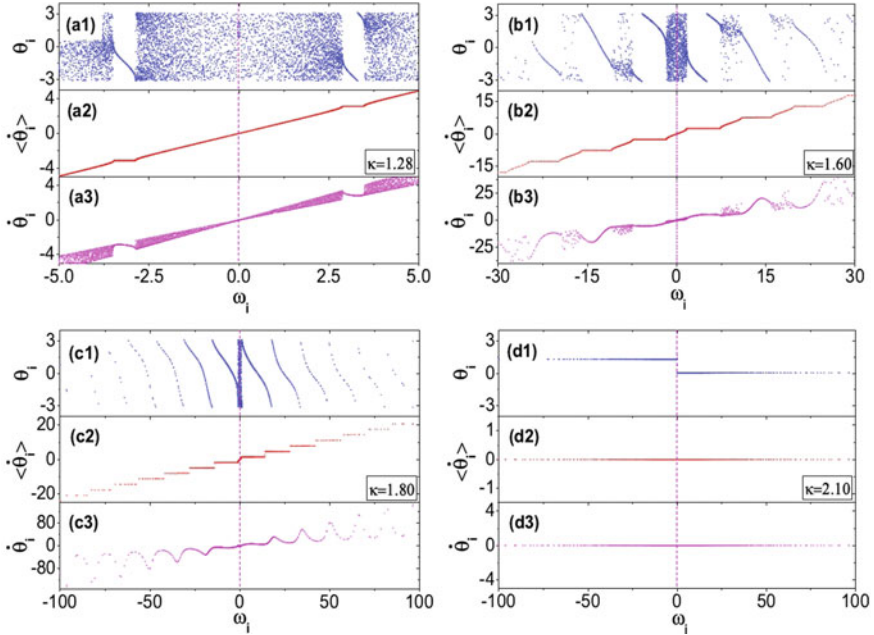
Fig. 3 The main features of Bellerophon states. (Color online). Snapshots of the instantaneous phase θ_i (upper plots), the average speed $\langle \dot{\theta}_i \rangle$ (middle plots), and the instantaneous speed $\dot{\theta}_i$ (lower plots) *versus* natural frequencies $\{\omega_i\}$ of the oscillators. $\kappa = 1.28$ (**a**), 1.60 (**b**), 1.80 (**c**), and 2.10 (**d**, the fully synchronized state). All the other parameters are specified in the text. *Bellerophon* states are those reported in panels (**a**)–(**c**). Reprinted from Ref. [18]

(*in pairs*) as κ increases, and each pair contains oscillators which are symmetric in terms of their natural frequencies. Oscillators inside each cluster have the same average frequency [see the staircase structure of Fig. 3b2], but different instantaneous frequencies [Fig. 3b3]. The set of clusters coexists with a thermal bath of drifting oscillators that are not synchronized. In Fig. 3c, one has the results for $\kappa = 1.80$. This is also a *Bellerophon* state, but different from that of Fig. 3b. The coherent clusters now occupy almost all the range of natural frequencies, except for a small narrow zone around the central frequency. Finally, Fig. 3d ($\kappa = 2.10$) refers to the fully coherent phase, where two giant clusters are formed. In each cluster, oscillators with positive or negative frequencies coincide with each other totally: they feature now the same instantaneous speed, so that the whole system behaves like two giant oscillators.

The final step consists in gathering information on the system's macroscopic and microscopic details related to the emergence of Bellerophon states. This is partly unveiled in Fig. 4a, which shows that the staircases of coherent clusters at $\kappa = 1.60$ satisfy in fact a certain rule: all clusters' frequencies are *quantized*, and they can be expressed as $\pm(2n - 1)\Omega_1, n = 1, 2, \dots$ [23], where Ω_1 is the lowest frequency, i.e., the principle (or base) frequency of the system. Accordingly, depending on
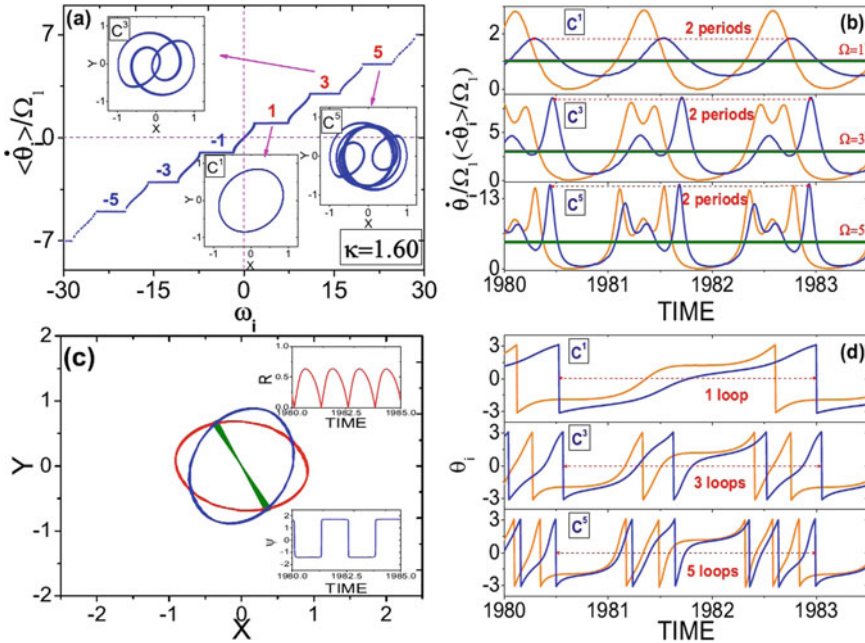
Fig. 4 **Microscopic properties of the state of Fig. 3(b)**. (Color online). **a** The average frequencies for each coherent clusters, arranged in a staircase structure. Notice that each plateau is located at an odd-numbered multiple of a principle frequency Ω_1. **b** Time series of the instantaneous speeds of clustered oscillators. In the panel, two sample oscillators are arbitrarily chosen for clusters C^1 (top), C^3 (middle), and C^5 (bottom). Straight lines mark the average speed. **c** Order parameters for all oscillators with positive (blue oval) and negative (red oval) frequency, and order parameter for all oscillators (green lines). The insets represent the evolution of the global coherence $R(t)$ and average phase $\Psi(t)$, respectively, which are typically oscillatory. **d** Time series of the instantaneous phases corresponding to (**b**). The parameters' choices are described in the text. Reprinted from Ref. [18]

their multiple to Ω_1, clusters can be named as $C^1, C^3, C^5, ...$, respectively. The fundamental point here is that, although the average speeds of oscillators inside each cluster are equal to each other, their instantaneous frequencies are generally different and quite heterogeneous, forming the characteristic cusped pattern totally analogous to that featured by the average frequencies of the oscillators within the CS. Within each cluster, therefore, oscillators are "*mode locked*", but their instantaneous phases and frequencies are fully unlocked.

On the other hand, Fig. 4b shows that the instantaneous frequencies of oscillators inside the same cluster evolve periodically, while different oscillators follow different periodic patterns. In other words, the instantaneous frequency of each oscillator evolves uniquely. This makes *Bellerophon* states essentially different with respect to other coherent states observed in Kuramoto-like models, such as the partially coherent state [7], the standing wave state [20, 21], the traveling wave state [20, 22], and the CS [10, 11], where oscillators inside the coherent cluster are typically
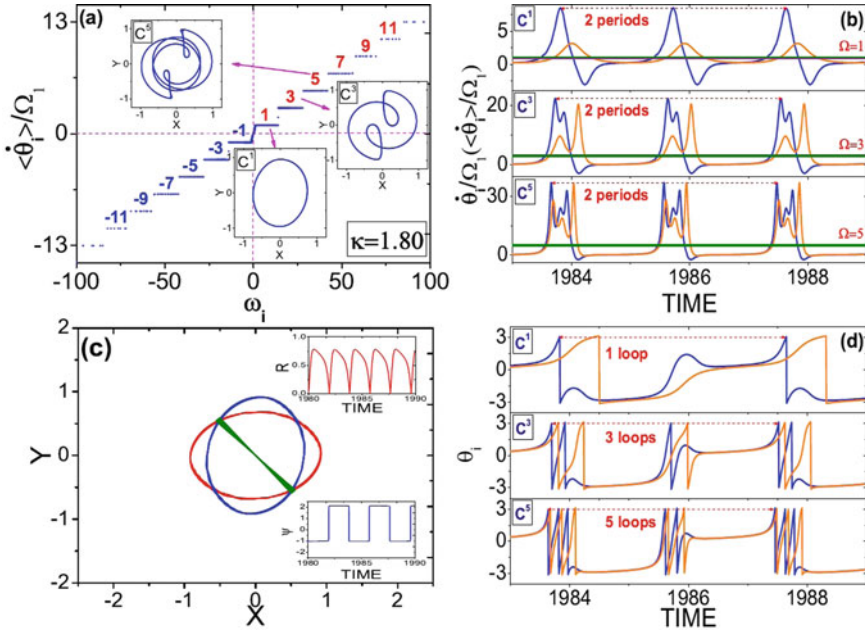
Fig. 5 Microscopic properties of the state of Fig. 3(**c**). (Color online). The panels report the same quantities as in the caption of Fig. 4. In panel (**b**), negative instantaneous speeds are observed during certain time intervals, and the phases decrease accordingly as in (**d**). This implies that although some oscillators go positively on average, they do go back for certain time intervals during one loop, just like shuttle-run. Reprinted from Ref. [18]

frequency-locked. Moreover, even though the instantaneous speed of the clusters' oscillators varies non-uniformly during one period (particularly for those clusters with large n), the average speeds during one period for all oscillators in a certain cluster turn out to be the same, i.e., an odd-numbered multiple of Ω_1.

Since the instantaneous frequencies characterize the rotations of oscillators along the unit circle, Bellerophon states correspond to collective behaviors having intriguing topological features [visible in Fig. 4d]: during one period $T_1 = 2\pi/\Omega_1$, the oscillators in C^1 perform all one loop along the unit circle, and in the mean time, the oscillators in C^3 and C^5 rotate three loops and five loops, respectively. In analogy, oscillators in C^{2n-1} will perform $2n - 1$ loops. Looking more deeply into the results shown in Fig. 4b, one further finds that the instantaneous speeds for all coherent oscillators experience in fact two periods during one loop, i.e. each oscillator repeats its motion during the two half periods. In panel (a) of Fig. 4, we report the local value of the order parameter (the value contributed by only those oscillators in a certain cluster) in the complex plane, for C^1, C^3 and C^5. Due to the complicated phase relationships among oscillators in each cluster [as it can be seen in Fig. 4d], the resulting value is typically periodic or quasi-periodic, and follows a rather complicated orbit. Essentially, each cluster can be seen as a *mesoscopic oscillator*, with

properties described by the Kuramoto order parameter averaged over the oscillators belonging to that cluster. Figure 4c reports the order parameters for all positive and negative frequencies (including the drifting oscillators). In phase space, orbits appear as two smeared ovals, reflecting the quasi-periodic motion of the total order parameter, as shown in the insets of Fig. 4c.

Figure 5 reports the main features of the *Bellerophon* state which is observed at $\kappa = 1.80$. The emerging multi-clustered state shares a lot of traits and peculiarities with that of Fig. 4, but it also displays other new properties. One of these [visible in Fig. 5a] is that all oscillators join here the synchronized clusters, except for a small fraction localized in a narrow frequency area around 0. A second important point is that, although the average speed is positive, some oscillators have a negative instantaneous speed within two time intervals in one period [as it can be seen in Fig. 5b], meaning that those units rotate inversely twice during one loop. Figure 5d shows the behavior of two time intervals in one period, during which the phases of those oscillators decrease. A further peculiar trait is that the principle period T_1 becomes larger and larger as κ increases, with $T_1 \to \infty$ as $\kappa \to 2$, where the system enters a fully synchronized state of two static clusters [see Fig. 3d]. In other words, for moderately large values of κ the system is made of multi-cluster oscillatory coherent states, whose averaged frequencies are multiples of the principle frequency Ω_1 of the system. Besides the situations observed in Figs. 1e, f, such oscillatory states occur also during explosive synchronization as, for instance, one can see in Fig. 1d $(1.7 < \kappa < 2)$. In these states, oscillators form symmetric synchronized cluster pairs, with quantized average frequencies. Oscillators having the same average speed have different instantaneous speeds, forming a characteristic cusped pattern and leading to very complicated (yet collectively organized) motions along the unit circle.

3 Discussion

Let us start by remarking that *Bellerophon* states are generic states of partial coherence occurring in globally coupled nonidentical oscillators, when frequencies are widely distributed. Along this Manuscript, we concentrated on a specific model system [that of Eq. (1)] and on a particular frequency distribution. Such a choice (which was originally adopted by us in Ref. [18]) is only due to the need of having a well defined framework where the novel states could be properly illustrated. However, far from being limited to these circumstances, Bellerophon states occur also in other Kuramoto-like models where either the coupling strengths are properly weighted, or the ensemble is made of two competing populations [19].

In summary, Bellerophon states constitute a novel, asymptotic, coherent phase of globally coupled oscillators. Such a coherent phase is essentially different from all previous phases described in Kuramoto-like models. Within this novel state, oscillators form quantized clusters, where their instantaneous frequencies are not locked, but they behave periodically. Most importantly, their average values are the same. *Bellerophon* states represent therefore a higher-order form of coherence: individ-

ual oscillators inside each cluster do effectively influence each other, at the same time at which they still have a relative freedom. Due to their unconditional and ubiquitous appearance, our study paves the possibility that the quantized features of Bellerophon states are actually the fundamental building blocks behind the spontaneous emergence of collective rhythms in more general systems of interacting oscillators.

References

1. Afraimovich V, Verichev NN, Rabinovich MI (1986) Radiophys Quantum Electron 29:795
2. Kuramoto Y (1984) Chemical oscillations, waves and turbulence. Springer
3. Zhang X, Hu X, Kurths J, Liu Z (2013) Phys Rev E 88:010802
4. Hu X et al (2014) Sci Rep 4:7262
5. Zhang X, Boccaletti S, Guan S, Liu Z (2015) Phys Rev Lett 114:038701
6. Strogatz SH, Mirollo RE (1991) J Stat Phys 63:613
7. Strogatz SH (2000) Physica D 143:1
8. Lee D-S (2005) Phys Rev E 72:026208, Guan S, Wang X, Lai Y-C, Lai C-H (2008) Phys Rev E 77:046211, Stout J, Whiteway M, Ott E, Girvan M, Antonsen TM (2011) Chaos 21:025109
9. Pazó D (2005) Phys Rev E 72(046211), ómez-Gardeñes JG, ómez, A. Arenas SG, Moreno Y (2011) Phys Rev Lett 106:128701, Leyva I et al (2012) Phys Rev Lett 108:168702, Li P, Zhang K, Xu X, Zhang J, Small M (2013) Phys Rev E 87:042803, Leyva I et al (2013) Sci Rep 3(1281), Leyva I et al (2013) Phys Rev E 88:042808
10. Kuramoto Y, Battogtokh D (2002) Nonlinear phenom. Complex Syst 5(380), Shima S-I, Kuramoto Y (2004) Phys Rev E 69:036213
11. Abrams DM, Strogatz SH (2004) Phys Rev Lett 93(174102), Omel'chenko OE, Maistrenko YL, Tass, PA (2008) Phys Rev Lett 100:044105
12. Wolfrum M, Omel'chenko OE (2011) Phys Rev E 84:015201(R)
13. Abrams DM, Mirollo R, Strogatz SH, Wiley DA (2008) Phys Rev Lett 101:084103
14. Sethia GC, Sen A, Atay FM (2008) Phys Rev Lett 100:144102
15. Omelchenko I, Omel'chenko OE, Hövel P, Schöll E (2013) Phys Rev Lett 110:224101
16. Tinsley MR, Nkomo S, Showalter K (2012) Nat Phys 8(662), Hagerstrom AM et al (2012) Nat Phys 8(658), Nkomo S, Tinsley MR, Showalter K (2013) Phys Rev Lett 110:244102
17. Afraimovich V, Shilnikov LP (2014) Int J Bifurc Chaos 24:1440002
18. Bi H et al (2016) Phys Rev Lett 117:204101
19. Qiu T, Boccaletti S, Bonamassa I, Zou Y, Zhou J, Liu Z, Guan S (2016) Sci Rep 6:36713, Qiu T, Bonamassa I, Boccaletti S, Liu Z, Guan S (2018) Sci Rep 8:12950
20. Martens EA, Barreto E, Strogatz SH, Ott E, So P, Antonson TM (2009) Phys Rev E 79:026204
21. Pazó D, Montbrió E (2009) Phys Rev E 80:046215
22. Iatsenko D, Petkoski S, McClintock PVE, Stefanovska A (2013) Phys Rev Lett 110:064101
23. Engelbrecht JR, Mirollo R (2012) Phys Rev Lett 109:034103

Chatter Dynamics and Stability of the Impulsive van der Pol Equation

Shasha Zheng and Xilin Fu

Abstract As a classical model of nonlinear vibration, van der Pol equation has been widely used in the field of natural science and engineering. However, the effect of instantaneous mutations on the system exists objectively. The impulsive van der Pol equation becomes a special kind of discontinuous system due to the emergence of impulse which exhibits complex dynamic behaviors. In this chapter, we consider it as a switched system and adopt the flow theory of discontinuous systems to deal with the effect of impulse, and investigate its dynamics including chatter and stability criteria. By analyzing features from discontinuous point of view, several concepts of flow theory are briefly reviewed. Then several stability criteria for equilibrium are presented, based on various metric functions. Finally, we apply our analysis and criteria to a practical impulsive problem and illustrate different motions as well as the periodic oscillation under the stimulation of impulse.

1 Introduction

Nonlinear phenomena, which can not be described by linear models, widely exist in the field of natural science and engineering technology, such as the swing phenomenon of pendulum, oscillation mechanism of self-excited circuit and other practical applications closely related to our life. Therefore, nonlinear dynamics arise as tools in various interdisciplinary fields for scientific research and further analysis. H. Poincaré's qualitative theory in ordinary differential equations and quantitative calculations in celestial theory lead the earliest development of nonlinear science [1]. From early twentieth century, radio technology promoted the nonlinear vibration theory [2], and several famous nonlinear differential equations appeared in succession [3]. Especially when damping or resistances exist, second-order differential equation plays an important role in providing mechanical models for many practical nonlin-

S. Zheng (✉) · X. Fu
Shandong Normal University, 88 East Wenhua Road, Ji'nan, China
e-mail: shui925@sina.com

X. Fu
e-mail: xilinfu@hotmail.com

ear vibration problems, which can be transformed into a general form as the famous
Lienard equation

$$x^{''} + g(x)x^{'} + f(x) = 0, \tag{1}$$

where $f(x)$ is an odd function and $g(x)$ is an even function representing the damping
item, or a specific form of Eq. (1), named the van der Pol equation

$$x^{''} - \varepsilon(1 - x^2)x^{'} + x = 0, \tag{2}$$

where $\varepsilon > 0$ is the damping coefficient parameter.

As we know, the van der Pol oscillator model Eq. (2) was proposed by Balthasar
van der Pol [4]. Subsequently, van der Pol continued his research by adding a har-
monic forcing term to demonstrate oscillation in the study of circuits containing
vacuum tubes [5], and proved that such model could also be applied to a broad range
of circumstances [6]. With respect to damping and perturbation, the van der Pol equa-
tion could be employed as a general mathematical model to understand the complex
nonlinear phenomena of physical systems. From the 50s of twentieth century, some
systemical research on the qualitative analysis of the isolated closed trajectory for
Eq. (2) have been done in the field of electronics and mathematical dynamics [7–9].

However, the above research all relied on geometric theory for continuous systems.
Once the state was varied or switched, the dynamics and qualitative analysis of
oscillation would require new method. It was shown that, if the damping coefficient
ε was positive, as the value of ε increased, the system would first encounter a limit
cycle and then be heavily damped, especially when certain ε lead to an irregular
noise, it was one of the first reported discoveries of deterministic chaos; when $\varepsilon \leq 1$,
the negative damping oscillation phenomenon showed a stronger trend, which might
cause unsteadiness even bifurcations. For the complex oscillation when the state was
interrupted with a threshold, in 2014, we optimized the LC oscillator circuit model
with a second-order vibration switched system and took a different approach to its
dynamical analysis [10]. In order to solve the problem of energy consumptions and
instability in application, current tracking control technology was used to sustain the
free vibrations of triode, and an impulsive switched van der Pol equation was given as

$$\begin{cases} x'' - \mu f(x)x' + p_0^2 x = 0, & \varphi(t, x, x') \neq 0, \\ x(t^+) = h_1(x(t)), & \varphi(t, x, x') = 0, \\ x'(t^+) = h_2(x(t), x'(t)), & \varphi(t, x, x') = 0, \end{cases} \tag{3}$$

where μ is the damping coefficient parameter as ε, $f(x)$ is the general nonlinear
damping item, and p_0 is the perturbation parameter, $\varphi \in C^{'}(R_+ \times R^2, R)$ in t is
the threshold function, h_1 and h_2 are impulse functions, $x(t^+) = \lim_{\varepsilon \to 0^+} x(t + \varepsilon)$ and
$x'(t^+) = \lim_{\varepsilon \to 0^+} x'(t + \varepsilon)$ are the right limits of the state at discontinuity point.

The van der Pol equation with such impulsive effects becomes a special kind of
discontinuous system due to the emergence of impulse, and it owns more practi-
cal significants to research on its complex dynamical behaviors in many practicing

fields, such as switchability, chatter, grazing motion, stick motion, sliding motion and fragmentation. Moreover, when complex dynamical behavior appears its stability analysis needs new techniques different with continuous and traditional methods of impulsive differential equation.

As an important tool for nonlinear dynamics, discontinuous system has been investigated systemically over the past few decades, from the non-smooth theory of Filippov [11] to the flow switchability theory of Luo [12–15]. To overcome the limitations of continuous methods in dealing with impulse, this chapter adopts methods of discontinuous dynamical system to research on the complex dynamical behaviors of impulsive van der Pol equation. That is, the flow theory around the time-varying impulsive surface boundary can be used to discuss chatter dynamics. Based on such analysis, attractors including equilibrium point and periodic motion can be studied through the method of local singularity theory and mapping theory in discontinuous dynamical system, in which the latter has been studied in [16]. Therefore, subsequent sections are arranged as follows. In Sect. 2, we will review the chatter dynamics of impulsive van der Pol equation, analyze the model's features from discontinuous point of view, and introduce several criteria making chatter phenomenon appear or not. In Sect. 3, several basic conceptions of stability will be given, and the analytical conditions for the stability of equilibrium will be discussed based on various metric functions in discontinuous systems. General stability condition based on the G-function will be presented, which is equivalent to the traditional Lyapunov stability condition. In addition, another stability condition based on the L-function will also be presented. In Sect. 4, the complex dynamical analysis will be applied on a practical impulsive problem in engineering. Section 5 is the conclusion and further work.

2   Chatter Dynamics

Many evolution processes are characterized by the fact that the state would experience a sudden change at certain moments, especially in the field of engineering. Nowadays, it is universal for a dynamical system to experience transient phenomena in practical problems involving thresholds, in which impulse provides an adequate description of such sharp system change [17–19]. In 2013, we established a link between the pulse phenomena and chatter phenomena in an impulsive dynamical system by discuss the collision times of the flow and the impulsive surface boundary, viewed the impulsive system as a global discontinuous one consisting of several uniquely-continuous subsystems and investigated its chatter dynamics [20, 21]. That is, pulse phenomena means the motion would hit the same impulsive surface finite number of times, which is just like the significant chatter phenomena of mechanical systems provided in [22].

In practical, chatter arises from vibro-impacts when the moving parts of a mechanical system repeatedly contact with each other, and causes the system to exhibit complex nonlinear dynamics, especially discontinuity [23]. Unfortunately, various properties of the discontinuity bring more complex dynamical behaviors to the global discontinuous system than those separately continuous subsystems. Owing to the

Fig. 1 A self-excited oscillator includes a triode in LC circuit and a pulse controller
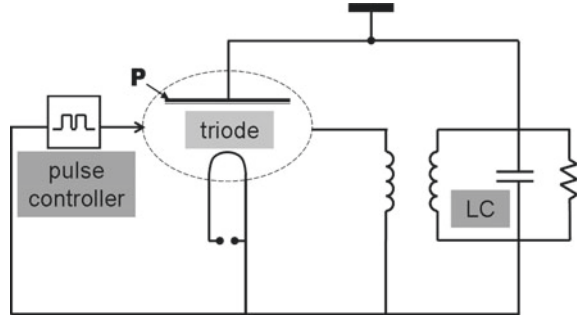
convenience of the theory of flow switchability in handling discontinuous systems presented in [12], Fu and Zheng also extended a typical machining model into a second-order impulsive equation and utilized such theory into the practical chatter dynamics [24, 25]. By analyzing the energy change at the discontinuous separation boundary, without restricting the global rigorous conditions for system, the previous work was definitely simplified .

For the van der Pol equation with interrupted state provided in [10], its chatter dynamic analysis can be given by flow theory as well.

For Eq. (3), the continuous part

$$x^{''} - \mu f(x) x^{'} + p_0^2 x = 0 \tag{4}$$

is a more generalized typical motion form of Eq. (2), where x originally portrays the oscillation voltage across the LC circuit (including inductor, capacitor and nonlinear resistance) and the triode (including plate electrode P, grid electrode and the base electrode) as shown in Fig. 1, the damping item $f(x)$ can represent different kinds of systems by modulating parameters and function expressions, and p_0 represents the perturbation for fixed frequency of the circuit. On the other hand, the discrete part of Eq. (3) plays an important role when the plate electrode P is saturated. Once the oscillation voltage satisfies certain conditions, that is, at those discontinuous moments satisfying switching control law $\varphi(t, x, x') = 0$(which is proceeded from the critical state for x when the base electrode emits electrons with a fixed acceleration), the pulse controller in Fig. 1 will work according to impulse functions h_1 and h_2, inducing x into $h_1(x(t))$ and x' into $h_2(x(t), x'(t))$. Therefore, the original continuous system Eq. (4) becomes an impulsive switched system Eq. (3) due to the impact effect of the pulse controller, in which equation $\varphi(t, x, x') = 0$ portrays several obstacle time-varying surfaces named impulse surface [18] and denoted by Σ.

For a standard format, introduce the state vector $\mathbf{x} = (x_1, x_2)^{\mathrm{T}} \in \Omega \subset R \times R$, where $x_1 = x$, $x_2 = x'$, and the equivalent form of Eq. (3) can be given as

$$\begin{cases} \dot{\mathbf{x}} = \mathbf{F}(t, \mathbf{x}), & \varphi(t, \mathbf{x}) \neq 0, \\ \mathbf{x}(t^+) = \mathbf{h}(\mathbf{x}(t)), & \varphi(t, \mathbf{x}) = 0, \end{cases} \tag{5}$$

where the vector function $\mathbf{F} = (x_2, \mu f(x_1)x_2 - p_0^2 x_1)^{\mathrm{T}}$ and $\mathbf{h} = (h_1, h_2)^{\mathrm{T}}$.

As analyzed before, the implicit function generated by φ or itself represents a dynamical time-varying boundary in state space in $R \times R$, dividing (x_1, x_2)-space into following two domains varying as time passes,

$$\Omega_1 = \{\mathbf{x} | \varphi(t, \mathbf{x}) > 0\}, \text{ and}$$
$$\Omega_2 = \{\mathbf{x} | \varphi(t, \mathbf{x}) < 0\}.$$

And the time-varying separation boundary is defined as

$$S = \{\mathbf{x} | \varphi(t, \mathbf{x}) = 0\},$$

which can be seen as the impulse surface.

As for different domains in state space, given any $\mathbf{x}^{(i)} = (x_1^{(i)}, x_2^{(i)})^{\mathrm{T}} \in \Omega_i \subset R \times R, i = 1, 2$, the behaviors for different solutions in different domains can be described as a C^{r_i}-continuous system($r_i \geq 1$) with the form of

$$\dot{\mathbf{x}}^{(i)} = \mathbf{F}^{(i)}(t, \mathbf{x}^{(i)}), \tag{6}$$

where $\mathbf{x}^{(i)} = (x^{(i)}, x^{(i)'})^{\mathrm{T}}$ is a point in ith sub-domain of phase space for Eq. (5), $\mathbf{F}^{(i)}(t, \mathbf{x}^{(i)})$ is the vector field for the state $\mathbf{x}^{(i)}$ and all time t in Ω_i, and the continuous solution for Eq. (6) given by

$$\mathbf{x}^{(i)}(t) = \Phi(t_0, \mathbf{x}^{(i)}(t_0), t) \tag{7}$$

is C^{r_i+1}-continuous with initial point $(t_0, \mathbf{x}^{(i)}(t_0))$. On the other hand, from the perspective of dynamics, such solution can be treated as an *intra-domain flow*

$$\mathbf{x}_t^{(i)} = \Phi(\mathbf{x}_0^{(i)}, t - t_0),$$

where $\Phi(\mathbf{x}_0^{(i)}, t - t_0)$ satisfies initial condition

$$\mathbf{x}^{(i)}(t_0) = \Phi(\mathbf{x}_0^{(i)}, 0).$$

And for comparison, the *reference flow* $\bar{\mathbf{x}}_t$ which always lies on the boundary is determined regarding to the intra-domain flow $\mathbf{x}_t^{(i)}$, satisfying

$$\begin{cases} \varphi(t, \bar{\mathbf{x}}_t) = 0, \\ \dot{\bar{\mathbf{x}}}_t = \mathbf{F}^{(0)}(t, \bar{\mathbf{x}}_t), \end{cases} \tag{8}$$

where function $\mathbf{F}^{(0)}$ comes from the derivative condition for the reference flow.

To discuss the chatter phenomena of the system, conceptions of collision point in flow theory will be given.

Definition 1 Consider a solution $\mathbf{x}(t) = \Phi(t_0, \mathbf{x}_0, t)$ of dynamical system Eq. (5) with initial condition $(t_0, \mathbf{x}_0)$. We call point $(t^*, \mathbf{x}(t^*))$ is a collision point of the solution $\mathbf{x}(t)$ for the impulse surface S in the whole space, if there is a t^*, such that $\varphi(t^*, \mathbf{x}(t^*)) \doteq \varphi(t^*) = 0$.

Then, we state definitions of absence and presence of chatter phenomena based on the numbers of the collision points.

Definition 2 For dynamical system Eq. (5), the absence of chatter phenomena is that, there is at most only one collision point of any solution starting from state space Ω_α ($\alpha \in \{1, 2\}$) for the impulse surface S, i.e., there is at most only one t^*, such that $(t^*, \mathbf{x}(t^*)) \in \Sigma$; the presence of chatter phenomena is that, there are at least two collision points of any solution starting from state space Ω_α ($\alpha \in \{1, 2\}$) for the impulse surface S.

Here we give three different sufficient conditions to make the chatter phenomena absent by using the idea of flow theory.

Lemma 1 *Consider dynamical systems Eqs. (5) and (8) with corresponding flows* $\mathbf{x}_t^{(\alpha)}(\alpha \in \{1, 2\})$ *and* $\bar{\mathbf{x}}_t$. *Suppose that for the impulse surface S, the corresponding normal vector is* $\boldsymbol{n}_S(t, \bar{\mathbf{x}}_t)$. *For any solution of Eq. (5) starting from $(t_0, \mathbf{x}_0)$ in $\Omega_\alpha(\alpha \in \{1, 2\})$, there is at most only one collision point for the impulse surface S, i.e., the chatter phenomena of Eq. (5) is absent, if any one of following conditions is satisfied,* (H_1) *for $\forall t \geq t_0$, there exists a $B(t) \in L^{'}(R_+, R_+)$, such that*

$$\boldsymbol{n}_S^{\mathrm{T}}(t, \bar{\mathbf{x}}_t) \cdot \boldsymbol{F}^{(\lambda)} \geq B(t), \text{ for } \lambda \in \{0, \alpha\}, \alpha = 1, 2,$$

where $\int_t^\infty B(s)ds = \infty$, and

$$\left. \begin{array}{ll} \boldsymbol{F}^{(\alpha)} = \boldsymbol{F}^{(\alpha)}(t, x_t^{(\alpha)}), & \text{in } \Omega_\alpha, \\ \boldsymbol{F}^{(0)} = \boldsymbol{F}^{(0)}(t, \bar{\mathbf{x}}_t) = \dot{\bar{\mathbf{x}}}_t, & \text{on } S; \end{array} \right\}$$

(H_2)

$$\text{for } \boldsymbol{n}_S^{\mathrm{T}} \cdot (\boldsymbol{x}^{(\alpha)} - \bar{\boldsymbol{x}}) < 0, \ G_S^{(\alpha)}(t, \boldsymbol{x}^{(\alpha)}) \geq 0; \text{ or,}$$

$$\text{for } \boldsymbol{n}_S^{\mathrm{T}} \cdot (\boldsymbol{x}^{(\alpha)} - \bar{\boldsymbol{x}}) > 0, \ G_S^{(\alpha)}(t, \boldsymbol{x}^{(\alpha)}) \neq 2V'(t),$$

where $\alpha = 1, 2$;
(H_3) *for $\boldsymbol{n}_S^{\mathrm{T}} \cdot (\boldsymbol{x}^{(\alpha)} - \bar{\boldsymbol{x}}) < 0$,*

$$G_S^{(\alpha)}(t, \boldsymbol{x}^{(\alpha)}) \geq 0; \text{ or,}$$

for $\boldsymbol{n}_S^{\mathrm{T}} \cdot (\boldsymbol{x}^{(\alpha)} - \bar{\boldsymbol{x}}) > 0$, when $G_S^{(\alpha)}(t, \boldsymbol{x}^{(\alpha)}) = 2V'(t)$,

$$G_S^{(1,\alpha)}(t, \boldsymbol{x}^{(\alpha)}) > 0,$$

where $\alpha = 1, 2$.

Here $G_S^{(\alpha)}(t, \mathbf{x}^{(\alpha)}) = \mathbf{n}_S^T(t, \overline{\mathbf{x}}) \cdot \dot{\mathbf{x}}^{(\alpha)}$ and $G_S^{(1,\alpha)}(t, \mathbf{x}^{(\alpha)}) = DG_S^{(\alpha)}(t, \mathbf{x}^{(\alpha)})$ are G-functions, and $\mathbf{n}_S(t, \overline{\mathbf{x}}_t) = (\nabla \varphi)^T$ is corresponding normal vector on the time-varying separation boundary S, where $\nabla = (\partial/\partial x_1, \partial/\partial x_2)^T$ is the Hamiltonian operator. $V(t)$ comes from $Y = x' - V(t)$ showing the critical state for x. The proof and more details of the chatter dynamic analysis can be referred in [10].

3 Stability Analysis

With the guarantee of the absent of chatter, corresponding flow behaviors including periodic motion and the stability of equilibrium could be investigated as similar as a continuous system. However, once the conditions of lemma could not be satisfied, the dynamics will be more complicated. Due to the changes of characters brought by discontinuity, it is far from an easy task to the systematic qualitative work of such system. Up to now, we have discussed the periodic motion with specific periodic impulsive excitations, and presented analytical conditions for such periodic motion from certain mapping structures [17]. In this chapter, further investigations about the stability of equilibrium will be carried out on dynamics of such switched discontinuous system Eq. (3). As such system possesses both the continuous characteristics of differential systems and discrete characteristics of impact discontinuity, we will apply the flow theory in discrete and switching dynamical systems provided in [26], and investigate corresponding stability properties by various metric functions, which is different from the traditional Lyapunov stability condition.

3.1 Preliminaries

In actual operation, because of the periodic property of the van der Pol oscillation, saturation current will appear regularly in Fig. 1. Suppose those switching moments for critical state in Eq. (3) could be calculated explicitly from equation $\varphi(t, x, x') = 0$ as $t = t_k (k = 1, 2, ...)$, by which the impulse surface Σ_k could be regarded as a sequence of surfaces in the whole space. That is to say, it is at fixed switching moments t_k that the plate electrode P is saturated and aborted. Furthermore, $t_k = kT (k = 1, 2, ...)$, where T is the period of oscillation. So that, the pulse controller will work cyclically as well, complementing electrons, smoothing the abrupt change of state, and finally modulating the system by the Newton's law of restitution, which can be applied as the effect of impulsive control strategy in general mechanical problems [27]. To be specific, when critical state is reached, the pulse controller will excite the system based on certain impulse functions h_1 and h_2, making the stimulation adhere to impulse-momentum law and Newton's law. And the impulse functions can be applied as $h_1(x(t)) = e_1 x(t)$ and $h_2(x(t), x'(t)) = e_2 x'(t)$, where e_1 and e_2 are coefficients of restitution, representing the ratio for electron's velocity and acceleration after and before each stimulation, respectively, which can be determined through experi-

ments. In this way, the state of Eq. (3) will experience a relative perturbation acting instantaneously, in other words, a specific form of impulse, inducing discontinuity.

Thus, to analyze the complex qualitative property of practical oscillation for Eq. (3), we just need to investigate on the following certain case

$$\begin{cases} x'' - \mu f(x)x' + p_0^2 x = 0, & t \neq t_k, \\ x(t^+) = e_1 x(t), & t = t_k, \\ x'(t^+) = e_2 x'(t), & t = t_k, \end{cases} \tag{9}$$

where t_ks$(k \in Z)$ are switching moments.

Just like a traditional impulsive differential system at fixed moments, Eq. (9) can be seen as a hybrid system that is composed of a family of continuous subsystems and corresponding discrete jumps between each two subsystems. And in application, it originally gives the evolution process of the oscillation circuit subject to impulsive effects, that is, at moments except those t_ks cyclically, the solution of Eq. (9) will move in accordance with the self-excited oscillation Eq. (4); when at switching moments $t = t_k$ $(k \in Z)$, the solution will experience an instantaneous switch in obedience to the impulse functions, which is left continuous, and assume that it will not encounter another changing immediately after one jump, that is, for an arbitrary $\delta > 0$, there will be a moment s, such that, $t_k < s < \delta$ and $s \neq t_l$, $\forall l \in Z$. Thus, in the following discussion, we will pay attention to the right limits of the state at switching moments.

Recently, some geometric and theoretical work about discontinuous limit cycle have been obtained for quantitative results of Eq. (9) [28]. While to analyze and predict the precise motion of a solution especially when impulse occurs, there are still many work to do. Here, we will focus on the system's dynamical behaviors near the switching moments and apply the flow theory to investigate on the stability of equilibrium. As we know, trivial solution is the equilibrium of Eq. (4), which behaves the same way in Eq. (9) according to special impulse functions. We denote such equilibrium as $\mathbf{x}(t_0, 0, t) \doteq \mathbf{x}^*$.

As mentioned above, such discontinuous dynamical system caused by impacts can be deemed as a global discontinuous one consisting of several sub-switching systems, with its state-space of motion consisting of many continuous sub-domains. Hence, on account of those switching moments $t = t_k(k = 1, 2, ...)$, there is a division about the phase space $(x, x') \in \Omega \subset R \times R$ into several sub-domains and adjacent boundaries varying as time passes, with the following definitions.

For dynamical system Eq. (9) with finite number of times impulses, where the impulse time is $t_k(k \in Z)$, the sub-domain between ith and $(i + 1)$th impulse for motion of Eq. (9) without any impulse when $t \in (t_i, t_{i+1})$ is given as

$$\Omega_i = \{(x(t), x'(t)) | x'(t) \neq V, \ t \in (t_i, t_{i+1}), \ t_i = kT, \ k \in Z\}, \ i = 1, 2, ..., m,$$

where V is the threshold for $x'(t)$ derived from the acceleration of electrons; and the jth impulse surface as separation boundary at t_j is given as

$$\partial \Omega_j = \{(x_j, x_j') | x_j' = V, \ t = t_j, \ t_j = kT, \ k \in Z\}, \ j = 1, 2, ..., n,$$

where $x_j = x(t_j)$, $x'_j = x'(t_j)$.

Thus, the universal phase space for total motion with several sub-domains and adjacent boundaries can be given as

$$\Omega = \left(\bigcup_{i=1}^{m} \Omega_i \right) \cup \left(\bigcup_{j=1}^{n} \partial \Omega_j \right),$$

on which Eq. (9) is a switched system with respective subsystems in each sub-domain.

As described in Sect. 2, the vector form of Eq. (9) can be given as

$$\begin{cases} \dot{\mathbf{x}} = \mathbf{F}(t, \mathbf{x}), & t \neq t_k, \\ \mathbf{x}(t^+) = \mathbf{h}(\mathbf{x}(t)), & t = t_k, \end{cases} \tag{10}$$

where the vector function $\mathbf{F} = (x_2, \mu f(x_1)x_2 - p_0^2 x_1)^{\mathrm{T}}$ and $\mathbf{h} = (e_1 x_1, e_2 x_2)^{\mathrm{T}}$. The vector form for its continuous part Eq. (4) and the intra-domain flow can be given as Eqs. (6) and (7), where i extends to $i \in \{1, 2, ..., m\}$ instead of $i \in \{1, 2\}$.

Meanwhile, given any $(x_j, x'_j) \in \partial \Omega_j \subset \Omega$, according to the definition of separation boundary $\partial \Omega_j$, the transport law at time $t = t_j$ is governed by equation

$$\mathbf{g}^{(j,j+1)}(\mathbf{x}_j^{(j)}, \mathbf{x}_j^{(j+1)}) = 0, \tag{11}$$

where the superscript $(j, j + 1)$ represents the intra-flow changing from $\mathbf{x}^{(j)}$ to $\mathbf{x}^{(j+1)}$, and here $\mathbf{x}_j^{(j)} = \mathbf{x}^{(j)}(t_j)$, while $\mathbf{x}_j^{(j+1)} = \mathbf{x}^{(j+1)}(t_j^+)$ is the right limit of the state, without causing ambiguity. Governing function Eq. (11) for behaviors of motion on the separation boundary $\partial \Omega_j$ can be derived from corresponding transport law of switching in Eq. (10).

Therefore, with the combination of the subsystems Eq. (6) in sub-domain Ω_is and the transport laws Eq. (11) on separation boundary $\partial \Omega_j$s, Eq. (9) (or its vector form Eq. (10)) could be investigated separately according to each vector field and governing function. Specifically, the discontinuous flow of switching system Eq. (9) can be separated into several continuous intra-flows according to Eq. (7). As a whole, the union of all the intra-flows of the subsystems in a certain queue series on $\Omega = (\bigcup_{i=1}^{m} \Omega_i) \cup (\bigcup_{j=1}^{n} \partial \Omega_j)$ can be considered as a *resultant flow* (or resultant solution) $\gamma(t_0, t)$ given by

$$\gamma(t_0, \mathbf{x}_0, t) \doteq \gamma(t_0, t) = \bigcup_{i=1}^{m_0 - 1} \gamma^{(i)}(t_{i-1}, t_i) \bigcup \gamma^{(m_0)}(t_{m_0 - 1}, t), \tag{12}$$

where $t \in (t_{m_0 - 1}, t_{m_0})$, $m_0 \in \{1, 2, ..., m\}$, $\mathbf{x}_0$ represents initial point which can be omitted when the initial condition is not emphasized, and each

$$\gamma^{(i)}(t_{i-1}, t_i) = \{\mathbf{x}^{(i)}(t) | \mathbf{x}^{(i)}(t) = \Phi(t_{i-1}, \mathbf{x}_{i-1}^{(i)}, t) \text{ in } \Omega_i \text{ for all } t \in [t_{i-1}, t_i]\},$$

with $\mathbf{x}_{i-1}^{(i)} = \mathbf{x}^{(i)}(t_{i-1})$.

From the above discussion, any global flow of the switching system Eq. (9) can be managed by various continuous intra-flows in different sub-domains, while the resultant flow keep them together in union, which can be adopted in study of stability properties. In the following, we will introduce several basic concepts and metric functions for stability.

3.2 Basic Conceptions

To investigate the stability in the vicinity of equilibrium for the switching system consisting of several subsystems in phase space, corresponding metric functions are defined by relative displacement function provided in [26] as follows.

Definition 3 For switched dynamical system Eq. (9) and the equilibrium point $\mathbf{x}^*$ in phase space, consider a division $\Omega = (\bigcup_{i=1}^{m} \Omega_i) \cup (\bigcup_{j=1}^{n} \partial\Omega_j)$ on account of impulse moments t_ks$(k = 1, 2, ...)$ and a flow $\mathbf{x}$ of Eq. (9). The relative displacement function for the flow $\mathbf{x}$ to the point $\mathbf{x}^*$ is defined by

$$d(\mathbf{x}, \mathbf{x}^*) = \|\mathbf{x} - \mathbf{x}^*\|. \tag{13}$$

If there is a monotonically increasing or decreasing metric function of the relative displacement function

$$V(\mathbf{x}, \mathbf{x}^*) = V(d(\mathbf{x}, \mathbf{x}^*)) \doteq E, \tag{14}$$

with the property of

$$V(\mathbf{x}, \mathbf{x}^*) = \min(\text{or max}), \text{ if } d(\mathbf{x}, \mathbf{x}^*) = 0,$$

such monotonic function $V(\mathbf{x}, \mathbf{x}^*)$ is called a generalized measuring function of Eq. (9) in the neighbourhood of $\mathbf{x}^*$.

If $E = C \equiv const$, there will be a surface in the phase space, demonstrated by

$$V(\mathbf{x}, \mathbf{x}^*) = E = C, \tag{15}$$

which is called the equi-measuring function surface of $\mathbf{x}^*$.

In addition, for different values of $E = E_i(i = 1, 2, ...)$, we can get a set of the equi-measuring function surfaces, filling the entire domain of the neighbourhood of $\mathbf{x}^*$. And for each $E = E_i$, the normal vector of the equi-measuring function surface $V(\mathbf{x}, \mathbf{x}^*) = E_i$ is expressed by

$$\mathbf{n}_v(\mathbf{x}, \mathbf{x}^*) = \nabla V(\mathbf{x}, \mathbf{x}^*),$$

where the subscript v represents equi-measuring function surface, and the Hamiltonian operator symbol ∇ can be calculated as Sect. 2.

Based on measuring functions and equi-measuring function surfaces, corresponding G-function can be defined as another metric function useful for analysis across time-varying boundary. In virtue of the discontinuity of global flow, such metric function can be given in each subsystem as follows.

Definition 4 For switched dynamical system Eq. (9) with equilibrium point $\mathbf{x}^*$ in phase space, and the i-th subsystem Ω_i with vector field $\mathbf{F}^{(i)}(t, \mathbf{x}^{(i)})$ in Eq. (6), consider an intra-flow $\mathbf{x}^{(i)}$ of Eq. (9) approaches the equi-measuring function surface with corresponding constant $E = C$ in Eq. (15) at time t. The metric G-function at the constant measuring function level about point $\mathbf{x}^*$ is defined as

$$G_v(\mathbf{x}^{(i)}, \mathbf{x}^*, t) = [\mathbf{n}_v(\mathbf{x}^{(i)}, \mathbf{x}^*)]^{\mathrm{T}} \cdot \mathbf{F}^{(i)}(t, \mathbf{x}^{(i)}). \tag{16}$$

Remark 1 The metric G-function is the dot product of vector field $\mathbf{F}^{(i)}(t, \mathbf{x}^{(i)})$ for the i-th subsystem Ω_i and the normal vector $\mathbf{n}_v(\mathbf{x}^{(i)}, \mathbf{x}^*)$, with a geometric meaning of the component for flow's vector field in normal direction of equi-measuring function surfaces at different moment, which is a metric parameter to measure dynamical behaviors of any subsystems to the equi-measuring function surfaces.

Followed by the metric V-functions and G-functions, additional functions describing increments between different moments about the measuring function will be proposed as follows.

Definition 5 For an intra-flow $\mathbf{x}^{(i)}$ of switched dynamical system Eq. (9) in the i-th subsystem Ω_i with vector field $\mathbf{F}^{(i)}(t, \mathbf{x}^{(i)})$ in Eq. (6), $\mathbf{x}^*$ is the equilibrium point in phase space, $V(\mathbf{x}^{(i)}, \mathbf{x}^*)$ in Eq. (14) is corresponding measuring function with the relative displacement function $d(\mathbf{x}^{(i)}, \mathbf{x}^*)$ in Eq. (13). For any time $t \in (t_{i-1}, t_i]$, the total change of the measuring function for time interval $[t_{i-1}, t]$ in the vicinity of point $\mathbf{x}^*$ is defined as

$$\begin{aligned} L^{(i)}(\mathbf{x}^*, t_{i-1}, t) &= \int_{t_{i-1}}^{t} \frac{dE^{(i)}(t)}{dt} \\ &= \int_{t_{i-1}}^{t} G_v(\mathbf{x}^{(i)}, \mathbf{x}^*, t) dt \\ &= \int_{t_{i-1}}^{t} [\mathbf{n}_v(\mathbf{x}^{(i)}, \mathbf{x}^*)]^{\mathrm{T}} \cdot \mathbf{F}^{(i)}(t, \mathbf{x}^{(i)}) dt \\ &= V(\mathbf{x}^{(i)}(t), \mathbf{x}^*) - V(\mathbf{x}_{i-1}^{(i)}, \mathbf{x}^*), \end{aligned} \tag{17}$$

where $\mathbf{x}_{i-1}^{(i)} = \mathbf{x}^{(i)}(t_{i-1}^+)$.

When $t = t_i$ in Eq. (17), the total change of the measuring function between t_{i-1} and t_i is the increment of the measuring function about the i-th subsystem Ω_i in Eq. (6) as follows

$$\begin{aligned} L^{(i)}(\mathbf{x}^*, t_{i-1}, t_i) &= \int_{t_{i-1}}^{t_i} G_v(\mathbf{x}^{(i)}, \mathbf{x}^*, t) dt \\ &= \int_{t_{i-1}}^{t_i} [\mathbf{n}_v(\mathbf{x}^{(i)}, \mathbf{x}^*)]^{\mathrm{T}} \cdot \mathbf{F}^{(i)}(t, \mathbf{x}^{(i)}) dt \\ &= V(\mathbf{x}_i^{(i)}, \mathbf{x}^*) - V(\mathbf{x}_{i-1}^{(i)}, \mathbf{x}^*), \end{aligned} \tag{18}$$

where $\mathbf{x}_i^{(i)} = \mathbf{x}^{(i)}(t_i)$ and $\mathbf{x}_{i-1}^{(i)} = \mathbf{x}^{(i)}(t_{i-1}^+)$.

From Eq. (18), we can obtain the total change of the measuring function in the i-th subsystem, which can be regarded as the quantity increment of the equi-measuring function surface.

On the other hand, once a flow arrives adjacent boundary from a subsystem, according to Eq. (9), it will jump and change into another intra-flow abruptly, causing a different kind of increment. Such quantity increment of the equi-measuring function surface for the switching from subsystem Ω_i to adjacent subsystem Ω_{i+1} through separation boundary $\partial\Omega_{i+1}$ at time $t = t_i$ according to transport law Eq. (11) is defined as

$$L_\Delta^{(i,i+1)}(\mathbf{x}^*, t_i) = V(\mathbf{x}_i^{(i+1)}, \mathbf{x}^*) - V(\mathbf{x}_i^{(i)}, \mathbf{x}^*), \tag{19}$$

where the subscript Δ represents the incremental quantity, and the superscript $(i, i+1)$ represents the intra-flow changing from $\mathbf{x}^{(i)}$ to $\mathbf{x}^{(i+1)}$, in addition, here $\mathbf{x}_i^{(i)} = \mathbf{x}^{(i)}(t_i)$, while $\mathbf{x}_i^{(i+1)} = \mathbf{x}^{(i+1)}(t_i^+)$ is the right limit of the state, without causing ambiguity.

It is shown that, the above increment functions L-functions are all pertaining to the averaging of a intra-flow or different passable intra-flows to the equi-measuring function surface $V(\mathbf{x}^{(i)}, \mathbf{x}^*) = C$ for a certain time interval. To determine the global increase or decrease for a switching system, we have to refer to the case of global flow. Consider the global resultant flow $\gamma(t_0, t)(t \in (t_{m_0-1}, t_{m_0}), m_0 \in \{1, 2, ...\})$ given in Eq. (12), we can define corresponding resultant L-function along $\gamma(t_0, t)$ as

$$L(\mathbf{x}^*, t_0, t) = \sum_{i=1}^{m_0-1} [L^{(i)}(\mathbf{x}^*, t_{i-1}, t_i) + L_\Delta^{(i,i+1)}(\mathbf{x}^*, t_i)] + L^{(m_0)}(\mathbf{x}^*, t_{m_0-1}, t). \tag{20}$$

Note that each quantity increment of the equi-measuring function surface for a time interval or at certain switching moment are computed as Eqs. (18) and (19), together with the change of the measuring function Eq. (17) within sub-domain, Eq. (20) can be computed out and reduced into a simple form of

$$L(\mathbf{x}^*, t_0, t) = V(\mathbf{x}^{(m_0)}(t), \mathbf{x}^*) - V(\mathbf{x}_0, \mathbf{x}^*), \tag{21}$$

where $\mathbf{x}_0$ is the initial point, and $t \in (t_{m_0-1}, t_{m_0}), m_0 \in \{1, 2, ...\}$.

Take the above definitions as the basis, we will give definition of various stability for equilibrium of the switched dynamical system Eq. (9) as follows.

Definition 6 For switched dynamical system Eq. (9), the trivial solution $\mathbf{x}^*$ is said to be
(i) stable, if for every $\varepsilon > 0, t_0 \geq 0$, there exists a $\delta = \delta(t_0, \varepsilon) > 0$, such that for every resultant solution $\gamma(t_0, \mathbf{x}_0, t)$ of initial problem Eq. (9), $\|\mathbf{x}_0\| < \delta$ implies that $\|\gamma(t_0, \mathbf{x}_0, t)\| < \varepsilon$, when $t \geq t_0$;
(ii) uniformly stable, if δ in (i) is independent of t_0;
(iii) asymptotically stable, if for every $\varepsilon > 0, t_0 \geq 0$, there exists a $\eta = \eta(t_0) > 0$ and a moment $T = T(t_0, \varepsilon) > 0$, such that for every resultant solution $\gamma(t_0, \mathbf{x}_0, t)$ of

initial problem Eq. (9), $\|\mathbf{x}_0\| < \eta$ implies that $\|\gamma(t_0, \mathbf{x}_0, t)\| < \varepsilon$, when $t \geq t_0 + T$; (iv) uniformly asymptotically stable, if for every $\varepsilon > 0$, there is some $\eta > 0$, for $\forall t_0 \geq 0$, there exists a moment $T = T(\eta, \varepsilon) > 0$, such that for every resultant solution $\gamma(t_0, \mathbf{x}_0, t)$ of initial problem Eq. (9), $\|\mathbf{x}_0\| < \eta$ implies that $\|\gamma(t_0, \mathbf{x}_0, t)\| < \varepsilon$, when $t \geq t_0 + T$.

3.3 Stability Criteria

In this section, unlike the traditional Lyapunov stability condition, on account of the special properties of equi-measuring function surfaces and various metric functions, we will give the following theories to investigate the stability of discontinuous system Eq. (9).

Theorem 1 *For switched dynamical system Eq. (9) with impulsive effect on domain* $\Omega = (\bigcup_{i=1}^{m} \Omega_i) \cup (\bigcup_{j=1}^{N} \partial\Omega_j)$, *consider the i-th dynamical subsystem* Ω_i *with vector field* $\mathbf{F}^{(i)}(t, \mathbf{x}^{(i)})$ *in Eq. (6), and the resultant flow* $\gamma(t_0, t)$ *in Eq. (12). If the measuring function* $V(\mathbf{x}, \mathbf{x}^*)$ *in Eq. (14) monotonically increases with the relative displacement function* $d(\mathbf{x}, \mathbf{x}^*)$ *in Eq. (13), and for any time* $t \geq t_0$, *the following conditions are satisfied,*
(C_1) *for intra-flow* $\mathbf{x}^{(k)} \in \gamma^{(k)}(t_{k-1}, t_k)$ *with* $t \in [t_{k-1}, t_k]$,

$$G_v(\mathbf{x}^{(k)}, \mathbf{x}^*, t) = [\mathbf{n}_v(\mathbf{x}^{(k)}, \mathbf{x}^*)]^{\mathrm{T}} \cdot \mathbf{F}^{(k)}(t, \mathbf{x}^{(k)}) < 0,$$

and
(C_2) *for transport law from intra-flow* $\mathbf{x}^{(k)}$ *to* $\mathbf{x}^{(k+1)}$ *at switching moment* $t = t_k$,

$$L_{\Delta}^{(k,k+1)}(\mathbf{x}^*, t_k) \leq 0,$$

where $k = 1, 2, ..., m$.
Then the trivial solution $\mathbf{x}^*$ *of Eq. (9) is uniformly asymptotically stable.*

Proof Suppose the resultant solution of Eq. (9) starting from $(t_0, \mathbf{x}_0)$ is denoted as $\gamma(t_0, \mathbf{x}_0, t)$ for $t \geq t_0$. For an arbitrary $\varepsilon > 0$, suppose that $\varepsilon < a_0$, where a_0 is a certain small positive number. In virtue of the condition that the measuring function in Eq. (14) monotonically increases with the relative displacement function in Eq. (13), it is obvious that,

$$V(\mathbf{x}, \mathbf{x}^*) = \min, \text{ if } d(\mathbf{x}, \mathbf{x}^*) = 0.$$

Without loss of generality, denote $l = \min_{\varepsilon \leq d(\mathbf{x}, \mathbf{x}^*) \leq a_0} V(\mathbf{x}, \mathbf{x}^*)$, which is a positive number.

Consider condition (C_1), for the resultant solution $\gamma(t_0, \mathbf{x}_0, t)(t \in (t_{m_0-1}, t_{m_0})$, $m_0 \in \{1, 2, ..., m\})$, we can find a positive number M small enough, satisfying

$$G_v(\gamma(t_0, \mathbf{x}_0, t), \mathbf{x}^*, t) \leq -M < 0.$$

By integration term by term, and together with condition (C_2), according to Eqs. (16), (17) and (19), it gives

$$
\begin{aligned}
&V(\gamma(t_0, \mathbf{x}_0, t), \mathbf{x}^*) - V(\mathbf{x}_0, \mathbf{x}^*) \\
&= L(\mathbf{x}^*, t_0, t) \\
&= \sum_{i=1}^{m_0-1}[L^{(i)}(\mathbf{x}^*, t_{i-1}, t_i) + L_\Delta^{(i,i+1)}(\mathbf{x}^*, t_i)] + L^{(m_0)}(\mathbf{x}^*, t_{m_0-1}, t) \\
&= \sum_{i=1}^{m_0-1}[\int_{t_{i-1}}^{t_i} G_v(\mathbf{x}^{(i)}, \mathbf{x}^*, t)dt] + \int_{t_{m_0}}^{t} G_v(\mathbf{x}^{(m_0)}, \mathbf{x}^*, t)dt \\
&\quad + \sum_{i=1}^{m_0-1}[L_\Delta^{(i,i+1)}(\mathbf{x}^*, t_i)] \\
&\leq -M(t - t_0).
\end{aligned}
$$

On the other hand, there exists a certain positive number $\eta > 0$, when $\|\mathbf{x}_0\| < \eta$, it gives

$$V(\mathbf{x}_0, \mathbf{x}^*) < V(\eta, \mathbf{x}^*),$$

in virtue of the condition that the measuring function is monotonically increasing with the relative displacement function.

Therefore, taking $T = \frac{1}{M}[V(\eta, \mathbf{x}^*) - l]$, it is obtained for $t \geq t_0 + T$ that,

$$V(\gamma(t_0, \mathbf{x}_0, t), \mathbf{x}^*) < l = \min_{\varepsilon \leq d(\mathbf{x}, \mathbf{x}^*) \leq a_0} V(\mathbf{x}, \mathbf{x}^*),$$

which implies

$$\|\gamma(t_0, \mathbf{x}_0, t)\| < \varepsilon,$$

and finally leads to the completion of proof.

Theorem 2 *For switched dynamical system Eq. (9) with impulsive effect, under the same notation of Theorem 1. If the measuring function $V(\mathbf{x}, \mathbf{x}^*)$ in Eq. (14) is minimum when $d(\mathbf{x}, \mathbf{x}^*) = 0$ in Eq. (13), and for any time $t \geq t_0$, (C_2) is kept while (C_1) is replaced by*
(C_1') for intra-flow $\mathbf{x}^{(k)} \in \gamma^{(k)}(t_{k-1}, t_k)$ with $t \in [t_{k-1}, t_k]$,

$$G_v(\mathbf{x}^{(k)}, \mathbf{x}^*, t) = [\mathbf{n}_v(\mathbf{x}^{(k)}, \mathbf{x}^*)]^\mathrm{T} \cdot \mathbf{F}^{(k)}(t, \mathbf{x}^{(k)}) \leq 0,$$

where $k = 1, 2, ..., m$.
Then the trivial solution $\mathbf{x}^*$ of Eq. (9) is uniformly stable.

Proof Suppose the solution of Eq. (9) starting from $(t_0, \mathbf{x}_0)$ is denoted as $\gamma(t_0, \mathbf{x}_0, t)$ for $t \geq t_0$. For an arbitrary $\varepsilon > 0$, suppose that $\varepsilon < a_0$, where a_0 is a certain small positive number. In virtue of the condition that the measuring function $V(\mathbf{x}, \mathbf{x}^*)$ in Eq. (14) is minimum when $d(\mathbf{x}, \mathbf{x}^*) = 0$, in the bounded closed set $[\varepsilon, a_0]$, denote

$$l = \min_{\varepsilon \leq d(\mathbf{x}, \mathbf{x}^*) \leq a_0} V(\mathbf{x}, \mathbf{x}^*) > 0, \tag{22}$$

therefore, for the positive number $l > 0$, there exists a certain positive number $\delta > 0$, when $\|\mathbf{x}\| < \delta$, it gives

$$V(\mathbf{x}, \mathbf{x}^*) < \frac{l}{2}. \tag{23}$$

Next, we will show that for every resultant solution $\gamma(t_0, \mathbf{x}_0, t)$ of initial problem Eq. (9), once the condition $\|\mathbf{x}_0\| < \delta$ was satisfied, it would be implied that

$$\|\gamma(t_0, \mathbf{x}_0, t)\| < \varepsilon,$$

for $t \geq t_0$.

Or else, assume there exists a resultant solution $\gamma(t_0, \mathbf{x}_0, t)$ of Eq. (9) satisfying the initial condition $\|\mathbf{x}_0\| < \delta$, and there exists a moment $t_1 > t_0$, which is not a switching moment, such that

$$\|\gamma(t_0, \mathbf{x}_0, t)\| < \varepsilon,$$

for $t \in [t_0, t_1)$, but

$$\|\gamma(t_0, \mathbf{x}_0, t_1)\| = \varepsilon. \tag{24}$$

Suppose the moment t_1 satisfies $t_{m_1-1} < t_1 < t_{m_1}$ for a certain $m_1 \in \{1, 2, ..., m\}$, and for the measuring function $V(\mathbf{x}, \mathbf{x}^*)$, make integration from t_0 to t_1 for every intervals. According to Eqs. (16), (17) and (19), together with (C_1') and (C_2), it gives

$$
\begin{aligned}
&V(\gamma(t_0, \mathbf{x}_0, t_1), \mathbf{x}^*) - V(\mathbf{x}_0, \mathbf{x}^*) \\
&= L(\mathbf{x}^*, t_0, t_1) \\
&= \sum_{i=1}^{m_1-1}[L^{(i)}(\mathbf{x}^*, t_{i-1}, t_i) + L_\Delta^{(i,i+1)}(\mathbf{x}^*, t_i)] + L^{(m_1)}(\mathbf{x}^*, t_{m_1-1}, t_1) \\
&= \sum_{i=1}^{m_1-1}[\int_{t_{i-1}}^{t_i} G_v(\mathbf{x}^{(i)}, \mathbf{x}^*, t)dt] + \int_{t_{m_1}}^{t} G_v(\mathbf{x}^{(m_1)}, \mathbf{x}^*, t)dt \\
&+ \sum_{i=1}^{m_1-1}[L_\Delta^{(i,i+1)}(\mathbf{x}^*, t_i)] \\
&\leq 0,
\end{aligned}
$$

i.e.,

$$V(\gamma(t_0, \mathbf{x}_0, t_1), \mathbf{x}^*) \leq V(\mathbf{x}_0, \mathbf{x}^*). \tag{25}$$

Therefore, as $\|\mathbf{x}_0\| < \delta$, in virtue of the relation of Eq. (23), it is obtained that

$$V(\mathbf{x}_0, \mathbf{x}^*) < \frac{l}{2}.$$

On the other hand, in Eq. (24), as $\|\gamma(t_0, \mathbf{x}_0, t_1)\| = \varepsilon$, which is consistent with the range for Eq. (22) of the minimum of the measuring function, together with Eq. (25), it is implied that

$$l \leq V(\gamma(t_0, \mathbf{x}_0, t_1), \mathbf{x}^*) \leq V(\mathbf{x}_0, \mathbf{x}^*) < \frac{l}{2},$$

which comes to a contradiction against the positive number and the proof is completed.

Theorem 3 *Under the same assumptions of Theorem 1, if the measuring function $V(\boldsymbol{x}, \boldsymbol{x}^*)$ in Eq. (14) monotonically increases with the relative displacement function $d(\boldsymbol{x}, \boldsymbol{x}^*)$ in Eq. (13), and (C_1) and (C_2) are replaced by*

(C_3) for global resultant solution $\gamma(t_0, \boldsymbol{x}_0, t)$ in domain $\Omega = \bigcup\limits_{i=1}^{m^*} \Omega_i, t \in (t_{m^*-1}, t_{m^*}),$ $m^* \in \{1, 2, ...\},$

$$L(\boldsymbol{x}^*, t_0, t) \leq V_{min} - V(\boldsymbol{x}_0, \boldsymbol{x}^*),$$

where V_{min} is the minimum of the measuring function, and $(t_0, \boldsymbol{x}_0)$ is the initial point of Eq. (9).

Then the trivial solution $\boldsymbol{x}^*$ of Eq. (9) is uniformly stable.

Proof For the resultant solution $\gamma(t_0, \mathbf{x}_0, t)$ and an arbitrary $\varepsilon > 0$, take $\delta = \frac{\varepsilon}{2} > 0$. In virtue of the condition that the measuring function in Eq. (14) monotonically increases with the relative displacement function, when initial condition $\|\mathbf{x}_0\| < \delta$ is satisfied, we can get

$$V(\mathbf{x}_0, \mathbf{x}^*) < V(\delta, \mathbf{x}^*). \tag{26}$$

As V_{min} is the minimum of the measuring function, when $\|\mathbf{x}_0\| < \delta$, it is obvious that

$$V(\mathbf{x}_0, \mathbf{x}^*) \geq V_{min}. \tag{27}$$

On the other hand, based on (C_3) and the former equivalent form of corresponding resultant L-function Eq. (21) along $\gamma(t_0, \mathbf{x}_0, t)$ in domain $\Omega = \bigcup\limits_{i=1}^{m^*} \Omega_i$ for $t \in (t_{m^*-1}, t_{m^*}), \ m^* \in \{1, 2, ...\}$, it implies that

$$V(\gamma^{(m^*)}(t_{m^*-1}, t), \mathbf{x}^*) - V(\mathbf{x}_0, \mathbf{x}^*) \leq V_{min} - V(\mathbf{x}_0, \mathbf{x}^*),$$

in which $\gamma^{(m^*)}(t_{m^*-1}, t) \subset \gamma(t_0, \mathbf{x}_0, t)$ is the last portion of the resultant flow in Ω_{m^*}, according to the definition in Eq. (12).

Together with Eqs. (26) and (27), it gives that

$$V(\gamma^{(m^*)}(t_{m^*-1}, t), \mathbf{x}^*) \leq V(\delta, \mathbf{x}^*).$$

Take the condition of the monotonicity of the measuring function and the value of $\delta = \frac{\varepsilon}{2}$ into account, the above relation gives

$$\|\gamma^{(m^*)}(t_{m^*-1}, t)\| < \frac{\varepsilon}{2},$$

for $t \in (t_{m^*-1}, t_{m^*})$, $m^* \in \{1, 2, ...\}$, that is,

$$\|\gamma(t_0, \mathbf{x}_0, t)\| < \frac{\varepsilon}{2},$$

which finally leads to the completion of proof.

Remark 2 Based on the resultant L-function along the resultant solution $\gamma(t_0, \mathbf{x}_0, t)$, we can get a stability criterion with weaker conditions than Theorems 1 and 2 with metric G-function and several quantity increment functions, which are all more simplified than traditional Lyapunov stability criteria requiring rigorous global conditions.

Next, we will present another benefit of the resultant L-function $L(\mathbf{x}^*, t_0, t)$ of the resultant solution in investigating periodic dynamics as follows.

Corollary 1 *For switched dynamical system Eq. (9) with impulsive effect on domain* $\Omega = (\bigcup\limits_{i=1}^{m} \Omega_i) \cup (\bigcup\limits_{j=1}^{N} \partial\Omega_j)$, *if there is a periodic motion with period of T_0 in the vicinity of equilibrium $\mathbf{x}^*$, then the resultant L-function $L(\mathbf{x}^*, t_0, t_0 + T_0) = 0$.*

Here, we omit the proof of this corollary, which can be found out in our periodic work.

4 Applications

In this section, the stability criteria will be applied in a practical problem with a specific impulsive model at fixed points, and the analytical prediction for equilibrium and periodic motions will be illustrated.

In the first place, we consider the van der Pol oscillation Eq. (9) which is subdued to specific impulse functions modeled by the Newton's law of restitution, and take $f(x) = 1$ as a specific damping item. As a special case of the single freedom vibration system, its vector form is given as follows

$$\begin{cases} \dot{\mathbf{x}} = \mathbf{F}(t, \mathbf{x}), & t \neq t_k, \\ \mathbf{x}(t^+) = \mathbf{h}(\mathbf{x}(t)), & t = t_k, \end{cases} \tag{28}$$

where $t_k (k \in Z)$ are impulse moments, $\mathbf{x} = (x_1, x_2)^T \in \Omega \subset (R \times R)$ with $x_1 = x$ and $x_2 = x'$, the vector function $\mathbf{F} = (x_2, \mu x_2 - p_0^2 x_1)^T$ and $\mathbf{h} = (e_1 x_1, e_2 x_2)^T$, and it is obvious that the trivial solution $\mathbf{x}^*$ is its equilibrium.

Note that the general solution of the differential equation without impulse effect in Eq. (28) is given by

$$x(t) = e^{\frac{\mu}{2}t}\left(C_1\sin(\frac{\sqrt{4p_0^2 - \mu^2}}{2}t) + C_2\cos(\frac{\sqrt{4p_0^2 - \mu^2}}{2}t)\right), \qquad (29)$$

where the integral constants $C_i (i = 1, 2)$ depend on initial conditions.

And for the particular solution of initial problem, for simplicity, suppose the first impact occurs at $t_0 = kT$ ($k \in Z$), in which T is the period of the pulse controller. Suppose (t_0, x_0, x_0') is some point on a certain switching boundary. By integration for the continuous part, a particular solution for Eq. (28) with the initial condition $(t_0, x_0^+, x_0'^+)$, where $x(t_0^+) = x_0^+$, $x'(t_0^+) = x_0'^+$, is given as

$$x(t, x_0^+, x_0'^+, t_0) = e^{\frac{\mu}{2}(t-t_0)}\{\frac{2}{\sqrt{4p_0^2 - \mu^2}}\sin(\frac{\sqrt{4p_0^2-\mu^2}}{2}(t - t_0))x_0'^+$$
$$+ \left[\frac{-\mu}{\sqrt{4p_0^2-\mu^2}}\sin(\frac{\sqrt{4p_0^2-\mu^2}}{2}(t - t_0)) + \cos(\frac{\sqrt{4p_0^2-\mu^2}}{2}(t - t_0))\right]x_0^+\}, \qquad (30)$$

in which $C_1 = \frac{2x_0'}{\sqrt{4p_0^2-\mu^2}}$, $C_2 = 0$, and most important, $t \in (t_0, t_0 + T]$ represents the continuous motion within one sub-domain. And the derivative gives as

$$x'(t, x_0^+, x_0'^+, t_0) = e^{\frac{\mu}{2}(t-t_0)}\{\left[\frac{\mu}{\sqrt{4p_0^2-\mu^2}}\sin(\frac{\sqrt{4p_0^2-\mu^2}}{2}(t - t_0)) + \cos(\frac{\sqrt{4p_0^2-\mu^2}}{2}(t - t_0))\right]x_0'^+$$
$$- \frac{2p_0^2}{\sqrt{4p_0^2-\mu^2}}\sin(\frac{\sqrt{4p_0^2-\mu^2}}{2}(t - t_0))x_0^+\}, \qquad (31)$$

where $t \in (t_0, t_0 + T]$ as well.

As discussed in Sect. 3, take $V(\mathbf{x}, \mathbf{x}^*) = V(d(\mathbf{x}, \mathbf{x}^*)) = d^2 = x_1^2 + x_2^2$ as the measuring function, and the normal vector of the equi-measuring function surface is expressed by

$$\mathbf{n}_v(\mathbf{x}, \mathbf{x}^*) = \nabla V(\mathbf{x}, \mathbf{x}^*)$$
$$= \frac{\partial V(\mathbf{x},\mathbf{x}^*)}{\partial \mathbf{x}}$$
$$= (\frac{\partial V(\mathbf{x},\mathbf{x}^*)}{\partial x_1}, \frac{\partial V(\mathbf{x},\mathbf{x}^*)}{\partial x_2})^{\mathrm{T}}$$
$$= (2x_1, 2x_2)^{\mathrm{T}}.$$

Therefore, suppose such intra-flow for $t \in (t_0, t_0 + T]$ is kept in sub-domain Ω_{i_0}, according to the definition of the metric G-function at the constant measuring function level about $\mathbf{x}^*$ and the component of Eq. (28) in Ω_{i_0}, Eq. (16) gives

$$G_v(\mathbf{x}^{(i_0)}, \mathbf{x}^*, t) = [\mathbf{n}_v(\mathbf{x}^{(i_0)}, \mathbf{x}^*)]^{\mathrm{T}} \cdot \mathbf{F}^{(i_0)}(t, \mathbf{x}^{(i_0)})$$
$$= 2(1 - p_0^2)x_1x_2 + 2\mu x_2^2. \qquad (32)$$
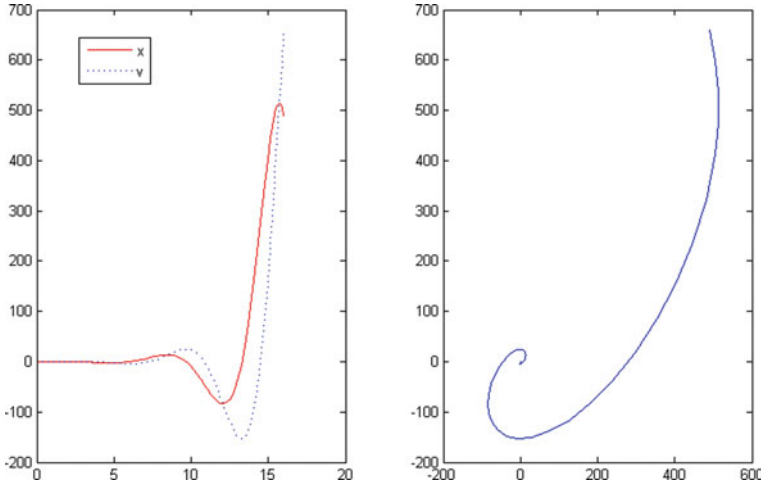
Fig. 2 The original continuous motion for an intra-flow for Eq. (28) without the impulsive effect with certain parameters showing instability of equilibrium

With the application of theorems in Sect. 3, we can get the critical parameters of μ for stability of equilibrium with Eq. (32), that is, $\mu \in (0, \mu_S(p_0))$ where $\mu_S(p_0) = \frac{x_0}{x_0'}(1 - p_0^2)$. Actually, when we portray the original curve of Eqs. (29)–(31), certain parameters and initial conditions will show instability phenomena after some time scale as shown in Fig. 2. Consider following parameters for numerical illustrations of the original continuous motion for Eq. (28) without the effect of impulse with $t_f = 16.100$, and

$$\mu = 1.001, \ p_0 = 1.118, \ t_0 = 0, \ x_0 = 0.200, \ x_0' = 0.002,$$

where the initial condition $(0.200, 0.002)$ and $\mu > \mu_S(p_0)$ indicate the increase of amplification and final instability of equilibrium after certain time scale, which conform to the results in Sect. 3. The solid and dashed curves in the left figure represent the original continuous oscillation response x and its derivative, respectively; and the phase diagram for the original trajectory is shown on the right with a smooth border but an unstable tendency after certain time scale.

By contrast, consider the effect of impulse when pulse controller works as we have presented in [10] and a global specific periodic motion can be obtained by taking appropriate initial conditions and coefficients of restitution. Choose $T = \frac{4\pi}{\sqrt{4p_0^2 - \mu^2}}$ such that once the intra-flow comes to the boundary, a modified state will be guaranteed, extending to a global piecewise motion as Fig. 3 shown with initial conditions and parameters as

$$x_0 = 1.000, \ x_0' = 0.100, \ e_1 = 0.990, \ e_2 = 1.730, \ T = 6.283, \ t_f = 29.050.$$
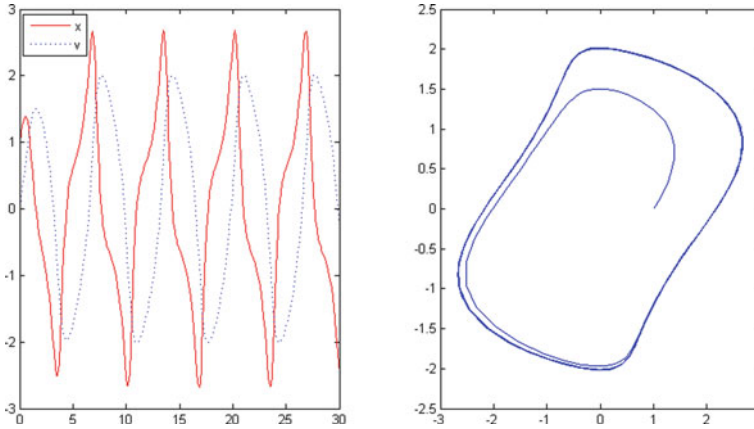
Fig. 3 Optimized motion of solution for Eq. (28) showing periodic oscillation response to the stimulation of impulse

As the optimized curve shown in Fig. 3, it is because at those switching moments the pulse controller works with impulse functions generating sinusoidal signals to the system, we can easily observe a periodic motion but a sightly abrupt decrease when the oscillator reaches limits for switching. Meanwhile, the equilibrium still shows instability because of the value of μ.

Besides, once the intra-flow comes to the boundary $\partial\Omega_{i_0+1}$, the quantity increment of the equi-measuring function surface at time $t = t_{i_0}$ according to transport law Eq. (19) and the impulse functions in Eq. (28) is given by

$$L_{\Delta}^{(i_0,i_0+1)}(\mathbf{x}^*, t_{i_0}) = V(\mathbf{x}^{(i_0+1)}(t_{i_0}^+), \mathbf{x}^*) - V(\mathbf{x}^{(i_0)}(t_{i_0}), \mathbf{x}^*)$$
$$= (e_1^2 - 1)x_1^2 + (e_2^2 - 1)x_2^2,$$

satisfying $L_{\Delta}^{(i_0,i_0+1)}(\mathbf{x}^*, t_{i_0}) = 0$ when the above initial conditions and coefficients of restitution are taken, which conforms to the corollary in Sect. 3.

5   Conclusions

The dynamics of a kind of van der Pol equation with impulsive effect are investigated. For the equation with interrupted state, due to the changes of characters brought by discontinuity, we take a different approach to its dynamical analysis and utilize the flow theory in discontinuous dynamical systems. Viewing the hybrid system as a global one consisting of every subsystem in each sub-domains, we focus on the local singularity of the switched system. Especially by constructing various metric functions, stability criteria of equilibrium are discussed. Different from the traditional geometric theory for continuous van der Pol equation, local properties governed by

transport law near the time-varying boundaries are investigated by metric G-function, L-function, etc., without considering the global rigorous conditions of Lyapunov stability criteria. The results are more general than the previous work especially when impulse occurs. We also find that it is beneficial for periodic motion research to utilize metric functions. Applying the analysis and criteria to a specific impulsive model, different motions as well as the periodic oscillation under the stimulation of impulse are illustrated as well. More complex motions and systematic qualitative work of the switched van der Pol equation, as well as bifurcations are investigated at present and will be reported in the future.

References

1. Teschl Gerald (2011) Ordinary differential equations and dynamical systems. American Mathematical Society, Providence, Rhode Island
2. Stoker JJ (1950) Nonlinear vibrations. Interscience Publishers, New York
3. Wang HQ (1992) Nonlinear vibrations. Higher Education Press, Beijing
4. van der Pol B (1920) A theory of the amplitude of free and forced triode vibrations. Radio Review, 1: 701–710, 754–762
5. van der Pol B (1927) Forced oscillations in a circuit with non-linear resistance (reception with reactive triode). The London, Edinburgh, and Dublin Philos Mag J Sci Ser 7, 3:65–80
6. van der Pol B, van der Mark J (1928) The heartbeat considered as a relaxation oscillation, and an electrical model of the heart. The London, Edinburgh, Dublin Philos Mag J Sci Ser 7, 6:763–775
7. Flaherty JE, Hoppensteadt FC (1978) Frequency entrainment of a forced van der Pol oscillator. Stud Appl Math 58:5–15
8. Levi M (1981) Qualitative analysis of the periodically forced relaxation oscillations. Mem Amer Math Soc 32(244)
9. Guckenheimer J, Holmes P (1983) Nonlinear oscillations, dynamical systems, and bifurcations of vector fields. Springer-Verlag, New York
10. Fu XL, Zheng SS (2014) Chatter dynamic analysis for van der Pol Equation with impulsive effect via the theory of flow switchability. Commun Nonlinear Sci Numer Simul 19:3023–3035
11. Filippov AF (1988) Differential equations with discontinuous righthand sides. Kluwer Academic Publishers, Dordrecht
12. Luo ACJ (2005) A theory for non-smooth dynamical systems on connectable domains. Commun. Nonlinear Sci Numer Simul 10:1–55
13. Luo ACJ (2008) Global transversality, resonance and chaotic dynamics. World Scientific Publishing Company
14. Luo ACJ (2009) Discontinuous dynamical systems on time-varying domains. Higher Education Press, Beijing
15. Luo ACJ (2012) Discontinuous dynamical systems. Higher Education Press, Beijing
16. Zheng SS, Fu XL (2015) Periodic motion of the van der Pol equation with impulsive effect. Int J Bifurc Chaos 25(9):1550119
17. Lakshmikantham V, Bainov DD, Simeonov PS (1989) Theory of impulsive differential equations. World Scientific, Singapore

18. Fu XL, Yan BQ, Liu YS (2005) Introduction of impulsive differential systems. Science Press, Beijing
19. Benchohra M, Henderson J, Ntouyas S (2006) Impulsive differential equations and inclusions. vol.2 of Contemporary Mathematics and Its Applications. Hindawi Publishing Corporation, New York
20. Zheng SS, Fu XL (2013) Pulse phenomena for impulsive dynamical systems. Discontin Nonlinearity Complex 2(3):225–245
21. Zheng SS, Fu XL (2013) Chatter dynamics on impulse surfaces in impulsive differential systems. J Appl Nonlinear Dyn 2(4):373–396
22. Taylor F (1907) On the art of cutting metals. Trans ASME 28
23. Shaw SW, Holmes PJ (1983) A periodically forced piecewise linear oscillator. J Sound Vib 90(1):129–155
24. Fu XL, Zheng SS (2014) New approach in dynamics of regenerative chatter research of turning. Commun Nonlinear Sci Numer Simul 19:4013–4023
25. Zheng SS, Fu XL (2015) Chatter dynamic analysis for a planing model with the effect of pulse. J Appl Anal Comput 5(4):767–780
26. Luo ACJ (2012) Discrete and switching dynamical systems. Beijing, Higher Education Press
27. Zhai HM, Ding Q (2013) Stability and nonlinear dynamics of a vibration system with oblique collisions. J Sound Vib 332:3015–3031
28. Akhmet M, Turan M (2013) Bifurcation of discontinuous limit cycles of the van der Pol equation. Math Comput Simul 95:39–54

Complex Motions in an Inclined Impact Pair with a Periodic Excitation

Xilin Fu and Yanyan Zhang

Abstract Using the flow switchability theory of the discontinuous dynamical systems, the complex dynamics of an inclined impact oscillator under periodic excitation are investigated in this chapter. According to impact discontinuity different domains and boundaries are defined. And then the occurrence and vanishing conditions of stick motions and grazing motions are obtained analytically. Furthermore the generic mapping structure of periodic motions are given, and the existence conditions of two periodic motions without stick are investigated in detailed.

1   Introduction

The complex dynamics of the discontinuous dynamical systems have been drawing many researchers' attentions, among them complicated dynamical behaviors of vibro-impact systems are one of foci, because impact is one of two basic forms of interaction between two or more moving parts in mechanical engineering.

In 1966, Masri and Caughey [1] investigated the theoretical exact solutions of symmetric two-impact-per-cycle periodic motion in a horizontal impact damper, and obtained their asymptotically stable regions. Bapat et al. [2, 3] investigated an impact pair under periodical excitation by experimental observations and theoretical analysis, periodic motions were analytically predicted using the closed form solution, and verified that the effect of small higher frequency components on the periodic motion were negligible. Shaw and Holmes [4] studied periodic motions and chaotic motions of a single-degree-of-freedom piecewise linear oscillator by digital simulation. Luo and coworkers [5, 6] studied periodic motion and their period-doubling bifurcations in a horizontal impact pair under sinusoidally periodic excitation, obtained existence conditions and stability results analytically and numerically. The analytical conditions for stick motions and grazing motions of such pair were investigated by the theory of flow switchability for the discontinuous dynamical systems in Guo and Luo [7] and Luo and Guo [8], the generic mapping structure of period motions

X. Fu (✉) · Y. Zhang
Shandong Normal University, 88, East Wenhua Road, Ji'nan, China
e-mail: yanrzhang@sdnu.edu.cn

were obtained. Yue [9] studied dynamical behaviors of a symmetric impact oscillator between two rigid stops, stability and bifurcations of the symmetric periodic motion were obtained using symmetric Poincaré map. Wen et al. [10] used the spectrum of the largest Lyapunov exponent in parameter plane to investigate a peculiar discontinuous bifurcation phenomenon derived from grazing bifurcation. The above discussions investigated intensively dynamical behaviors of the horizontal impact systems, however the bouncing ball, whose dynamics were influenced by gravity, were also one of the studied foci. In 1982, Holmes [11] investigated the dynamical behavior of a ball bouncing vertically on a periodically vibrating table using a difference equation derived. Furthermore, Luo and Han [12] predicted stability and bifurcation of periodic motions for such bouncing ball using differential equations derived, and the analytical predictions for stick motions and grazing motions were developed in Guo and Luo [13] and Luo and Guo [8], periodic motions with or without stick were also studied by mapping dynamics of the discontinuous dynamical systems. In Luo and Guo [8], the complex dynamics of a generalized Fermi acceleration oscillator were also studied. Using Poincaré maps, Okniński and Radziszewski [14, 15] investigated dynamics of a bouncing ball colliding with a table movingly under different periodical excitation by analytical and numerical investigation. Based on Peterka's approach, the stable periodic solutions of a cantilever beam model with a mass impacting against a harmonically moving frame were investigated analytically and numerically in Czolczynski et al. [16]. The inclined impact oscillators, which affected by gravity and inclination, had more rich and complicated dynamical behaviors, however there were less paper to study it. Bapat [17] investigated the dynamical motions of an inclined impact damper with friction under sinusoidal force theoretically and numerically. Heiman et al. [18, 19] investigated periodic motions with one, two, three impacts per cycle and their bifurcations in an inclined impact pair under horizontal periodic excitation using Poincaré maps, and digital simulations in the forms of stability plots were given to illustrate theoretical results. The periodic motions with two alternative impacts per cycle in such pair were investigated using the discrete maps theory of discontinuous dynamical systems in Zhang and Fu [20], the period-n motions after period-doubling of periodic motions with two alternative impacts per cycle are investigated in Zhang and Fu [21], the analytical prediction for these periodic motions were obtained.

   The results aforementioned on the inclined impact pair paid less attentions to the motion switchability, stick motions and grazing motions. This paper is to give analytical conditions of stick motions and grazing motions in such inclined impact pair with periodical excitation using the flow switchability theory of the discontinuous dynamical systems in Fu and Zhang [22], and on this basis the generalized mapping structure of periodic motion with or without stick will be obtained, finally the existence conditions of two specific periodic motions with impacts only on one side of the inclined slot are to be presented. About such oscillator, more detailed stability and bifurcation trees or parameter maps are being discussed.

2 Physical Model

An inclined impact pair is shown in Fig. 1, which consists of a base with mass M and a ball with mass m. An inclined rectangular slot is in the base, which has inclined angle θ and length d, and the ball moves freely without friction in such clearance. The base is driven under periodical displacement excitation $X(t) = A \sin(\omega t + \tau)$ in the horizontal direction, where A, ω and τ are excitation amplitude, excitation frequency and phase angle of the base, respectively. When the ball reaches the side of the slot, impact between the ball and the base can occur, so the impact restitution coefficient e ($0 < e < 1$) is supposed. Assume $m \ll M$, the repeated impacts can not change the motion of the base. The origin of the absolute coordinates is set at the middle point of the clearance while the base is at the equilibrium position. For the ball, (x, t) is its absolute displacement, and (y, t) is its relative displacement to the base, that is $y = x - X \cos\theta$.

   The motions of the ball in such pair can be divided into two cases, one is non-stick motion or free-flight motion, another is stick motion. Non-stick motion is the motion that the ball moves freely between two sides of the slot and does not move together with the base. In such case, the equation of the motion for the ball is described as

$$\ddot{x} = -g \sin\theta, \tag{1}$$

where g is the gravitational acceleration. At the same time the motion of the base remains

$$\ddot{X} = -A\omega^2 \sin(\omega t + \tau). \tag{2}$$

From (1) and (2), for $t \in (t_k, t_{k+1})$ we have

$$
\begin{aligned}
x &= -\tfrac{1}{2}g \sin\theta (t^2 - t_k^2) + (g \sin\theta t_k + \dot{x}^+(t_k))(t - t_k) + x^+(t_k), \\
\dot{x} &= -g \sin\theta (t - t_k) + \dot{x}^+(t_k),
\end{aligned} \tag{3}
$$

or

Fig. 1 Physical model of the inclined impact pair

$$X(t) = A\sin(\omega t + \tau)$$
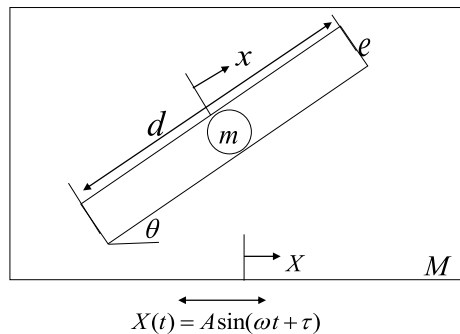
$$y = -A\cos\theta[\sin(\omega t + \tau) - \sin(\omega t_k + \tau)] - \tfrac{1}{2}g\sin\theta(t^2 - t_k^2)$$
$$+(\dot{y}_k + g\sin\theta t_k + A\omega\cos\theta\cos(\omega t_k + \tau))(t - t_k) + y_k^+, \qquad (4)$$
$$\dot{y} = -A\omega\cos\theta[\cos(\omega t + \tau) - \cos(\omega t_k + \tau)] - g\sin\theta(t - t_k) + \dot{y}_k^+,$$

where $()^+$ shows the state immediately after an impact, $x^+(t_k)$ and $\dot{x}^+(t_k)$ are absolute displacement and velocity of the ball, $y^+(t_k)$ and $\dot{y}^+(t_k)$ are relative displacement and velocity of the ball to the base.

According to the conservation law of momentum and $m \ll M$, the impact process between the ball and the frame is described as

$$x^+ = x^-, \quad X^+ = X^-, \quad |x^+ - X^+\cos\theta| = d/2;$$
$$\dot{X}^+ = \dot{X}^-, \quad \dot{x}^+ = [(m - Me)\dot{x}^- + M(1 + e)\dot{X}^-\cos\theta]/(M + m),$$

or

$$y^+ = y^- = \pm\frac{d}{2}, \quad \dot{y}^+ = -e\dot{y}^-,$$

where $()^-$ denote the state before an impact.

The stick motion is the motion that the ball comes to one side of the slot and moves together with the base. Such motion of the ball can be shown as

$$\ddot{x} = -\frac{M}{M + m}A\omega^2\sin(\omega t + \tau)\cos\theta, \qquad (5)$$

and the equation of the motion for the base is

$$\ddot{X} = -\frac{M}{M + m}A\omega^2\sin(\omega t + \tau). \qquad (6)$$

3   Flow Switchability

Using the theory of flow switchability of the discontinuous dynamical systems, the switching complexity for the motions of the ball in such oscillator will be developed in this section.

3.1   Domains and Boundaries

Due to impacts between the ball and the base, domains and boundaries with or without stick in absolute coordinates are shown in Fig. 2 and Fig. 3, respectively.

For non-stick motion of the ball, domain Ω_0 is defined as

Fig. 2 Absolute domain and boundaries without stick
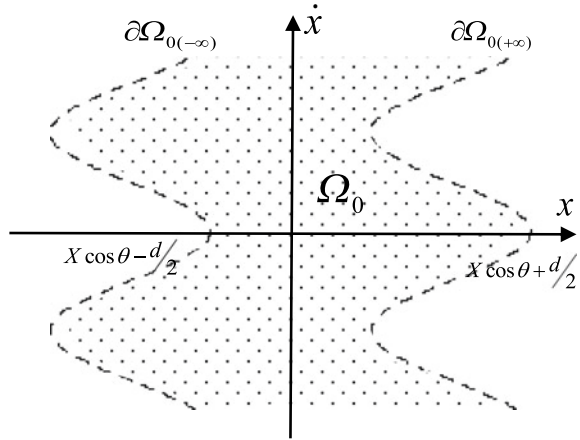
Fig. 3 Absolute domains and boundaries with stick
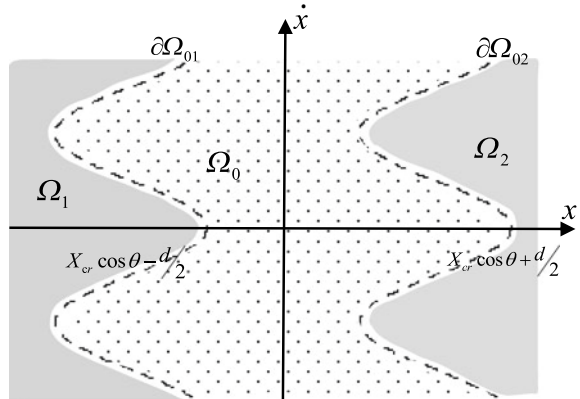
$$\Omega_0 = \{(x, \dot{x})|\ x \in (X \cos\theta - \frac{d}{2}, X \cos\theta + \frac{d}{2}),\ \dot{x} \in (-\infty, +\infty)\}.$$

The corresponding impact boundaries are defined as

$$\begin{aligned}
\partial\Omega_{0(+\infty)} &= \{(x, \dot{x})|\ \varphi_{0(+\infty)} \equiv x - X\cos\theta - d/2 = 0,\ \dot{x} \neq \dot{X}\cos\theta\}, \\
\partial\Omega_{0(-\infty)} &= \{(x, \dot{x})|\ \varphi_{0(-\infty)} \equiv x - X\cos\theta + d/2 = 0,\ \dot{x} \neq \dot{X}\cos\theta\},
\end{aligned} \tag{7}$$

where equation $\varphi_{\alpha\beta} = 0$ determines boundary $\partial\Omega_{\alpha\beta}$ in phase space. Herein $\alpha = 0$ and $\beta = \pm\infty$ represent the boundary, on which no flow in a subdomain can pass into another one without any transport law. The domain and boundaries for motions of the ball without stick are sketched in Fig. 2. Domain Ω_0 is represented by dotted area and impact boundaries $\partial\Omega_{0(+\infty)}$, $\partial\Omega_{0(-\infty)}$ are depicted by dashed curves.

The appearance and vanishing of stick motion will form new domains and boundaries. For stick motion of the ball, domains Ω_0 and Ω_1, Ω_2 are defined as

$$\Omega_0 = \{(x, \dot{x})|\ x \in (X_{cr} \cos\theta - d/2,\ X_{cr} \cos\theta + d/2),\ \dot{x} \neq \dot{X} \cos\theta\},$$
$$\Omega_1 = \{(x, \dot{x})|\ x \in (-\infty,\ X_{cr} \cos\theta - d/2),\ \dot{x} = \dot{X} \cos\theta,\ x = X \cos\theta - d/2\},$$
$$\Omega_2 = \{(x, \dot{x})|\ x \in (X_{cr} \cos\theta + d/2, +\infty),\ \dot{x} = \dot{X} \cos\theta,\ x = X \cos\theta + d/2\}.$$

$$(8)$$

The corresponding stick boundaries are defined as

$$\partial\Omega_{01} = \partial\Omega_{10} = \{(x, \dot{x})|\ \varphi_{10} \equiv x - X_{cr} \cos\theta + d/2 = 0,\ \dot{x} = \dot{X}_{cr} \cos\theta\},$$
$$\partial\Omega_{02} = \partial\Omega_{20} = \{(x, \dot{x})|\ \varphi_{20} \equiv x - X_{cr} \cos\theta - d/2 = 0,\ \dot{x} = \dot{X}_{cr} \cos\theta\},$$

$$(9)$$

where X_{cr} and $\dot{X}_{cr}$ represent the displacement and velocity of the base for appearance and vanishing of stick motion. As sketched in Fig. 3, domain Ω_0 is represented by dotted area, Ω_1, Ω_2 are represented by shaded regions, the corresponding stick boundaries $\partial\Omega_{01}$, $\partial\Omega_{02}$ are depicted by dashed curves.

Based on the above domains and boundaries, the equations of the motion for the ball in absolute coordinates is rewritten in vector form of

$$\dot{\mathbf{x}}_{(\lambda)} = \mathbf{f}_{(\lambda)}(\mathbf{x}_{(\lambda)}, t),\ \ \lambda = 0, 1, 2, \tag{10}$$

where $\mathbf{x}_{(\lambda)} = (x_{(\lambda)}, \dot{x}_{(\lambda)})^T$, $\mathbf{f}_{(\lambda)} = (\dot{x}_{(\lambda)}, f_{(\lambda)})^T$,
and for non-stick motion ($\lambda = 0$),

$$f_{(0)}(\mathbf{x}_{(0)}, t) = -g \sin\theta, \tag{11}$$

and for stick motion ($\lambda = 1, 2$),

$$f_{(\lambda)}(\mathbf{x}_{(\lambda)}, t) = -\frac{M}{M + m} A\omega^2 \sin(\omega t + \tau) \cos\theta. \tag{12}$$

The corresponding motion for the base in absolute coordinates are also revised in vector form of

$$\dot{\mathbf{X}}_{(\lambda)} = \mathbf{F}_{(\lambda)}(\mathbf{X}_{(\lambda)}, t), \lambda = 0, 1, 2,$$

where $\mathbf{X}_{(\lambda)} = (X_{(\lambda)}, \dot{X}_{(\lambda)})^T$, $\mathbf{F}_{(\lambda)} = (\dot{X}_{(\lambda)}, F_{(\lambda)})^T$, and

$$F_{(0)}(\mathbf{X}_{(0)}, t) = -A\omega^2 \sin(\omega t + \tau),\ \ F_{(\lambda)}(\mathbf{X}_{(\lambda)}, t) = -\frac{M}{M + m} A\omega^2 \sin(\omega t + \tau).$$

Developing analytical switching conditions in absolute coordinates is more difficult because the discontinuous boundaries in absolute coordinates are time-varying, however in relative coordinates, such problem can become simpler.

Relative domains Ω_0 and Ω_1, Ω_2 for the motions of the ball are defined as

$$
\begin{aligned}
\Omega_0 &= \{(y, \dot{y})|\ y \in (-d/2, +d/2),\ \dot{y} \in (-\infty, +\infty)\}, \\
\Omega_1 &= \{(y, \dot{y})|\ y = -d/2,\ \dot{y} = 0\}, \\
\Omega_2 &= \{(y, \dot{y})|\ y = +d/2,\ \dot{y} = 0\}.
\end{aligned}
\tag{13}
$$

Relative impact boundaries $\partial\Omega_{0(+\infty)}$, $\partial\Omega_{0(-\infty)}$ are defined as

$$
\begin{aligned}
\partial\Omega_{0(+\infty)} &= \{(y, \dot{y})|\ \varphi_{0(+\infty)} \equiv y - d/2 = 0,\ \dot{y} \neq 0\}, \\
\partial\Omega_{0(-\infty)} &= \{(y, \dot{y})|\ \varphi_{0(-\infty)} \equiv y + d/2 = 0,\ \dot{y} \neq 0\},
\end{aligned}
\tag{14}
$$

and relative stick boundaries $\partial\Omega_{0i}$, $\partial\Omega_{i0}$ $(i = 1, 2)$ are determined by

$$
\begin{aligned}
\partial\Omega_{01} &= \partial\Omega_{10} = \{(y, \dot{y})|\ \varphi_{10} \equiv \dot{y}_{cr} = 0,\ y_{cr} = -d/2\}, \\
\partial\Omega_{02} &= \partial\Omega_{20} = \{(y, \dot{y})|\ \varphi_{20} \equiv \dot{y}_{cr} = 0,\ y_{cr} = d/2\},
\end{aligned}
\tag{15}
$$

where $\partial\Omega_{01}$, $\partial\Omega_{02}$ represent lower and upper stick boundaries, respectively. y_{cr}, $\dot{y}_{cr}$ represent relative displacement and velocity of the ball for appearance and vanishing of stick motion.

Figure 4 shows relative domains and boundaries for the motion of the ball. Domain Ω_0 is shown by dotted area, impact boundaries $\partial\Omega_{0(+\infty)}$, $\partial\Omega_{0(-\infty)}$ are represented by dashed lines, stick domains and boundaries become two solid dots on line $y = \pm d/2$.

In relative coordinates, the equation of relative motion for the ball is

$$
\dot{\mathbf{y}}_{(\lambda)} = \mathbf{g}_{(\lambda)}(\mathbf{y}_{(\lambda)}, \mathbf{X}_{(\lambda)}, t) \text{ with } \dot{\mathbf{X}}_{(\lambda)} = \mathbf{F}_{(\lambda)}(\mathbf{X}_{(\lambda)}, t), \lambda = 0, 1, 2,
\tag{16}
$$

where $\mathbf{y}_{(\lambda)} = (y_{(\lambda)}, \dot{y}_{(\lambda)})^T$, $\mathbf{g}_{(\lambda)} = (\dot{y}_{(\lambda)}, g_{(\lambda)})^T$.

Fig. 4 Relative domains and boundaries
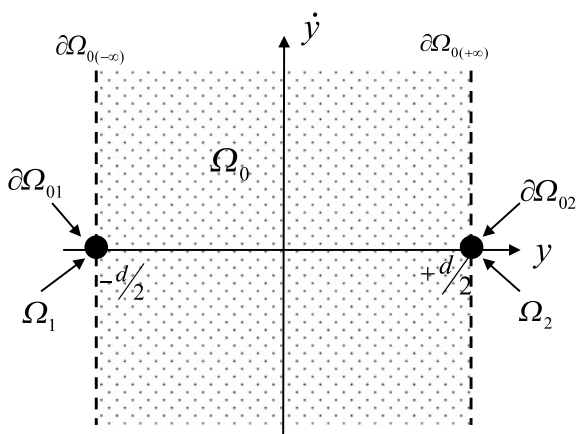
For non-stick motion ($\lambda = 0$),

$$g_{(0)}(\mathbf{y}_{(0)}, \mathbf{X}_{(0)}, t) = -g\sin\theta + A\omega^2\sin(\omega t + \tau)\cos\theta, \tag{17}$$

and for stick motion ($\lambda = 1, 2$),

$$g_{(\lambda)}(\mathbf{y}_{(\lambda)}, \mathbf{X}_{(\lambda)}, t) = 0. \tag{18}$$

3.2   Switching Results

According to the theory on flow switchability of the discontinuous dynamical system in [23] and [24], the switching conditions of stick motions and grazing flows in the inclined impact oscillator will be investigated in relative coordinates.

From Eqs. (14) and (15), the normal vectors of relative boundaries $\mathbf{n}_{\partial\Omega_{01}}$, $\mathbf{n}_{\partial\Omega_{02}}$ and $\mathbf{n}_{\partial\Omega_{0(+\infty)}}$, $\mathbf{n}_{\partial\Omega_{0(-\infty)}}$ are determined, as

$$\mathbf{n}_{\partial\Omega_{01}} = \mathbf{n}_{\partial\Omega_{02}} = (0, 1)^T, \quad \mathbf{n}_{\partial\Omega_{0(+\infty)}} = \mathbf{n}_{\partial\Omega_{0(-\infty)}} = (1, 0)^T. \tag{19}$$

Theorem 1 *When the ball comes to stick boundary $\partial\Omega_{0i}(i = 1, 2)$ at time t_m, stick motion on corresponding boundary appears iff the following conditions can be obtained*

$$\left.\begin{array}{l} \mod(\omega t_m + \tau, 2\pi) \in (0, \arcsin\frac{g\tan\theta}{A\omega^2}) \\ \qquad\bigcup(\pi - \arcsin\frac{g\tan\theta}{A\omega^2}, 2\pi) \textit{ if } g\tan\theta \leq A\omega^2, \\ \mod(\omega t_m + \tau, 2\pi) \in (0, 2\pi) \textit{ if } g\tan\theta > A\omega^2 \end{array}\right\} \textit{ on } \partial\Omega_{01}, \tag{20}$$

or

$$\left.\begin{array}{l} \mod(\omega t_m + \tau, 2\pi) \in (\arcsin\frac{g\tan\theta}{A\omega^2}, \\ \qquad \pi - \arcsin\frac{g\tan\theta}{A\omega^2}) \textit{ if } g\tan\theta < A\omega^2, \\ \textit{no stick}-\textit{motion} \qquad \textit{ if } \quad g\tan\theta \geq A\omega^2 \end{array}\right\} \textit{ on } \partial\Omega_{02}. \tag{21}$$

Proof For the impact pair, when the flow in domain Ω_0 passes over boundary $\partial\Omega_{0i}$ into domain Ω_i ($i = 1, 2$), stick motion appears. So such flow is the semi-passable flow, which can be determined by Theorem 2.1 in [23], then $0-$order $G-$functions for stick boundaries are needed.

From Definition 3.5 in [24], the $0-$order $G-$functions for stick boundaries are

$$\begin{aligned} G_{\partial\Omega_{0i}}^{(0,i)}(\mathbf{y}_{(i)}, t_{m\pm}) &= \mathbf{n}_{\partial\Omega_{0i}}^T \cdot \mathbf{g}_{(i)}(\mathbf{y}_{(i)}, \mathbf{X}_{(i)}, t_{m\pm}), \\ G_{\partial\Omega_{0i}}^{(0,0)}(\mathbf{y}_{(0)}, t_{m\pm}) &= \mathbf{n}_{\partial\Omega_{0i}}^T \cdot \mathbf{g}_{(0)}(\mathbf{y}_{(0)}, \mathbf{X}_{(0)}, t_{m\pm}), \end{aligned} \tag{22}$$

where $i = 1, 2$ indicate stick motion on lower and upper side of the clearance, respectively, t_m is switching time on corresponding boundary.

Using Eqs. (17) and (18), (22) can be computed as

$$
\begin{aligned}
G_{\partial\Omega_{0i}}^{(0,i)}(\mathbf{y}_{(i)}, t_{m\pm}) &= g_{(i)}(\mathbf{y}_{(i)}, \mathbf{X}_{(i)}, t_{m\pm}) = 0, \\
G_{\partial\Omega_{0i}}^{(0,0)}(\mathbf{y}_{(0)}, t_{m\pm}) &= g_{(0)}(\mathbf{y}_{(0)}, \mathbf{X}_{(0)}, t_{m\pm}) = -g\sin\theta + A\omega^2\sin(\omega t_m + \tau)\cos\theta.
\end{aligned}
\tag{23}
$$

By Theorem 2.1 in [23], the switching conditions for stick motion can be obtained as

$$
(-1)^i G_{\partial\Omega_{0i}}^{(0,0)}(\mathbf{y}_{(0)}, t_{m-}) > 0 \text{ and } (-1)^i G_{\partial\Omega_{0i}}^{(0,i)}(\mathbf{y}_{(i)}, t_{m+}) > 0.
$$

Therefore

$$
(-1)^i g_{(0)}(\mathbf{y}_{(0)}, \mathbf{X}_{(0)}, t_{m-}) > 0 \text{ and } (-1)^i g_{(i)}(\mathbf{y}_{(i)}, \mathbf{X}_{(i)}, t_{m+}) > 0.
\tag{24}
$$

The onset conditions of stick motions are determined from Eqs. (23) and (24) as

$$
(-1)^i \cdot (-g\sin\theta + A\omega^2\sin(\omega t_m + \tau)\cos\theta) > 0.
\tag{25}
$$

Solving inequality (25) obtains occurrence conditions for the ball to stick with the base on lower or upper side of the slot as Eqs. (20) and (21). $\qquad\square$

Theorem 2 *Once stick motion exists in domain $\Omega_i (i = 1, 2)$, such stick motion will vanish at time t_m iff the following conditions can be satisfied*

$$
\left.\begin{aligned}
\mathrm{mod}(\omega t_m + \tau, 2\pi) &= \arcsin\frac{g\tan\theta}{A\omega^2} \text{ if } g\tan\theta \leq A\omega^2, \\
&\quad\text{no vanishing exists if } \quad g\tan\theta > A\omega^2.
\end{aligned}\right\} \text{ on } \partial\Omega_{10},
\tag{26}
$$

or

$$
\mathrm{mod}(\omega t_m + \tau, 2\pi) = \pi - \arcsin\frac{g\tan\theta}{A\omega^2} \text{ if } g\tan\theta < A\omega^2 \text{ on } \partial\Omega_{20}.
\tag{27}
$$

Proof Stick motion vanishes, which means the flow will move back into non-stick domain, that is the flow in domain Ω_i ($i = 1, 2$) passes through boundary $\partial\Omega_{i0}$ into domain Ω_0. So such flow is also the semi-passable flow. Due to $G_{\partial\Omega_{0i}}^{(0,i)}(\mathbf{y}_{(i)}, t_{m\pm}) = 0$, high order G-functions are needed.

From Definition 3.6 in [24], $1-$order $G-$functions for stick boundaries are

$$
\begin{aligned}
G_{\partial\Omega_{0i}}^{(1,i)}(\mathbf{y}_{(i)}, t_{m\pm}) &= \mathbf{n}_{\partial\Omega_{0i}}^T \cdot D\mathbf{g}_{(i)}(\mathbf{y}_{(i)}, \mathbf{X}_{(i)}, t_{m\pm}), \\
G_{\partial\Omega_{0i}}^{(1,0)}(\mathbf{y}_{(0)}, t_{m\pm}) &= \mathbf{n}_{\partial\Omega_{0i}}^T \cdot D\mathbf{g}_{(0)}(\mathbf{y}_{(0)}, \mathbf{X}_{(0)}, t_{m\pm}).
\end{aligned}
\tag{28}
$$

From (17) and (18), the above G-functions can be computed as

$$
\begin{aligned}
G_{\partial\Omega_{0i}}^{(1,i)}(\mathbf{y}_{(i)}, t_{m\pm}) &= \frac{d}{dt}g_{(i)}(\mathbf{y}_{(i)}, \mathbf{X}_{(i)}, t_{m\pm}) = A\omega^3\cos(\omega t_m + \tau)\cos\theta, \\
G_{\partial\Omega_{0i}}^{(1,0)}(\mathbf{y}_{(0)}, t_{m\pm}) &= \frac{d}{dt}g_{(0)}(\mathbf{y}_{(0)}, \mathbf{X}_{(0)}, t_{m\pm}) = A\omega^3\cos(\omega t_m + \tau)\cos\theta.
\end{aligned}
\tag{29}
$$

Using Theorem 2.1 in [23], the criteria for vanishing of stick motion are given for $\partial\Omega_{i0}$ by

$$\left.\begin{array}{ll} G_{\partial\Omega_{0i}}^{(0,i)}(\mathbf{y}_{(i)}, t_{m-}) = 0, & G_{\partial\Omega_{0i}}^{(0,0)}(\mathbf{y}_{(0)}, t_{m+}) = 0, \\ (-1)^i G_{\partial\Omega_{0i}}^{(1,i)}(\mathbf{y}_{(i)}, t_{m-}) < 0, & (-1)^i G_{\partial\Omega_{0i}}^{(1,0)}(\mathbf{y}_{(0)}, t_{m+}) < 0. \end{array}\right\} \tag{30}$$

Substituting (23) and (29) into (30) leads to

$$\left.\begin{array}{l} g_{(i)}(\mathbf{y}_{(i)}, \mathbf{X}_{(i)}, t_{m-}) = 0, \\ g_{(0)}(\mathbf{y}_{(0)}, \mathbf{X}_{(0)}, t_{m+}) = -g\sin\theta + A\omega^2\sin(\omega t_m + \tau)\cos\theta = 0, \\ (-1)^i \frac{d}{dt} g_{(i)}(\mathbf{y}_{(i)}, \mathbf{X}_{(i)}, t_{m-}) = (-1)^i \cdot (A\omega^3\cos(\omega t_m + \tau)\cos\theta) < 0, \\ (-1)^i \frac{d}{dt} g_{(0)}(\mathbf{y}_{(0)}, \mathbf{X}_{(0)}, t_{m+}) = (-1)^i \cdot (A\omega^3\cos(\omega t_m + \tau)\cos\theta) < 0. \end{array}\right\} \tag{31}$$

Further simplification of the above equations yields the vanishing conditions of stick motions as (26) and (27). $\qquad\square$

For such pair, when the ball reaches the boundary from a domain and just touches this boundary with zero relative velocity or no interaction force, and then moves back into this domain, grazing phenomenon occurs. Thus grazing motion is tangential flow, its analytical conditions can be developed using Theorem 2.9 in [23].

Theorem 3 *(1) The flow for the motion of the ball in domain $\Omega_i (i = 1, 2)$ reaches stick boundary $\partial\Omega_{i0}$ at time t_m without interaction force between the ball and the base, grazing motion on such stick boundary will occur iff*

$$\left.\begin{array}{l} \mathrm{mod}(\omega t_m + \tau, 2\pi) \in (\pi/2, 3\pi/2) \;\; on \;\; \partial\Omega_{10}, \\ or \\ \mathrm{mod}(\omega t_m + \tau, 2\pi) \in (-\pi/2, \pi/2) \;\; on \;\; \partial\Omega_{20}. \end{array}\right\} \tag{32}$$

(2) The flow for the motion of the ball in domain Ω_0 reaches stick boundary $\partial\Omega_{0i}$ at time t_m with relative velocity and acceleration being zero, grazing motion on such stick boundary will occur iff

$$\left.\begin{array}{l} \left.\begin{array}{ll} \mathrm{mod}(\omega t_m + \tau, 2\pi) = \arcsin\frac{g\tan\theta}{A\omega^2} & if \quad g\tan\theta < A\omega^2 \\ no \; grazing \; motion \; exists & if \quad g\tan\theta \geq A\omega^2 \end{array}\right\} on \; \partial\Omega_{01}, \\ or \\ \left.\begin{array}{ll} \mathrm{mod}(\omega t_m + \tau, 2\pi) = \pi - \arcsin\frac{g\tan\theta}{A\omega^2} & if \quad g\tan\theta < A\omega^2 \\ no \; grazing \; motion \; exists & if \quad g\tan\theta \geq A\omega^2 \end{array}\right\} on \; \partial\Omega_{02}. \end{array}\right\} \tag{33}$$

Proof From Theorem 2.9 in [23], the occurrence of grazing motion on stick boundaries requires

$$\left.\begin{aligned}
G^{(0,i)}_{\partial\Omega_{0i}}(\mathbf{y}_{(i)}, t_{m\pm}) = 0, \quad & (-1)^i G^{(1,i)}_{\partial\Omega_{0i}}(\mathbf{y}_{(i)}, t_{m\pm}) > 0 \quad \text{for} \quad \partial\Omega_{i0}, \\
G^{(0,0)}_{\partial\Omega_{0i}}(\mathbf{y}_{(0)}, t_{m\pm}) = 0, \quad & (-1)^i G^{(1,0)}_{\partial\Omega_{0i}}(\mathbf{y}_{(0)}, t_{m\pm}) < 0 \quad \text{for} \quad \partial\Omega_{0i}.
\end{aligned}\right\} \tag{34}$$

Substituting (23) and (29) into (34) leads to

$$\left.\begin{aligned}
(-1)^i \cdot (A\omega^3 \cos(\omega t_m + \tau)\cos\theta) > 0 \quad & \text{for} \quad \partial\Omega_{i0}, \\
(-1)^i \cdot (-g\sin\theta + A\omega^2 \sin(\omega t_m + \tau)\cos\theta) = 0, \\
(-1)^i \cdot (A\omega^3 \cos(\omega t_m + \tau)\cos\theta) < 0
\end{aligned}\right\} \quad \text{for} \quad \partial\Omega_{0i}. \right\} \tag{35}$$

Further simplification of (35) yields the occurrence conditions of grazing motion on stick boundaries as (32) and (33).   □

Theorem 4 *The flow for the motion of the ball in domain Ω_0 reaches impact boundary $\partial\Omega_{0(\pm\infty)}$ at time t_m, grazing motion on such impact boundary is to occur iff the following conditions are obtained*

$$\left.\begin{aligned}
\dot{x}_{(0)}(t_m) - A\omega\cos(\omega t_m + \tau)\cos\theta = 0, \quad & and \\
\operatorname{mod}(\omega t_m + \tau, 2\pi) \in (\arcsin\tfrac{g\tan\theta}{A\omega^2}, & \\
\qquad \pi - \arcsin\tfrac{g\tan\theta}{A\omega^2}) \quad if \quad g\tan\theta < A\omega^2, & \left.\right\} on\ \partial\Omega_{0(-\infty)} \\
no\ grazing\ motion\ exists \qquad if \quad g\tan\theta \geq A\omega^2. & \\
or & \\
\operatorname{mod}(\omega t_m + \tau, 2\pi) \in (0, \arcsin\tfrac{g\tan\theta}{A\omega^2}) & \\
\qquad \bigcup(\pi - \arcsin\tfrac{g\tan\theta}{A\omega^2}, 2\pi) \quad if \quad g\tan\theta \leq A\omega^2, & \left.\right\} on\ \partial\Omega_{0(+\infty)} \\
\operatorname{mod}(\omega t_m + \tau, 2\pi) \in (0, 2\pi) \qquad if \quad g\tan\theta > A\omega^2. &
\end{aligned}\right\} \tag{36}$$

Proof From Definition 3.5 and Definition 3.6 in [24], the 0−order and 1−order G−functions for impact boundaries $\partial\Omega_{0(\pm\infty)}$ are determined by

$$\begin{aligned}
G^{(0,0)}_{\partial\Omega_{0(+\infty)}}(\mathbf{y}_{(0)}, t_{m\pm}) &= \mathbf{n}^T_{\partial\Omega_{0(+\infty)}} \cdot \mathbf{g}_{(0)}(\mathbf{y}_{(0)}, \mathbf{X}_{(0)}, t_{m\pm}), \\
G^{(0,0)}_{\partial\Omega_{0(-\infty)}}(\mathbf{y}_{(0)}, t_{m\pm}) &= \mathbf{n}^T_{\partial\Omega_{0(-\infty)}} \cdot \mathbf{g}_{(0)}(\mathbf{y}_{(0)}, \mathbf{X}_{(0)}, t_{m\pm}), \\
G^{(1,0)}_{\partial\Omega_{0(+\infty)}}(\mathbf{y}_{(0)}, t_{m\pm}) &= \mathbf{n}^T_{\partial\Omega_{0(+\infty)}} \cdot D\mathbf{g}_{(0)}(\mathbf{y}_{(0)}, \mathbf{X}_{(0)}, t_{m\pm}), \\
G^{(1,0)}_{\partial\Omega_{0(-\infty)}}(\mathbf{y}_{(0)}, t_{m\pm}) &= \mathbf{n}^T_{\partial\Omega_{0(-\infty)}} \cdot D\mathbf{g}_{(0)}(\mathbf{y}_{(0)}, \mathbf{X}_{(0)}, t_{m\pm}).
\end{aligned} \tag{37}$$

By (17), (37) can be computed as

$$\begin{aligned}
G^{(0,0)}_{\partial\Omega_{0(\pm\infty)}}(\mathbf{y}_{(0)}, t_{m\pm}) &= \dot{y}_{(0)} = \dot{x}_{(0)} - A\omega\cos(\omega t_m + \tau)\cos\theta, \\
G^{(1,0)}_{\partial\Omega_{0(\pm\infty)}}(\mathbf{y}_{(0)}, t_{m\pm}) &= -g\sin\theta + A\omega^2 \sin(\omega t_m + \tau)\cos\theta.
\end{aligned} \tag{38}$$

From Theorem 2.9 in [23], the appearance of grazing motion on impact boundaries requires

$$
\left.
\begin{aligned}
G^{(0,0)}_{\partial \Omega_{0(-\infty)}}(\mathbf{y}_{(0)}, t_{m\pm}) = 0, \quad G^{(1,0)}_{\partial \Omega_{0(-\infty)}}(\mathbf{y}_{(0)}, t_{m\pm}) > 0 \quad \text{for} \quad \partial \Omega_{0(-\infty)}, \\
G^{(0,0)}_{\partial \Omega_{0(+\infty)}}(\mathbf{y}_{(0)}, t_{m\pm}) = 0, \quad G^{(1,0)}_{\partial \Omega_{0(+\infty)}}(\mathbf{y}_{(0)}, t_{m\pm}) < 0 \quad \text{for} \quad \partial \Omega_{0(+\infty)}.
\end{aligned}
\right\}
\tag{39}
$$

Combining (38) into (39) yields

$$
\left.
\begin{aligned}
\dot{x}_{(0)}(t_m) - A\omega \cos(\omega t_m + \tau)\cos\theta = 0, \quad \text{and} \\
-g\sin\theta + A\omega^2 \sin(\omega t_m + \tau)\cos\theta > 0 \quad \text{for} \quad \partial \Omega_{0(-\infty)}, \\
-g\sin\theta + A\omega^2 \sin(\omega t_m + \tau)\cos\theta < 0 \quad \text{for} \quad \partial \Omega_{0(+\infty)}.
\end{aligned}
\right\}
\tag{40}
$$

Solving (40) obtains the graze conditions on impact boundaries as (36).   □

To demonstrate the analytical conditions of stick motions and grazing flows in the inclined impact pair, the motions will be shown through time histories of displacement and velocity, corresponding trajectory in phase space. The starting points of motions are depicted by asterisk, the switching points are represented by hollow points or solid points. The component of displacement curves or velocity curves of the base in the inclined direction are represented by dashed curves, and for the motions of the ball, the curves of displacement or velocity and the corresponding trajectories are shown by solid curves.

Consider system parameters as $A = 10$, $\omega = 1$, $\theta = \pi/6$, $g = 9.81$, $e = 0.8$, $\tau = 0$, $d = 20$, $M = 1$, $m = 0.0001$ to illustrate a stick motion on lower side of the slot in Fig. 5. The initial conditions are $t_0 = 5.356754$, $x_0 = -16.923712$, $\dot{x}_0 = 5.202136$. The time histories of displacement is depicted in Fig. 5a, and the time histories of velocity is in Fig. 5b. It can be seen that stick motion occurs in such initial conditions. The solid point stands for vanishing points of stick motion. The corresponding trajectory of stick motion are shown in Fig. 5c. After vanishing of stick motion on lower side of the slot, the ball moves freely and impacts such boundary again.

Changing the above parameters as $e = 0.4$, $d = 1$ can demonstrate a grazing motion on lower side of the slot in Fig. 6. The initial conditions are $t_0 = 0.699899$, $x_0 = 6.078421$, $\dot{x}_0 = 4.537097$. The initial point on upper side of the slot, and then the ball contacts lower side of the slot as shown in Fig. 6a. However Fig. 6b shows that solid point is the point of intersection between solid curve and dashed one, that is, the relative velocity of the ball to the base is zero at the solid point. And then the ball leaves this boundary again. So the solid point is grazing point, a grazing motion on lower side of the slot appears. Figure 6b, c also demonstrate that the velocity of the ball is continuous at the solid point.
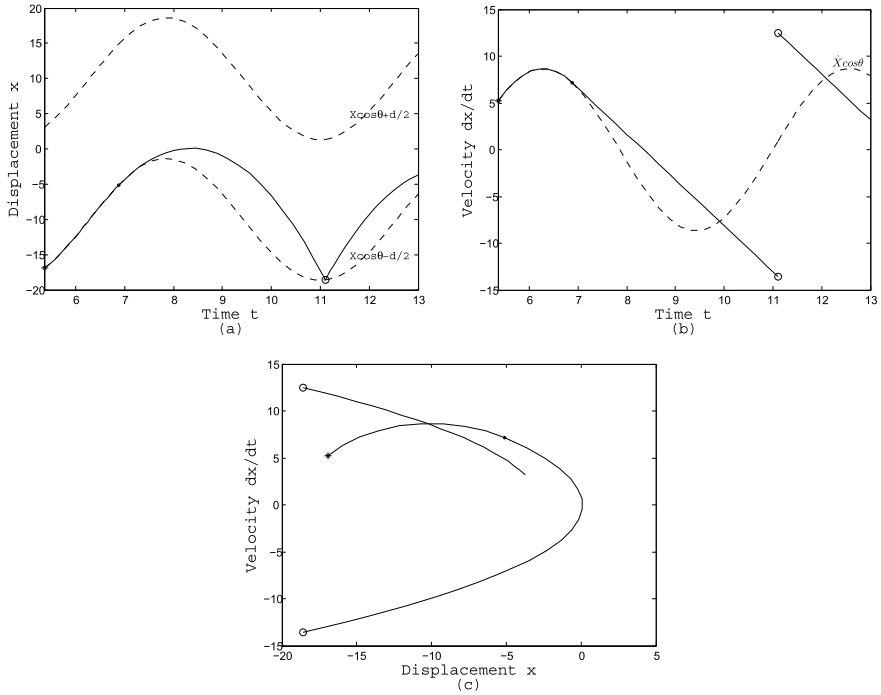
Fig. 5 Numerical simulation of a stick motion on lower side of the slot: **a** displacement-time history, **b** velocity-time history, **c** phase trajectory. ($A = 10$, $\omega = 1$, $\theta = \pi/6$, $g = 9.81$, $e = 0.8$, $\tau = 0$, $d = 20$, $M = 1$, $m = 0.0001$, $t_0 = 5.356754$, $x_0 = -16.923712$, $\dot{x}_0 = 5.202136$.)

4 Mapping Structures and Periodic Motions

In this section, the switching sets on the discontinuous boundaries will be defined, and then basic mappings and mapping structures can be obtained. Two specific periodic motions without stick are investigated in relative coordinates.

4.1 Periodic Motions with Stick

From (7), the switching sets without stick are defined as

$$\begin{aligned}
\varXi_{0(-\infty)} &= \{(x_k, \dot{x}_k, t_k)|x_k = X_k \cos\theta - d/2, \ \dot{x}_k \neq \dot{X}_k \cos\theta\}, \\
\varXi_{0(+\infty)} &= \{(x_k, \dot{x}_k, t_k)|x_k = X_k \cos\theta + d/2, \ \dot{x}_k \neq \dot{X}_k \cos\theta\},
\end{aligned} \tag{41}$$

where $\varXi_{0(-\infty)}$, $\varXi_{0(+\infty)}$ are defined on $\partial\varOmega_{0(-\infty)}$ and $\partial\varOmega_{0(+\infty)}$, respectively.
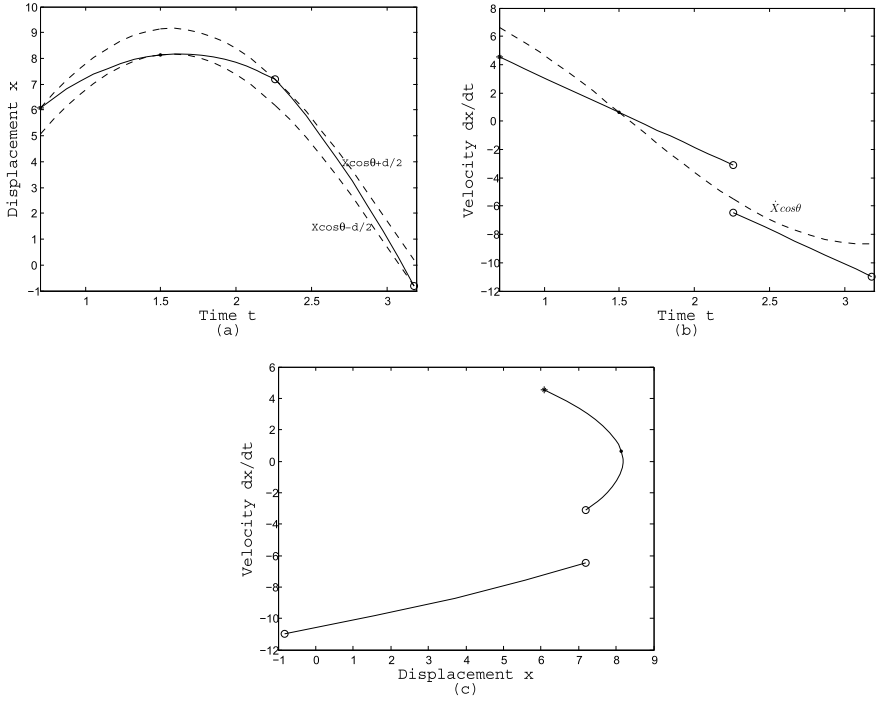
Fig. 6 Numerical simulation of a grazing motion on lower side of the slot: **a** displacement-time history, **b** velocity-time history, **c** phase trajectory. ($A = 10$, $\omega = 1$, $\theta = \pi/6$, $g = 9.81$, $e = 0.4$, $\tau = 0$, $d = 1$, $M = 1$, $m = 0.0001$, $t_0 = 0.699899$, $x_0 = 6.078421$, $\dot{x}_0 = 4.537097$.)

The basic mappings without stick are defined as

$$
\begin{aligned}
P_1 : \ & \Xi_{0(-\infty)} \rightarrow \Xi_{0(+\infty)}, \quad P_2 : \ \Xi_{0(+\infty)} \rightarrow \Xi_{0(-\infty)}, \\
P_3 : \ & \Xi_{0(-\infty)} \rightarrow \Xi_{0(-\infty)}, \quad P_4 : \ \Xi_{0(+\infty)} \rightarrow \Xi_{0(+\infty)}.
\end{aligned}
\tag{42}
$$

The switching sets and generic mappings defined above are sketched in Fig. 7.

From (7) and (8), the switching sets with stick are defined as

$$
\begin{aligned}
\Xi_{01} &= \{(x_k, \dot{x}_k, t_k) | x_k = X_k \cos\theta - d/2, \ \dot{x}_k = \dot{X}_k \cos\theta\}, \\
\Xi_{02} &= \{(x_k, \dot{x}_k, t_k) | x_k = X_k \cos\theta + d/2, \ \dot{x}_k = \dot{X}_k \cos\theta\}, \\
\Xi_{0(-\infty)} &= \{(x_k, \dot{x}_k, t_k) | x_k = X_k \cos\theta - d/2, \ \dot{x}_k \neq \dot{X}_k \cos\theta\}, \\
\Xi_{0(+\infty)} &= \{(x_k, \dot{x}_k, t_k) | x_k = X_k \cos\theta + d/2, \ \dot{x}_k \neq \dot{X}_k \cos\theta\},
\end{aligned}
\tag{43}
$$

where the switching sets Ξ_{0i} ($i = 1, 2$) are defined on $\partial\Omega_{0i}$.

Fig. 7 The switching sets and basic mappings without stick
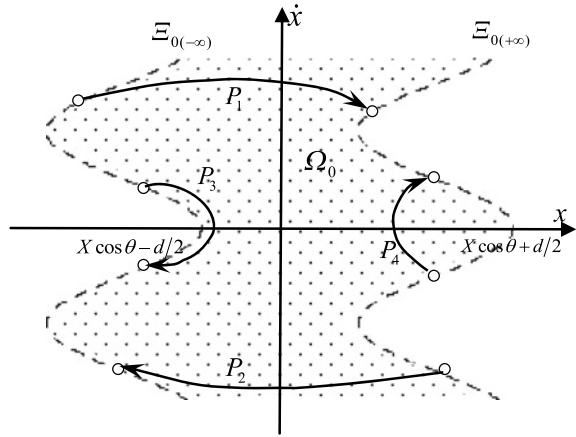
Fig. 8 The switching sets and basic mappings with stick
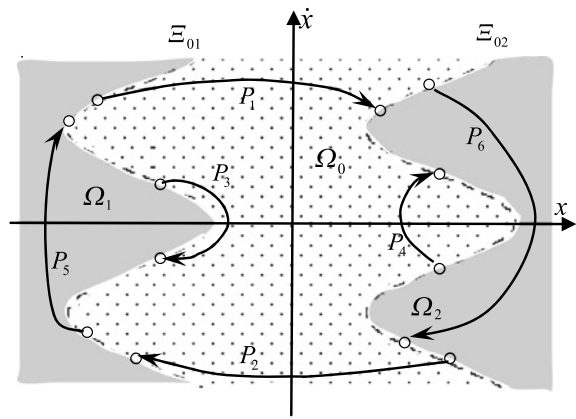
The basic mappings with stick are defined as

$$
\begin{aligned}
&P_1 : \; \Xi_{01} \rightarrow \Xi_{0(+\infty)}, \; \text{or} \; \Xi_{0(-\infty)} \rightarrow \Xi_{02}, \\
&P_2 : \; \Xi_{02} \rightarrow \Xi_{0(-\infty)}, \; \text{or} \; \Xi_{0(+\infty)} \rightarrow \Xi_{01}, \\
&P_3 : \; \Xi_{0(-\infty)} \rightarrow \Xi_{01}, \; P_4 : \; \Xi_{0(+\infty)} \rightarrow \Xi_{02}, \\
&P_5 : \; \Xi_{01} \rightarrow \Xi_{01}, \; P_6 : \; \Xi_{02} \rightarrow \Xi_{02},
\end{aligned} \tag{44}
$$

where P_1 and P_2 are global mappings, P_3, P_4 and P_5, P_6 are local mappings. The six generic mappings are shown in Fig. 8.

Based on the above discussions, the governing equations of generic mappings P_j ($j = 1, 2, 3, 4$) can be expressed by

$$
\begin{cases}
f_1^{(j)}(x_k, \dot{x}_k, t_k, x_{k+1}, \dot{x}_{k+1}, t_{k+1}) = 0, \\
f_2^{(j)}(x_k, \dot{x}_k, t_k, x_{k+1}, \dot{x}_{k+1}, t_{k+1}) = 0,
\end{cases} \tag{45}
$$

where

$$
\begin{aligned}
x_k &= X_k \cos\theta - d/2, \quad x_{k+1} = X_{k+1}\cos\theta + d/2 \quad \text{for } P_1,\\
x_k &= X_k \cos\theta + d/2, \quad x_{k+1} = X_{k+1}\cos\theta - d/2 \quad \text{for } P_2,\\
x_k &= X_k \cos\theta - d/2, \quad x_{k+1} = X_{k+1}\cos\theta - d/2 \quad \text{for } P_3,\\
x_k &= X_k \cos\theta + d/2, \quad x_{k+1} = X_{k+1}\cos\theta + d/2 \quad \text{for } P_4.
\end{aligned}
$$

The governing equations of stick mappings P_5, P_6 can be expressed by

$$
\begin{cases}
f_1^{(\alpha)}(x_k, \dot{x}_k, t_k, x_{k+1}, \dot{x}_{k+1}, t_{k+1}) = 0,\\
f_2^{(\alpha)}(x_{k+1}, \dot{x}_{k+1}, t_{k+1}) = g_{(0)}(\mathbf{0}, \mathbf{X}_{k+1}, t_{k+1}) = 0,
\end{cases}
$$

with $\alpha = 5, 6$, where

$$
\left.
\begin{aligned}
& x_k = X_k \cos\theta - d/2, \ \ \dot{x}_k = \dot{X}_k \cos\theta,\\
& x_{k+1} = X_{k+1}\cos\theta - d/2, \ \ \dot{x}_{k+1} = \dot{X}_{k+1}\cos\theta,\\
& \mod(\omega t_k + \tau, 2\pi) \in (0, \arcsin\tfrac{g\tan\theta}{A\omega^2}) \bigcup (\pi - \arcsin\tfrac{g\tan\theta}{A\omega^2}, 2\pi),\\
& \mod(\omega t_{k+1} + \tau, 2\pi) \in (0, \pi/2)
\end{aligned}
\right\} \ \text{for mapping } P_5,
$$

and

$$
\left.
\begin{aligned}
& x_k = X_k \cos\theta + d/2, \ \ \dot{x}_k = \dot{X}_k \cos\theta,\\
& x_{k+1} = X_{k+1}\cos\theta + d/2, \ \ \dot{x}_{k+1} = \dot{X}_{k+1}\cos\theta,\\
& \mod(\omega t_k + \tau, 2\pi) \in (\arcsin\tfrac{g\tan\theta}{A\omega^2}, \pi - \arcsin\tfrac{g\tan\theta}{A\omega^2}),\\
& \mod(\omega t_{k+1} + \tau, 2\pi) \in (\pi/2, \pi)
\end{aligned}
\right\} \ \text{for mapping } P_6.
$$

To study the periodic motion or chaos with or without stick in the inclined impact pair, the generalized mapping structure is introduced as

$$
P_{n_k \cdots n_2 n_1} \equiv P_{n_k} \circ \cdots \circ P_{n_2} \circ P_{n_1}, \tag{46}
$$

where P_{n_j} ($n_j \in \{1, 2, \cdots, 6\}$, $j = 1, 2, \cdots, k$) are defined in (44).

The mapping structure of the motion with $m-$times repeated mapping structure (46) can be expressed as

$$
P_{n_k \cdots n_2 n_1}^{(m)} \equiv \underbrace{(P_{n_k} \circ \cdots \circ P_{n_2} \circ P_{n_1}) \circ \cdots \circ (P_{n_k} \circ \cdots \circ P_{n_2} \circ P_{n_1})}_{m-\text{items}}. \tag{47}
$$

Considering a motion with specific mapping structure

$$
\begin{aligned}
P &\equiv \underbrace{P_{2^{k_{4l}} 6^{k_{3l}} 4^{m_l} 1^{k_{2l}} 5^{k_{1l}} 3^{n_l}} \circ \cdots \circ P_{2^{k_{41}} 6^{k_{31}} 4^{m_1} 1^{k_{21}} 5^{k_{11}} 3^{n_1}}}_{l-\text{items}}\\
&= P_{2^{k_{4l}} 6^{k_{3l}} 4^{m_l} 1^{k_{2l}} 5^{k_{1l}} 3^{n_l} \ldots 2^{k_{41}} 6^{k_{31}} 4^{m_1} 1^{k_{21}} 5^{k_{11}} 3^{n_1}},
\end{aligned} \tag{48}
$$

where $k_j \in \{0, 1\}$, $m_s, n_s \in \mathbf{N}$ ($s = 1, 2, \cdots, l$).

Define vectors $\mathbf{Y}_k = (\dot{x}_k, t_k)^T$. The motions of mapping structure (48) can be determined by

$$
\mathbf{Y}_{k+\sum\limits_{s=1}^{l}(k_{4s}+k_{3s}+m_s+k_{2s}+k_{1s}+n_s)} = P\mathbf{Y}_k
$$
$$
= P_{2^{k_{4l}}6^{k_{3l}}4^{m_l}1^{k_{2l}}5^{k_{1l}}3^{n_l}\dots2^{k_{41}}6^{k_{31}}4^{m_1}1^{k_{21}}5^{k_{11}}3^{n_1}} \mathbf{Y}_k.
\tag{49}
$$

Based on the algebraic equations for mapping (46)–(49), a set of nonlinear algebraic equations for mapping structure (48) can be obtained as

$$
\begin{aligned}
&\mathbf{f}^{(3)}(\mathbf{Y}_k, \mathbf{Y}_{k+1}) = \mathbf{0}, \cdots, \mathbf{f}^{(5)}(\mathbf{Y}_{k+n_1}, \mathbf{Y}_{k+n_1+1}) = \mathbf{0}, \cdots, \\
&\mathbf{f}^{(1)}(\mathbf{Y}_{k+k_{11}+n_1}, \mathbf{Y}_{k+k_{11}+n_1+1}) = \mathbf{0}, \cdots, \\
&\mathbf{f}^{(2)}(\mathbf{Y}_{k+\sum\limits_{s=1}^{l}(k_{4s}+k_{3s}+m_s+k_{2s}+k_{1s}+n_s)-1}, \mathbf{Y}_{k+\sum\limits_{s=1}^{l}(k_{4s}+k_{3s}+m_s+k_{2s}+k_{1s}+n_s)}) = \mathbf{0}.
\end{aligned}
\tag{50}
$$

The periodic motions pertaining to such mapping structure requires

$$
\mathbf{Y}_{k+\sum\limits_{s=1}^{l}(k_{4s}+k_{3s}+m_s+k_{2s}+k_{1s}+n_s)} = \mathbf{Y}_k.
\tag{51}
$$

Solving (50) and (51) can generate all switching sets of periodic motions (48). Once the results of switching points for a specific periodic motions are obtained, its local stability and bifurcations analysis can be completed through the corresponding Jacobian matrix and its eigenvalues (referring [22]). However, the occurrence or vanishing of stick motions and graze motions can't be predicted by eigenvalue analysis, which should be determined by the flow switchability theory of the discontinuous dynamical systems, that is, Theorems 1–4 should be used.

4.2 Periodic Motions Without Stick

If only periodic motions without stick and grazing are considered, it is simpler to investigate such motions in relative coordinates. The periodic motions with two alternative impacts on two side of slot have be done in [20, 21]. Next we will study periodic motions $P = P_4$ with one impact on lower side of the slot.

From (4), the governing equations of mapping $P = P_4$ in relative coordinates are

$$
\begin{aligned}
&\dot{y}_{i+1} = -A\omega\cos\theta[\cos(\omega t_{i+1}+\tau) - \cos(\omega t_i+\tau)] - g\sin\theta(t_{i+1}-t_i) - e\dot{y}_i, \\
&0 = y_{i+1} - y_i = -A\cos\theta[\sin(\omega t_{i+1}+\tau) - \sin(\omega t_i+\tau)] \\
&\qquad - \tfrac{1}{2}g\sin\theta(t_{i+1}^2 - t_i^2) + (-e\dot{y}_i + g\sin\theta t_i + A\omega\cos\theta\cos(\omega t_i+\tau))(t_{i+1}-t_i).
\end{aligned}
\tag{52}
$$

where $(t_i, \dot{y}_i)$ is initial value, $(t_i, \dot{y}_i)$, $(t_{i+1}, \dot{y}_{i+1})$ are on the lower side of the slot, and for briefness, the notations $"+""" -"$ are deleted.

The period-1 motion $P = P_4$ under N cycles of base motion should satisfy

$$t_{i+1} = t_i + \frac{2N\pi}{\omega}, \quad \dot{y}_{i+1} = \dot{y}_i, \quad \dot{y}_i \leq 0. \tag{53}$$

Substituting (53) into (52) obtains

$$\dot{y}_i = -\frac{g \sin\theta}{1+e} \cdot \frac{2N\pi}{\omega}, \tag{54}$$

and

$$e\dot{y}_i - A\omega \cos\theta \cos(\omega t_i + \tau) + g \sin\theta \cdot \frac{N\pi}{\omega} = 0. \tag{55}$$

Further simplifying (55) leads to

$$\cos(\omega t_i + \tau) = \frac{1-e}{1+e} \cdot \frac{gN\pi \cdot \tan\theta}{A\omega^2}. \tag{56}$$

Result 1 For the inclined impact pair, when one impact period-1 motion $P = P_4$ occurs, the initial velocity and parameters satisfy (54) and (56).

It is can be seen that the initial velocity has nothing to do with excitation amplitude and initial phase angle when periodic motion $P = P_4$ appears.

Similar to (46), for periodic motion after period doubling of period-1 motion $P = P_4$, the mapping becomes

$$P = \underbrace{P_4 \circ P_4 \circ \cdots \circ P_4}_{k}, \tag{57}$$

that is the ball impacts continuously lower side of the slot under N cycles of base motion, $\dot{y}_{i+k} = \dot{y}_i$, $t_{i+k} = t_i + NT$, $T = 2\pi/\omega$ are needed. When $k \to \infty$, the chaotic motions will appear.

In order to study period-k periodic motion (57), the impact time interval parameters $q_j (j = 1, 2, \ldots, k)$ are introduced as

$$0 \leq q_j \leq 1, \quad \sum_{j=1}^{k} q_j = 1, \quad t_{i+j} - t_{i+j-1} = q_j NT. \tag{58}$$

Substituting (58) into (52) leads to

$$\dot{y}_{i+j} = -A\omega\cos\theta\cos(\omega t_i + \tau)[\cos(\sum_{s=1}^{j} q_s NT\omega) - \cos(\sum_{s=1}^{j-1} q_s NT\omega)]$$

$$+ A\omega\cos\theta\sin(\omega t_i + \tau)[\sin(\sum_{s=1}^{j} q_s NT\omega) - \sin(\sum_{s=1}^{j-1} q_s NT\omega)]$$

$$- g\sin\theta q_j NT - e\dot{y}_{i+j-1},$$

$$0 = -A\cos\theta\cos(\omega t_i + \tau)[(\sin(\sum_{s=1}^{j} q_s NT\omega) - \sin(\sum_{s=1}^{j-1} q_s NT\omega))$$

$$- \cos(\sum_{s=1}^{j-1} q_s NT\omega)q_j NT\omega] \tag{59}$$

$$- A\cos\theta\sin(\omega t_i + \tau)[(\cos(\sum_{s=1}^{j} q_s NT\omega)$$

$$- \cos(\sum_{s=1}^{j-1} q_s NT\omega)) + \sin(\sum_{s=1}^{j-1} q_s NT\omega)q_j NT\omega]$$

$$- \frac{1}{2}g\sin\theta(q_j NT)^2 - e\dot{y}_{i+j-1}q_j NT.$$

Using mathematical induction and (59) gives

$$\dot{y}_{i+j} = -A\omega\cos\theta r_1^{(j)}\cos(\omega t_i + \tau) + A\omega\cos\theta r_2^{(j)}\sin(\omega t_i + \tau)$$

$$- g\sin\theta r_3^{(j)}NT + (-1)^j e^j \dot{y}_i,$$

$$0 = -A\cos\theta\cos(\omega t_i + \tau)[S^{(j)} - S^{(j-1)} - \omega q_j NT(er_1^{(j-1)} + C^{(j-1)})] \tag{60}$$

$$- A\cos\theta\sin(\omega t_i + \tau)[C^{(j)} - C^{(j-1)} + \omega q_j NT(er_2^{(j-1)} + S^{(j-1)})]$$

$$+ g\sin\theta q_j(NT)^2(-\frac{1}{2}q_j + er_3^{(j-1)}) + (-1)^{j-1}e^{j-1}\dot{y}_i q_j NT,$$

where

$$r_1^{(j)} = \sum_{m=1}^{j}(-e)^{j-m}[C^{(m)} - C^{(m-1)}], \quad r_2^{(j)} = \sum_{m=1}^{j}(-e)^{j-m}[S^{(m)} - S^{(m-1)}],$$

$$r_3^{(j)} = \sum_{m=1}^{j}(-e)^{j-m}q_m, \quad C^{(j)} = \cos(\sum_{s=1}^{j} q_s NT\omega), \quad S^{(j)} = \sin(\sum_{s=1}^{j} q_s NT\omega).$$

From (60), we have

$$\cos(\omega t_i + \tau) = (D_1^{(j)} + D_2^{(j)}\dot{y}_{i+j} + D_3^{(j)}\dot{y}_i)/(A\omega\cos\theta D^{(j)}),$$
$$\sin(\omega t_i + \tau) = (D_4^{(j)} + D_5^{(j)}\dot{y}_{i+j} + D_6^{(j)}\dot{y}_i)/(A\omega\cos\theta D^{(j)}), \tag{61}$$

where

$$D^{(j)} = a_{11}^{(j)}a_{22}^{(j)} - a_{12}^{(j)}a_{21}^{(j)}, \quad D_1^{(j)} = a_{13}^{(j)}a_{22}^{(j)} - \omega a_{12}^{(j)}a_{23}^{(j)}, \quad D_2^{(j)} = a_{22}^{(j)},$$
$$D_3^{(j)} = a_{14}^{(j)}a_{22}^{(j)} - \omega a_{12}^{(j)}a_{24}^{(j)}, \quad D_4^{(j)} = \omega a_{11}^{(j)}a_{23}^{(j)} - a_{21}^{(j)}a_{13}^{(j)}, \quad D_5^{(j)} = -a_{21}^{(j)},$$
$$D_6^{(j)} = \omega a_{11}^{(j)}a_{24}^{(j)} - a_{21}^{(j)}a_{14}^{(j)},$$

and

$$a_{11}^{(j)} = -r_1^{(j)}, \quad a_{21}^{(j)} = S^{(j)} - S^{(j-1)} - \omega q_j NT(er_1^{(j-1)} + C^{(j-1)}),$$
$$a_{12}^{(j)} = r_2^{(j)}, \quad a_{22}^{(j)} = C^{(j)} - C^{(j-1)} - \omega q_j NT(er_2^{(j-1)} + S^{(j-1)}),$$
$$a_{13}^{(j)} = g \sin\theta NT r_3^{(j)}, \quad a_{14}^{(j)} = -(-e)^j,$$
$$a_{23}^{(j)} = g\sin\theta q_j(NT)^2(-\frac{1}{2}q_j + er_3^{(j-1)}), \quad a_{24}^{(j)} = (-e)^{j-1}q_j NT.$$

For period-k motions $P = \underbrace{P_4 \circ P_4 \circ \cdots \circ P_4}_{k}$, $\dot{y}_{i+k} = \dot{y}_i$ is satisfied, and from (61), we have

$$\cos(\omega t_i + \tau) = (D_1^{(k)} + (D_2^{(k)} + D_3^{(k)})\dot{y}_i)/(A\omega\cos\theta D^{(k)}),$$
$$\sin(\omega t_i + \tau) = (D_4^{(k)} + (D_5^{(k)} + D_6^{(k)})\dot{y}_i)/(A\omega\cos\theta D^{(k)}). \tag{62}$$

Thus, the existence conditions of period-k motions $P = \underbrace{P_4 \circ P_4 \circ \cdots \circ P_4}_{k}$ are

$$A = \frac{1}{\omega\cos\theta D^{(k)}}\sqrt{[D_1^{(k)} + (D_2^{(k)} + D_3^{(k)})\dot{y}_i]^2 + [D_4^{(k)} + (D_5^{(k)} + D_6^{(k)})\dot{y}_i]^2}, \tag{63}$$

and solving (61) and (62) obtains

$$\dot{y}_i = \dot{y}_{i+k} = \frac{b_{11}^{(j)} - b_{21}^{(j)}}{b_{12}^{(j)} - b_{22}^{(j)}}, \quad j = 1, 2, \cdots, k-1, \tag{64}$$

where

$$b_{11}^{(j)} = \frac{D_2^{(j)}}{D^{(j)}} \cdot \frac{D_4^{(k)}}{D^{(k)}} - \frac{D_2^{(j)}}{D^{(j)}} \cdot \frac{D_4^{(j)}}{D^{(j)}}, \qquad b_{21}^{(j)} = \frac{D_5^{(j)}}{D^{(j)}} \cdot \frac{D_1^{(k)}}{D^{(k)}} - \frac{D_5^{(j)}}{D^{(j)}} \cdot \frac{D_1^{(j)}}{D^{(j)}},$$
$$b_{12}^{(j)} = \frac{D_3^{(j)}}{D^{(j)}} \cdot \frac{D_6^{(j)}}{D^{(j)}} - \frac{D_3^{(j)}}{D^{(j)}} \cdot \frac{D_5^{(k)} + D_6^{(k)}}{D^{(k)}}, \quad b_{22}^{(j)} = \frac{D_5^{(j)}}{D^{(j)}} \cdot \frac{D_3^{(j)}}{D^{(j)}} - \frac{D_5^{(j)}}{D^{(j)}} \cdot \frac{D_2^{(k)} + D_3^{(k)}}{D^{(k)}}.$$

Result 2 For the inclined impact pair, the existence of k impacts period-k motion $P = \underbrace{P_4 \circ P_4 \circ \cdots \circ P_4}_{k}$ requires all parameters satisfying (63) and (64).
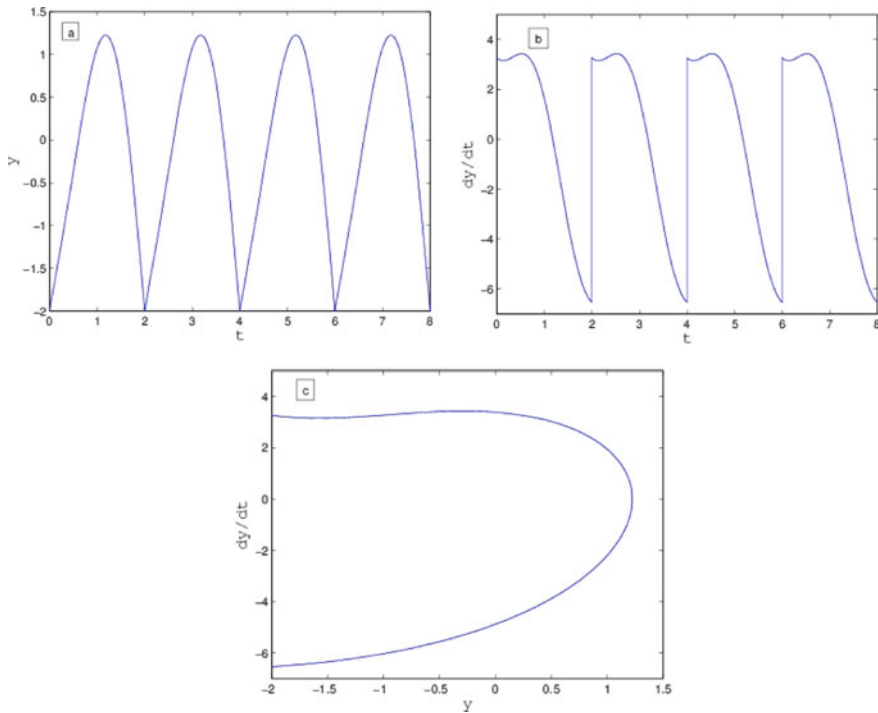
Fig. 9 Periodic motion $P = P_4$

The stability and bifurcations of periodic motion $P = P_4$ and $P = \underbrace{P_4 \circ P_4 \circ \cdots \circ P_4}_{k}$ can be developed using the eigenvalue analysis, which are completed through the linearization of Poincaré mapping of periodic motions (referring [20, 21]).

To help one understand the analytical results, periodic motion with only impact on lower side of the slot are demonstrated in Figs. 9 and 10 in form of the time-displacement curves, the time-velocity curves and the phase diagram.

In Fig. 9, period-1 motion $P = P_4$ is demonstrated, parameters $A = 0.7, \omega = \pi, \theta = \pi/6, \tau = 0.538, e = 0.5, g = 9.81, d = 4$ are chosen, the initial conditions are $t_0 = 0, \dot{y}_0 = -6.54$. From the parameters relations and stability analysis, it can be seen: the initial velocity $\dot{y}_0$ is not affected by the change of excitation phase and amplitude when $P = P_4$ occurs; when $A < 0.601$, $P = P_4$ can not appear; when $A = 0.601$, the saddle-node bifurcation occurs; when $A \in (0.601, 0.604)$, $P = P_4$ is stable node; when $A \in (0.604, 0.831)$, $P = P_4$ is stable focus; when $A \in (0.831, 0.876)$, $P = P_4$ is stable node; when $A = 0.876$, the period-doubling bifurcation of $P = P_4$ occurs and period-2 motion $P = P_4 \circ P_4$ appears.

Changing the parameters in Fig. 9 as $A = 1.5$, $\tau = 5.712$, $d = 8$ depicts periodic motion $P = P_4 \circ P_4$ in Fig. 10. Periodic motion $P = P_4 \circ P_4$ is periodic motion
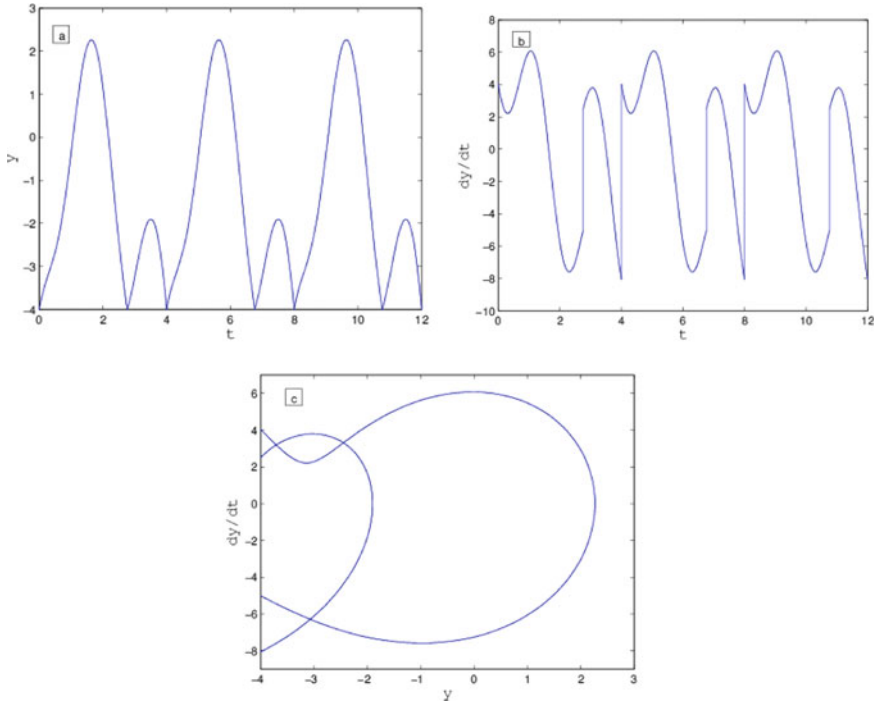
Fig. 10 Periodic motion $P = P_4 \circ P_4$

with both two impacts on lower side of the clearance. The initial conditions are $t_0 = 0$, $\dot{y}_0 = -8.06$. It can be seen that the time between impacts is different, that is the impact time parameters $q \neq 1/2$, which is similar to the case of period-1 periodic motion $P = P_1 \circ P_2$ in [20].

5 Conclusions

In this chapter, the complex motions of an inclined impact oscillator with an external excitation were investigated using the theory of flow switchability for the discontinuous dynamical systems. Based on domains and boundaries defined, the occurrence or vanishing conditions of stick motions and grazing flows on various discontinuous boundaries were presented. Then periodic motions were investigated by mapping dynamics of the discontinuous dynamical systems, the generic mappings and generalized mappings structures were shown, the analytical existence conditions of two periodic motions without stick were obtained. The numerical simulations were presented to provide a better understanding of complicated dynamics of such pair.

References

1. Masri SF, Caughey TK (1966) On the stability of the impact damper. J Appl Mech 33(3):586–92
2. Bapat CN, Popplewell N, Mclachlan K (1983) Stable periodic motions of an impact-pair. J Sound Vib 87(1):19–40
3. Bapat CN, Bapat C (1988) Impact-pair under periodic excitation. J Sound Vib 120(1):53–61
4. Shaw SW, Holmes PJ (1983) A periodically forced piecewise linear oscillator. J Sound Vib 90(1):129–55
5. Han RPS, Luo ACJ, Deng W (1995) Chaotic motion of a horizontal impact pair. J Sound Vib 181(2):231–50
6. Luo ACJ (2004) Period-doubling induced chaotic motion in the LR model of a horizontal impact oscillator. Chaos, Solitons Fractals 19(4):823–39
7. Guo Y, Luo ACJ (2012) Parametric analysis of bifurcation and chaos in a periodically driven horizontal impact pair. Int J Bifurc Chaos 22(11):1250268
8. Luo ACJ, Guo Y (2013) Vibro-Impact Dyn. John Wiley, New York
9. Yue Y (2011) The dynamics of a symmetric impact oscillator between two rigid stops. Nonlinear Anal Real World Appl 12(1):741–50
10. Wen G, Yin S, Xu H et al (2016) Analysis of grazing bifurcation from periodic motion to quasi-periodic motion in impact-damper systems. Chaos, Solitons Fractals 83:112–18
11. Holmes PJ (1982) The dynamics of repeated impacts with a sinusoidally vibrating table. J Sound Vib 84(2):173–89
12. Luo ACJ, Han RPS (1996) The dynamics of a bouncing ball with a sinusoidally vibrating table revisited. Nonlinear Dyn 10(1):1–18
13. Guo Y, Luo ACJ (2012) Analytical dynamics of a ball bouncing on a vibrating table. In: Proceedings of the ASME 2012 international mechanical engineering congress and exposition. IMECE2012-86075
14. Okniński A, Radziszewski B (2009) Dynamics of impacts with a table moving with piecewise constant velocity. Nonlinear Dyn 58(3):515–523
15. Okniński A, Radziszewski B (2014) Bouncing ball dynamics: Simple model of motion of the table and sinusoidal motion. Int J Non-linear Mech 65:226–235
16. Czolczynski K, Blazejczyk-Okolewska B, Okolewski A (2016) Analytical and numerical investigations of stable periodic solutions of the impacting oscillator with a moving base. Int J Mech Sci 115:325–38
17. Bapat CN (1995) The general motion of an inclined impact damper with friction. J Sound Vib 184(3):417–27
18. Heiman MS, Sherman PJ, Bajaj AK (1987) On the dynamics and stability of an inclined impact pair. J Sound Vib 114(3):535–47
19. Heiman MS, Bajaj AK, Sherman PJ (1988) Periodic motions and bifurcations in dynamics of an inclined impact pair. J Sound Vib 124(1):55–78
20. Zhang YY, Fu XL (2015) On periodic motions of an inclined impact pair. Commun Nonlinear Sci Numer Simul 20(3):1033–42
21. Zhang YY, Fu XL (2019) Stability of periodic motions in an inclined impact pair. Eur Phy J Spec Top 228:1441–1457
22. Fu XL, Zhang YY (2015) Stick motions and grazing flows in an inclined impact oscillator. Chaos, Solitons Fractals 76:218–30
23. Luo ACJ (2009) Discontinuous dynamical systems on time-varying domains. Higher Education Press, Beijing
24. Luo ACJ (2011) Discontinuous dynamical systems. Higher Education Press, Beijing

Nonlinear Dynamics of Deep Open-Ocean Convection: An Analytical Approach

Dmitry V. Kovalevsky and Igor L. Bashmachnikov

Abstract Deep open-ocean convection is a complex multiscale nonlinear dynamical phenomenon observed in few localized regions of the World Ocean. The results of Whitehead's 'tank model' [Whitehead, Stratified convection with multiple states, Ocean Modelling, 2(3–4), 109–121, 2000] show that the dynamic system, that includes a deep convection in a localized convective site and water exchange with a neighboring ocean basin, can exist in multiple steady states. We generalize this 'tank model' for the case of non-zero salinity of the upper layer, which brings the model closer to the real ocean conditions. We then derive exact analytical solutions of the nonlinear transitional dynamics for different model dynamic regimes, and discuss oceanographic implications of the modified model.

1 Introduction

Nonlinearity is a fundamental feature of ocean dynamics throughout the entire spectrum of their spatial and temporal scales—from large-scale ocean circulation to oceanic turbulence [4, 12, 15, 16, 22, 32, 36]. Consequently, the majority of ocean dynamics models, especially realistic computational models, are substantially nonlinear.

Strongly nonlinear ocean dynamics can result in abrupt changes that, dependent on the characteristic timescales, might often be considered as discontinuous transitions. Particularly, models allowing multiple steady states are often prone to abrupt transitions [10, 15, 33, 34, 37, 41].

D. V. Kovalevsky
Climate Service Center Germany (GERICS), Helmholtz-Zentrum Hereon, Fischertwiete 1, 20095 Hamburg, Germany
e-mail: dmitrii.kovalevskii@hereon.de

I. L. Bashmachnikov (✉)
Saint Petersburg State University, Universitetskaya emb. 7-9, 199034 St. Petersburg, Russia
e-mail: i.bashmachnikov@spbu.ru

Nansen International Environmental and Remote Sensing Centre, 14th Line 7 office 49 Vasilievsky Island, 199034 St. Petersburg, Russia

Bistability of the Earth's climate system, manifested in the past as series of transitions between glacial and inter-glacial periods, can be related to bistability of certain ocean phenomena, including deep open-ocean convection [7, 9, 13]. This deep mixing of ocean water to 1000–2000 m depth has been observed only in a few localized regions of the World Ocean. One of the most important regions is located in the Greenland Sea. In this region the largest volume of water of the meridional overturning circulation cell of the Atlantic Ocean is formed [1, 2, 9, 11, 14, 19, 25, 29].

The Atlantic meridional overturning circulation (AMOC) represents a simplified concept of the ocean current system, integrally describing the oceanic mass and heat exchange between the polar and the tropical regions [7]. In this conceptual system the warm and saline tropical water flows in the upper ocean layer to the Arctic through the Atlantic gateway. Intensively releasing heat to the atmosphere in the subpolar regions, part of the water sinks down as the water column becomes gravitationally unstable, and further returns southwards as the deep ocean flow, at the depths of 1000-4000 m. Therefore, the regions of deep convection in the subpolar North Atlantic form a link between the upper and the lower limbs of the AMOC. Another link, closing the loop, is a gradual upward water flux as a result of the vertical turbulent exchange in the tropics and wind-induced upwelling in the Southern Ocean [9]. Being an intrinsic part of this circulation cell, variations of the intensity of deep ocean convection should modify the intensity of the meridional overturning circulation, affecting the Earth climate system [24, 26]. However, due to a number of positive and negative feedbacks, the inter-dependence of the intensity of deep convection and of the intensity of AMOC is not straightforward [9, 30].

The intensity of the deep convection, in particular, is affected by heat and haline/freshwater fluxes to the deep convection sites. For example, a model study suggests that a decrease of salinity in the Greenland Sea can decrease and totally stop the deep convection in the region [35].

The multi-scale dynamic process of deep open-ocean convection has been studied within different, primarily nonlinear, ocean general circulation and box models [3, 8, 10, 15, 27, 28, 33, 34, 37, 41].

The Whitehead's 'tank model' [37] might be seen as an interesting hybrid of two classes of ocean models, where a one-dimensional mixed layer model is fused with a box model. This simplified dynamic system can be used to model inter-dependence between the intensity of the deep convection and that of cross-basin fluxes at different levels (a proxy for the AMOC). It is also important that this model allows multiple steady states, and that the theoretical results [37] were later confirmed in series of laboratory experiments [38–40]. The model regimes were originally studied by [37] who combined analytical and numerical methods. The full analytical description of the model's steady states in the particular case of a constant (time-independent) heat flux from the ocean to the atmosphere was obtained in our previous study [5].

However, in the original version of Whitehead's 'tank model' above, an assumption of zero salinity of the upper layer restrain applying the model results to the real ocean. In the present chapter we generalize the Whitehead's 'tank model' to account for a realistic salinity of the upper water layer (Sect. 2), derive exact analytical solu-

tions for the transitional dynamics of the modified nonlinear model (Sect. 3), and discuss oceanographic implications of the model (Sect. 4).[1]

2 Whitehead's 'Tank Model' with Saline Upper Layer

In the present section, we describe the setup of the modified Whitehead's 'tank model' (Sect. 2.1), which includes realistic salinity of the upper layer of the 'big basin'. This brings the model closer to the real ocean conditions (see a discussion and numerical estimates in Sect. 4), as compared to its original version described in [37], as well as our recent analytical study [5], where fresh upper layer was used (zero salinity). Further on, we discuss the model equations (Sect. 2.2).

2.1 Model Description

The Whitehead's 'tank model' [37] was developed to describe laboratory experiments in a tank composed by two interconnected basins: a 'big basin' and a 'small basin' (Fig. 1). As both the laboratory apparatus and the related mathematical model were designed to simulate development of deep open-ocean convection and its effect on the cross-basin exchange, the 'small basin' should represent a localized ocean convective region (Fig. 1, to the left), while the 'big basin'—a much larger neighbouring ocean region (Fig. 1, to the right).

In the present model configuration, water structure in the 'big basin' is characterized by the upper layer of depth d, temperature T_0 and salinity S_1 and the lower layer of the same temperature T_0 and salinity S_0 ($S_0 > S_1$). As mentioned above, we generalize the model by [37] by considering the upper layer salinity S_1 to be different from zero: $0 \leq S_1 < S_0$.

The water exchange between the basins takes place at three levels: the upper level (zero depth in the mathematical model), the mid-depth level (depth $D/2$) and the bottom level (depth D). We will always assume that the upper layer in the 'big basin' is shallower than the mid-depth level, i.e.

$$d < \frac{D}{2}. \tag{1}$$

The flow between the basins at i-th depth will be denoted as Q_i ($i = 1, 2, 3$). We will assume that the flow Q_i is positive ($Q_i > 0$) when it is directed from the 'big

---

[1] In a subsequent paper [23] written well after submission of the present book chapter, we make further generalizations of the Whitehead's 'tank model' by extending its analytical treatment to the case of an arbitrary temperature and salinity of the layers in the 'big basin' for both constant and temperature-dependent heat fluxes to the atmosphere in the 'small basin'.
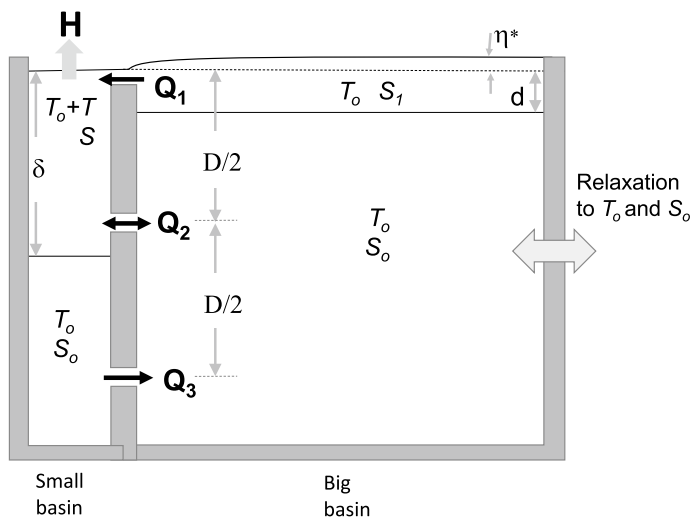
Fig. 1 The 'tank model' setup. The system under study consists of two water basins, a big one and a small one. The 'big basin' has time-independent water temperature T_0 and salinity $S = S_0$ of the lower layer and T_0 and $S = S_1$ of the upper layer. The depth of the upper layer (d) is fixed. In the 'small basin', exposed to the surface cooling, the convective upper layer has a varying depth δ, temperature $T_0 + T$ ($T < 0$) and salinity S. The exchange between the basins is at depths 0, $D/2$, and D. See Sect. 2.1 for further detail

basin' to the 'small basin', and is negative ($Q_i < 0$) when the flow is in the opposite direction.

Temperature (T_0) and salinity (S_0, S_1) for both layers in the 'big basin' are assumed to be maintained at the constant level, not affected by water exchange with the 'small basin'.

The 'small basin' is exposed to surface cooling, with the surface heat flux H maintained at the constant level (we assume that $H > 0$). Here surface cooling and water exchange with the 'big basin' lead to development of a convective layer of depth δ. These processes also modify the temperature anomaly of the convective layer (T), i.e. the temperature difference between the 'small basin' and the 'big basin', as well as the salinity of the convective layer (S) in the 'small basin'. Note that the temperature anomaly is always negative ($T < 0$).

2.2 Model Equations and Non-Dimensional Variables

In the spirit of hydraulic models, we assume that the flow Q_i is proportional to the pressure difference between the 'big' and the 'small' basin at the depth level i,

$$Q_i = C_i \left(p_{0i} - p_i \right), \qquad i = 1, 2, 3, \tag{2}$$

where p_{0i} is the pressure in the 'big' basin, p_i is the pressure in the 'small' basin, and C_i is the 'inverse hydraulic resistance', characterizing the intensity of water exchange between the basins for a unit pressure difference. In the model we assume that the 'inverse hydraulic resistance' at the second (mid-depth) and the third (bottom) level are identical, while the inverse hydraulic resistance at the first (upper) level is smaller than either of them,

$$C_1 = \gamma C, \qquad C_2 = C_3 = C, \tag{3}$$

where γ is a positive scaling factor, less than unity,

$$0 < \gamma < 1. \tag{4}$$

The linear equation of state for seawater is used,

$$\rho(T, S) = \rho_0 (1 + \beta S - \alpha T), \tag{5}$$

where ρ_0 is the reference density at $T = 0$, $S = 0$ (recall that T is the temperature deviation from T_0, not the water temperature itself), α is the coefficient of thermal expansion and β is the coefficient of haline contraction (we assume $\alpha = $ const, $\beta = $ const).

Performing a quasi-hydrostatic analysis for the present version of the model with the saline upper layer, analogous to the analysis made by [37] for the case of the fresh upper layer, we identify three threshold levels of the temperature anomaly T,

$$T_{\text{nil}} = -\frac{\beta(S_0 - S_1)}{\alpha}\left[1 - 2\frac{d}{D}\right], \tag{6}$$

$$T_{\text{c}} = -\frac{\beta(S_0 - S_1)}{\alpha}\left[1 - \frac{2\gamma}{1 + 2\gamma}\frac{d}{D}\right], \tag{7}$$

$$T_{\text{cc}} = -\frac{\beta(S_0 - S_1)}{\alpha}\left[1 + \frac{2\gamma}{1 - \gamma}\frac{d}{D}\right]. \tag{8}$$

T_{nil} is the upper boundary of the temperature anomalies compatible with a steady water exchange between the basins, T_{c} separates dynamic *Regime A* from *Regime B*, and T_{cc} separates dynamic *Regime B* from *Regime C*. Here for *Regime A* there is no flow at the bottom level; for *Regime B* there is a water exchange at all the three levels, with an outflow to the 'big' basin at the mid-depth level; and for *Regime C* there is again a water exchange at all the three levels, now with an inverse flow (to the 'small' basin) at the mid-depth level.

It is convenient to rewrite the problem using non-dimensional variables. To do this, we introduce the characteristic temperature T_{s} (in °C),

$$T_{\text{s}} = \frac{\beta(S_0 - S_1)}{\alpha}, \tag{9}$$

and the characteristic flow Q_s (in m^3/s),

$$Q_s = \frac{\gamma}{\gamma + 2} C \rho_0 g \beta \left(S_0 - S_1\right) D. \tag{10}$$

We also define the characteristic rate of the heat flux between the basins W_s (in W), the characteristic sea-surface heat flux H_s (in W/m^2), and the characteristic timescale t_s (in s),

$$W_s = \rho_0 c_p T_s Q_s, \qquad H_s = \frac{W_s}{A_0}, \qquad t_s = \frac{A_0 \delta}{W_s}. \tag{11}$$

In (10)–(11) g is the gravity acceleration, c_p is the specific heat capacity of water, A_0 is the surface area of the 'small' basin, and δ is the equilibrium depth of the upper layer in the 'small' basin (regarding calculation of δ, see [37] and a brief discussion in [5]).

Then, we introduce a non-dimensional parameter $\widetilde{d}$ defining the geometry of the problem: $\widetilde{d}$ is the ratio of the depth d of the upper layer to the depth D,

$$\widetilde{d} = \frac{d}{D}. \tag{12}$$

(Hereafter, the non-dimensional variables and parameters will be marked with tilde.) In view of (1),

$$0 < \widetilde{d} < \frac{1}{2}. \tag{13}$$

The state variables of the system, the non-dimensional temperature anomaly $\widetilde{T}$ and the scaled salinity anomaly $\widetilde{S}$, are now defined as

$$\widetilde{T} = \frac{T}{T_s}, \qquad \widetilde{S} = \frac{S - S_1}{S_0 - S_1} \tag{14}$$

and are often referred below just as temperature and salinity.

After introducing the non-dimensional inter-basin flows $\widetilde{Q}_i$ and the sea-surface heat flux $\widetilde{H}$,

$$\widetilde{Q}_i = \frac{Q_i}{Q_s}, \qquad \widetilde{H} = \frac{H}{H_s}, \tag{15}$$

and also defining the non-dimensional time

$$t' = \frac{t}{t_s} \tag{16}$$

(below the prime in t' will be omitted), we can finally write the non-dimensional dynamic system describing an evolution of the state variables (14) as

$$\dot{\widetilde{T}} = -\widetilde{H} + \widetilde{T}\left[\widetilde{Q}_1 \cdot \mathbf{1}\left(-\widetilde{Q}_1\right) + \widetilde{Q}_2 \cdot \mathbf{1}\left(-\widetilde{Q}_2\right) + \widetilde{Q}_3 \cdot \mathbf{1}\left(-\widetilde{Q}_3\right)\right], \quad (17a)$$

$$\dot{\widetilde{S}} = \widetilde{Q}_2\left[\widetilde{S} \cdot \mathbf{1}\left(-\widetilde{Q}_2\right) + \mathbf{1}\left(\widetilde{Q}_2\right)\right] + \widetilde{Q}_3\left[\widetilde{S} \cdot \mathbf{1}\left(-\widetilde{Q}_3\right) + \mathbf{1}\left(\widetilde{Q}_3\right)\right]. \quad (17b)$$

Here the unit step function $\mathbf{1}(x)$ is defined as

$$\mathbf{1}(x) \equiv \begin{cases} 1, & x \geq 0, \\ 0, & x < 0. \end{cases} \quad (18)$$

In particular, the three non-dimensional thresholds for $\widetilde{T}$ corresponding to (6)–(8) take the form

$$\widetilde{T}_{\text{nil}} = -\left[1 - 2\widetilde{d}\right], \quad (19)$$

$$\widetilde{T}_{\text{c}} = -\left[1 - \frac{2\gamma}{1 + 2\gamma}\widetilde{d}\right], \quad (20)$$

$$\widetilde{T}_{\text{cc}} = -\left[1 + \frac{2\gamma}{1 - \gamma}\widetilde{d}\right]. \quad (21)$$

The dependence of three temperature thresholds (19)–(21) from the parameter γ is visualized in Fig. 2 for a particular case of $\widetilde{d} = 0.1$. The upper boundary for temperature ($\widetilde{T}_{\text{nil}}$) does not depend on γ. The threshold separating *Regimes A* and *B* ($\widetilde{T}_{\text{c}}$) steadily and moderately increases with γ, while the threshold separating *Regimes B* and *C* ($\widetilde{T}_{\text{cc}}$) steadily decreases with γ, demonstrating a singular behaviour for $\gamma = 1$ ($\widetilde{T}_{\text{cc}} \to -\infty$ when $\gamma \to 1 - 0$). $\widetilde{T}_{\text{c}}$ and $\widetilde{T}_{\text{cc}}$ coincide for $\gamma = 0$.

From mathematical standpoint, generalizing the Whitehead's 'tank model' to the case of the saline upper layer results in multiplying the formulae by the salinity difference $(S_0 - S_1)$ appearing in (6)–(10), while in the case of the fresh upper layer the formulae are multiplied by S_0 only [5, 37]. Also, an expression for the scaled salinity $\widetilde{S}$ in (14) becomes somewhat more complex than before. However, it should be stressed that all expressions with non-dimensional parameters retain the same form as in the previous publications [5, 37].

In Sect. 3.2 below the dynamic system (17), its fixed points and its nonlinear transitional dynamics for *Regimes A-C* will be considered in detail.

3 Transitional Dynamics: Exact Analytical Solutions

The dynamic system (17) is nonlinear. However, it can be treated analytically in depth. In our previous work [5] we derived exact analytical expressions for the fixed points, and also studied their stability within the Lyapunov theory. By solving the linearized dynamic system, we might also explore the transitional dynamics of the 'tank' model in the linear approximation, generally, valid for small perturbations from equilibria.
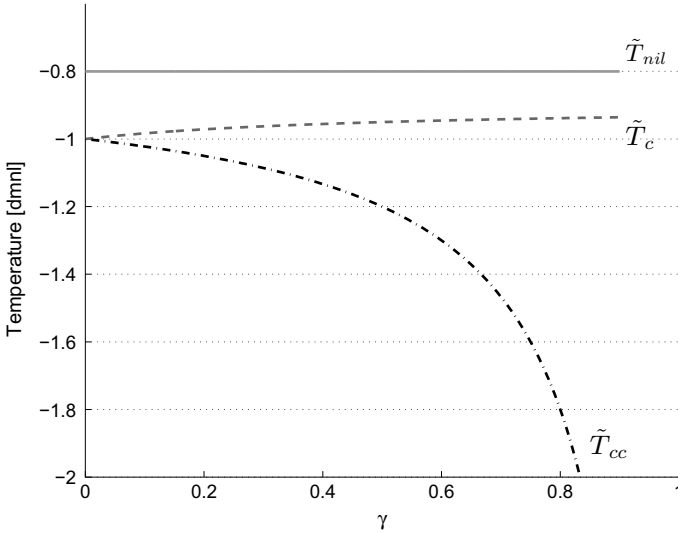
Fig. 2 Dependences of three non-dimensional temperature thresholds, $\widetilde{T}_{\text{nil}}$, $\widetilde{T}_{\text{c}}$, and $\widetilde{T}_{\text{cc}}$, on γ for $\widetilde{d} = 0.1$. See Sect. 2.2 for further details

However, this nonlinear model, quite surprisingly, allows, in many cases, derivation of exact closed-form solutions of the system of nonlinear equations. Therefore, we can go beyond the linear dynamics and explore rigorously the dynamics of *finite* perturbations.

In Sect. 3.1 below we provide a generic framework for studying the transitional dynamics of the 'tank model' in all its three dynamic regimes (*Regimes A-C*). Mathematically the analysis will be repeatedly reduced to the Riccati equation. An in-depth analysis of transitional solutions of the 'tank model' will be then provided in Sect. 3.2.

3.1 A Generic Model of Transitional Dynamics

In this section we provide a theory of the Riccati equation that will be extensively used in Sect. 3.2 below to derive exact analytical solutions for all three dynamic regimes of the 'tank model'.

3.1.1 Symmetric Case: A Special Riccati Equation

Consider an ordinary differential equation (ODE)

$$\dot{y} + ay^2 = b, \tag{22}$$
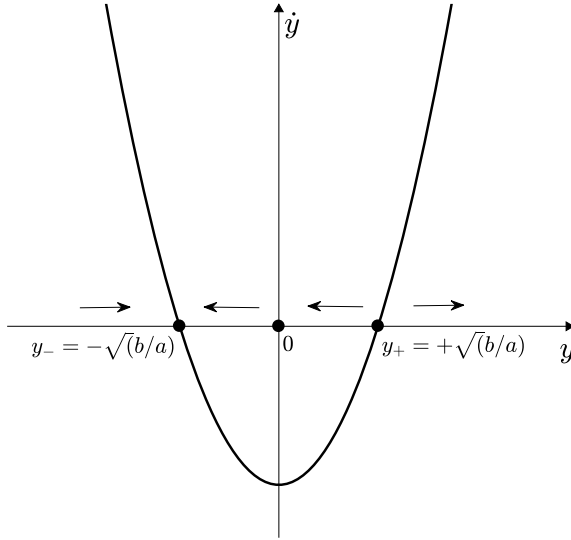
Fig. 3 The $(y, \dot{y})$ plane for a special Riccati equation (22). Arrows mark the directions of evolution of y for finite perturbations near the points of equilibria. The fixed point y_- is stable, while the fixed point y_+ is unstable

where both parameters a and b are constant and negative:

$$a < 0, \qquad b < 0. \tag{23}$$

We will call this ODE *a special Riccati equation*, although, strictly speaking, this is only a particular case of a conventional special Riccati equation $\dot{y} + ay^2 = bt^\alpha$ with $\alpha = 0$ [21].

Obviously, Eq. (22) with the sign constraints for its parameters as in (23) has two fixed points

$$y_- = -\sqrt{\frac{b}{a}}, \qquad y_+ = +\sqrt{\frac{b}{a}}, \tag{24}$$

of which the positive one $(y_+ = +\sqrt{b/a})$ is unstable, while the negative one $(y_- = -\sqrt{b/a})$ is stable (Fig. 3). Indeed, for a perturbation

$$\delta y = y - y_-, \tag{25}$$

we get the linearized Eq. (22) in the form

$$\delta \dot{y} = -\frac{\delta y}{\tau_{\text{lin}}}, \tag{26}$$

where

$$\frac{1}{\tau_{\text{lin}}} = 2\sqrt{ab}. \tag{27}$$

From (25)–(26), if the initial condition of the Riccati equation y_0 (at $t = 0$) is close enough to the stable fixed point y_-, the convergence to the equilibrium approximately obeys the exponential law

$$y(t) \sim y_- + (y_0 - y_-) \exp\left(-\frac{t}{\tau_{\text{lin}}}\right). \tag{28}$$

The Riccati equation (22) can be integrated in a closed form. In the case of sign constraints (23) and, consequently, of $ab > 0$, the exact analytical solution of (22) takes the form [21]

$$y(t) = \frac{y_0\sqrt{ab} + b \tanh\left(\sqrt{ab} \cdot t\right)}{\sqrt{ab} + ay_0 \tanh\left(\sqrt{ab} \cdot t\right)}, \tag{29}$$

that, in view of (24) and (27), can be rewritten as

$$y(t) = y_- \frac{y_0 + y_- \tanh\left(\frac{t}{2\tau_{\text{lin}}}\right)}{y_- + y_0 \tanh\left(\frac{t}{2\tau_{\text{lin}}}\right)}. \tag{30}$$

If the initial condition coincides with the fixed point ($y_0 = y_+$), then $y(t) \equiv y_+$ for all $t > 0$. However, this equilibrium is unstable. For the initial values of y_0 less than y_+ ($-\infty < y_0 < y_+$) $y(t)$ converges to the stable fixed point y_- at $t \to +\infty$. On the contrary, for $y_0 > y_+$ the solution manifests a singular behavior reaching *infinite* value at *finite* time. This dependence of asymptotic behavior of $y(t)$ on the initial condition can be easily seen from (30), given that $\tanh x \to 1$ when $x \to +\infty$, and that $y_- = -y_+$.

At big t, given

$$\tanh kt \sim 1 - 2 \exp\left(-2kt\right), \qquad k > 0, \qquad t \to +\infty, \tag{31}$$

we can easily derive from (30) the asymptotic law of convergence

$$y(t) \sim y_- \left[1 + 2\frac{y_0 - y_-}{y_0 + y_-} \exp\left(-\frac{t}{\tau_{\text{lin}}}\right)\right], \tag{32}$$

that is close to (28), as expected, when y_0 is close to y_-.

3.1.2   Asymmetric Case: A General Riccati Equation

Consider now an ODE

$$\dot{y} + ay^2 + dy = b, \tag{33}$$

where all three parameters are constant and negative:

$$a < 0, \quad d < 0, \quad b < 0 \tag{34}$$

(as will always be the case in applications to *Regimes A-C* below). We will call this ODE *a general Riccati equation*, although, again, this is only a particular case of the conventional general Riccati equation, where the parameters a, d, b entering (33) may be arbitrary continuous functions $a(t)$, $d(t)$, $b(t)$ [21].

The two fixed points of (33), the roots of a quadratic equation

$$ay^2 + dy - b = 0, \tag{35}$$

are

$$y^*_\pm = -\frac{d \pm \sqrt{d^2 + 4ab}}{2a}. \tag{36}$$

Given the sign constraints (34), the two roots of (35) are real and have opposite sings: $y^*_- < 0$, $y^*_+ > 0$.

By substituting the variable,

$$\widetilde{y} = y + \frac{d}{2a}, \tag{37}$$

the general Riccati equation (33) is reduced to its special form (22) analysed in Sect. 3.1.1 above,

$$\dot{\widetilde{y}} + a\widetilde{y}^2 = b + \frac{d^2}{4a}, \tag{38}$$

where the signs of two effective parameters obey the same constraints as in the previous section. Therefore, all results derived in Sect. 3.1.1 are applicable for (38) as well.

In particular, the analogues of Eqs. (24) and (27) take the form

$$\widetilde{y}_\pm = \pm\sqrt{\frac{b}{a} + \frac{d^2}{4a^2}}, \tag{39}$$

$$\frac{1}{\tau^*_{\text{lin}}} = 2\sqrt{ab + \frac{d^2}{4}}. \tag{40}$$

The exact analytical solution of (33) is

$$y(t) = \widetilde{y}_- \frac{\left(y_0 + \frac{d}{2a}\right) + \widetilde{y}_- \tanh\left(\frac{t}{2\tau_{\text{lin}}^*}\right)}{\widetilde{y}_- + \left(y_0 + \frac{d}{2a}\right) \tanh\left(\frac{t}{2\tau_{\text{lin}}^*}\right)} - \frac{d}{2a}, \tag{41}$$

while the solution of the linearized equation, analogous to (28), takes the form

$$y(t) \sim y_-^* + \left(y_0 - y_-^*\right) \exp\left(-\frac{t}{\tau_{\text{lin}}^*}\right). \tag{42}$$

3.2   Exact Analytical Solutions for Different Dynamic Regimes

Based on the generic model of transitional dynamics reducible to the Riccati equation, we now derive exact analytical solutions for the transitional dynamics in all three model regimes (*Regimes A-C*). As we will see, in the case of *Regimes A-B*, the full analytical description of the model behavior is possible, while in a more complex *Regime C* the rigorous analytical description of the 'tank model' can be derived only partially.

3.2.1   *Regime A:* Flows at Upper and Mid-Depth Levels Only

In *Regime A*, there is flow from the 'big' basin to the 'small' basin at upper level ($\widetilde{Q}_1 > 0$) exactly balanced by flow from the 'small' basin to the 'big' basin at the mid-depth level ($\widetilde{Q}_2 < 0$); there is no flow at the bottom level ($\widetilde{Q}_3 = 0$). For these constraints on the flows, a general dynamic system (17) takes the form

$$\dot{\widetilde{T}} = -\widetilde{H} - \widetilde{Q}_1\widetilde{T}, \tag{43a}$$

$$\dot{\widetilde{S}} = -\widetilde{Q}_1\widetilde{S}. \tag{43b}$$

As shown by [37], the mutually balancing flows at the upper and the mid-depth levels take the form

$$\widetilde{Q}_1 = -\widetilde{Q}_2 = -\frac{\gamma + 2}{2\,(\gamma + 1)}\left[1 + \widetilde{T} - 2\widetilde{d}\right]. \tag{44}$$

As follows from (43), also obvious from the design of the model (Fig. 1), the equilibrium salinity in *Regime A* is equal to zero, $\widetilde{S}^{\text{A}} = 0$. (Note that, according to (14), in the dimensional form this means that the salinity of the mixed layer in the 'small' basin, S, is equal to that of the upper layer in the 'big' basin, S_1.) In view of the model design, we restrict our analysis of nonlinear transitional dynamics to finite temperature perturbations. As shown in [5], the exact dynamic equation for $\widetilde{T}$ in *Regime A* takes the form

$$\dot{\widetilde{T}} = \frac{\gamma+2}{2(\gamma+1)}\widetilde{T}^2 - \frac{\gamma+2}{2(\gamma+1)}\widetilde{T}_{\text{nil}}\widetilde{T} - \widetilde{H}, \tag{45}$$

where $\widetilde{T}_{\text{nil}}$ is provided by (19). The stable fixed point of (45) is

$$\widetilde{T}_-^{\text{A}} = -\frac{1}{2}\left[|\widetilde{T}_{\text{nil}}| + \sqrt{\widetilde{T}_{\text{nil}}^2 + 8\frac{\gamma+1}{\gamma+2}\widetilde{H}}\right]. \tag{46}$$

Regime A with steady flow and the equilibrium (46) is possible for a certain range of values of the sea-surface heat flux $\widetilde{H}$

$$0 < \widetilde{H} < \widetilde{H}^{\text{AB}}, \tag{47}$$

where a threshold heat flux $\widetilde{H}^{\text{AB}}$ is defined as

$$\widetilde{H}^{\text{AB}} = -\frac{\gamma+2}{2\gamma+1}\widetilde{d}\widetilde{T}_{\text{c}} \tag{48}$$

(note that $\widetilde{H}^{\text{AB}} > 0$ in view of $\widetilde{T}_{\text{c}} < 0$, see (20)).

The nonlinear temperature dynamic Eq. (45) takes the form of the general Riccati equation (33) with the signs of parameters as in (34). Therefore, we can now apply to (45) the theory presented in Sect. 3.1.2. In particular, the characteristic timescale (40) is explicitly given as

$$\frac{1}{\tau_{\text{lin}}^{\text{A}}} = \frac{\gamma+2}{2(\gamma+1)}\sqrt{\widetilde{T}_{\text{nil}}^2 + 8\frac{\gamma+1}{\gamma+2}\widetilde{H}}, \tag{49}$$

and the exact analytical solution (41) for the nonlinear transitional dynamics of finite temperature perturbations can be expressed as

$$\widetilde{T}^{\text{A}}(t)$$
$$= -\frac{1}{2}\left[|\widetilde{T}_{\text{nil}}| - \sqrt{\widetilde{T}_{\text{nil}}^2 + 8\frac{\gamma+1}{\gamma+2}\widetilde{H}} \times \frac{(2\widetilde{T}_0 + |\widetilde{T}_{\text{nil}}|) - \sqrt{\widetilde{T}_{\text{nil}}^2 + 8\frac{\gamma+1}{\gamma+2}\widetilde{H}} \times \tanh\left(\frac{t}{2\tau_{\text{lin}}^{\text{A}}}\right)}{\sqrt{\widetilde{T}_{\text{nil}}^2 + 8\frac{\gamma+1}{\gamma+2}\widetilde{H}} - (2\widetilde{T}_0 + |\widetilde{T}_{\text{nil}}|) \times \tanh\left(\frac{t}{2\tau_{\text{lin}}^{\text{A}}}\right)}\right], \tag{50}$$

where $\widetilde{T}_0$ is the initial condition for $\widetilde{T}$ at $t = 0$, and $\tau_{\text{lin}}^{\text{A}}$ is provided by (49). As expected, for initial conditions compatible with *Regime A* ($\widetilde{T}_{\text{c}} < \widetilde{T}_0 < \widetilde{T}_{\text{nil}}$), the solution (50) converges to the stable fixed point (46) when $t \to +\infty$.

3.2.2   *Regime B:* Flows at All Levels

In *Regime B*, there are flows at all three levels. At the upper level, the flow is directed from the 'big' basin to the 'small' basin ($\widetilde{Q}_1 > 0$), while at the mid-depth

and at the bottom levels the flows are directed from the 'small' basin to the 'big' basin ($\widetilde{Q}_2 < 0$, $\widetilde{Q}_3 < 0$). A general dynamic system (17) takes the same form as in *Regime A* (Sect. 3.2.1, (43)). However, the flows $\widetilde{Q}_i$ ($i = 1, 2, 3$) are now given by the expressions [37]

$$\widetilde{Q}_1 = -\frac{3}{2}\left[1 + \widetilde{T} - \widetilde{S}\right] + 2\widetilde{d}, \tag{51}$$

$$\widetilde{Q}_2 = \frac{1 - \gamma^{-1}}{2}\left[1 + \widetilde{T} - \widetilde{S}\right] - \widetilde{d}, \tag{52}$$

$$\widetilde{Q}_3 = \frac{2 + \gamma^{-1}}{2}\left[1 + \widetilde{T} - \widetilde{S}\right] - \widetilde{d}, \tag{53}$$

and the expression for $\widetilde{Q}_1$ in (43) should be substituted now by (51).

In equilibrium, we again have $\widetilde{S}^{\mathrm{B}} = 0$ (or $S = S_1$ in the dimensional form), therefore we restrict again our analysis of the nonlinear transitional dynamics to finite temperature perturbations. The exact dynamic equation for $\widetilde{T}$ in *Regime B* takes the form [5]

$$\dot{\widetilde{T}} = \frac{3}{2}\widetilde{T}^2 + \left(\frac{3}{2} - 2\widetilde{d}\right)\widetilde{T} - \widetilde{H}, \tag{54}$$

with the stable fixed point of (54)

$$\widetilde{T}^{\mathrm{B}}_- = -\frac{1}{3}\left[\left(\frac{3}{2} - 2\widetilde{d}\right) + \sqrt{\left(\frac{3}{2} - 2\widetilde{d}\right)^2 + 6\widetilde{H}}\right]. \tag{55}$$

The steady flow and the equilibrium (55) for *Regime B* is possible in the range of the sea-surface heat fluxes $\widetilde{H}$

$$\widetilde{H}^{\mathrm{AB}} < \widetilde{H} < \widetilde{H}^{\mathrm{BC}}, \tag{56}$$

where the threshold heat flux $\widetilde{H}^{\mathrm{AB}}$ is provided by (48), and the threshold heat flux $\widetilde{H}^{\mathrm{BC}}$ is equal to

$$\widetilde{H}^{\mathrm{AB}} = -\frac{\gamma + 2}{1 - \gamma}\widetilde{d}\widetilde{T}_{\mathrm{cc}} \tag{57}$$

($\widetilde{H}^{\mathrm{BC}} > 0$ in view of $\widetilde{T}_{\mathrm{cc}} < 0$, see (21)).

The nonlinear temperature dynamics Eq. (54) takes again the form of the general Riccati equation (33) with the same signs of the parameters as in (34). Applying to (54) the results from Sect. 3.1.2, we get the characteristic timescale (40):

$$\frac{1}{\tau^{\mathrm{B}}_{\mathrm{lin}}} = \sqrt{\left(\frac{3}{2} - 2\widetilde{d}\right)^2 + 6\widetilde{H}}, \tag{58}$$

while the exact analytical solution (41) of the nonlinear transitional dynamics can be explicitly written as

$$
\widetilde{T}^{B}(t)
$$

$$
= -\frac{1}{3}\left[\left(\frac{3}{2} - 2\widetilde{d}\right) - \sqrt{\left(\frac{3}{2} - 2\widetilde{d}\right)^{2} + 6\widetilde{H}} \times \frac{\left[3\widetilde{T}_{0} + \left(\frac{3}{2} - 2\widetilde{d}\right)\right] - \sqrt{\left(\frac{3}{2} - 2\widetilde{d}\right)^{2} + 6\widetilde{H}} \times \tanh\left(\frac{t}{2\tau_{\text{lin}}^{B}}\right)}{\sqrt{\left(\frac{3}{2} - 2\widetilde{d}\right)^{2} + 6\widetilde{H}} - \left[3\widetilde{T}_{0} + \left(\frac{3}{2} - 2\widetilde{d}\right)\right] \times \tanh\left(\frac{t}{2\tau_{\text{lin}}^{B}}\right)}\right], \quad (59)
$$

where τ_{lin}^{B} is given by (58). Like above, for the initial conditions compatible with *Regime B* ($\widetilde{T}_{\text{cc}} < \widetilde{T}_{0} < \widetilde{T}_{\text{c}}$), the solution (59) converges to the stable fixed point (55) for $t \to +\infty$.

The difference between the exact nonlinear solution (59) and the approximate linearized transitional dynamics

$$
\widetilde{T}(t) \sim \widetilde{T}_{-}^{B} + \left(\widetilde{T}_{0} - \widetilde{T}_{-}^{B}\right) \exp\left(-\frac{t}{\tau_{\text{lin}}^{B}}\right), \quad (60)
$$

for *Regime B* is presented in Figs. 4 and 5.

Figure 4 corresponds to the case $\gamma = 0.25$, $\widetilde{d} = 0.04$. $\widetilde{d}$ is chosen as the characteristic ratio of the pycnocline depth to the water depths in the Greenland Sea (see Sect. 4 for more detail). The value of γ is based on estimates of the oceanic water transport from the Arctic to the Greenland Sea, which at the mid-depth levels is 4 times that of the fresher upper layer [31]. However, strictly speaking, the real value of γ is largely uncertain. Figure 5 corresponds to the case $\gamma = 0.75$, $\widetilde{d} = 0.1$.
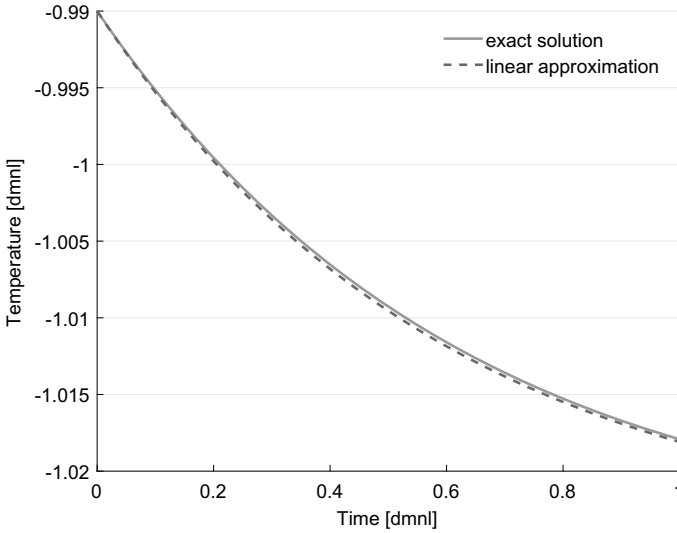
Fig. 4 A linear approximation and the exact nonlinear solution for transitional dynamics for *Regime B* with $\gamma = 0.25$ and $\widetilde{d} = 0.04$
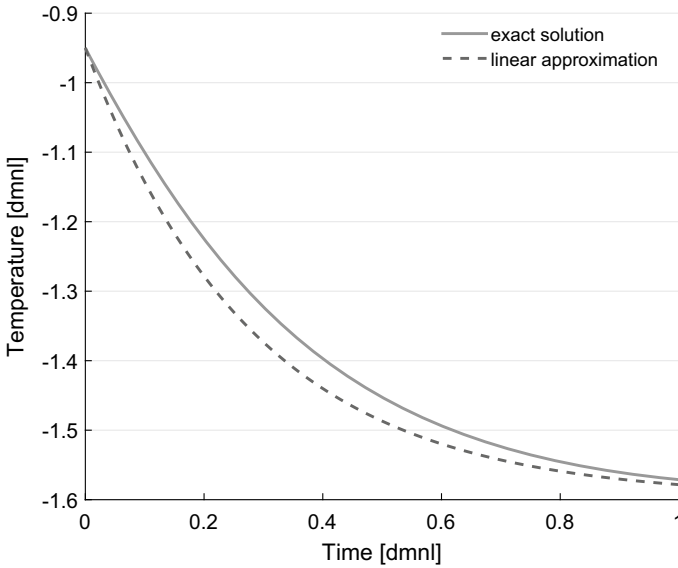
Fig. 5 A linear approximation and the exact nonlinear solution for transitional dynamics for *Regime B* with $\gamma = 0.75$ and $\widetilde{d} = 0.1$

In both examples, the initial conditions for temperature $\widetilde{T}_0$ are chosen to be very close (yet a bit lower) than the temperature threshold $\widetilde{T}_c(\gamma, \widetilde{d})$, while the surface heat fluxes $\widetilde{H}$ are chosen in such a way that the equilibrium temperature $\widetilde{T}^B$ is very close (yet a bit higher) than the temperature threshold $\widetilde{T}_{cc}(\gamma, \widetilde{d})$. This means that, in the course of convergence to the equilibrium, the temperature will pass virtually through the whole temperature range $\widetilde{T}_{cc}(\gamma, \widetilde{d}) < \widetilde{T} < \widetilde{T}_c(\gamma, \widetilde{d})$, where *Regime B* is valid.

Figure 4 shows that the linear approximation virtually coincides with the exact nonlinear solution. In Fig. 5, the linear approximation also is found to approximate the transitional dynamics fairly well, however, some differences between the linear approximation and the exact nonlinear solution do exist.

3.2.3 *Regime C:* Flows at All Levels, Inverse Flow at Mid-Depth Level

For *Regime C*, there are flows at all three levels. However, the flow at the mid-depth level is now oppositely directed to that in *Regime B*, i.e. from the 'big' basin to the 'small' basin. Consequently, the flows at different depth levels have the following signs: $\widetilde{Q}_1 > 0$, $\widetilde{Q}_2 > 0$, $\widetilde{Q}_3 < 0$. The dynamic system (17) now takes the form

$$\dot{\widetilde{T}} = -\widetilde{H} + \widetilde{Q}_3\widetilde{T}, \tag{61a}$$

$$\dot{\widetilde{S}} = \widetilde{Q}_2 + \widetilde{Q}_3\widetilde{S}. \tag{61b}$$

The same expressions (51)–(53) for the flows $\widetilde{Q}_i$ for *Regime B*, are also applicable for *Regime C*.

A distinctive feature of *Regime C* is non-zero salinity in the stable fixed point: $\widetilde{S} > 0$ or, in the dimensional form, $S > S_1$. Explicitly, as shown in [5], the stable fixed point $\left(\widetilde{T}_-^C, \widetilde{S}_-^C\right)$ is

$$\widetilde{T}_-^C = -\frac{\gamma \widetilde{H}}{2} \frac{\left(3 - 2\widetilde{d}\right) + \sqrt{\left(3 - 2\widetilde{d}\right)^2 + \frac{8}{\gamma}\left[(2\gamma + 1)\,\widetilde{H} - (\gamma + 2)\,\widetilde{d}\right]}}{(2\gamma + 1)\,\widetilde{H} - (\gamma + 2)\,\widetilde{d}}, \qquad (62)$$

$$\widetilde{S}_-^C = \frac{1}{2\gamma + 1}\left[(1 - \gamma) + (\gamma + 2)\,\frac{\widetilde{d}}{\widetilde{H}}\,\widetilde{T}_-^C\right]. \qquad (63)$$

The steady flow in *Regime C* with the equilibrium (62)–(63) is possible when

$$\widetilde{H} > \widetilde{H}^{BC}, \qquad (64)$$

where $\widetilde{H}^{BC}$ is provided by (57).

In general, it is not possible to analytically integrate this dynamic system (61), and we cannot provide analytical solutions for temperature and salinity for *Regime C*. However, for the transitional dynamics, one can derive exact analytical solutions for the flows at all three levels: $\widetilde{Q}_i$ ($i = 1, 2, 3$). The procedure is outlined below.

First, we note that, in view of (51)–(53), any flow can be derived from any other flow by a simple linear transform. In particular,

$$\widetilde{Q}_2\left(\widetilde{T}, \widetilde{S}\right) = a_0 \widetilde{Q}_3\left(\widetilde{T}, \widetilde{S}\right) + b_0, \qquad (65)$$

where the parameters a_0, b_0 are equal to

$$a_0 = -\frac{1 - \gamma}{2\gamma + 1}, \qquad b_0 = -\frac{\gamma + 2}{2\gamma + 1}\widetilde{d}. \qquad (66)$$

By substituting (65) into (61), we rewrite the salinity dynamic equation as

$$\dot{\widetilde{S}} = b_0 + \widetilde{Q}_3\left(\widetilde{S} + a_0\right). \qquad (67)$$

We now define a new variable z as the difference between non-dimensional temperature and salinity,

$$z \equiv \widetilde{T} - \widetilde{S}, \qquad (68)$$

and note that, according to (53), the flow $\widetilde{Q}_3$ can be expressed as a function of z only:

$$\widetilde{Q}_3[z] = \frac{2\gamma + 1}{2\gamma}[1 + z] - \widetilde{d}. \qquad (69)$$

The flows $\widetilde{Q}_1$ and $\widetilde{Q}_2$ can, of course, be expressed as linear functions of z in a similar way.

We now subtract (67) from (61) and obtain the nonlinear ODE of the single variable z:

$$\dot{z} = \widetilde{Q}_3[z](z - a_0) - \left(\widetilde{H} + b_0\right). \tag{70}$$

Explicitly, (70) is again the general Riccati equation

$$\dot{z} = \frac{2\gamma + 1}{2\gamma}z^2 + \left(\frac{\gamma + 2}{2\gamma} - \tilde{d}\right)z - \left(\widetilde{H} - \frac{1 - \gamma}{2\gamma} - \tilde{d}\right). \tag{71}$$

Therefore, it is possible to write down an explicit analytical solution for (71), in a similar way, as it has been done for *Regimes A* and *B* (Sects. 3.2.1–3.2.2). We do not provide here an explicit formula for $z(t)$. However, we note that, as soon as $z(t)$ is found, the flow $\widetilde{Q}_3(t)$ can be obtained from (69), while the flows $\widetilde{Q}_1(t)$ and $\widetilde{Q}_2(t)$ can be derived from similar linear expressions.

Having found $\widetilde{Q}_3(t) \equiv \widetilde{Q}_3[z(t)]$, we return to (61) in order to derive a solution for $\widetilde{T}(t)$ in the closed form. Considering now (61) as a first-order linear ODE with $\widetilde{Q}_3(t)$ already known,

$$\dot{\widetilde{T}} = \widetilde{Q}_3(t)\widetilde{T} - \widetilde{H}, \tag{72}$$

we obtain the solution of (72) as [21]

$$\widetilde{T}(t) = \exp\left(-F\left(t\right)\right)\left[\widetilde{T}_0 - \widetilde{H}\int_0^t \exp\left(F\left(\tau\right)\right)d\tau\right], \tag{73}$$

where

$$F(t) = -\int_0^t \widetilde{Q}_3(\tau)d\tau. \tag{74}$$

However, the integral in the r.h.s of (74) cannot be taken in the closed form, and therefore we cannot provide explicit analytical solutions for $\widetilde{T}(t)$ and $\widetilde{S}(t)$ for *Regime C*.

4 Implications for the Ocean

In this Section we make an attempt to apply the mathematical model above, initially developed for a laboratory 'tank model', to deep convection and inter-basin exchange in the real ocean. Below we compare numerical estimates of some dimensional model parameters to observations during deep convection events in the Greenland Sea.

The subpolar seas (for example, the Greenland Sea) are connected to the Arctic Ocean (from where they get cold water of low salinity), as well as to the mid-latitude/tropical Atlantic Ocean (from where they get warm water of high salinity). In the central areas of the subpolar seas, a mixture of these two water sources form

the thermohaline properties of the upper ocean (T_0 and S_1), which influence the deep convection region (Q_1 in the model, Fig. 1). Following the model design, we take S_0 to be the salinity of the deep levels in the Greenland Sea. T_0 and S_0 in the deep Greenland Sea are close to those in the adjacent areas of the deep North Atlantic, which justifies using the same values in the model design. For the deep convective region in the Greenland Sea (74.5–76°N, 3°W–1°E), the water depth at the convective site is taken $D = 3600$ m.

The model parameters, describing thermohaline water properties and their vertical structure in the region, are derived from EN4 Hadley Center data base[2] (1950–2016, the gridded data set) and ARMOR data base[3] (1993–2016). EN4 data are based on the commonly used World Ocean data-base,[4] but pass a more rigorous error-checking procedure [17]. ARMOR is a novel data-set that merges in situ and satellite-based data into an optimum interpolation gridding procedure [18]. The analysis of the mixed layer depth using both datasets suggests that the characteristic depth of the upper layer in the 'big basin' (e.g. out of the deep convection region) is $d = 150$ m (according to (12), this gives $\widetilde{d} \sim 0.042$). The characteristic salinity of the upper layer of the 'big basin' is $S_1 = 34.7$ and that of the lower layer is $S_0 = 34.9$. The temperature in the 'big basin' is taken $T_0 = $-0.5 °C, which is the mean water temperature below the seasonal thermocline in the region. The coefficient of thermal expansion (α) varies significantly with water pressure, temperature and salinity. For salinity 35, temperature 0 °C and pressure from 0 m to 2000 m, α changes from $0.5 \cdot 10^{-4}$ °C^{-1} to $1.1 \cdot 10^{-4}$ °C^{-1}. For the numerical estimates below we take the values of $\alpha = 0.7 \cdot 10^{-4}$ °C^{-1}. Coefficient of haline contraction only weakly varies with water salinity and pressure and with a good accuracy can be taken as $\beta = 7.6 \cdot 10^{-4}$.

Substituting the model parameters above in (9) and (6), we get the characteristic temperature $T_s \sim 2.17$ °C and the upper threshold for temperature anomaly $T_{nil} \sim$-1.99 °C. The latter estimate means that during a deep convective event water temperature in the deep convective site should be at least 2 °C lower than in the neighboring ocean. This agrees fairly well with existing observations. Thus, during deep convection events in the central Greenland Sea, it has been registered a decrease of potential temperature from (-0.8)–(-0.5) °C to (-1.9)–(-1.3) °C, i.e. by 0.5–1.4 °C [6, 25]. Also, in [20] it is registered up to 0.5 °C temperature drop in the deep convection chimney in the northern Greenland Sea, compared to the surrounding ocean.

It is worth mentioning that if we make the same estimates for the case of the fresh upper layer (by setting $S_1 = 0$ and retaining the values of all other parameters), we get $T_s \sim 378$ °C, $T_{nil} \sim$-273.15 °C—a tremendously low temperature anomaly that makes the model with the fresh upper layer not directly applicable to the real ocean phenomena.

Numerical estimates of other model parameters, dependent on the sea-surface flux H, are more challenging since the derived solutions are sensitive to the values of the non-dimensional heat flux $\widetilde{H}$, which, in turn, depends on the 'inverse hydraulic

---

[2] https://www.metoffice.gov.uk/hadobs/en4/.

[3] http://marine.copernicus.eu/.

[4] https://www.nodc.noaa.gov/OC5/WOD13/.

resistance' C (see (10), (11), and (15))—a free phenomenological model parameter that characterizes the intensity of the upper ocean volume flux relative to that at mid-depth and in the deep ocean. Estimating of this latter parameter is not a straightforward task due to complexity of the Greenland Sea exchange with the surrounding basins.

5 Conclusions

In the present chapter we performed a generalization of the Whitehead's 'tank model' to the case of non-zero salinity of upper ocean layer, which makes the model applicable for real-ocean phenomena. Indeed, while maintaining a fresh water layer in a laboratory apparatus is a manageable technical task, in particular, successfully implemented in the tank experiments reported by [38–40], the same assumption is not applicable for the open-ocean, where the difference in salinity between the upper and the mid-depth layers in the subpolar regions forms a few percent.

At the same time, the introduction of the saline upper layer did not bring much of a conceptual change to the model from the purely mathematical standpoint. Indeed, the results with the non-zero salinity of the upper ocean S_1 are equivalent to those with fresh upper layer, when the parameter S_0 in the 'big basin' is treated as the difference between the water salinity of the lower and of the upper layers. As it was discussed in Sect. 2.2, while the dimensional model equations are modified, the properly normalized non-dimensional equations are not. Therefore, most of the results of the model with the fresh upper layer reported previously [5, 37] are inherited in the case of the saline upper layer. Importantly, in the case of the constant (time-independent) sea-surface heat flux, for a given set of the model parameters, the steady state of the model is unique and stable for any of three possible dynamic regimes (*Regimes A-C*).

While the theoretical analysis of the 'tank model' reported in earlier publications was primarily focused on its steady states, in the present chapter we explored the transitional dynamics of the nonlinear model in detail. We derived exact analytical solutions for the nonlinear model. With high complexity of the hydrodynamic phenomena, deriving exact analytical solutions of dynamic equations is possible only for a limited number of fluid dynamic models in general, and of ocean dynamic models in particular. In this respect, we regard this study as a certain contribution to a collection of analytically tractable fluid dynamics/ocean models.

Although strongly simplifying oceanographic conditions in the subpolar seas, the present model can be used for exploring a link between the intensity of the convection in the subpolar basin and the intensity of its exchange with the neighbouring areas of the North Atlantic. In particular, for a given configuration of the model parameters, the model provides threshold values for a heat release from the ocean, that results in a non-zero flux in the lower layer (the transition from *Regime A* to *Regime B*), as well as in a change in the direction of the mid-depth flux (the transition from *Regime B* to *Regime C*). The change from one regime to another results in different dependences

between the deep convection intensity and the intensity of the AMOC, as well as of variations of the thermohaline properties of the outflow with intensification of the heat release from the ocean to the atmosphere in a subpolar basin (see also [5]). The implications of these results need to be further explored in the oceanographic framework.

Despite its conceptual simplicity, the 'tank model' manifests interesting dynamics with a rich variety of possible dynamic regimes. Analytical methods are applicable not only for the simplest case of the constant surface heat flux studied here. It is important extending the theoretical analysis to more complex setups with time-varying heat fluxes. Allowing for the non-linearity of the equation of state of ocean water by assuming dependence of the coefficient of thermal expansion (α) on temperature and depth is also important, as this will modify the model dynamics in the areas of deep convection. These modifications will further bring the model closer to the real ocean conditions and allow for a richer behavior of the dynamic system.

References

1. Alekseev GV, Johannessen OM, Korablev AA, Ivanov VV, Kovalevsky DV (2001a) Interannual variability in water masses in the Greenland Sea and adjacent areas. Polar Res 20(2):201–208. https://doi.org/10.1111/j.1751-8369.2001.tb00057.x, https://onlinelibrary.wiley.com
2. Alekseev GV, Johannessen OM, Kovalevskii DV (2001b) Development of convective motions under the effect of local perturbations of sea-surface density. Izvestiya-Atmos Ocean Phys 37(3):341–350
3. Androsov A, Rubino A, Romeiser R, Sein DV (2005) Open-ocean convection in the Greenland Sea: preconditioning through a mesoscale chimney and detectability in SAR imagery studied with a hierarchy of nested numerical models. Meteorologische Zeitschrift 14(6):693–702. https://doi.org/10.1127/0941-2948/2005/0078
4. Aranson IS, Afraimovich VS, Rabinovich MI (1989) Multidimensional strange attractors and turbulence. Sov Sci Rev Sect C Math Phys Rev 8:293–376
5. Bashmachnikov IL, Kovalevsky DV (2019) Exact solutions and stability analysis of a nonlinear model of open-ocean deep convection that allows multiple steady states. Discontinuity, Nonlinearity, and Complexity 8(2):169–186. https://doi.org/10.5890/DNC.2019.06.005
6. Bönisch G, Blindheim J, Bullister JL, Schlosser P, Wallace DWR (1997) Long-term trends of temperature, salinity, density, and transient tracers in the central Greenland Sea. J Geophys Res: Oceans 102(C8):18553–18571. https://doi.org/10.1029/97JC00740, https://agupubs.onlinelibrary.wiley.com
7. Broecker WS (1998) Paleocean circulation during the last deglaciation: a bipolar seesaw? Paleoceanography 13(2):119–121. https://doi.org/10.1029/97PA03707, https://agupubs.onlinelibrary.wiley.com
8. Brugge R, Jones HL, Marshall JC (1991) Non-hydrostatic ocean modelling for studies of open-ocean deep convection. In: Chu PC, Gascard JC (eds) Deep convection and deep water formation in the oceans. Elsevier Oceanography Series, vol 57. Elsevier, pp 325–340. https://doi.org/10.1016/S0422-9894(08)0075-8, http://www.sciencedirect.com/science/article/pii/S0422989408700758

9. Buckley MW, Marshall J (2016) Observations, inferences, and mechanisms of the Atlantic Meridional Overturning Circulation: a review. Rev Geophys 54(1):5–63. https://doi.org/10.1002/2015RG000493, https://agupubs.onlinelibrary.wiley.com

10. Cessi P (1994) A simple box model of stochastically forced thermohaline flow. J Phys Oceanogr 24(9):1911–1920. https://doi.org/10.1175/1520-0485(1994)024<1911:ASBMOS>2.0.CO;2

11. Chu PC (1991) Geophysics of deep convection and deep water formation in oceans. In: Chu PC, Gascard JC (eds) Deep convection and deep water formation in the oceans. Elsevier Oceanography Series, vol 57. Elsevier, pp 3–16. https://doi.org/10.1016/S0422-9894(08)70057-6, http://www.sciencedirect.com/science/article/pii/S0422989408700576

12. Ciani D, Carton X, Bashmachnikov I, Chapron B, Perrot X (2015) Influence of deep vortices on the ocean surface. Discont Nonlinearity Complex 4(3):281–311. https://doi.org/10.5890/DNC.2015.09.006

13. Cuffey KM, Clow GD (1997) Temperature, accumulation, and ice sheet elevation in central Greenland through the last deglacial transition. J Geophys Res: Oceans 102(C12):26383–26396. https://doi.org/10.1029/96JC03981, https://agupubs.onlinelibrary.wiley.com

14. Dickson RR, Osborn TJ, Hurrell JW, Meincke J, Blindheim J, Adlandsvik B, Vinje T, Alekseev G, Maslowski W (2000) The Arctic Ocean response to the North Atlantic Oscillation. J Clim 13(15):2671–2696. https://doi.org/10.1175/1520-0442(2000)013<2671:TAORTT>2.0.CO;2

15. Dijkstra HA (2005) Nonlinear physical oceanography: a dynamical systems approach to the large-scale ocean circulation and El Niño, 2nd edn. Publishers, Dordrecht/Norwell, Mass, Kluwer Acad

16. Garwood RW (1991) Enhancements to deep turbulent entrainment. In: Chu PC, Gascard JC (eds) Deep convection and deep water formation in the oceans. Elsevier Oceanography Series, vol 57. Elsevier, pp 197–213. https://doi.org/10.1016/S0422-9894(08)70068-0, http://www.sciencedirect.com/science/article/pii/S0422989408700680

17. Good SA, Martin MJ, Rayner NA (2013) EN4: quality controlled ocean temperature and salinity profiles and monthly objective analyses with uncertainty estimates. J Geophys Res: Oceans 118(12):6704–6716. https://doi.org/10.1002/2013JC009067, https://agupubs.onlinelibrary.wiley.com

18. Guinehut S, Dhomps AL, Larnicol G, Le Traon PY (2012) High resolution 3-D temperature and salinity fields derived from in situ and satellite observations. Ocean Sci 8(5):845–857. https://doi.org/10.5194/os-8-845-2012, https://www.ocean-sci.net/8/845/2012/

19. Johannessen OM, Sandven S, Johannessen JA (1991) Eddy-related winter convection in the Boreas Basin. In: Chu PC, Gascard JC (eds) Deep convection and deep water formation in the ocean. Elsevier Oceanography Series, vol 57. Elsevier, pp 87–105. https://doi.org/10.1016/S0422-9894(08)70062-X, http://www.sciencedirect.com/science/article/pii/S042298940870062X

20. Johannessen OM, Lygre K, Eldevik T (2013) Convective chimneys and plumes in the Northern Greenland Sea, American Geophysical Union (AGU), pp 251–272. https://doi.org/10.1029/158GM17, https://agupubs.onlinelibrary.wiley.com

21. Kamke E (1959) Differentialgleichungen: Lösungsmethoden und Lösungen. I. Gewöhnliche Differentialgleichungen. [Differential Equations: Solution Methods and Solutions. I. Ordinary differential equations.] 6. verbesserte Auflage. Leipzig

22. Killworth PD (1979) On 'chimney' formations in the ocean. J Phys Oceanogr 9(3):531–554. https://doi.org/10.1175/1520-0485(1979)009<0531:OFITO>2.0.CO;2

23. Kovalevsky DV, Bashmachnikov IL (2020) An analytical model of open-ocean deep convection with multiple steady states. Ocean Model 154:101680. https://doi.org/10.1016/j.ocemod.2020.101680. https://www.sciencedirect.com/science/article/pii/S1463500320301827

24. Lockwood J (2001) Abrupt and sudden climatic transitions and fluctuations: a review. Int J Clim 21(9):1153–1179. https://doi.org/10.1002/joc.630, https://rmets.onlinelibrary.wiley.com

25. Marshall J, Schott F (1999) Open-ocean convection: observations, theory, and models. Rev Geophys 37(1):1–64. https://agupubs.onlinelibrary.wiley.com, https://doi.org/10.1029/98RG02739

26. Marshall J, Armour KC, Scott JR, Kostov Y, Hausmann U, Ferreira D, Shepherd TG, Bitz CM (2014) The ocean's role in polar climate change: asymmetric Arctic and Antarctic responses to greenhouse gas and ozone forcing. Philos Trans R Soc Lond A: Math Phys Eng Sci 372 (2019). https://doi.org/10.1098/rsta.2013.0040, http://rsta.royalsocietypublishing.org/content/372/2019/20130040.full.pdf
27. Mikolajewicz U, Sein DV, Jacob D, Königk T, Podzun R, Semmler T (2005) Simulating Arctic sea ice variability with a coupled regional atmosphere-ocean-sea ice model. Meteorologische Zeitschrift 14(6):793–800. https://doi.org/10.1127/0941-2948/2005/0083
28. Moore GWK, Våge K, Pickart RS, Renfrew IA (2015) Decreasing intensity of open-ocean convection in the Greenland and Iceland seas. Nat Clim Change 5(9):877. https://doi.org/10.1038/nclimate2688
29. Nagurnyi AP, Bogorodskii PV, Popov AV, Svyashchennikov PN (1985) Intense formation of cold bottom waters on the Greenland Sea surface. Trans (Doklady) USSR Acad Sci (in Russian) 284(2):478
30. Proshutinsky A, Dukhovskoy D, Timmermans ML, Krishfield R, Bamber JL (2015) Arctic circulation regimes. Philosop Trans R Soc Lond A: Math Phys Eng Sci 373(2052). https://doi.org/10.1098/rsta.2014.0160, http://rsta.royalsocietypublishing.org/content/373/2052/20140160.full.pdf
31. Schauer U, Fahrbach E, Østerhus S, Rohardt G (2004) Arctic warming through the Fram Strait: Oceanic heat transport from 3 years of measurements. J Geophys Res: Oceans 109(C6). https://doi.org/10.1029/2003JC001823, https://agupubs.onlinelibrary.wiley.com
32. Scott JR, Marotzke J, Stone PH (1999) Interhemispheric thermohaline circulation in a coupled box model. J Phys Oceanogr 29(3):351–365. https://doi.org/10.1175/1520-0485(1999)029<0351:ITCIAC>2.0.CO;2
33. Stommel H (1961) Thermohaline convection with two stable regimes of flow. Tellus 13(2):224–230. https://doi.org/10.1111/j.2153-3490.1961.tb00079.x, https://onlinelibrary.wiley.com
34. Stommel HM, Young WR (1993) The average T-S relation of a stochastically forced box model. J Phys Oceanogr 23(1):151–158. https://doi.org/10.1175/1520-0485(1993)023<0151:TAROAS>2.0.CO;2
35. Vellinga M, Wu P (2008) Relations between northward ocean and atmosphere energy transports in a coupled climate model. J Clim 21(3):561–575. https://doi.org/10.1175/2007JCLI1754.1
36. Volchenkov D (2010) Critical hydrodynamics: from turbulence to tsunami waves, to synaptic eddies, ch. 12. In: Marcuso RJ (ed) Turbulence: theory. Types and Simulation, NOVA Science Publishers Inc, USA, pp 407–478
37. Whitehead JA (2000) Stratified convection with multiple states. Ocean Model 2(3):109–121. https://doi.org/10.1016/S1463-5003(00)00012-3, http://www.sciencedirect.com/science/article/pii/S1463500300000123
38. Whitehead JA (2009) Abrupt transitions and hysteresis in thermohaline laboratory models. J Phys Oceanogr 39(5):1231–1243. https://doi.org/10.1175/2008JPO4087.1
39. Whitehead JA, Bradley K (2006) Laboratory studies of stratified convection with multiple states. Ocean Model 11(3):333–346. https://doi.org/10.1016/j.ocemod.2005.01.002, http://www.sciencedirect.com/science/article/pii/S1463500305000119
40. Whitehead JA, Raa LT, Tozuka T, Keller JB, Bradley K (2005) Laboratory observations and simple models of slow oscillations in cooled salt-stratified bodies. Tellus A 57(5):798–809. https://doi.org/10.1111/j.1600-0870.2005.00150.x, https://onlinelibrary.wiley.com
41. Zickfeld K, Slawig T, Rahmstorf S (2004) A low-order model for the response of the Atlantic thermohaline circulation to climate change. Ocean Dyn 54(1):8–26. https://doi.org/10.1007/s10236-003-0054-7

On the Necessary Conditions for Preserving the Nonnegative Cone: Mixed Diffusion

Messoud Efendiev and Vitali Vougalter

Abstract The chapter deals with the easily verifiable necessary condition of the preservation of the nonnegativity of the solutions of a system of parabolic equations in the case of the mixed diffusion when the standard Laplacian in the first m variables is added to the Laplace operator in the rest of the variables in a fractional power in the space of an arbitrary dimension. This necessary condition is crucial for the applied analysis community since it imposes the necessary form of the system of equations that must be treated mathematically.

1 Introduction

The solutions of various systems of convection-diffusion-reaction equations arising in biology, physics or engineering describe such quantities as population densities, pressure or concentrations of nutrients and chemicals. Hence, a natural property to require for the solutions is their nonnegativity. Models that do not guarantee the nonnegativity are not valid or break down for small values of the solution. In many situations, showing that a particular model fails to preserve the nonnegativity leads to the better understanding of the model and its limitations. One of the first steps in analyzing ecological or biological or bio-medical models mathematically is to test whether solutions originating from the nonnegative initial data remain nonnegative (as long as they exist). In other words, the model under consideration ensures that the nonnegative cone is positively invariant. We recall that if the solutions (of a given

M. Efendiev (✉)
Helmholtz Zentrum München, Institut für Computational Biology, Ingolstädter Landstrasse 1, Neunerberg 85764, Germany
e-mail: messoud.efendiyev@marmara.edu.tr

Department of Mathematics, Marmara University, Istanbul, Turkey

V. Vougalter
Department of Mathematics, University of Toronto, Toronto, ON M5S 2E4, Canada
e-mail: vitali@math.toronto.edu

evolution PDE) which correspond to the nonnegative initial data remain nonnegative as long as they exist, we say that the system satisfies the nonnegativity property.

For scalar equations the nonnegativity property is a direct consequence of the maximum principle (see [2] and the references therein). However, for systems of equations the maximum principle is not valid. In the particular case of monotone systems the situation resembles the case of scalar equations, sufficient conditions for preserving the nonnegative cone can be found in [9, 10]. For systems including the standard diffusion, transport and general interaction terms (not necessarily monotone) the necessary and sufficient conditions for preserving the nonnegative cones were obtained in [2].

In the present work we aim to prove a simple and easily verifiable criterion, that is, the necessary condition for the nonnegativity of solutions of systems of nonlinear convection-mixed diffusion-reaction equations arising in the modelling of life sciences. We believe that it could provide the modeler with a tool, which is easy to verify, to approach the question of positive invariance of the model.

The present article deals with the preservation of the nonnegativity of solutions of the system of reaction-diffusion equations in the space of an arbitrary dimension $d \in \mathbb{N}, \ d \geq 2$, namely

$$\frac{\partial u}{\partial t} = A[\alpha \Delta_{x,m} - \beta(-\Delta_{x,d-m})^s]u + \sum_{l=1}^{d} \Gamma^l \frac{\partial u}{\partial x_l} - F(u), \qquad (1.1)$$

where the Laplace operators

$$\Delta_{x,m} := \sum_{l=1}^{m} \frac{\partial^2}{\partial x_l^2}, \quad \Delta_{x,d-m} := \sum_{l=m+1}^{d} \frac{\partial^2}{\partial x_l^2}, \quad 1 \leq m \leq d-1, \quad 0 < s < 1,$$

$A, \Gamma^l, \ 1 \leq l \leq d$ are $N \times N$ matrices with constant coefficients, which is relevant to the cell population dynamics in Mathematical Biology. Here $\alpha, \beta > 0$ are constants as well. The case of $\beta = 0$ corresponds to the normal diffusion treated in [2]. The situation when $\alpha = 0$ corresponds to the anomalous diffusion studied recently in [3]. As distinct from the present article, the power of the negative Laplace operator in [3] was restricted to $0 < s < \dfrac{1}{4}$ due to the solvability conditions for the Poisson type equation involving the fractional Laplacian in one dimension (see [14]). Note that the model analogous to (1.1) can be used to study such branches of science as the Damage Mechanics, the temperature distribution in Thermodynamics. In the present work the space variable x corresponds to the cell genotype, $u_k(x, t)$ stands for the cell density distributions for various groups of cells as functions of their genotype and time,

$$u(x, t) = (u_1(x, t), u_2(x, t), \ldots, u_N(x, t))^T.$$

The operator $(-\Delta_{x,d-m})^s$ in system (1.1) describes a particular case of the anomalous diffusion actively treated in the context of different applications in plasma physics and turbulence [1, 4], surface diffusion [5, 7], semiconductors [8] and so on. Anomalous diffusion can be described as a random process of particle motion characterized by the probability density distribution of jump length. The moments of this density distribution are finite in the case of normal diffusion, but this is not the case for the anomalous diffusion. Asymptotic behavior at infinity of the probability density function determines the value s of the power of the negative Laplacian [6]. The operator $(-\Delta_{x,d-m})^s$ is defined by virtue of the spectral calculus. Front propagation problems with anomalous diffusion were treated actively in recent years (see e.g. [11, 12]). The solvability of the single equation involving the Laplacian with drift relevant to the fluid mechanics was studied in [13]. Let us assume here that (1.1) contains the square matrices with the entries constant in space and time

$$(A)_{k,j} := a_{k,j}, \quad (\Gamma^l)_{k,j} := \gamma^l_{k,j}, \quad 1 \le k, j \le N, \quad 1 \le l \le d$$

and that the given matrix A is an $N \times N$ matrix with a positive symmetric part $A + A^* > 0$ (parabolicity assumption) for the sake of the well posedness of problem (1.1). Here A^* denotes the adjoint of matrix A. Hence, system (1.1) can be rewritten in the form

$$\frac{\partial u_k}{\partial t} = \sum_{j=1}^{N} a_{k,j} [\alpha \Delta_{x,m} - \beta(-\Delta_{x,d-m})^s] u_j + \sum_{l=1}^{d} \sum_{j=1}^{N} \gamma^l_{k,j} \frac{\partial u_j}{\partial x_l} - F_k(u), \quad (1.2)$$

where $1 \le k \le N$ and $0 < s < 1$. In the present article the interaction of species term

$$F(u) = (F_1(u), F_2(u), ..., F_N(u))^T,$$

which in principle can be linear, nonlinear or even nonlocal. Let us assume its smoothness in the theorem below for the sake of the well posedness of our problem (1.1), although, we are not focused on the well posedness issue in the present work. From the perspective of applications, the space dimension can be chosen arbitrarily, $d \in \mathbb{N}, d \ge 2$ since the space variable here corresponds to the cell genotype but not to the usual physical space. Let us denote the inner product as

$$(f(x), g(x))_{L^2(\mathbb{R}^d)} := \int_{\mathbb{R}^d} f(x)\bar{g}(x)dx. \quad (1.3)$$

As for the vector functions, their inner product is defined using their components as

$$(u, v)_{L^2(\mathbb{R}^d, \mathbb{R}^N)} := \sum_{k=1}^{N} (u_k, v_k)_{L^2(\mathbb{R}^d)}. \quad (1.4)$$

Obviously, (1.4) induces the norm

$$\|u\|^2_{L^2(\mathbb{R}^d,\mathbb{R}^N)} = \sum_{k=1}^{N} \|u_k\|^2_{L^2(\mathbb{R}^d)}.$$

By the nonnegativity of a vector function below we mean the nonnegativity of the each of its components. Our concern is not the study of the existence of solutions but their qualitative behavior. Hence, in the sequel we assume that for any initial data

$$u_0 \in K^+ := \{u : \mathbb{R}^d \to \mathbb{R}^N \mid u_i(x,t) \geq 0 \ a.e. \ in \ \mathbb{R}^d, \ i = 1, ..., N\}$$

there exists a unique solution (satisfying the appropriate estimates) to carry out our calculations. Our main proposition is as follows.

Theorem 1 *Let $F : \mathbb{R}^N \to \mathbb{R}^N$, such that $F \in C^1$, the initial condition for problem (1.1) is $u(x, 0) = u_0(x) \geq 0$ and $u_0(x) \in L^2(\mathbb{R}^d, \mathbb{R}^N)$, $d, N \in \mathbb{N}$, $d, N \geq 2$. Then in order to preserve the non-negative cone for system (1.1) the necessary condition is that the matrices A and Γ are diagonal and for all $1 \leq k \leq N$*

$$F_k(s_1, ..., s_{k-1}, 0, s_{k+1}, ..., s_N) \leq 0 \tag{1.5}$$

holds , where $s_l \geq 0$ and $1 \leq l \leq N$, $l \neq k$.

Remark 1 In the case of the linear interaction of species, namely when $F(u) = Lu$, where L is a matrix with elements $b_{i,j}$, $1 \leq i, j \leq N$ constant in space and time, our necessary condition leads to the condition that the matrix L must be essentially nonpositive, that is $b_{i,j} \leq 0$ for $i \neq j$, $1 \leq i, j \leq N$.

Remark 2 Our proof yields that, the necessary condition for preserving the nonnegative cone is carried over from the ODE (the spatially homogeneous case, as described by the ordinary differential equation $u'(t) = -F(u)$) to the case of the anomalous diffusion and the convective drift term.

Remark 3 In the forthcoming papers we intend to consider the following cases:

(a) the necessary and sufficient conditions of the present work,
(b) the density-dependent diffusion matrix,
(c) the stochastic perturbation of the deterministic case,
(d) the effect of the delay term in the cases (a), (b) and (c).

Remark 4 Note that in the present work as distinct from [3] we do not assume the nonnegativity of the off diagonal elements of the matrix A.

    We proceed to the proof of our main statement.

2   The Preservation of the Nonnegativity of the Solution of the System with Mixed Diffusion

Proof of Theorem 1. We note that the maximum principle actively used for the studies of solutions of single parabolic equations does not apply to systems of such equations. Let us consider a time independent, square integrable, nonnegative vector function $v(x)$ and estimate

$$\left(\left.\frac{\partial u}{\partial t}\right|_{t=0}, v\right)_{L^2(\mathbb{R}^d, \mathbb{R}^N)} = \left(\lim_{t\to 0^+} \frac{u(x, t) - u_0(x)}{t}, v(x)\right)_{L^2(\mathbb{R}^d, \mathbb{R}^N)}.$$

By virtue of the continuity of the inner product, the right side of the equality above is equal to

$$\lim_{t\to 0^+} \frac{(u(x, t), v(x))_{L^2(\mathbb{R}^d, \mathbb{R}^N)}}{t} - \lim_{t\to 0^+} \frac{(u_0(x), v(x))_{L^2(\mathbb{R}^d, \mathbb{R}^N)}}{t}. \tag{2.1}$$

We choose the initial condition for our system $u_0(x) \geq 0$ and the constant in time vector function $v(x) \geq 0$ to be orthogonal to each other in $L^2(\mathbb{R}^d, \mathbb{R}^N)$. This can be achieved, for example for

$$u_0(x) = (\tilde{u}_1(x), \ldots, \tilde{u}_{k-1}(x), 0, \tilde{u}_{k+1}(x), \ldots, \tilde{u}_N(x)), \quad v_j(x) = \tilde{v}(x)\delta_{j,k}, \tag{2.2}$$

with $1 \leq j \leq N$, where $\delta_{j,k}$ is the Kronecker symbol and $1 \leq k \leq N$ is fixed. Hence, the second term in (2.1) vanishes and (2.1) is equal to

$$\lim_{t\to 0^+} \frac{\sum_{k=1}^N \int_{\mathbb{R}^d} u_k(x, t)v_k(x)dx}{t} \geq 0$$

by means of the nonnegativity of all the components $u_k(x, t)$ and $v_k(x)$ involved in the formula above. Hence, we obtain

$$\sum_{j=1}^N \int_{\mathbb{R}^d} \left.\frac{\partial u_j}{\partial t}\right|_{t=0} v_j(x)dx \geq 0.$$

By means of (2.2), only the *k*th component of the vector function $v(x)$ is nontrivial. This gives us

$$\int_{\mathbb{R}^d} \left.\frac{\partial u_k}{\partial t}\right|_{t=0} \tilde{v}(x)dx \geq 0.$$

Therefore, by means of (1.2) we derive

$$\int_{\mathbb{R}^d} \left[\sum_{j=1,\ j\neq k}^{N} a_{k,j}[\alpha\Delta_{x,m} - \beta(-\Delta_{x,d-m})^s]\tilde{u}_j(x) + \sum_{l=1}^{d}\sum_{j=1,\ j\neq k}^{N} \gamma_{k,j}^{l}\frac{\partial \tilde{u}_j}{\partial x_l} - \right.$$

$$\left. - F_k(\tilde{u}_1(x), \ldots, \tilde{u}_{k-1}(x), 0, \tilde{u}_{k+1}(x), \ldots, \tilde{u}_N(x)) \right]\tilde{v}(x)dx \geq 0.$$

Since the nonnegative, square integrable function $\tilde{v}(x)$ can be chosen arbitrarily, we arrive at

$$\sum_{j=1,\ j\neq k}^{N} a_{k,j}[\alpha\Delta_{x,m} - \beta(-\Delta_{x,d-m})^s]\tilde{u}_j(x) + \sum_{l=1}^{d}\sum_{j=1,\ j\neq k}^{N} \gamma_{k,j}^{l}\frac{\partial \tilde{u}_j}{\partial x_l} -$$

$$- F_k(\tilde{u}_1(x), \ldots, \tilde{u}_{k-1}(x), 0, \tilde{u}_{k+1}(x), \ldots, \tilde{u}_N(x)) \geq 0 \quad a.e. \qquad (2.3)$$

For the purpose of the scaling, we replace all the $\tilde{u}_j(x)$ by $\tilde{u}_j\left(\dfrac{x}{\varepsilon}\right)$ in the inequality above, where $\varepsilon > 0$ is a small parameter. This gives us

$$\sum_{j=1,\ j\neq k}^{N} a_{k,j}\left[\frac{\alpha}{\varepsilon^2}\Delta_{y,m} - \frac{\beta}{\varepsilon^{2s}}(-\Delta_{y,d-m})^s\right]\tilde{u}_j(y) + \sum_{l=1}^{d}\sum_{j=1,\ j\neq k}^{N} \frac{\gamma_{k,j}^{l}}{\varepsilon}\frac{\partial \tilde{u}_j(y)}{\partial y_l} -$$

$$- F_k(\tilde{u}_1(y), ..., \tilde{u}_{k-1}(y), 0, \tilde{u}_{k+1}(y), ..., \tilde{u}_N(y)) \geq 0 \quad a.e. \qquad (2.4)$$

Obviously, the $\dfrac{1}{\varepsilon^2}$ term in the left side of (2.4) is the leading one as $\varepsilon \to 0$. In the case of $a_{k,j} < 0$ we can choose here $\tilde{u}_j(y) = e^{y^2}$ in a neighborhood of the origin, smooth and decaying to zero at the infinity. A trivial calculation yields that $\Delta_{y,m}\tilde{u}_j(y) > 0$ near the origin. If $a_{k,j} > 0$, then we can consider $\tilde{u}_j(y) = e^{-y^2}$ around the origin, smooth and tending to zero at the infinity. An easy computation shows that $\Delta_{y,m}\tilde{u}_j(y) < 0$ in a neighborhood the origin. Thus, the left side of (2.4) can be made as negative as possible which will violate inequality (2.4). Note that the last term in the left side of (2.4) will remain bounded. Therefore, for the matrix A involved in system (1.1), the off diagonal terms should vanish, such that

$$a_{k,j} = 0, \quad 1 \leq k, j \leq N, \quad k \neq j.$$

Hence, from (2.4) we arrive at

$$\sum_{l=1}^{d}\sum_{j=1,\ j\neq k}^{N} \frac{\gamma_{k,j}^{l}}{\varepsilon}\frac{\partial \tilde{u}_j(y)}{\partial y_l} -$$

$$- F_k(\tilde{u}_1(y), ..., \tilde{u}_{k-1}(y), 0, \tilde{u}_{k+1}(y), ..., \tilde{u}_N(y)) \geq 0 \quad a.e. \qquad (2.5)$$

In the case of $\gamma_{k,j}^l < 0$ involved in the sum in the left side of (2.5), we can choose $\tilde{u}_j(y) = e^{\sqrt{y^2+1}}$ in a neighborhood of the origin, smooth and decaying to zero at the infinity, such that

$$\frac{\partial \tilde{u}_j(y)}{\partial y_l} = \frac{y_l}{\sqrt{y^2+1}} e^{\sqrt{y^2+1}} > 0, \quad y_l > 0$$

near the origin. If $\gamma_{k,j}^l > 0$, we consider $\tilde{u}_j(y) = e^{-\sqrt{y^2+1}}$ near the origin, smooth and decaying to zero at the infinity, such that

$$\frac{\partial \tilde{u}_j(y)}{\partial y_l} = -\frac{y_l}{\sqrt{y^2+1}} e^{-\sqrt{y^2+1}} < 0, \quad y_l > 0$$

in a neighborhood of the origin. By making the parameter ε sufficiently small, we can violate the inequality in (2.5). This yields for $1 \leq l \leq d$ that

$$\gamma_{k,j}^l = 0, \quad 1 \leq k, j \leq N, \quad k \neq j.$$

Therefore, by virtue of (2.3) we arrive at

$$F_k(\tilde{u}_1(x), ..., \tilde{u}_{k-1}(x), 0, \tilde{u}_{k+1}(x), ..., \tilde{u}_N(x)) \leq 0 \quad a.e.,$$

where $\tilde{u}_j(x) \geq 0$ and $\tilde{u}_j(x) \in L^2(\mathbb{R}^d)$ with $1 \leq j \leq N, \ j \neq k$. □

Remark 5 Let us assume that the components of the reaction term satisfy for all $1 \leq k \leq N$

$$F_k(t, s_1, ..., s_{k-1}, 0, s_{k+1}, ..., s_N) \leq 0,$$

where $s_l \geq 0$ with $1 \leq l \leq N, \ l \neq k$ and $F \in C_{t,x}^1, \ t \in [0, \tau], \ x \in \mathbb{R}^d$ for some $\tau > 0$. Then it is not difficult to see that the analog of Theorem 1 holds.

References

1. Carreras B, Lynch V, Zaslavsky G (2001) Anomalous diffusion and exit time distribution of particle tracers in plasma turbulence model. Phys Plasmas 8:5096–5103
2. Efendiev MA (2013) Evolution equations arising in the modelling of life sciences. In: International series of numerical mathematics, vol 163. Birkhäuser/Springer, Basel, 217 pp
3. Efendiev MA, Vougalter V (2021) Verification of biomedical processes with anomalous diffusion, transport and interaction of species. In: Nonlinear dynamics, chaos, and complexity. Springer. https://doi.org/10.1007/978-981-15-9034-4_5
4. Solomon T, Weeks E, Swinney H (1993) Observation of anomalous diffusion and Lévy flights in a two-dimensional rotating flow. Phys Rev Lett 71:3975–3978
5. Manandhar P, Jang J, Schatz GC, Ratner MA, Hong S (2003) Anomalous surface diffusion in nanoscale direct deposition processes. Phys Rev Lett 90:4043–4052

6. Metzler R, Klafter J (2000) The random walk's guide to anomalous diffusion: a fractional dynamics approach. Phys Rep 339:1–77
7. Sancho J, Lacasta A, Lindenberg K, Sokolov I, Romero A (2004) Diffusion on a solid surface: anomalous is normal. Phys Rev Lett 92:250601
8. Scher H, Montroll E (1975) Anomalous transit-time dispersion in amorphous solids. Phys Rev B 12:2455–2477
9. Smith H (2008) Monotone dynamical systems. An introduction to the theory of competitive and cooperative systems, mathematical surveys and monographs, vol 41. American Mathematical Society
10. Volpert AI, Volpert VA, Volpert VA (1994) Traveling wave solutions of parabolic systems. Translations of mathematical monographs. American Mathematical Society, Providence, RI, p 448
11. Volpert VA, Nec Y, Nepomnyashchy AA (2010) Exact solutions in front propagation problems with superdiffusion. Phys D 239(3–4):134–144
12. Volpert VA, Nec Y, Nepomnyashchy AA (2013) Fronts in anomalous diffusion-reaction systems. Philos Trans R Soc Lond Ser A Math Phys Eng Sci 371(1982):20120179, 18pp
13. Vougalter V, Volpert V (2012) On the solvability conditions for the diffusion equation with convection terms. Commun Pure Appl Anal 11(1):365–373
14. Vougalter V, Volpert V (2018) Solvability of some integro-differential equations with anomalous diffusion. Regularity and stochasticity of nonlinear dynamical systems. Nonlinear system complex, vol 21. Springer, Cham, pp 1–17

Multi-scale Analysis of Urban Spatial Structures Acquired from *OpenStreetMap*

Dimitri Volchenkov and Veniamin Smirnov

In memoriam of Valentin Afraimovich (1945–2018), a visionary scientist, respected colleague, generous mentor, and loyal friend.

Abstract We propose computationally feasible statistical algorithms for the automated assessment of isolation and integration of urban locations and neighborhoods by using maps acquired from the *OpenStreetMap* service. Integration and isolation defined by observing the properties of scale-dependent random walks on city street maps are not always opposites. While isolation worsens economic and social mobility prospects in sprawling metropolitan areas, some secluded places homing the wealthiest can be characterized as being in *integrated isolation* in the city.

1 Introduction

Urbanization has been the dominant demographic trend in the entire world during the last half century. Rural to urban migration, international migration, and the reclassification or expansion of existing city boundaries have been among the major reasons for increasing urban population. The essentially fast growth of cities in the last decades urgently calls for a profound insight into the common principles stirring the structure of urban developments all over the world [1, 2].

D. Volchenkov (✉) · V. Smirnov
Department of Mathematics and Statistics, Broadway and Boston, Texas Tech University, Lubbock, TX 79409-1042, USA
e-mail: dimitri.volchenkov@ttu.edu

V. Smirnov
e-mail: veniamin.smirnov@ttu.edu

A belief in the influence of the built environment on humans was common in architectural and urban thinking for centuries [2, 3]. Cities generate more interactions with more people than rural areas because they are central places of trade that benefit those who live there. People moved to cities because they intuitively perceived the advantages of urban life [1]. City residence converted a compact space pattern into a pattern of relationships by constraining mutual proximity between people. Spatial organization of a place has an extremely important effect on the way people moving through spaces and meeting other people by chance [4]. Compact neighborhoods can foster casual social interactions among neighbors, while creating barriers to interaction with people outside a neighborhood. Spatial configuration promotes peoples encounters, as well as making it possible for them to avoid each other, shaping social patterns [5].

In our work, we propose feasible statistical algorithms for the automated assessment of isolation and integration of urban locations and neighborhoods by using maps acquired from the *OpenStreetMap* service, a collaborative project to create a free editable map of the world. Map data in the project is collected from scratch by volunteers performing systematic ground surveys using tools such as a handheld GPS unit, a notebook, digital camera, or a voice recorder. The data is then entered into the OpenStreetMap database being freely available for downloading.

In our approach, isolation of a place in a complex fabric of a city is quantified statistically by the relative first-passage time of isotropic random walks (with no self-intersections) on the city street map measured in the decibel scale. The proposed *isolation index* helps to detect sprawling, low-density, auto-dependent urban developments in American cities (see Fig. 2 representing the isolation pattern in the city of Lubbock wandering across planes of West Texas).

Sociologists think that isolation in sprawling metropolitan areas worsens an area's economic prospects and fuel poverty and crime by reducing opportunities for commerce and engendering a sense of isolation in inhabitants [2, 6]. Suburban sprawl also hurts social mobility by lowering a poor child's chances of moving up the economic ladder as an adult [7]. Although structural isolation defined above can be combated by constructing the new city belt roads that would encompass the isolated regions and cut-off neighborhoods, building new roads just makes the problem worse, as increasing road capacity would lead to more traffic and more sprawl in the future.

The *integration index* of a place is introduced in our work as a relative share of *infinite paths* (assuming all of them are equally probable) hosted by the place in the city street map measured also in the decibel scale. Places hosting the lion shares of infinite paths (existing in the connected graphs even if the graphs are small) play the role of hubs featuring the global mobility patterns in the structure (see Fig. 3 representing the integration pattern in the city of Lubbock). By comparing the integration and isolation patterns shown in Figs. 2 and 3, we may see that integration and isolation defined above are not always opposites. Some secluded places in the city can be characterized as being in *integrated isolation*, and this wording is more than an oxymoron, as the *wealthiest* people live there.

In the present work, we report on the patterns of isolation and integration in the city of Lubbock, TX (USA). Our approach may be implemented for the detailed automated expertise illuminating the hidden community structures of any urban pattern and the associated transport networks that may include many transportation modes. In Sect. 2, we discuss spatial graphs of urban environments, as well as the software libraries used by us for getting the urban spatial graph of the city of Lubbock, TX. In Sect. 3, we introduce the major mathematical tool of our analysis, the infinite family of anisotropic scale-dependent random walks (ARW) defined on finite undirected connected graphs. In Sect. 4, we discuss the stationary distributions and balance equation for the ARWs. in Sect. 5, we describe the family of probabilistic metrics attributed to ARWs that are used to quantify accessibility of nodes in the spatial graphs and their roles in hosting the path of different lengths. We apply the proposed measures of isolation and integration to the urban street map of the city of Lubbock in Sect. 6. We conclude in the last section.

2   Spatial Graphs of Urban Environments

In traditional urban researches, the dynamics of an urban pattern come from the landmasses, the physical aggregates of buildings delivering place for people and their activities [1, 8]. The relationships between certain components of the urban texture are often measured along streets and routes considered as edges of a planar graph, while the traffic end points and street junctions are treated as nodes. Such a primary graph representation of urban networks is grounded on relations between junctions through the segments of streets. The usual city map based on Euclidean geometry can be considered as an example of primary city graphs.

In *space syntax theory* [4, 8], built environments are treated as systems of spaces of vision subjected to a configuration analysis. Being irrelevant to the physical distances, spatial graphs representing the urban environments are removed from the physical space. It has been demonstrated in multiple experiments that spatial perception shapes people understanding of how a place is organized and eventually determines the pattern of local movement [8]. The aim of the space syntax study is to estimate the relative proximity between different locations and to associate these distances to the densities of human activity along the links connecting them [9–11].

In our work, we use the graph representation of the transportation system of Lubbock acquired from *OpenStreetMap* file located at https://dataverse.harvard.edu/dataverse/osmnx-street-networks. We used *Python*'s *lxml* library to parse raw data and to construct an adjacency matrix. The data set was cleaned by removing non connected parts, such as the Preston Smith International airport that is not a structural part of the city. There are 10,421 nodes in the spatial graph representing the city street map of Lubbock, including but not limited to residential, secondary, tertiary roads, trunk links, highways etc. Both *Python's Numpy* library and *Matlab* were used to perform calculations, to avoid possible errors, also *Matlab* was used to draw colored maps representing the isolation and integration patterns in the city.

3   Discrete Time Anisotropic Scale-Dependent Random Walks

For a finite set V, $|V| = N$, we denote the space of real functions on V as $\mathfrak{F}(V)$. The inner product $(f, g) = \sum_{i \in V} f(i)g(i)$ associates each pair of functions f, g in the space $\mathfrak{F}(V)$ with a scalar quantity. A graph is a collection of ordered pairs $G \subseteq V \times V$ (called *edges*) with respect to a binary relation of adjacency $\smile$ defined on V (called *vertices*). The linear *adjacency operator* $\mathcal{A}$ is defined on all $f \in \mathfrak{F}(V)$ by $(\mathcal{A}f)(i) = \sum_{j \smile i} f(j)$, where $j \smile i$ is whenever i and j are adjacent. The adjacency operator $\mathcal{A}$ can be uniquely represented (with the fixed canonical basis) by a $N \times N-$ matrix $\mathbf{A}$, the *adjacency matrix* of the graph, such that

$$A_{ij} = \begin{cases} 1, & \text{if } i \text{ and } j \text{ are adjacent,} \\ 0, & \text{otherwise.} \end{cases} \tag{1}$$

The adjacency matrix allows us to analyze graphs and their structure by means of the well known operations with matrices. The adjacency matrix is non-negative and irreducible if there is at least a single path from any vertex to any other vertex in the graph. The entries of its positive integer power, A_{ij}^n equal the numbers of walks of length $n \geq 1$ connecting the vertices i and j in the graph G. Let $\mathbf{deg}_n \in \mathbb{Z}^N$ be the vector whose elements $\deg_n(i)$, $i = 1, \ldots, N$, are the numbers of paths of length $n \geq 1$ available from $i \in V$. The adjacency operator defines the following dynamical system [12],

$$\mathbf{deg}_{n+1} = \mathbf{A} \, \mathbf{deg}_n, \tag{2}$$

mapping the vector $\mathbf{deg}_n$ into the vector $\mathbf{deg}_{n+1}$.

The discrete time *locally anisotropic* (i.e., direction dependent) nearest neighbor *random walks* is defined by the following stochastic matrices:

$$T_{ij}(n+1) = \frac{A_{ij} \, \deg_n(j)}{\deg_{n+1}(i)} = A_{ij} \frac{\sum_{s=1}^{N} A_{js}^n}{\sum_{r=1}^{N} A_{sr}^{n+1}}, \quad n \geq 0. \tag{3}$$

Theorem 1 *In the random walk defined by (3), all possible paths of length $n \geq 1$ starting at the node $i \in V$ of the graph G are chosen with equal probability.*

Proof The first order random walk $T(1)_{ij} = A_{ij}/\deg_1(i)$ is *locally isotropic*, since all 1-paths available for the random walker at every vertex of the graph are chosen with equal probability.

For the random walks of order $n = 2$, the transition probability (3) reads as following:

$$T_{ij}(2) = \frac{A_{ij} \sum_{s=1}^{N} A_{js}}{\sum_{s=1}^{N} A_{is} \sum_{r=1}^{N} A_{sr}}, \tag{4}$$

so that each walk of length 2 starting at the node i is chosen with equal probability. Although all walks of length 2 starting at the node i are *equiprobable* under the transition operator (4), the probabilities of transition to the nearest neighbors from the node i might be different. The nearest neighbors providing more opportunities for lengthy paths than others are more preferable. The resulting random walk (4) is a direction dependent random walk (locally anisotropic). The further conclusion is inductive and self evident.   □

Theorem 2 *The series of locally anisotropic random walks (3) converges as $n \to \infty$ to a random walk, in which all infinitely long paths starting at every node of the graph are equally probable, viz.,*

$$\lim_{n \to \infty} T_{ij}(n) \ = \ T_{ij}(\infty) \ = \ \frac{A_{ij}\psi_{1j}}{\alpha_1\psi_{1i}}, \tag{5}$$

where ψ_1 is the completely positive eigenvector of the graph adjacency matrix $\mathbf{A}$ belonging to its maximal eigenvalue α_1.

Proof The N eigenvalues of the graph adjacency matrix $\mathbf{A}$ are assumed to be ordered, such as $\alpha_1 > \alpha_2 \geq \ldots$. The n−th order degree of the node $i \in V$ is

$$\deg_n(i) \equiv \sum_j (A^n)_{ij} \ = \ \sum_k \alpha_k^n \psi_{ik} \underbrace{\sum_j \psi_{kj}}_{\gamma_k} \ \equiv \ \sum_k \alpha_k^n \gamma_k \psi_{ik}$$
$$= \alpha_1^n \gamma_1 \psi_{i1} \left(1 + \sum_{k>1} \left(\frac{\alpha_k}{\alpha_1}\right)^n \frac{\gamma_k}{\gamma_1} \frac{\psi_{kj}}{\psi_{1j}} \right) \simeq_{n \to \infty} \alpha_1^n \gamma_1 \psi_{i1}, \tag{6}$$

since the last sum in (6) is dominated by the largest eigenvalue α_1 of the adjacency matrix in the limit $n \gg 1$. Therefore

$$\lim_{n \to \infty} T_{ij}(n) \ = \ \frac{A_{ij}\psi_{j1}\gamma_1\alpha_1^{n-1}}{\psi_{i1}\gamma_1\alpha_1^n} \ = \ \frac{A_{ij}\psi_{j1}}{\alpha_1\psi_{i1}}. \tag{7}$$

Finally, it is easy to check that the matrix (5) is a stochastic matrix, since $\sum_j A_{ij}\psi_{j1} = \alpha_1\psi_{i1}$.   □

4 Stationary Distributions and Balance Equations of Anisotropic Random Walks

For a random walk defined on a connected undirected graph, the Perron - Frobenius theorem [13] asserts the unique strictly positive probability vector $\vec{\pi} = (\pi_1, \ldots, \pi_N)$, which is the left eigenvector of the transition matrix $\mathbf{T}$ belonging to the maximal eigenvalue $\mu = 1$, $\vec{\pi}\,\mathbf{T} \ = \ 1 \cdot \vec{\pi}$, is the *stationary distribution* of the random walk on the graph. The condition of *detailed balance* is defined by

$$\pi_i \, T_{ij} \;=\; \pi_j \, T_{ji}, \tag{8}$$

from which it follows that a random walk defined on an undirected graph is *time reversible*: it is also a random walk if considered backward.

Theorem 3 *For the anisotropic random walk $T_{ij}(n)$, $n \geq 1$, the stationary distribution is*

$$\pi_i(n) \;=\; \frac{\deg_n(i) \deg_{n-1}(i)}{2E_n}, \quad 2E_n \equiv \sum_i \deg_n(i) \deg_{n-1}(i). \tag{9}$$

Proof

$$
\begin{aligned}
\sum_i \pi_i(n) \frac{A_{ij} \deg_j(n-1)}{\deg_i(n)} &= \sum_i \frac{\deg_n(i) \deg_{n-1}(i)}{2E_n} \frac{A_{ij} \deg_{n-1}(j)}{\deg_n(i)} \\
&= \frac{\deg_n(j) \deg_{n-1}(j)}{2E_n} \;=\; \pi_j(n).
\end{aligned}
\tag{10}
$$

The detailed balance condition is satisfied by (9):

$$
\begin{aligned}
\pi_i(n) T_{ij}(n) &= \pi_j(n) T_{ji}(n) \\
&= \frac{A_{ij} \deg_{n-1}(i) \deg_{n-1}(j)}{2E_n}.
\end{aligned}
\tag{11}
$$

$\square$

For $n = 1$, the normalization factor $2E_1 = 2E$, where E is the total number of edges in the graph, since $\deg_0(i) = 1$. The stationary distribution equals $\pi_i(1) = \deg_1(i)/2E$, $2E = \sum_i \deg_1(i)$.

Theorem 4 *([14, 15]) For the limiting anisotropic random walk $T_{ij}(\infty)$, the stationary distribution is*

$$\pi_i(\infty) \;=\; \psi_{1i}^2 \tag{12}$$

where ψ_1 is the major eigenvector of the graph adjacency matrix $\mathbf{A}$ belonging to the maximal eigenvalue α_1.

Proof

$$\sum_i \pi_i(\infty) \frac{A_{ij} \psi_{1j}}{\alpha_1 \psi_{1i}} \;=\; \psi_{1j}^2 \;=\; \pi_j(\infty). \tag{13}$$

The detailed balance condition is satisfied by (12):

$$\pi_i(\infty) T_{ij}(\infty) \;=\; \pi_j(\infty) T_{ji}(\infty) \;=\; \frac{A_{ij} \psi_{1i} \psi_{1j}}{\alpha_1}. \tag{14}$$

$\square$

5   Exploring Graphs with Random Walks

The stationary distribution of random walks (3) of length $n \geq 1$ defined on a connected undirected graph $G(V, E)$ determines a unique measure on V, $\mu_n = \sum_{j \in V} \pi_i(n) \delta_j$, with respect to which the transition operator (3) becomes self-adjoint,

$$\widehat{T_{ij}}(n) \;=\; \left(\hat{\pi}^{1/2}(n)\, \mathbf{T}(n)\, \hat{\pi}^{-1/2}(n) \right)_{ij} \tag{15}$$

where $\hat{\pi}(n)$ is the diagonal matrix of the densities of nodes $\pi_i(n)$ (9) in the random walk $T_{ij}(n)$.

In the present section, we remove the index n (the length of equally probable walks in (3)) from our notations. All formulas and conclusions discussed and derived in this section are equally suitable for any anisotropic random walks.

Diagonalizing the symmetrized transition matrix (15), we obtain $\widehat{\mathbf{T}} \;=\; \Psi\, \mathbf{M}\, \Psi^\top$, where Ψ is an orthonormal matrix of eigenvectors, $\Psi^\top \;=\; \Psi^{-1}$, and $\mathbf{M}$ is a diagonal matrix with entries $1 = \mu_1 > \mu_2 \geq \ldots \geq \mu_N > -1$ (here, we do not consider bipartite graphs, for which $\mu_N = -1$).

1. **The probability to find a random walker in and out of a node:** The Perron-Frobenius eigenvector $\vec{\psi}_1$ belonging to the major eigenvalue $\mu_1 = 1$, $\vec{\psi}_1 \widehat{\mathbf{T}} = \vec{\psi}_1$, determines the density of nodes in the graph G visited by the random walks [2, 16],

$$\pi_i \;=\; \psi_{1,i}^2, \quad i = 1, \ldots, N. \tag{16}$$

   The Euclidean norm of other eigenvectors in the orthogonal complement of $\vec{\psi}_1$, $\sum_{s=2}^{N} \psi_{s,i}^2 = 1 - \pi_i > 0$, is the probability to find a random walker out of $i \in V$. The inverse density of the node i,

$$\mathcal{R}_i \;\equiv\; \frac{1}{\psi_{1,i}^2}, \tag{17}$$

   defines the expected *recurrence time* to the node $i \in V$ [16], characterizing the (local) connection of the node to the graph.

2. **The first-hitting time:** The expected number of steps a *self-avoiding* random walker (never revisiting any visited node) started from the node i needs to reach j for the first time is called the *first-hitting time*, [2, 16]. The first-hitting time satisfies the following equation, $\mathcal{H}_{ij} = 1 + \sum_{i \sim v} \mathcal{H}_{vj} T_{vi}$, withe the boundary condition $\mathcal{H}_{ii} = 0$, reflecting the fact that the first step takes a random walker to a neighbor $v \in V$ of the starting node $i \in V$, and then it has to reach the node j from there. The spectral representation of $\mathcal{H}_{ij}$ [2, 16] is given by

$$\mathcal{H}_{ij} \;=\; \sum_{s=2}^{N} \frac{1}{1 - \mu_s} \left(\frac{\psi_{s,j}^2}{\psi_{1,j}^2} - \frac{\psi_{s,i} \psi_{s,j}}{\psi_{1,i}\, \psi_{1,j}} \right). \tag{18}$$

3. **Random target access time:** The *random target access time* is the expected number of steps required for a self-avoiding random walker to reach a target node chosen randomly in the graph with the stationary density π [2, 16], viz.,

$$\mathcal{T}_G \equiv \sum_{j \in V} \pi_j \, \mathcal{H}_{ij} \;=\; \sum_{s=2}^{N} \frac{1}{1 - \mu_s} \;=\; \sum_{k=2}^{N} \tau_s, \qquad (19)$$

where $\tau_s = (1 - \mu_s)^{-1}$ is the rate parameter describing how quickly the diffusion mode s undergoes [2]. The random target access time (19) is a global spectral characteristic of the graph independent of the starting node $i \in V$.

4. **First-passage time:** The *first-passage time* is the expected number of steps required for a self-avoiding random walker to reach the node $i \in V$ for the first time started from a node randomly chosen in the graph with the stationary density π [2, 16], viz.,

$$\mathcal{F}_i \equiv \sum_{j \in V} \pi_j \, \mathcal{H}_{ji} \;=\; \sum_{s=2}^{N} \frac{1}{1 - \mu_s} \frac{\psi_{s,i}^2}{\psi_{1,i}^2} \;=\; \mathcal{R}_i \sum_{s=2}^{N} \frac{\psi_{s,i}^2}{1 - \mu_s}. \qquad (20)$$

The last equality in (20) establishes a relation between the recurrence time to a node $\mathcal{R}_i$ (the local connection of the node) and the first-passage time $\mathcal{F}_i$ characterizing the (global) *connectedness* of the node in the graph. Several models were developed to study the mean first-passage time taken by a walker to move from an arbitrary source to a target in complex media. For instance, such situations were usually encountered in predatory animals and biological cells, [17].

5. **Commute time:** The *commute time* is the expected number of steps required for a self-avoiding random walker started at $i \in V$ to reach $j \in V$ and then to return back to i [16], viz.,

$$\mathcal{K}_{ij} \equiv \mathcal{H}_{ij} + \mathcal{H}_{ji} \;=\; \sum_{s=2}^{N} \frac{1}{1 - \mu_s} \left(\frac{\psi_{s,i}}{\psi_{1,i}} - \frac{\psi_{s,j}}{\psi_{1,j}} \right)^2 \qquad (21)$$

that introduces the Euclidean metric in the projective space $P\mathbb{R}^{(N-1)}$ of vectors associated to the graph nodes. The average of the commute time with respect to the initial point of random walk, $\sum_i \pi_i \mathcal{K}_{ij} = \mathcal{T}_G + \mathcal{F}_j$, equals the sum of the first passage time to j from a random node in the graph and the random target access time required to reach the random node. The double average of the commute time equals the doubled random target access time, viz., $\sum_{i,j} \pi_i \mathcal{K}_{ij} \pi_j = 2\mathcal{T}_G$.

6 The City of Lubbock Is Running Away

Railroad paved way for Lubbock to become a hub [18]. After the first train steamed into town on Sept. 25, 1909, Lubbock had managed to quadruple its population to 4,000 in a 10-year period. Once town's dusty roads had been covered with bricks,
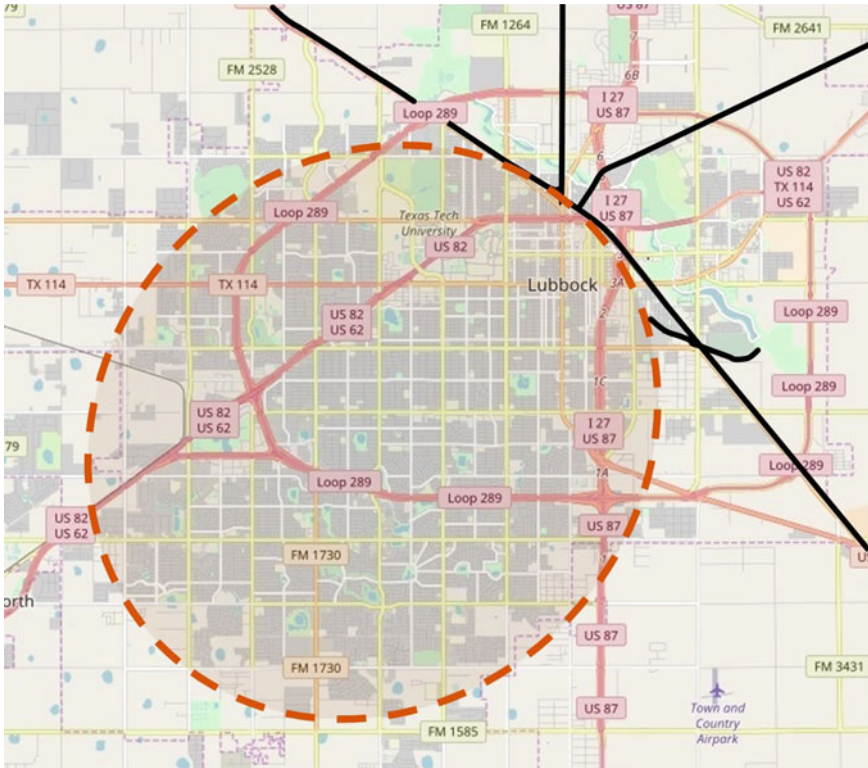
Fig. 1 The city of Lubbock is running away from the lasso of *Loop 289* marking the old city boundaries

Lubbock had been selected as the site of the new *Texas Technological College*, and the county's population had ballooned to almost 40,000 in 1930. Lubbock had accomplished the journey from town to city when *Loop 289* was completed by the mid-1960s (Fig. 1).

Although railway construction enhanced the city status in early days, its maintenance consumed large budgets, was complicated to organize, and had a considerable impact on the urban development of Lubbock. Railways barricade streets, cutting down the number of possible paths people can drive or walk, thus creating neighborhoods isolated from nearby areas. The large urban voids remained in north and east Lubbock cut off from other parts of the city by rails. Not surprising, the city fabric pushed away from the angle formed by the veering railway tracks and grew to the southwest anyhow, running away from the lasso of *Loop 289* marking the old city boundaries (Fig. 1).

The Texas Tech University is still anchored in the center and cannot follow the city running away. Situated on the boundary of the neighborhoods going downhill, the University mediates between the isolation and integration patterns in the city of Lubbock (Fig. 1).
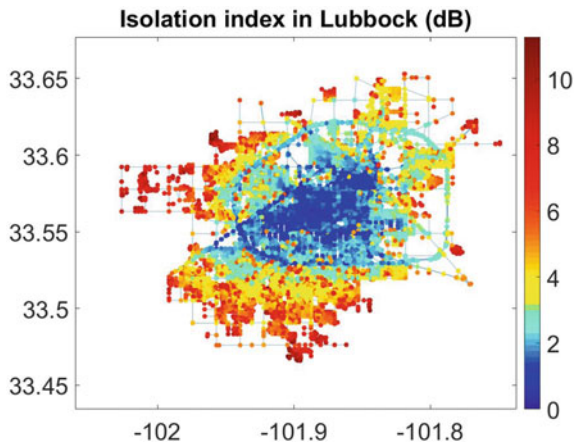
6.1 Isolation Index

Structural isolation is viewed as one of the top risk factors for area's economic, social and environmental prospects [19–24]. The notion of isolation acquires a statistical interpretation by means of random walks [1–3, 25, 26].

While the recurrence time of random walks to a node (17) depends upon the degree of *connectivity* of the node, a *local* structural characteristic of the node in the graph, the first-passage time to the node (20) is a *global* structural characteristic of the node quantifying its *connectedness*, since all possible paths to the node existing in the graph are taken into account by the first-passage time although some paths are rendered more probable than others [2]. The relatively low recurrence times are typical for well connected nodes, disregarding their role for the entire graph structure. For example, a bridge connecting the city districts situated on the opposite banks of a river is vital for the entire urban transportation system despite its limited connectivity to the immediate city neighborhoods [1]. The relatively low first-passage times indicate the high degree of importance of the nodes aggregating many a path for structural integrity of the entire graph even if their connectivity is low [2]. Being a global characteristic of a node in the graph, the first-passage time assigns *absolute accessibility scores* (20) to all nodes of the graph [3] and can be considered as a natural statistical centrality measure of the node within the graph [1]. The vertices of the urban street graph characterized by the shortest first-passage times are easy to reach by whatever origin-destination (Fig. 2). We introduce the *isolation index of a node* in the city street map acquired from the *OpenStreetMap* service by

$$\text{ISL}_i = 10 \cdot \log_{10} \tag{22}$$

in which $\mathcal{F}_i(1)$ is the first- passage time to the node $i \in V$ by isotropic random walks $\mathbf{T}(1)$. Isotropic random walks are insensitive to the structural peculiarities and

Fig. 2 Isolation index of nodes in the city graph of Lubbock, TX acquired from the *OpenStreetMap* service. The colored bar indicates the value of isolation index in the decibel scale—the isolated neighborhoods are red colored. The axis labels are the geographic coordinates

boundaries of the graph, covering all nodes with respect to their immediate connectivity [2]. The isolation index (22) is calculated as relative measure of accessibility and measured in the decibel scale. The high values of the isolation index defined in (22) are attributed to the places, which are difficult to access in comparison to those in a structural focus of a city. The spatial pattern of isolation in the city of Lubbock (red colored on Fig. 2) illuminates the sprawling urban areas homing the low-density communities located out of the old city boundaries. The colored bar in Fig. 2 indicates the value of isolation index in the decibel scale. The axis labels are the geographic coordinates.

6.2 Integration Index

We define the integration index of a node in the graph based on its accessibility by the ARW $\mathbf{T}(\infty)$ introduced by (5). This random walks are extremely sensitive to structural defects and graph boundaries [2, 14, 15]. Our definition is based on the idea of that well integrated places should host the majority of infinitely long paths possible in the spatial graph, eventually determining feasible movement patterns in the city (*see* Fig. 3).

We introduce the *integration index of a node* in the city street map acquired from the *OpenStreetMap* service by

$$\mathrm{Int}_i \;=\; 10 \cdot \log_{10} \frac{\min_{j \in V} \; \mathcal{F}_j(\infty)}{\mathcal{F}_i(\infty)} \; (dB) \tag{23}$$

in which $\mathcal{F}_i(\infty)$ is the first- passage time to the node $i \in V$ by ARW $\mathbf{T}(\infty)$. The walks $\mathbf{T}(\infty)$ are statistically bounded to the nodes hosting the lion share of infinite

Fig. 3 Integration index of nodes in the city graph of Lubbock, TX acquired from the *OpenStreetMap* service. The colored bar indicates the value of integration index in the decibel scale—the integrated neighborhoods are red colored. The axis labels are the geographic coordinates
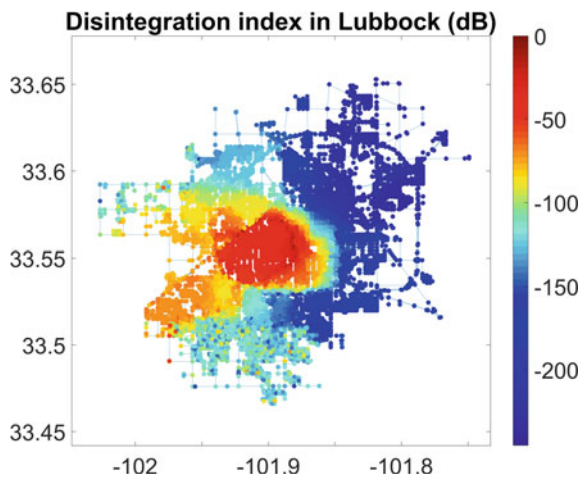
paths and repelling from defects and boundaries in the graph. By definition, the index (23) is somewhat opposite to the isolation index (22), but calculated with respect to anisotropic, direction sensitive walks $\mathbf{T}(\infty)$, not $\mathbf{T}(1)$. The index (23) is measured in the decibel scale, so that places weakly integrated into the city fabric are characterized by large negative numbers. It is evident from Fig. 3 that sprawling areas (apart from the northeastern part of the city cut off the downtown by railways dramatically reducing the number of possible infinitely long paths) are able to statistically accumulate essentially long paths and shift the mobility patterns in the city of Lubbock from the downtown to the southwest periphery.

7   Discussion and Conclusion

We have proposed the novel concepts and related computationally feasible statistical algorithms for the automated assessment of isolation and integration of the places in the urban street maps acquired directly from the *OpenStreetMap* service. We have introduced the isolation and integration indices of a place in the complex urban fabric based on the first-passage times of isotropic and anisotropic random walks defined on the spatial graph of the city. While the isolation index (22) allows for detecting sprawling areas (Fig. 3), the integration index (23) reveals the areas hosting the essentially long paths in the city graph attributed to the major mobility patterns possible in the urban structure (Fig. 2).

Encompassing a big share of possible movements, urban sprawl pulls the highly integrated places in the city of Lubbock out of the downtown, fostering the process of urban decay in the north-eastern parts of the city and at the center. In Fig. 4, we have summarized the distributions of social and economic variables over the city of Lubbock, TX. Lack of structural integration in the north-eastern areas of the city (blue colored) reduce opportunities for commerce, fuel poverty and crime, foster disparity of land prices and social inequality, in the long run. The highest crime rates
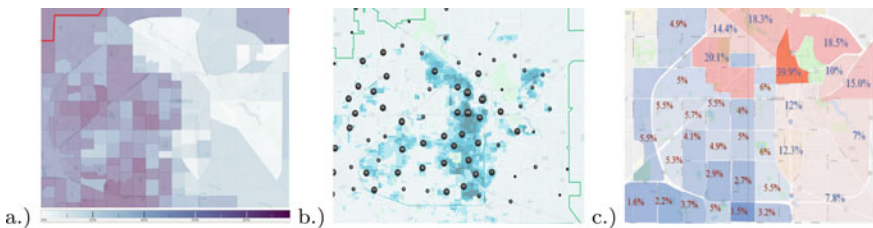

Fig. 4   The distribution of social and economic variables in the city of Lubbock, TX. **a** The racial composition of neighborhoods in Lubbock accordingly the US Census Bureau. The area of white population concentration are dark colored; **b** Lubbock crime rates and statistics density heat map (downloaded on 6/29/2018) from the Turlia website [27]. Trulia uses crime reports to provide valuable information on the relative safety of homes in the US; **c** Unemployment Rate in Lubbock, TX in Oct. 2018 accordingly the US Bureau of Labor Statistics

in the city of Lubbock are observed in the northeastern part of the city barricaded by railways, cutting down the number of paths people can drive or walk dramatically.

Interestingly, the isolation pattern in the city of Lubbock assessed by means of the isolation index (22) and shown in Fig. 2 does not visually match the distributions of the social and economic variables represented on Fig. 4. Furthermore, by comparing the integration and isolation patterns shown in Figs. 2 and 3, we see that statistically defined integration and isolation are not always opposite, since some secluded places in sprawling areas in the wealthy south-western part of Lubbock can be isolated although integrated.

The further development of the city road system (e.g., the new *Loop 88* that will lasso the running away city of Lubbock in *Wolfforth* by 2030) would alleviate isolation (22) by improving accessibility to the south-western sprawls, yet encouraging further sprawl and more road travel and worsening the social and economic conditions in the downtown and on the north-western periphery. The city of Lubbock will keep running southwest.

References

1. Blanchard Ph, Volchenkov D (2009) Mathematical analysis of urban spatial networks. Springer Series Understanding Complex Systems, Berlin, Heidelberg
2. Volchenkov D (2018) Grammar of complexity: from mathematics to a sustainable world. In: World scientific series. Nonlinear Physical Science
3. Volchenkov D, Blanchard PH (2008) Markov chain methods for analyzing urban networks. J Stat Phys 1572–9613 (Online), 13(2):1051–1069
4. Hillier B, Hanson J (1984) The social logic of space (1993, reprint, paperback edition ed). Cambridge University Press, Cambridge
5. Ortega-Andeane P, Jiménez-Rosas E, Mercado-Doménech S, Estrada-Rodrýguez C (2005) Space syntax as a determinant of spatial orientation perception. Int J Psychol 40(1):11–18
6. Chown M (2007) Equation can spot a failing neighborhood. New Sci , Lond
7. Smart Growth America Report (2014) Measuring sprawl 2014. https://www.smartgrowthamerica.org/app/legacy/documents/measuring-sprawl-2014.pdf
8. Hillier B (1999) Space is the machine: a configurational theory of architecture. Cambridge University Press. ISBN 0-521-64528-X
9. Hansen WG (1959) How accessibility shapes land use. J Am Inst Plann 25:73
10. Wilson AG (1970) Entropy Urban Reg Model. Pion Press, London
11. Batty M (2004) A new theory of space syntax. UCL Centre For Advanced Spatial Analysis Publications, CASA Working Paper, vol 75
12. Prisner E (1995) Graph dynamics, Boca Raton. CRC Press, FL
13. Horn RA, Johnson CR (1990) Matrix analysis. Cambridge University Press
14. Burda Z, Duda J, Luck JM, Waclaw B (2009) Localization of the maximal entropy random walk. Phys Rev Lett 102(16):160602. https://doi.org/10.1103/PhysRevLett.102.160602

15. Burda Z, Duda J, Luck JM, Waclaw B (2010) The various facets of random walk entropy. Acta Physica Polonica B 41(5):949–987
16. Lovász L (1993) Random walks on graphs: a survey. Bolyai Society Mathematical Studies, vol 2. Combinatorics, Paul Erdös is Eighty, 1 Keszthely (Hungary)
17. Shlesinger MF (2007) First encounters. Nature 450(1):40
18. Graves L (ed) (1962) A history Lubbock. West Texas Museum Association, Lubbock
19. Ewing R, Meakins G, Hamidi S, Nelson AC (2014) Relationship between urban sprawl and physical activity, obesity, and morbidity—update and refinement. Health Place 26:118–126
20. Berrigan D, Tatalovich Z, Pickle LW, Ewing R, Ballard-Barbash R (2014) Urban sprawl, obesity, and cancer mortality in the United States: cross-sectional analysis and methodological challenges. Int J Health Geograph 13:3
21. James P, Troped PJ, Hart JE, Joshu CE, Colditz GA, Brownson RC, Ewing R, Laden F (2013) Urban sprawl, physical activity, and body mass index: Nurses' Health Study and Nurses' Health Study II. Am J Public Health 103(2):369–75
22. Lee IM, Ewing R, Sesso HD (2009) The built environment and physical activity levels: the Harvard Alumni Health Study. Am J Prev Med 37(4):293–298
23. Ewing R, Brownson RC, Berrigan D (2006) Relationship between urban sprawl and weight of United States youth. Am J Prev Med 31(6):464–74
24. Ewing R, Schmid T, Killingsworth R, Zlot A, Raudenbush S (2003) Relationship between urban sprawl and physical activity, obesity, and morbidity. Am J Health Promot 18(1):47–57
25. Volchenkov D, Blanchard Ph (2008) Intelligibility and first passage times in complex urban networks. Proc R Soc A 464:2153–2167
26. Volchenkov D, Blanchard Ph (2011) Introduction to random walks and diffusions on graphs and databases, vol 10. Springer Series in Synergetics, Berlin, Heidelberg
27. https://www.trulia.com/real_estate/Lubbock-Texas/crime/